Adsorption and Ordering of Merocyanines on the Ag(100) surface

About the interplay of intermolecular and interfacial interactions

DISSERTATION

zur Erlangung des Doktorgrades (Dr. rer. nat.)
der Mathematisch-Naturwissenschaftlichen Fakultät
der Rheinischen Friedrich-Wilhelms-Universität Bonn

vorgelegt von

ANNA JULIANA KNY

aus Lüneburg

Bonn, 2025

Angefertigt mit Genehmigung der Mathematisch-Naturwissenschaftlichen Fakultät der Rheinischen Friedrich-Wilhelms-Universität Bonn.

Gutachter/Betreuer: Prof. Dr. Moritz Sokolowski
Gutachter: Prof. Dr. Christian Kumpf
Gutachter: Prof. Dr. Michael Gottfried

Tag der Promotion: 11.12.2025
Erscheinungsjahr: 2026

Abstract

Merocyanines (MCs) constitute pro-chiral donor-acceptor (D-A) molecules that exhibit high optical transition dipole moments. Although MCs are used in many optoelectronic devices, their chemical bonding to metal interfaces has not yet been investigated. To overcome this knowledge gap, this work presents a first surface science study that characterizes the structure formation of MC monolayers in dependence on the interplay of interfacial and intermolecular interactions.

The analysis was performed for a series of five structurally related, prototypical MCs on the Ag(100) surface. These exhibit a conjugated π-system that consists of a thiophene ring and a thiazole ring connected by a methine bridge. The D-A character of the molecules is induced by a tertiary amine (D) attached to the thiophene ring and a malononitrile group (A) attached to the thiazole ring. Alkyl side chains attached to the tertiary amine and the thiazole ring mainly impact the sterical demand of the MCs.

It could be demonstrated that the interfacial interactions cause the face-on adsorption of the MCs and the commensurate structural growth, while the intermolecular interactions determine the growth of enantiopure structures. Investigations were performed by a series of surface-sensitive techniques including scanning tunneling microscopy (STM), spot profile analyzing low energy electron diffraction (SPA-LEED), photoelectron spectroscopy (PES), and the normal incidence x-ray standing wave (NIXSW) technique. The intermolecular interactions were probed by a systematic variation of the alkyl side groups, leading to different MC phases due to the different sterical demands of the MCs.

The results reveal that hydrogen bonds between the D and A groups of neighboring MCs lead to enantiopure molecular tetramers on the surface. These tetramers are the primary building units of all observed MC phases. On a larger scale, the tetramers arrange in enantiopure long-range ordered structures that grow commensurate with the Ag(100) surface. Tetramers of different handedness are found in the respective mirror domains.

The commensurate growth is induced by strong interfacial interactions of the MCs, accompanied by charge exchange between the molecules and the Ag surface. The interfacial bonding is measurable in molecular adsorption distances that are, for HB238-A, 15% (C) to 24% (N) smaller than the sum of the respective van der Waals radii. In particular, a strong, covalent-like Ag-S binding was found. This manifests in a high vertical and lateral order of the S atoms in combination with short Ag-S bond lengths of 2.5 to 3.1 Å.

The Ag-S bond determines the adsorption sites of the tetramers and thus the commensurate growth of the MC structures. In general, the Ag atop sites were found to be the preferred adsorption sites of the S atoms. However, the intermolecular tetramer-tetramer interactions in the MC structures lift the four-fold symmetry of the tetramers for two of the three observed MC phases, as two MC molecules of the tetramer interact more strongly with the neighboring tetramers. These MC molecules are laterally distorted, resulting in altered intramolecular S S distances of up to +31% and adsorption sites that are symmetrically shifted by up to 1 Å away from the atop adsorption sites towards the bridge positions. Smaller vertical adsorption distances of the distorted molecules to the Ag(100) surface indicate that the distortions weaken the molecular π-system, leading to a stronger interfacial binding of these MCs.

Contents

1. Introduction

This thesis explores the epitaxial growth of prototypical merocyanine molecules on the Ag(100) surface. It contributes to a better understanding of the structure and the stability of merocyanine films used as active layers in organic optoelectronic devices [1, 2].

Recently, devices based on active layers made of organic functional molecules have been under extensive investigations [3–5]. Their broad application spectrum follows from the tunable layer properties. The properties of organic layers result from both the molecular structure and the molecular packing, i.e., from the intermolecular interactions [3, 6, 7]. The molecular structure of such functional molecules usually comprises a large π-system and functional groups, which together allow for an adjustment of the electronic properties to the required needs. In addition, sterical demanding side groups can modify the intermolecular interactions and hence, the molecular packing. Still, controlling the molecular packing in the active layers remains challenging, as most functional molecules form several polymorphic structures, and subtle kinetic effects may lead to different results [8].

One way to control the growth of organic layers is by using the template effect of an underlying surface with a defined structure [9, 10]. The template effect determines the arrangement of the molecules in contact with the surface, i.e., in the monolayer, induced by the reactivity and symmetry of the surface. A surface constitutes a reactive object as the lattice periodicity of the bulk material gets lost in one direction and open bonds are provided [11]. Molecules in the monolayer often adsorb in a flat-lying, *face-on* geometry in which the extended π-system is oriented parallel to the surface. Thus, the molecular packing in the monolayer is controlled by the interactions of the molecules with the surface, i.e., the interfacial interactions, and by the interactions between the molecules, i.e., by the intermolecular interactions. Especially the impact of the interfacial interactions on the molecular arrangement in the monolayer leads to the formation of structures that often differ from the molecular arrangement in the three-dimensional crystal lattice [12].

Molecules that adsorb in the second or third molecular layer do not have direct contact with the surface. Hence, these molecules are less influenced by the substrate interface, leading to an increasing importance of the intermolecular interactions. Without the interfacial interactions, the molecules prefer to arrange in the energetically preferred structures observed for the organic crystals, such that, for increasing coverage, structural transitions from the monolayer back to crystal-like structures become more likely [13]. As a consequence for devices, the molecular arrangement at an electrode surface is important because the different molecular packing of the first few layers can determine the resulting device properties and efficiencies [14].

One class of organic functional molecules under investigation is the class of merocyanine molecules. Merocyanines are donor-acceptor dyes with an odd number of carbon atoms in

the π-conjugated system [15]. The electron donor and electron acceptor groups are connected by a conjugated (poly-)methine bridge, allowing for intramolecular charge transfer [15]. This leads to significant electrostatic dipole moments and high oscillator strengths [16, 17]. For this reason, merocyanines are in focus for applications in optoelectronic devices such as organic photodetectors and organic field effect transistors [6, 18–21].

However, merocyanines are challenging for structural investigations on surfaces. Different from most of the functional molecules investigated on surfaces so far [12, 22, 23], merocyanines are non-planar, prochiral molecules of low symmetry. Functional groups determine the donor-acceptor strength and, hence, the degree of delocalization of the π-electrons. In addition, sterical demanding and structurally flexible alkyl side chains influence the molecular packing in the crystal lattice. These factors make the prediction of monolayer structures and the derivation of structural models from experimental results rather difficult. This might be one reason why only a few investigations about merocyanine monolayers on surfaces have been reported, yet [24–27].

The specific merocyanine investigated in this thesis is called 2-[5-(5-dibutyl-amino-thiophen-2-yl-methylene)-4-*tert*-butyl-5*H*-thiazol-2-ylidene]-malononitrile [28]. Due to historical reasons [1], the name is abbreviated as HB238-A in the following chapters. The donor and acceptor strengths of HB238-A are about equal, and thus, the π-system is completely delocalized [1]. This state is known as the *cyanine limit* and leads to high transition dipole moments of the molecules [1, 15]. Although HB238-A was intensively investigated in the form of spin-coated films [1, 2] and crystals [2, 29], no information about the structure formation at interfaces and in particular on surfaces has been reported at the start of this thesis.

This work aimed to understand the molecular ordering of HB238-A at the templating Ag(100) interface, starting from the question, whether HB238-A forms ordered structures on the Ag(100) surface or not. Unexpectedly, it was found that HB238-A forms enantiopure long-range ordered domains that grow commensurate with the underlying Ag(100) surface. The molecular arrangement of the molecules in the monolayer was observed to be different from the arrangement in the crystal structures. To find the reasons for the formation of this highly ordered structure, detailed investigations of the interfacial and intermolecular interactions were performed.

These included, on a first stage, spot profile analyzing low energy electron diffraction (SPA-LEED) measurements to determine the unit cell of the HB238-A monolayer and scanning tunneling microscopy (STM) measurements to determine the unit cell content. These measurements revealed a large HB238-A unit cell of $P2$ symmetry containing four molecules in an enantiopure arrangement that is stabilized by hydrogen bonds between the donor and acceptor groups of neighboring molecules. The large unit cell in combination with its commensurate structure indicates a strong binding of the merocyanine molecules to the Ag surface.

To investigate the interfacial interactions responsible for the commensurate growth of HB238-A, photoelectron spectroscopy (PES) measurements were performed. In addition, the sterical demand of the molecules was deliberately altered by investigating HB238-A derivatives of different alkyl side group lengths. This change in the sterical demand forced the molecules to arrange in a new packing on the Ag(100) surface. However, the

adsorption sites of the molecules in the new phases were found to be similar to those in the monolayer structure of HB238-A. The respective analysis was done by normal incidence x-ray standing wave (NIXSW) measurements and revealed that the molecular adsorption sites are mainly determined by strong covalent-like bonds between the S atoms of the merocyanines and the Ag(100) surface. Thus, we learn that the molecular adsorption sites of the investigated merocyanines are mainly determined by the strong interactions of the molecules with the Ag surface, while the formation of enantiopure structures is driven by the intermolecular interactions.

This thesis is structured as follows: Chapter 2 gives a brief overview of the published literature about merocyanines, their crystal structures, and their properties. In addition, Chapter 3 provides an introduction to the experimental techniques used in this thesis, followed by the experimental details and parameters, which are summarized in Chapter 4. Chapters 5 to 10 present the experimental results.

Chapter 5 starts with an introduction of an acquisition routine developed to increase the scan speed of SPA-LEED measurements. As the measurements show a slow dewetting of the merocyanine monolayers, this routine facilitated a detailed layer analysis by SPA-LEED measurements.

Chapter 6 introduces the structure formation of HB238-A on the Ag(100) surface, including the investigation of the interfacial interactions by PES. Structural changes in the monolayer with respect to the sterical demand of the molecules are reported in Chapter 7.

Concentrating on the interfacial binding of HB238-A, Chapter 8 presents the adsorption heights of the respective C, N, and S atoms. Based on these results, Chapter 9 describes the determination of the molecular adsorption sites for the different merocyanine phases. The results of this thesis are discussed in Chapter 11 to provide a detailed understanding of why the investigated merocyanines form commensurate and enantiopure monolayer structures.

Furthermore, Chapter 10 provides an excursion on the carpet-like growth of thin KCl(100) layers on the Ag(111) surface. These KCl layers might be used in the future to decouple merocyanine structures from the metallic substrate in order to investigate the optical layer properties. However, the results of this thesis indicate that the here reported merocyanine structures on Ag(100) cannot be transferred to other surfaces like KCl(100) that exhibit weaker interfacial interactions.

After the discussion, Chapter 12 presents a concluding summary of the results. As the content of Chapters 5, 6, and 10 is already published, these chapters only provide a summary of the respective publications. Reprints of the publications can be found in Appendix A.

2. Review of Literature

This chapter provides an overview of the general structural properties of merocyanines, followed by an introduction to the merocyanines used in this thesis. For the investigated merocyanines, crystal structures and the respective structure-defining intermolecular interactions are discussed, as these binding motifs are also found for the later presented monolayer structures. Furthermore, it also provides an overview of the few investigations on monolayers that have been published for merocyanines so far.

2.1. Merocyanines

Merocyanines belong to the class of polymethine dyes. The molecular structure can, in general, be described as a π-conjugated (poly-)methine chain that has two end groups, an electron-withdrawing group and an electron-donating group [18]. Different from the structurally similar polyene dyes, merocyanines exhibit an odd number of π-centers, i.e., sp^2-hybridized atoms [30]. Hence, merocyanines can undergo an intramolecular charge transfer, leading to a dipolar resonance structure as indicated in Figure 2.1.

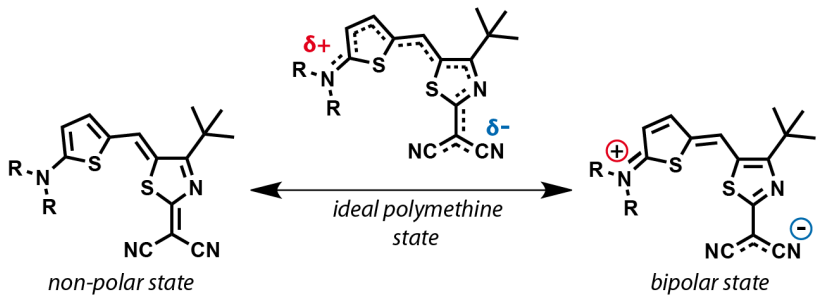

Figure 2.1.: General molecular structure of the merocyanines investigated in this thesis. R denotes the respective alkyl side chains. For HB238-A, R stands for *n*Bu groups. These merocyanines comprise nine sp^2-hybridized C atoms. Due to the donor-acceptor system, the non-polar molecular structure is in equilibrium with a bipolar resonance structure. The intermediate state in which the π-system is completely delocalized is called *ideal polymethine state*. Figure based on reference [30].

The advantage of merocyanines is based on their tunable properties. Variation of the electron-donating and withdrawing groups, and the length of the (poly-)methine chain, gives access to absorption bands in a wide spectral range from the ultraviolet to about 1600 nm [1, 30, 31]. Variation of the sterical demanding side groups can further tune the intermolecular interactions and the resulting properties in the condensed solid state [2,

6]. For these reasons, merocyanines have a broad application spectrum. Examples are nonlinear optics [32–34], optoelectronics [31, 35, 36], self-assembled aggregates [20, 37, 38], and reversible molecular-switches [27, 39–41].

2.2. Merocyanine HB238-A

The merocyanine HB238-A exhibits a 2-dibutylaminothiophene electron donating group and a 2-[4-(*tert*-butyl)thiazol-2(3H)-ylidene]-malononitrile electron withdrawing group [2]. The molecular structure of HB238-A is displayed in Figure 2.1. Here, R denotes the alkyl side chains and equals *n*Bu groups for HB238-A as displayed in Figure 2.4.

HB238-A was originally synthesized by Hannah Bürckstümmer (HB) in the group of Frank Würthner at the University of Würzburg [1, 28]. The trivial name of the molecule (HB238) was introduced during that time. However, as explained below, it is referred to as HB238-A in this thesis. Different names of HB238-A used in the literature refer to the specific alkyl side chains [2], or are related to the electron donor and acceptor groups [29]. However, HB238 remains the most common trivial name for this molecule [1, 42–44].

The properties of HB238-A have been studied intensively during the last few years [1, 29, 36, 42–44]. Due to the above-mentioned donor and acceptor groups, HB238-A exhibits a high ground-state dipole moment of 13.1 D (measured in 1,4-dioxane with a concentration of 10^{-6} M) [1]. The structure of the isolated molecule is close to the ideal polymethine state, also called *cyanine limit* [1]. The disappearing bond length alternation in this state results in a very small change of the dipole moment upon an optical excitation and thus in large transition dipole moments [1]. In addition, the sesquialteral bond order prevents a photoisomerization of the molecule [1, 15].

The high ground-state dipole moment leads to a preferred aggregation of HB238-A in π-stacked, anti-parallel dimers forming a kind of zig-zag pattern [2, 43]. As a consequence of the molecular arrangement, absorption spectra of HB238-A aggregates in solutions [44] and in annealed spin-coated films [2, 43] show intense, characteristic absorption bands which correspond to J-type and H-type transitions [43, 44]. However, due to its non-planar structure and the two flexible *n*Bu groups at the tertiary amine, several polymorphic crystal structures of HB238-A exist that are described in the next section.

2.3. Crystal structures of HB238-A

Due to its complex molecular structure, four different polymorphic crystal structures of HB238-A have been reported up to now [2, 29]. Their crystallographic parameters are summarized in Table 2.1. The data were measured for single crystals obtained by crystallization from solution, mainly using chloroform as solvent. In addition, structural phase transitions were observed for x-ray diffraction (XRD) measurements at different temperatures [29]. This applies to the polymorph P1, which transforms into polymorph P2 at low temperatures, exhibiting a slightly smaller unit cell.

Table 2.1.: Crystallographic parameters of reported HB238-A polymorphs. The data of P1, P2, and P3 were taken from reference [29], and the data of P4 from reference [2]. Z denotes the number of molecules per unit cell.

Polymorph	P1	P2	P3	P4
CCDC number	2073437	2073438	2073461	1856819
Temperature/K	300	100	100	100
Crystal system	monoclinic	monoclinic	monoclinic	monoclinic
Space group	$P2_1/c$	$P2_1/c$	$C2/c$	$P2_1$
a/Å	13.0876(10)	13.9396(17)	38.067(3)	8.6476(5)
b/Å	19.2985(12)	18.847(2)	10.0661(8)	19.3964(10)
c/Å	9.8422(8)	9.0814(9)	13.7086(11)	20.8670(11)
α/°	90	90	90	90
β/°	101.654(3)	105.608(6)	102.303(3)	99.038(2)°
γ/°	90	90	90	90
V/Å^3	2434.61	2297.88	5132.31	3456.61(32)
Z	4	4	8	6

Although all four crystal structures are monoclinic, the sizes of the unit cells, and accordingly also the numbers of molecules Z per unit cell, differ significantly. The reason for this is the different packing of the molecules as visible in Figure 2.2.

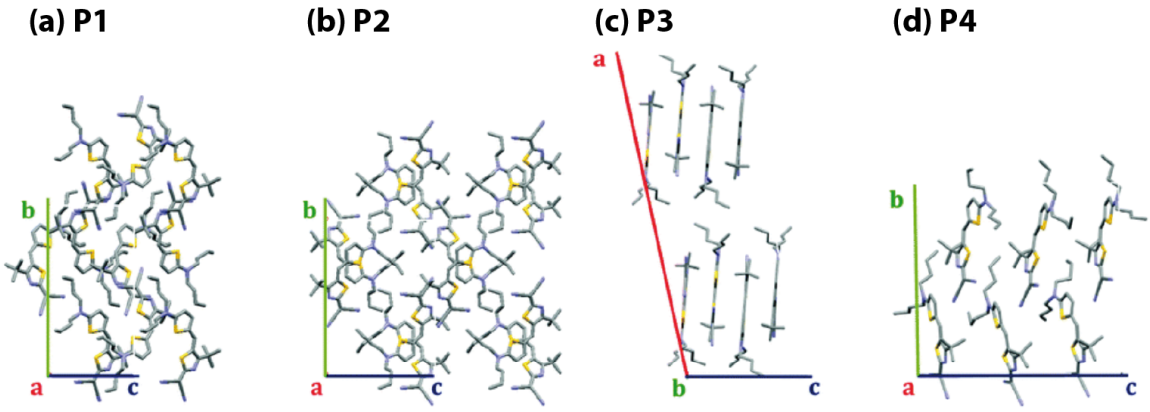

Figure 2.2.: Reported polymorphic crystal structures of HB238-A. The Figure is taken from reference [29] and has been slightly adapted. Molecules are presented as a wire model. Color code: S yellow, N blue, C gray.

The molecular arrangement in the crystal structures is defined by the intermolecular interactions. The molecular arrangements observed for the crystal structures, hence, constitute energetically preferred arrangements. For structures of molecules on surfaces, the same holds if the interfacial interactions are weak. Hence, it is worth discussing the

molecular arrangement within crystal planes in which the arrangement of the molecules is most planar. These molecular arrangements would not need to rearrange much when being transferred onto a surface. Thus, for weak interfacial interactions, it might be likely that similar molecular arrangements are found on the surface.

Surprisingly, the molecular arrangements in the depicted two-dimensional lattice planes of the polymorphs P1, P2, and P4 are similar. Only the molecular arrangement of polymorph P3 differs significantly. Accordingly, only the crystal structures of the polymorphs P3 and P4 (representing also P1 and P2) are displayed in Figure 2.3 as a top view and a side view of the most planar molecular arrangement. These will now be discussed in more detail.

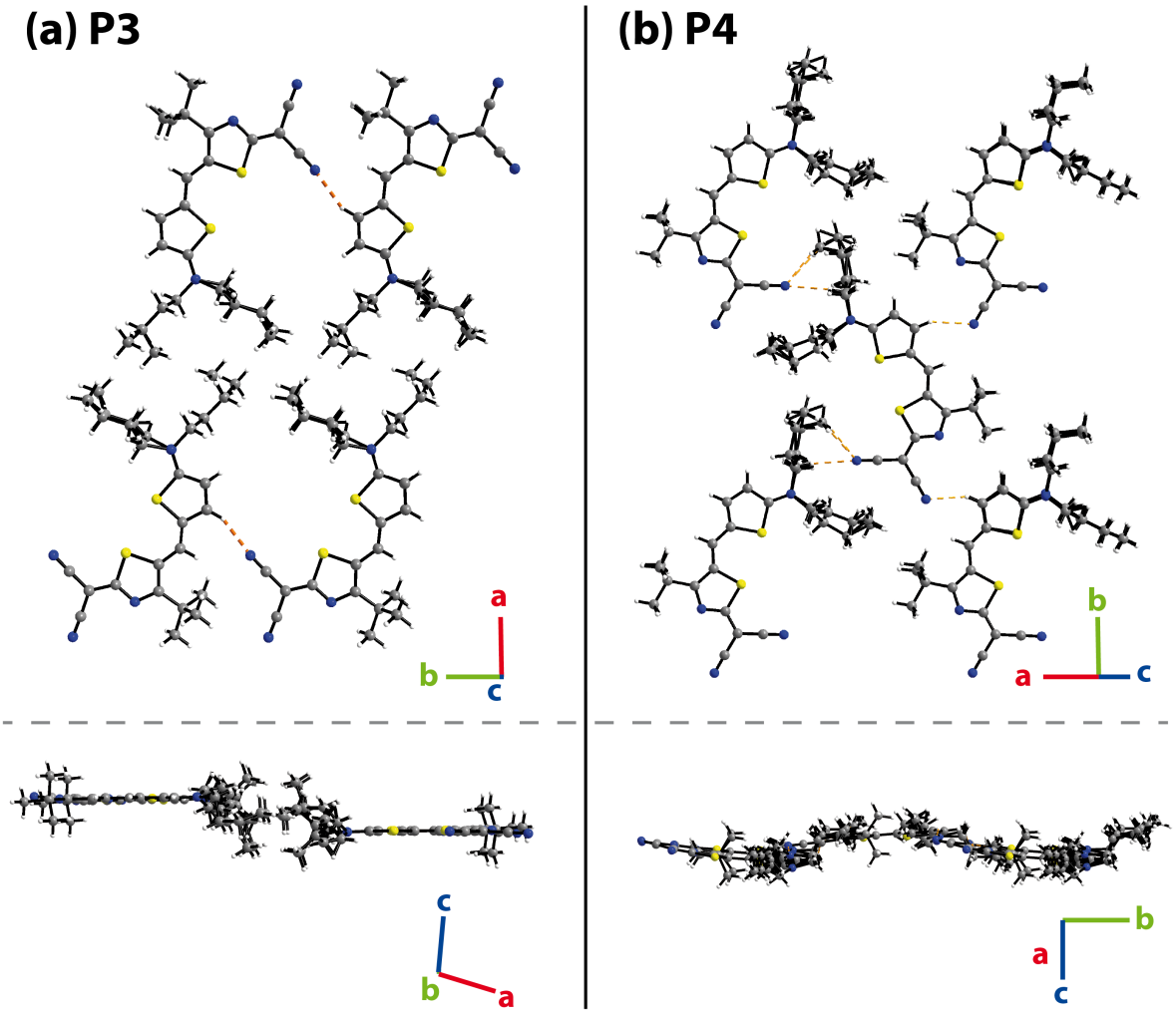

Figure 2.3.: Most planar molecular arrangement of HB238-A molecules in the polymorphic crystal structures P3 and P4, displayed in a top-view and a side-view. For better visibility of the molecules, a ball-and-stick model was used for the presentation. Color code as in Fig. 2.2. Hydrogen bonds are indicated by orange dotted lines.

As visible in Figure 2.2 (c), polymorph P3 forms stacks of parallel-oriented molecules. The distance between π-stacked molecules in this structure is about 3.5 Å. A cut through this structure perpendicular to the c-axis reveals long one-dimensional aggregates as displayed

in Figure 2.3 (a). Please note that the periodicity of the one-dimensional aggregate is along the b-axis. Each aggregate has a width of two molecules in the direction of the a-axis. Between successive molecules in b-direction, hydrogen bonds with a length of about 2.3 Å are formed between the nitrile groups and the hydrogen atoms at the thiophene rings of neighboring molecules. Please note that all lengths of hydrogen bonds reported in this thesis refer to the distance between the donor H atom and the acceptor (here, the N atom of the nitrile group). Between the two rows of molecules, van der Waals interactions between the *n*Bu groups stabilize the structure. However, the two rows of hydrogen-bonded molecules are not exactly in the same plane but are slightly shifted against each other in the direction of the c-axis, as visible in the lower part of Figure 2.3 (a).

In contrast to polymorph P3, polymorph P4 exhibits nearly planar molecular arrangements with two-dimensional periodicity. Molecules are oriented in a *head-to-tail* arrangement that could also be described as a *herringbone* arrangement. Again, hydrogen bonds form and are indicated as orange dotted lines. Their lengths vary from about 2.5 to 2.6 Å. As visible from the centered molecule, each molecule in this two-dimensional lattice plane is connected by hydrogen bonds to its nearest neighbors, i.e., to four molecules in total. The higher number of hydrogen bonds between the molecules of the P4 polymorph suggests a higher layer stability compared to the layer arrangement of molecules in polymorph P3. Most likely, due to the sterical demands of the *n*Bu and *t*Bu groups, the molecular arrangement is again not perfectly flat but shows a wave-like structure in the side view.

2.4. Derivatives of HB238

As reported by Liess et al. [2], a variation of the sterical demanding and structurally flexible alkyl side chains attached to the tertiary amine (R in Figure 2.1) can be used to tune the molecular packing. This offers interesting aspects, as changes in the alkyl side chains have only a minor impact on the molecular π-system and the respective molecular properties. Changes in the layer properties thus result from a different molecular arrangement due to altered intermolecular interactions. Hence, a variation of the alkyl side groups offers an elegant way to discriminate, characterize, and tune intermolecular interactions. For annealed spin-coated films, this was demonstrated by absorption spectra. While rigid and small side groups, e.g., Et groups, lead to the formation of H-type aggregates and the respective absorption bands, large and flexible side groups, e.g., Hex groups, lead to J-type aggregates [2].

The HB238-A derivatives investigated in this thesis are displayed in Figure 2.4. The alkyl side chains marked in purple were varied in their length from *n*Bu groups to Me groups. For simplicity, these derivatives are named HB238-B, HB238-C, and HB238-D. For reasons of consistency, the name of HB238 has been changed accordingly to HB238-A. Differently to HB238-A, only a few publications exist for the derivatives [2, 45]. In addition, a new HB238-A derivative was investigated in this thesis for the first time. For this derivative, the *t*Bu group of HB238-A was exchanged by an *i*Pr group as indicated in blue color in the lower part of Figure 2.4. The structural results of the respective monolayers on the Ag(100) surface are presented in Appendix C. The synthesis of this molecule was done in the group of K. Meerholz in Cologne [46]. This merocyanine was named HB238-E.

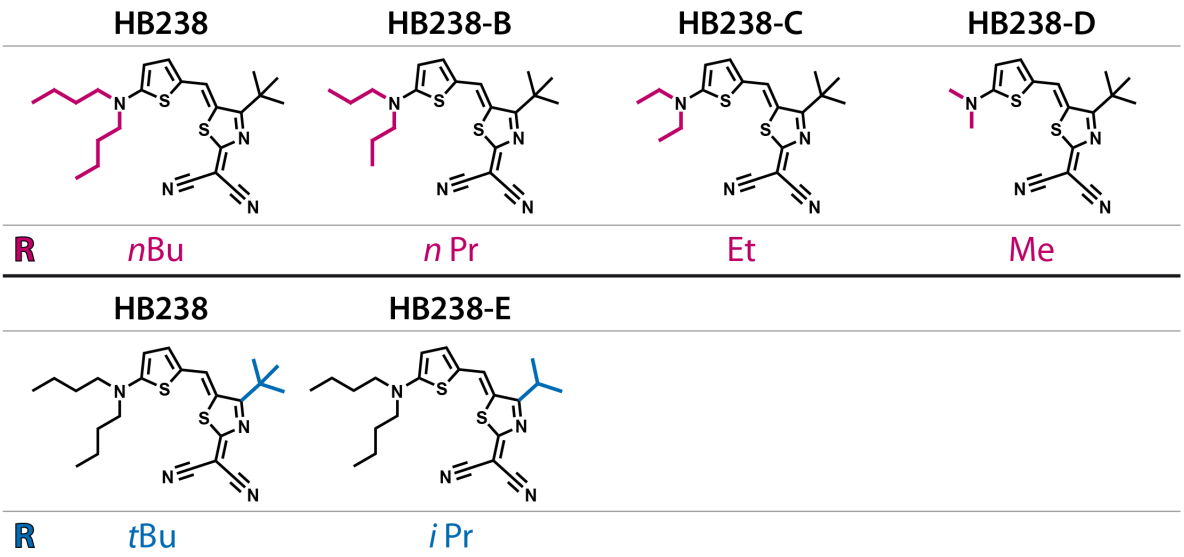

Figure 2.4.: HB238-A derivatives investigated in this thesis. The alkyl side groups (R) that were altered are indicated in purple and blue, respectively.

The crystal structures of HB238-B [45] and HB238-C [2] have been published on the basis of XRD data. Again, crystals were obtained from solution. An overview of the crystal structures, similar to Figures 2.2 and 2.3, is displayed in Figure 2.5. The respective parameters are listed in Table 2.2.

In contrast to HB238-A, the alkyl side chains of HB238-B are shorter by one CH_2-group. Still, the two-dimensional molecular arrangement is found to be quite similar to the molecular arrangement in polymorph P4. However, the side view in the lower part of Figure 2.5 reveals that the two-dimensional arrangement of the molecules in the b-c-plane appears to be nearly flat and thus favorable for a structure formation on a surface.

For HB238-C, the length of the alkyl side chains is further reduced, again by one CH_2-group. The molecules form, comparable to the HB238-A polymorph P3, hydrogen-bonded chains, here along the a-direction. However, different to the structure P3, the HB238-C molecules within this plane are all oriented in the same direction. Due to the chain formation, the number of hydrogen bonds per molecule is reduced to two. Please note that only the shortest hydrogen bonds are indicated here, and that additional hydrogen bonds, e.g., between the nitrile groups and the Et groups of neighboring molecules, are possible as their length would result in 2.8 Å. In the side-view, it becomes visible that the molecules are slightly tilted against each other, again forming a wave-like structure if further molecules in the c-direction are taken into account.

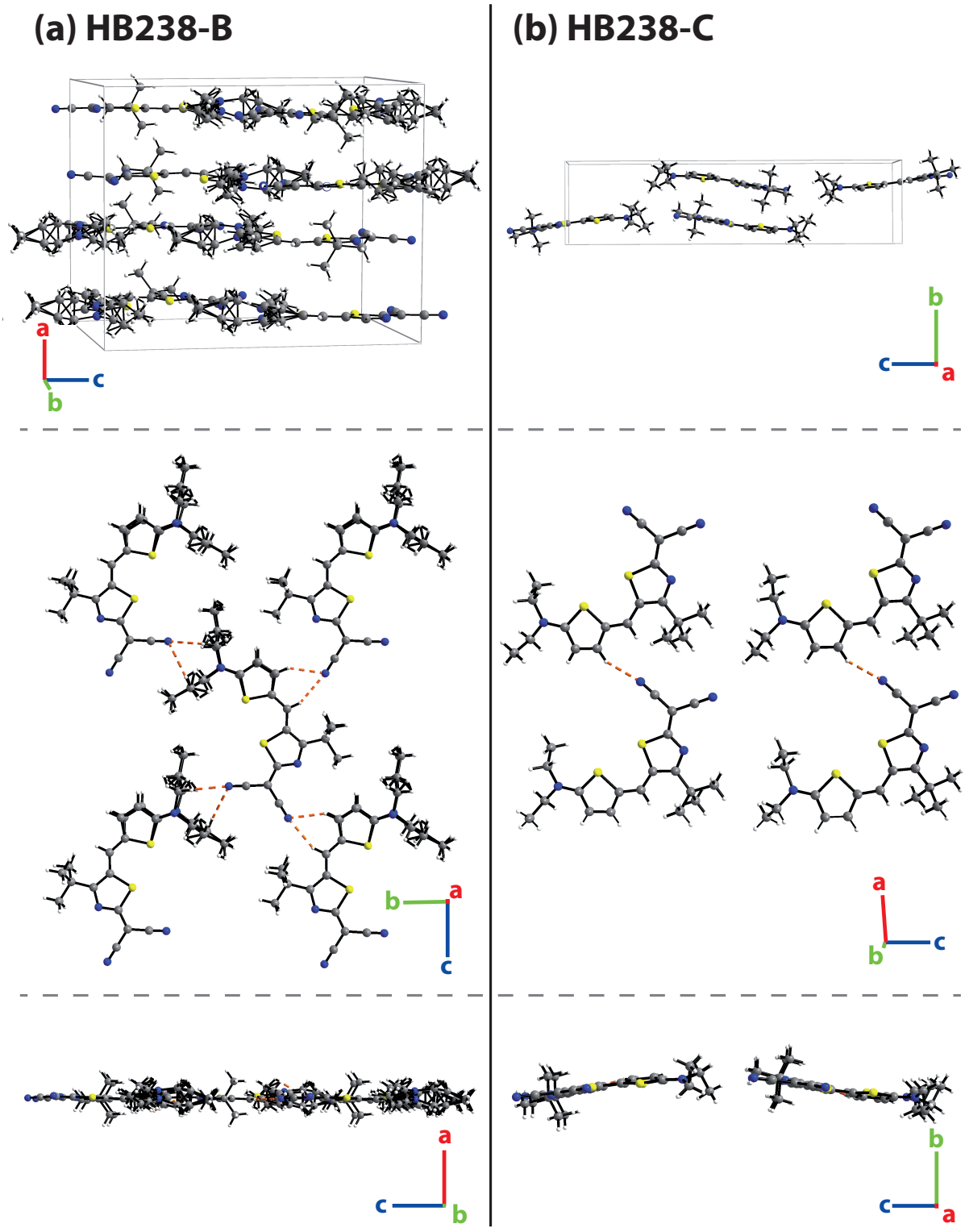

Figure 2.5.: Crystal structures of HB238-B [45] and HB238-C [2]. In addition to the bulk unit cell, the most planar molecular arrangement present in the crystal structures is displayed in a top-view and a side-view. Color code as in Fig. 2.2.

Table 2.2.: Crystallographic parameters for the merocyanines HB238-B [45] and HB238-C [2]. In both cases, single crystals were grown from a solution.

Compound	HB238-B	HB238-C
CCDC number	1496527	1856817
Chemical formula	$C_{21}H_{26}N_4S_2$	$C_{19}H_{22}N_4S_2$
Temperature/K	100(2)	100(2)
M/g mol^{-1}	398.58	370.52
Crystal color	green	blue
Crystal system	orthorhombic	monoclinic
Space group	Pbca	$P2_1/c$
a/Å	15.4428(5)	9.9527(18)
b/Å	14.3273(4)	6.9941(13)
c/Å	19.1045(5)	28.499(5)
α/°	90	90
β/°	90	93.565(5)
γ/°	90	90
V/Å^3	4226.9(2)	1980.0(6)
Z	8	4
ρ/g mol^{-3}	1.253	1.243

Even if we can identify in the crystal structures of HB238-A and the HB238-derivatives molecular arrangements in which the molecules form a nearly planar molecular layer, the structures that were observed for the adsorbed molecules on the Ag(100) surface are significantly different. This indicates a strong structural impact of the interactions of the molecules with the surface. However, the intermolecular binding motifs observed in all crystal structures, namely the hydrogen bonds between H atoms on the donor and the terminal CN groups on the acceptor groups of neighboring molecules, remain identical.

Please note that additional crystallographic data of the investigated merocyanines are presented in Appendix B. The respective XRD data were measured as part of this thesis for crystals that were obtained by temperature gradient sublimation. Accordingly, the presence of solvent molecules can be excluded for these crystal structures.

2.5. Merocyanine Monolayers

Up to today, only a few experimental reports about merocyanine monolayers exist in the literature. Early investigations considered the molecular ordering in Langmuir-Blodgett films [24]. Later, the molecular ordering at the solid-liquid interface [25, 26], in solution-processed monolayers [27], and in ultra high vacuum (UHV) on solid surfaces [41, 42, 47] was investigated.

One major motivation of merocyanine studies on surfaces in UHV is their application as molecular switches. Spiropyran molecules can undergo a thermally or photoinduced ring-opening reaction, which results in merocyanine molecules [41]. As spiropyran molecules are three-dimensional, colorless, and inert, the transition to the colorful, reactive, and π-conjugated merocyanine bears a high potential for later applications [41]. In this context, two different merocyanines were investigated on the Au(111) surface by Piantek and Bronner [40, 47], and by Riemann et al. [39].

These two merocyanines both show a dimer formation on the Au(111) surface. The dimers are stabilized by hydrogen bonds and are either separated from each other on the surface [39] or form chains that avoid lateral packing due to long-range repulsive interactions between the chains [40, 47]. The latter indicates a strong binding of the merocyanines to the surface, which was supported, i.e., by x-ray photoemission spectroscopy (XPS) measurements [47].

Yet, no monolayer studies about HB238-A and the above-mentioned derivatives were published. One exception is the recent publication by Öcal et al. [42] which reports about XPS and ultraviolet photoemission spectroscopy (UPS) data of HB238-A layers on Au(100), Ag(100), and Cu(100) surfaces that were measured in dependence on the HB238-A layer thickness. The data published for the Ag(100) surface by Öcal et al. is consistent with the data previously measured and published for HB238-A mono- and multilayers on the Ag(100) surface as part of this thesis [48].

3. Theoretical Background

The following chapter provides a brief overview of the experimental techniques applied in the context of this thesis. Especially, specific details that are important for the scientific context are summarized. For general or further information regarding the experimental techniques, please refer to the literature cited.

3.1. Surface sensitivity of electrons

The investigation of molecular monolayers on a substrate surface requires experimental techniques that allow for distinction between information detected from the bulk of the substrate and the surface, including the adsorbates. While scanning probe techniques like STM and atomic force microscopy (AFM) directly image the molecular structures on the surface, surface sensitivity of diffraction and photoemission experiments is not directly ensured.

For low energy electron diffraction (LEED) measurements and PES, the surface sensitivity depends on the electrons' inelastic scattering mean-free-path [11]. Electrons that are subject to inelastic scattering lose energy and are therefore separated from the signal of interest. For electron diffraction, the inelastic mean free path has an impact on both the incident and the diffracted electrons. For PES experiments, the photoelectrons are created in the sample by photoexcitation. Hence, the inelastic mean-free-path is important for electrons leaving the sample.

In both cases, a small inelastic mean-free-path causes the information to be obtained mainly from the uppermost few layers of the sample. A small inelastic mean-free-path of about 5 to 10 Å is achieved by kinetic energies (E_{kin}) of the electrons in a range of 10 to 1000 eV [49]. Hence, LEED measurements are performed with kinetic energies in a range of 20 to 500 eV. For photoemission experiments, i.e., XPS, the energy of the photon beam (E_{γ}) is set with respect to the binding energy of the investigated photoemission line (E_{bind}) and the work function of the sample (ϕ_{sample}) to obtain photoelectrons with a kinetic energy of about 100 eV ($E_{\mathrm{kin}} = E_{\gamma} - \phi_{\mathrm{sample}} - E_{\mathrm{bind}}$).

3.2. Low energy electron diffraction

The low energy electron diffraction (LEED) measurements performed for the structural analysis of the merocyanine layers were mainly performed by using a SPA-LEED device. A SPA-LEED device allows for high-resolution scans of the reciprocal space by using a channeltron detector. Furthermore, LEED measurements with multi channel plate (MCP)

devices were performed to safeguard the presence of the correct monolayer phases for subsequent STM and PES measurements. Detailed information about the LEED devices and their working principle can be found in references [50–52].

As mentioned above, LEED measurements are performed with electrons exhibiting a kinetic energy (E_{kin}) of 20 to 150 eV to provide surface sensitivity. These kinetic energies correspond to de Broglie wavelengths (λ_{el}) of $1 - 2.7$ Å. The conversion from the kinetic energy to the de Broglie wavelength is done by the following equation

$$\lambda_{\mathrm{el}} = \frac{h}{\sqrt{2 m_e E_{\mathrm{kin}}}} = \sqrt{\frac{150.4}{E_{\mathrm{kin}}/e\mathrm{V}}}\,\text{Å} = \sqrt{\frac{1.504}{E_{\mathrm{kin}}/e\mathrm{V}}}\,\mathrm{nm} \tag{3.1}$$

with h being Planck's constant and m_e being the mass of the electron [50].

The electrons that are elastically scattered by the first atomic layers of the sample are detected by the LEED device. The corresponding diffraction pattern reflects the two-dimensional translational symmetry of the sample surface and can be described by a two-dimensional Fourier transform of the surface lattice. This is possible as the diffraction pattern can be described by the kinematic diffraction theory, in which the multiscattering effects are summarized under the effective scattering factors [50].

For the interpretation of the experimental data, the following equations are important. They are summarized from refs. [50, 53]. The incident electron beam is described as a plane wave. The corresponding wave vector ($\mathbf{k}_0$) can be calculated by

$$|\mathbf{k}_0| = \frac{2\pi}{\lambda_{\mathrm{el}}}. \tag{3.2}$$

The components of the scattering vector parallel to the sample surface $\mathbf{k}_{||}^{hk}$ describe the positions of the diffraction spots. For normal incidence of the electron beam, they result in

$$|\mathbf{k}_{||}^{h,k}| = |\mathbf{k}_0| \sin\theta, \text{ with } \mathbf{k}_{||}^{h,k} = h \cdot \mathbf{a}_1^* + k \cdot \mathbf{a}_2^*. \tag{3.3}$$

Please note that here, h, k are the Miller indices of the diffraction spots, which are, hence, integer values. For a conventional LEED system, θ is the angle between the incident beam and the diffracted one. $\mathbf{a}_1^*$ and $\mathbf{a}_2^*$ are the reciprocal lattice vectors. The length of the respective real space lattice vectors $\mathbf{a}_1, \mathbf{a}_2$ can be calculated from the relations

$$\mathbf{a}_1^* \cdot \mathbf{a}_1 = |\mathbf{a}_1^*| \cdot |\mathbf{a}_1| \cdot \cos\gamma = 2\pi \text{ and } \mathbf{a}_2^* \cdot \mathbf{a}_2 = |\mathbf{a}_2^*| \cdot |\mathbf{a}_2| \cdot \cos\gamma = 2\pi \tag{3.4}$$

with $\gamma = 90° - \measuredangle(\mathbf{a}_1, \mathbf{a}_2)$.

In addition,

$$\mathbf{a}_1^* \cdot \mathbf{a}_2 = \mathbf{a}_2^* \cdot \mathbf{a}_1 = 0 \tag{3.5}$$

applies. In this thesis, the vectors $\mathbf{a}_1$ and $\mathbf{a}_2$ always refer to the unit cell vectors of the Ag(100) surface.

LEED was used to obtain information about the unit cell vectors of the merocyanine layer, i.e., the superstructure, which are denoted as $\mathbf{b}_1$ and $\mathbf{b}_2$. This also includes the length and the orientation of the unit cell vectors with respect to the substrate vectors

and the presence of symmetry equivalent domains, i.e., rotational and mirror domains. The unit cell vectors are reported with respect to the substrate lattice vectors using a superstructure matrix according to

$$\begin{pmatrix} \mathbf{b}_1 \\ \mathbf{b}_2 \end{pmatrix} = \begin{pmatrix} m_{11} & m_{12} \\ m_{21} & m_{22} \end{pmatrix} \begin{pmatrix} \mathbf{a}_1 \\ \mathbf{a}_2 \end{pmatrix}. \tag{3.6}$$

The superstructure lattice vectors can be described by a linear combination of the substrate vectors. For integer matrix elements, the structure that results from the combination of the superstructure and the substrate lattice exhibits a translational symmetry. These structures are referred to as commensurate.

3.3. Scanning tunneling microscopy

Scanning tunneling microscopy (STM) allows for the imaging of real space surface structures with atomic resolution. In particular, it was used in this thesis to gain information about the molecular arrangement of the merocyanine molecules in the unit cell. Detailed literature about the development and the theory of STM can be found in references [11, 54, 55] from which the following information is summarized, if not stated otherwise.

For gaining information about the molecular arrangement in the unit cell, bias-dependent measurements were performed in this thesis. That means that the same sample spot was measured for the same tunneling current I_t but for a series of different bias voltages U_bias. As both the tip and the sample are connected by the STM electronics, the Fermi levels (E_F) of the tip and the sample are aligned if no bias voltage is applied. Applying a bias voltage leads to an offset between the Fermi levels of the tip and the sample. This energy difference in the Fermi levels, E_bias, is calculated by the charge of the electron ($-e$) multiplied with the bias voltage and defines the energy range of electronic states (of the sample and the tip) which participate in the tunneling process.

The parameters given in this thesis refer to the convention that the bias voltage is applied to the sample. Accordingly, a negative bias voltage refers to tunneling from occupied electronic states of the sample to unoccupied states of the tip. As the wave function Ψ of the tunneling electrons decays exponentially in the gap between the tip and the sample according to

$$\Psi(z,E) = \Psi(0)\mathrm{e}^{-\kappa z} \text{ with } \kappa = \sqrt{\frac{2m_e}{\hbar^2}\left(\frac{\phi_\mathrm{tip}+\phi_\mathrm{sample}}{2} + \frac{E_\mathrm{bias}}{2} - E\right)}, \tag{3.7}$$

the tunneling probability $T(z,E) = |\Psi(z)|^2 = |\Psi(0)|^2\mathrm{e}^{-\kappa z}$ decreases for increasing tip-sample distances z [56]. Here, E denotes the energy of the electron with respect to the Fermi level of the sample and does not change during the tunneling process. ϕ_tip and ϕ_sample denote the work functions of the tip and the sample that define the height of the tunneling barrier. $\hbar = h/(2\pi)$ is the reduced Planck's constant. Accordingly, the tip-sample distance must change for varying U_bias values if I_t is kept constant.

However, it is important in the context of the present thesis to realize that STM is not directly imaging atomic positions, but the local density of states (LDOS) of the surface that is, to some extent, folded with the LDOS of the tip. Taking this into account, Tersoff and Hamann developed a model for the tunneling process, approximating the tip wave function to be spherical (s-wave function) [57, 58]. In this approach, the tunneling current is proportional to the LDOS of the sample (ρ_s) according to

$$I_t \propto U_{bias}\ \rho_s(E_F - E_{bias}), \tag{3.8}$$

if the LDOS is so flat that the density of states of the tip, ρ_t, can be assumed to be constant in the studied energy range [54]. Please note that Equation 3.8 refers to tunneling at the Fermi edge.

For the STM data presented in this thesis (excluding the data of Chapter 10), Pt/Ir STM tips were used. Accordingly, as the electron configuration of Pt is [Xe] $4f^{14}$ $5d^9$ $6s^1$, a tunneling through the $6s$-orbital is likely, and the tunneling current can be assumed to be mainly determined by the LDOS of the sample. However, it should be noted that the Tersoff-Hamann model is not limited to the tunneling through single orbitals, but applies to spherical STM tips in general.

For the W-tips used for the STM measurements of Chapter 10 an interpretation of the tunneling current by the Tersoff-Hamann model is limited as the tunneling occurs through the $d_{x^2-y^2}$-, p_z, and s-orbitals [59]. However, for the here presented results, atomic resolution was likely achieved by Cl^- modified tips and tunneling through the p_z orbital of the Cl^- ion as described by Li et al. in ref. [59].

3.4. Photoemission spectroscopy

Photoelectron spectroscopy (PES) probes the electron density of the occupied electronic states of a sample. In general, PES is divided into ultraviolet photoemission spectroscopy (UPS) measurements, which probe the valence band with photon energies up to 100 eV, and x-ray photoemission spectroscopy (XPS) measurements. The latter are performed with soft ($100 - 2100$ eV) and hard x-rays (> 2.1 keV) and probe the core levels of a sample. Detailed information about PES can be found in references [11, 60, 61].

A sketch illustrating the principle behind PES is given in Figure 3.1. A photon beam with an energy $E_\gamma = h\nu$ probes the sample. Photoelectrons of the sample are created in case that the photon energy is larger than the binding energy E_{bind} of the respective electron and the work function of the sample ϕ_{sample}. Created photoelectrons are left with a kinetic energy E_{kin} that equals $E_{kin} = E_\gamma - \phi_{sample} - E_{bind}$. However, please note that the analyzer measures the kinetic energy relative to the E_F. Accordingly, for the measured kinetic energy $E'_{kin} = E_{kin} + \phi_{sample}$ applies. By comparing PES spectra of thick molecular films, i.e., films with a negligible amount of molecules in contact to the substrate surface, and spectra of the monolayer, i.e., layers in which all molecules are supposed to have contact with the surface, information about the interfacial interactions can be obtained by analyzing the chemical shifts.

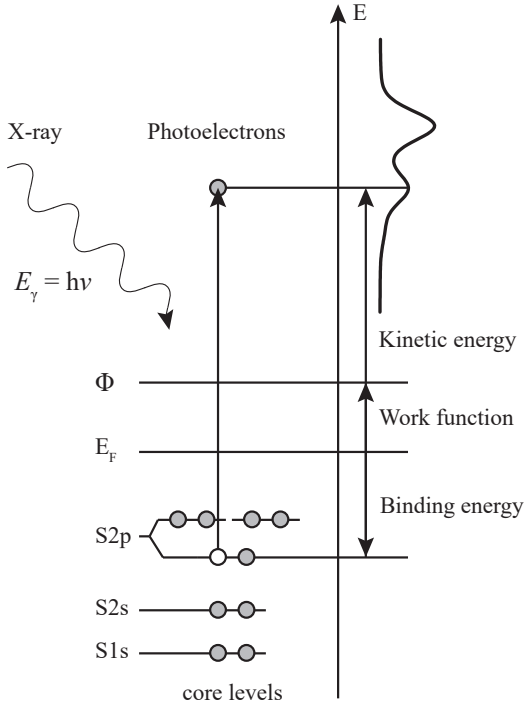

Figure 3.1.: Sketch illustrating the principle of XPS illustrated for the photoemission from the S2$p_{1/2}$ orbital. As per ref. [53]. Please note that the analyzer measures the kinetic energy E_{kin} relative to the E_{F}. Accordingly, for the measured kinetic energy $E'_{\mathrm{kin}} = E_{\mathrm{kin}} + \phi_{\mathrm{sample}}$ applies.

The binding energy of photoelectrons is influenced by initial and final state effects. Initial state effects occur for the neutral unexcited atom, due to the influence of the local electronic environment, also called chemical environment [11]. Final state effects result from the fact that the photoemission process is also related to the ionized final state. And the photoemission process is fast, such that the system may not be in an adiabatic equilibrium [11].

In the XPS spectra, final state effects become visible as satellites with lower kinetic energy, such as shake-up lines or as asymmetric line shapes of signals, which correspond to photoemission from the metal surface. These asymmetric line shapes occur due to a coupling of the photoelectrons to the conduction electrons [60]. Further effects that determine the line shapes, in particular, the full width at half maximum (FWHM), of the photoemission lines are the lifetime of the photohole, phonon broadening, the spectral resolution of the exciting x-ray beam, and the energy resolution of the analyzer [60, 62].

3.5. Normal incidence x-ray standing wave measurements

A structure determining method, based on XPS, is the normal incidence x-ray standing wave (NIXSW) technique that allows for the determination of element-specific adsorption heights with respect to the Bragg planes of the substrate. This method is not limited to the Bragg planes parallel to the substrate surface but can also be applied to determine the distances of atoms with respect to inclined Bragg planes. A set of adsorption distances to different Bragg planes can hence be used to determine the adsorption sites of the atoms on the surface, an approach referred to as triangulation. In the following sections, the most important information about NIXSW is presented, especially the details that are important for the evaluation of the merocyanine data. The information was summarized from references [11, 63–67], to which the reader is referred for further details.

3.5.1. The principle of NIXSW

The principle of NIXSW is illustrated in Figure 3.2. The incident and the, from the sample reflected x-ray beam interfere, creating a standing wave field that is not limited by the substrate surface, but extends into the vacuum. The periodicity of the standing wave field equals the periodicity of the measured Bragg planes.

In contrast to x-ray standing wave (XSW) measurements, NIXSW measurements are performed with a Bragg angle Θ_I that is close to 90° with respect to the measured Bragg plane. This has the advantage that the Bragg condition $2d_{hkl}\sin(\Theta_\mathrm{I}) = n\lambda$ exhibits a maximum for $\sin(\Theta_\mathrm{I}) = 90°$. Hence, it becomes insensitive to small angular deviations of individual grains in the sample and thus to the small mosaicity (typically <0.1°) that exists for metal single crystals. Here, d_{hkl} denotes the distance of the Bragg planes, and n is an integer that indicates the order of diffraction. The deviation of the incident beam from normal incidence is usually (at the I09 endstation, Diamond Light Source (DLS), UK) in a range of 3°. Thus, the reflected beam does not fall on the incident beam and can be monitored on a fluorescent screen via a camera. Monitoring the intensity of the reflected beam as a function of the wavelength λ, or the respective beam energy $E_\gamma = h \cdot \frac{c}{\lambda} = \frac{1.24\ \mathrm{keV}}{\lambda/\mathrm{nm}}$, results in the reflectivity curve.

For scanning the photon energy through the energy range defined by the reflectivity curve, the nodes of the standing wave field shift with a phase $\Phi(E_\gamma)$ that varies from π to 0 for increasing photon energies. For the low photon energy edge of the reflectivity curve, the anti-nodes of the standing wave field are located halfway between the Bragg planes. These anti-nodes shift for increasing photon energies by a distance $d_{hkl}/2$ to the position located directly at the Bragg planes. Accordingly, the absorption of radiation by the atoms of the substrate increases for an increasing overlap of the anti-nodes with the Bragg planes, and the intensity of the measured reflectivity, $R(E_\gamma)$, decreases. As a result, the reflectivity curves exhibit an asymmetric shape as depicted in Figure 3.2

The location of adsorbate atoms can be determined by the detection of the element-specific photoelectrons. While scanning through the photon energy range of the reflectivity curve, the highest photoemission is detected for the case where the anti-nodes hit the position of

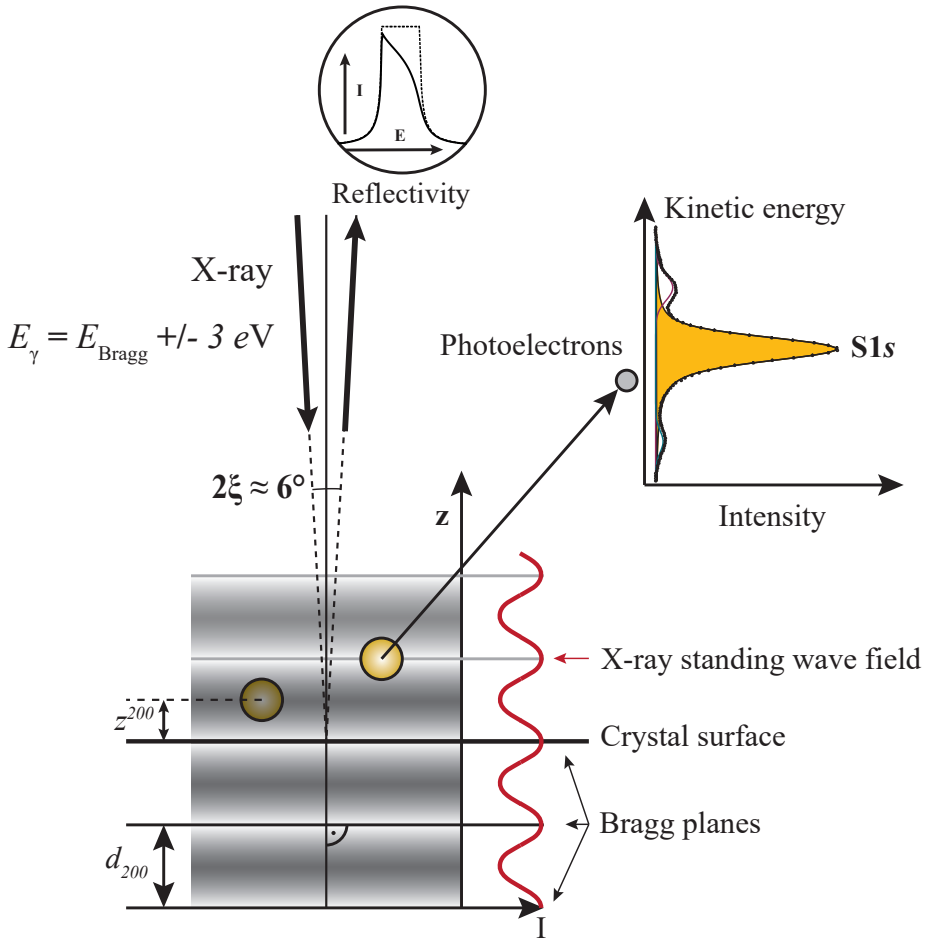

Figure 3.2.: Sketch illustrating the principle of NIXSW illustrated for the photoemission from the S1*s* orbital. Adapted from ref. [65].

the adsorbate atoms. The photoemission line integrals plotted against the photon energy (most often relative to the Bragg energy) lead to the measured photoemission yield curve. Accordingly, the shape of the photoemission yield curve strongly depends on the vertical positions of the adsorbate atoms with respect to the Bragg planes. For the data evaluation, the normalized intensity of the photoemission yield ($\frac{I}{I_0}$) is fitted according to

$$\frac{I}{I_0} = 1 + R(E_\gamma) + 2\sqrt{R(E_\gamma)} \cdot f_c \cdot \cos\left(\Phi(E_\gamma) - 2\pi \cdot p_c\right). \tag{3.9}$$

Here, the last term describes the interference of the incident and the reflected beam. The fit gives access to the values of the coherent fraction f_c and the coherent position p_c that can both range from 0 to 1. While the coherent fraction is a measure of the vertical disorder of the investigated adsorbate atoms, the coherent position gives the average vertical distance z^{hkl} with respect to the investigated Bragg planes according to

$$z^{hkl} = (n + p_c) \cdot d_{hkl}. \tag{3.10}$$

Here, n is again an integer. In this thesis, n equals 1 for the measurements at the (200) Bragg reflection and 0 for measurements at the (111) and the (220) Bragg reflections.

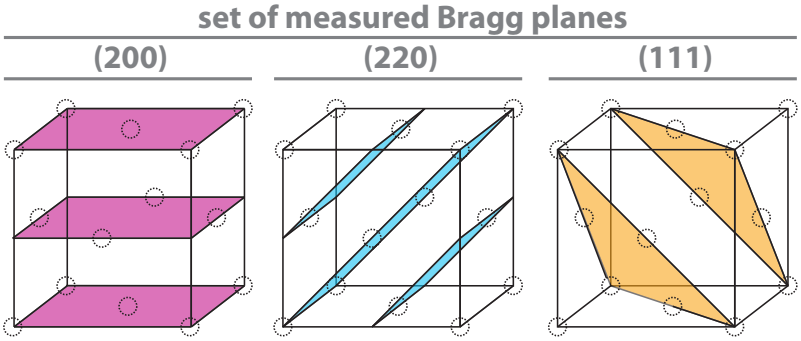

Figure 3.3.: (200), (220), and (111) Bragg planes of the Ag(100) crystal, measured in the context of the present thesis. Positions of the Ag atoms are indicated by dotted circles.

3.5.2. Non-dipolar corrections

However, the momentum of the photons of the incident and the reflected x-ray beam, in combination with the position of the photoelectron detector, leads to an overestimation of the photoelectrons that are created by the reflected x-ray beam. This leads to the need for the non-dipolar correction parameters S_R, $|S_\mathrm{I}|$, and ψ that apply as follows

$$\frac{I}{I_0} = 1 + S_\mathrm{R} \cdot R(E_\gamma) + 2|S_\mathrm{I}|\sqrt{R(E_\gamma)} \cdot f_\mathrm{c} \cdot \cos\left(\Phi(E_\gamma) - 2\pi \cdot p_\mathrm{c} + \psi\right). \tag{3.11}$$

They can be calculated from the scattering phase shifts δp and δd that can be extracted from the NIST database [68, 69].

3.5.3. Triangulation

If NIXSW data of one chemical species is measured for the Bragg plane parallel to the substrate surface and two Bragg planes non-parallel to the substrate surface, the respective adsorption sites can be determined in the vertical and lateral directions. This process is referred to as triangulation and will be described in Chapter 9 in more detail. The (200), (111), and (220) Bragg planes used for the triangulation in the present thesis are displayed in Figure 3.3. For each Bragg reflection, one set of f_c and p_c values is obtained. These values constitute average values that describe all respective scatterers in the structure, i.e., in the context of this thesis, the average adsorption distances of all S atoms.

For the theoretical calculations of the average f_c and p_c values from the proposed structural models, the following aspects have to be considered:

1. Structural models most often include symmetry non-equivalent atoms that exhibit different distances with respect to the measured Bragg planes.

2. The structures might exhibit structurally equivalent domains on the surface, i.e., rotational and mirror domains, that need to be taken into account.

In the present thesis, all investigated structures exhibited four symmetry equivalent domains, i.e., two rotational domains and two mirror domains, and eight S atoms per unit cell. For calculating the average values of f_c and p_c, the symmetry equivalent domains

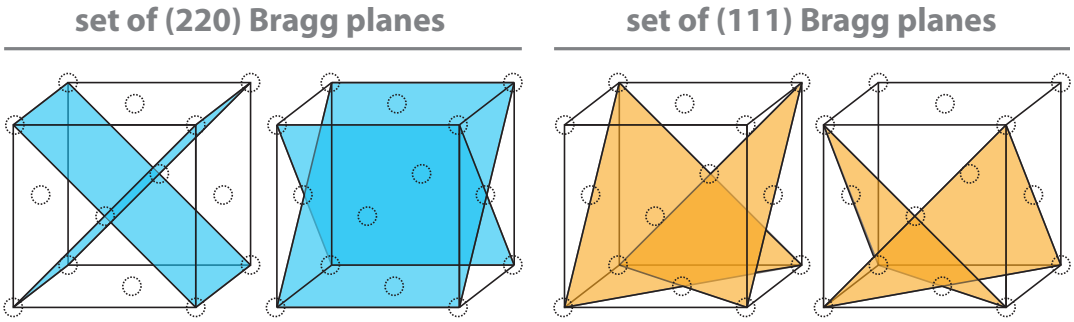

Figure 3.4.: Symmetry equivalent (220) and (111) Bragg planes of the Ag(100) crystal, used for the calculation of the average f_c and p_c. Thus, the calculation is equivalent to the calculation of two rotational and two mirror domains of the structures.

were considered by calculating only one domain, but for three additional Bragg planes that are symmetry equivalent to the Bragg plane measured. These, in total, four (220) and four (111) Bragg planes, are indicated in Figure 3.4. Due to the four-fold symmetry of the Ag(100) surface and the two-fold symmetry of the merocyanine structures, this procedure is equivalent to the calculation of f_c and p_c for two mirror and two rotational domains with respect to the measured Bragg plane.

The calculation of the averaged f_c and p_c values was performed as follows. Based on a Cartesian coordinate system, the distance z_{i,S_j}^{hkl} of the i individual donor (D) and acceptor (A) S atoms (S_j with j =A,D and $i = 1, ..., 4$) to the Bragg plane (hkl) can be calculated from the coordinates $\mathbf{r}^{i,S_j}$ with the normal vector $\mathbf{n}$ by

$$z_{i,S_j}^{hkl} = \mathbf{r}^{i,S_j} \cdot \mathbf{n} \text{ with } \mathbf{n} = \frac{1}{\sqrt{h^2+k^2+l^2}} \begin{pmatrix} h \\ k \\ l \end{pmatrix}. \tag{3.12}$$

The coherent position p_c^{i,S_j} and the coherent fraction f_c^{i,S_j} of the individual S atoms can be calculated by

$$p_c^{i,S_j} = \frac{z_{i,S_j}^{hkl}}{d_{hkl}} \bmod 1 \text{ and } f_c^{i,S_j} = m_{i,j}^{-1} \tag{3.13}$$

with $m_{i,j} = 4$ being the respective number of donor and acceptor S atoms in the unit cell of the merocyanine structure.

To average the values of p_c^{i,S_j} and f_c^{i,S_j}, the real and imaginary part of the so-called Argand vector [63] $\mathbf{P}_c^{i,S_j}$ were calculated by

$$\Re(\mathbf{P}_c^{i,S_j}) = f_c^{i,S_j} \cos(2\pi p_c^{i,S_j}) \text{ and } \Im(\mathbf{P}_c^{i,S_j}) = f_c^{i,S_j} \sin(2\pi p_c^{i,S_j}). \tag{3.14}$$

Finally, the average values, $p_c^{S_j}$ and $f_c^{S_j}$, were obtained from the averaged values of $\Re(\mathbf{P}_c^{i,S_j})$ and $\Im(\mathbf{P}_c^{i,S_j})$ that are denoted by $\overline{\Re(\mathbf{P}_c^{i,S_j})}$ and $\overline{\Im(\mathbf{P}_c^{i,S_j})}$, by

$$p_c^{S_j} = \arctan\left(\frac{\overline{\Im(\mathbf{P}_c^{i,S_j})}}{\overline{\Re(\mathbf{P}_c^{i,S_j})}}\right) \cdot (2\pi)^{-1} + 0.5 \tag{3.15}$$

and

$$f_{\mathrm{c}}^{S_j} = \sqrt{\left(\overline{(\Re(\mathbf{P}_{\mathrm{c}}^{i,S_j})}\right)^2 + \left(\overline{(\Im(\mathbf{P}_{\mathrm{c}}^{i,S_j})}\right)^2}. \tag{3.16}$$

Please note that the definition of the arctan in Equation 3.15 requires adding a value of 0.5 for negative values of $\Re(\mathbf{P}_{\mathrm{c}}^{i,S_j})$. These average values can now be directly compared to the experimentally obtained $p_{\mathrm{c}}^{S_j}$ and $f_{\mathrm{c}}^{S_j}$ values. Please note that these calculated $f_{\mathrm{c}}^{S_j}$ values do not take disorder effects into account, as they occur, e.g., due to vibrations of the molecules. Thus, the experimental $f_{\mathrm{c}}^{S_j}$ values are expected to be smaller than the calculated values.

The same procedure as explained here for the S1s orbital would also apply for the calculation of the p_{c} and f_{c} values of the other chemical components in the unit cell, i.e., the C and N atoms. However, for experimental reasons, i.e., beamtime and the low intensities of the C1s and N1s photoemission lines for the respective Bragg energies, triangulation of the NIXSW data was only performed for photoemission from the S1s orbital.

4. Experimental

Experiments reported in this thesis were performed in different UHV chambers with base pressures lower than 3×10^{-10} mbar. SPA-LEED, STM, and temperature programmed desorption spectroscopy (TPD) measurements were performed in Bonn. A detailed description of the respective UHV chambers can be found in references [70–72]. PES and NIXSW measurements were performed at the I09 endstation of the Diamond Light Source in Didcot, UK. All chambers allowed for sample cooling with liquid nitrogen or liquid helium. Additional combined room temperature (RT) STM/AFM measurements were performed in the lab of Adam Sweetman at the University of Leeds, UK. This chapter gives an overview of the most important experimental procedures, parameters, and setups.

4.1. Sample Preparation

4.1.1. Single crystal surfaces

Experiments were performed on the (100) and (111) surfaces of Ag single crystals. The Ag crystals were purchased from MaTecK with a surface roughness of less than 0.01 µm and a surface orientation accuracy better than 0.1°. These samples were cleaned by 20 min. sputter cycles at an argon pressure of 1×10^{-5} mbar with an accelerating voltage of 1 kV, and an emission current between 5 and 20 mA, depending on the setup. The resulting sample currents were about $5 - 10$ µA. Subsequently, the samples were annealed at elevated temperatures for about one hour.

The annealing temperatures were chosen according to the experimental requirements. For STM measurements, Ag(100) crystals were annealed at temperatures of 700 K to 750 K. At higher annealing temperatures of about 850 K, the formation of Ag clusters accompanied by the pinning of Ag steps at these clusters was observed. As the step pinning led to the observation of curved step edges [71, 73], annealing temperatures above 750 K were avoided for STM samples.

Ag(111) crystals used for STM measurements and Ag(100) crystals used for NIXSW measurements were annealed at 820 K. In the latter case, these high temperatures were used to improve the mosaicity of the samples and, hence, to decrease the FWHM of the measured reflectivity curve. After the annealing, the samples were cooled down to RT and checked by LEED, STM, or XPS to ensure a sufficient quality of the clean crystal surface. If necessary, i.e., in case of faint or broad substrate diffraction spots, or the observation of additional diffraction spots, the cleaning cycle was repeated.

In this thesis, the lattice constants of the Ag surfaces and the distances between the Bragg planes were derived from the literature value of the Ag bulk lattice constant. For a temperature of 25°C, this lattice constant is $a_{\mathrm{Ag}} = 4.0856 \pm 0.0020$ Å [74–77].

4.1.2. Preparation of Merocyanine layers

Merocyanines were deposited from home-built Knudsen cells as described in reference [70]. During the deposition, the metal single crystals had a temperature of 300 ± 5 K, if not stated otherwise. The Knudsen cell temperatures used for the deposition of the merocyanines were about 500 K. However, as the temperature of the Knudsen cells is measured indirectly, at a point attached to the heater, deviations of about 50 K were observed for using different Knudsen cells and the same merocyanine. Accordingly, the Knudsen cell temperatures are not specified in more detail here. A shutter mounted directly in front of the Knudsen cell was used to control the deposition process.

Typical deposition rates were lower than 0.1 ML/min. Please note that one monolayer (ML) was defined as one complete layer of the respective commensurate phase in the first molecular layer on the surface. The deposition rate is a decisive factor in the preparation of merocyanine layers, as different deposition rates led to the formation of different structural phases, especially for coverages in the multilayer range (visible in the TPD spectra presented in Appendix D). Hence, deposition rates were kept constant during the deposition process as much as possible to avoid obtaining a mixture of structural phases. In the case of the merocyanine HB238-D, two commensurate monolayer phases were observed. The small α-phase was obtained by deposition rates higher than 0.03 ML/min. The more stable Q-phase was prepared by deposition rates of about 0.02 ML/min. Variation of the deposition rate during the deposition led to a mixture of both phases.

At the experimental setup used for SPA-LEED and TPD measurements, deposition rates were monitored by a QMG422 quadrupole mass spectrometer (QMS) from Balzers/Pfeiffer, allowing for measurements in a range of $m/z = 1$ amu/e to 1000 amu/e. m/z is the mass-to-charge ratio of the detected ions with m being the ionic mass and z being the ionic charge [78]. For monitoring the deposition rate, the signal intensity of the ion $[\mathrm{MC}]^+$ was recorded over time. The m/z values for the $[\mathrm{MC}]^+$ ions of all investigated merocyanines (MC) are listed in Table 4.1.

Table 4.1.: Chemical formulas for the investigated merocyanines (MC). The mass-to-charge ratio m/z refers to the ion $[\mathrm{MC}]^+$ used to monitor the deposition rates by QMS measurements. It was calculated for the isotopes with the highest relative abundance [78].

Merocyanine (MC)	alkyl side groups	formula	m/z for $[\mathrm{MC}]^+$
HB238-A	*n*Bu, *t*Bu	$C_{23}H_{30}N_4S_2$	426.19
HB238-B	*n*Pr, *t*Bu	$C_{21}H_{26}N_4S_2$	398.16
HB238-C	Et, *t*Bu	$C_{19}H_{22}N_4S_2$	370.13
HB238-D	Me, *t*Bu	$C_{17}H_{18}N_4S_2$	342.10
HB238-E	*n*Bu, *i*Pr	$C_{22}H_{28}N_4S_2$	412.61

For measurements at the I09 endstation at the Diamond Light Source (XPS and NIXSW) where no QMS was accessible, the sample preparation parameters, i.e., heating rate of the evaporator and the deposition time, were determined and optimized beforehand with the Balzer/Pfeiffer QMS in the lab in Bonn. For STM measurements, which were performed in a different UHV chamber than the SPA-LEED and TPD experiments, a different Knudsen cell was used. Here, the deposition parameters were determined by successive depositions of the merocyanines followed by LEED and STM measurements to control the coverage and the structure formation.

4.1.3. Preparation of KCl layers

KCl was purchased from VWR with a purity higher than 99.5%. After filling the Knudsen cell, the KCl was degassed in UHV for about 12 h. During the KCl deposition, the Ag(111) sample was kept at 403 ± 5 K [79]. The reasons for this specific temperature are based on rearrangements of the Ag steps in contact with the KCl layer that will be discussed in Chapter 10, below. For the deposition, the Knudsen cell was kept at a temperature of 853 ± 2 K, resulting in a deposition rate of about 1.25 ± 0.05 ML/min. Again, please note that this temperature will most likely differ for other Knudsen cells. These parameters resulted in homogeneous, thin KCl layers of $2-3$ ML thickness suitable for STM measurements.

4.2. Spot profile analyzing low energy electron diffraction experiments

4.2.1. Experimental Setup

SPA-LEED experiments were performed using a third-generation device with a conical front end purchased from Scienta Omicron. The electron gun was equipped with a LaB_6 filament operated with a current of 1 A. As electron radiation can damage the organic layers, i.e., in the form of a dissociation of the molecules, low sample currents are favorable. Typical values used for the experiments reported here are about 1 nA. To improve the count rates for low sample currents, a channeltron aperture with an increased diameter of 300 µm, instead of 100 µm, was used. This allows for more diffracted electrons to enter the channeltron, and hence it increases the count rate for a given sample current [80]. However, the increase of the aperture also causes a decrease in the achievable resolution of the SPA-LEED device.

4.2.2. Data processing

For controlling the measurements, the spa4 software was used before the system was updated to the WinSPA software [81]. As already mentioned above, the diffraction patterns of merocyanines are sensitive to beam damage. However, due to their large real space unit cell and the corresponding high number of diffraction spots in reciprocal space, they need

long measurement times to achieve a good signal-to-noise ratio. To reduce the beam damage of the merocyanine layer, a routine was developed that adjusts the measurement time needed for each pixel of the reciprocal space in dependence on the count rate of that pixel, which is determined in a short pre-scan. For low count rates, the routine scans faster. Thus, it saves time when scanning the background of the diffraction pattern where only noise is detected, while it measures the diffraction spots longer and with higher statistics. The routine is published in ref. [82] and will be discussed in Chapter 5.

For the exact determination of the superstructure matrices, the diffraction patterns were deskewed by the program LEEDCal [83, 84]. The deskewing matrices were created from diffraction patterns measured for well-known commensurate structures with the same experimental parameters as the patterns of the merocyanine structures. For this purpose, the $c(8 \times 8)$ structure of 3,4,9,10-perylene-tetracarboxylic-dianhydride (PTCDA) on the Ag(100) surface [85] was used. A detailed description of the theory behind the deskewing process can be found in reference [84]. Finally, diffraction patterns were simulated using the programs LEEDLab [86] and Spot-Plotter [87].

4.2.3. Commensurability

To prove the commensurability of the merocyanine structures, detailed scans of areas were performed in which diffraction spots of different symmetry-equivalent domains coincide. Due to the large unit cells of the merocyanine monolayers in real space, unit cells in reciprocal space are small in comparison to the Ag(100) unit cell. Hence, already small deviations from a commensurate structure, noticeable as non-integer matrix elements in the respective superstructure matrices, cause huge displacements of the diffraction spots. Thus, spots in which diffraction spots of different symmetry-equivalent domains coincide for a commensurate structure are perfect for testing the superstructure matrix. In case of small deviations from integer numbers of the matrix elements, i.e., no commensurability, these spots would be distorted or split into groups of diffraction spots. However, for the present merocyanine structures, this was not the case, and we can ensure integer matrix elements, i.e., a commensurate structure formation, for all respective phases.

4.3. Temperature programmed desorption spectroscopy

TPD spectra were measured with a QMS of the company Balzers/Pfeiffer with a range of $m/z = 1$ amu/e to 1000 amu/e. Spectra were measured with a sampling rate of 2 Hz. A Feulner cup [88] was used to exclusively detect material that desorbed from the sample surface.

The sample heating was realized by a tungsten filament mounted on the rear side of the Ag(100) crystal and parallel sample cooling with liquid helium or liquid nitrogen. This ensured defined heating/cooling rates and minimized the desorption of merocyanines from the sample holder. The sample heating was controlled by a Eurotherm device and performed at 1 K/s to a maximum temperature of 850 K. Temperature, time, heating

power, and the, by the QMS detected signal of the desorbed molecules, were monitored by a LabView program [89] that was written by N. Humberg [90] and modified by B. Wolff [91].

4.4. Scanning tunneling microscopy measurements

STM measurements were mainly performed in Bonn with a variable temperature (VT) RHK Beetle type STM. For most of the experiments, an RHK SPM100 controller was used, which was later replaced by an RHK R10 device. The bias voltage (U_{Bias}) was applied to the sample. Thus, negative values of the bias voltage refer to tunneling from occupied electronic states of the sample to the unoccupied states of the STM tip. Measurements were performed in constant current (I_{t}) mode. STM tips were etched from a 0.1 mm thick Pt/Ir wire with a Pt/Ir mass ratio of 90:10. A helium cryostat and a 50 W tungsten filament below the sample stage allowed for STM measurements in a temperature range between 25 K and room temperature.

The STM measurements of thin KCl films on Ag(111) presented in Chapter 10, were performed in the lab of A. Sweetman in Leeds, UK. The Scienta Omicron instrument that was used in combination with a Nanonis controller allowed for STM and AFM measurements, respectively. Please note that the results of the performed AFM measurements are not included in the present thesis. STM measurements were performed at RT and in constant current mode. The bias voltage was applied to the tip. However, to avoid confusion, all bias voltage values reported in this thesis refer to the sample. The etched W-tips used for the measurements were cleaned by electron bombardment beforehand. To minimize the drift, the cryostat of the sample stage was heated to a temperature a few degrees above RT.

At both setups, correct length and height measurements were ensured by regular scanner calibrations. Calibration measurements were performed on clean Ag(100) surfaces with atomic resolution of the Ag lattice. For the calibration of the scanner in the lateral x-/y-directions, images were recorded with a 0°/90° rotation, respectively. This led to an alignment of the fast scanning direction with the x-/y-direction of the scanner. The calibration parameters were determined from the deviation of the measured lattice constants from the respective literature values. The same applies to the calibration in the z-direction, for which the height of steps of the Ag(100) crystal was measured.

4.4.1. Data processing

In Bonn, the software RHK XPMPro 2.0.1.5 [92] and later, the RHK software R10 7.0.2.0 [93] were used for controlling the STM measurements. In Leeds, the Nanonis software [94] was used.

The scanning probe data was evaluated by using the software Gwyddion [95] and WSxM [96]. Error lines were corrected, and the contrast and brightness of the images were adjusted. In special cases, merocyanine data were processed by correlation averaging using the periodicity of the molecular structures. This function is implemented in the

software WSxM and helps to emphasize structures in the unit cells that exhibit weak topographic contrast.

STM data of the merocyanines was deskewed using the lattice parameters obtained from the respective SPA-LEED measurements. For the assignment of the SPA-LEED lattice vectors to the lattice vectors observed in the STM measurements, scans were performed with the lattice vectors being parallel to the fast scanning direction. Detailed information about the determination of the lattice parameters from STM measurements can be found in the supporting information of ref. [79] (see Appendix A.3), which demonstrates the process for the example of KCl layers on the Ag(111) surface.

4.5. Photoelectron spectroscopy techniques

PES measurements were performed at the I09 endstation at the Diamond Light Source in Didcot, UK. The endstation uses radiation from an undulator in the electron storage ring of the synchrotron and is equipped with a nitrogen-cooled Si(111) double crystal monochromator and a grating monochromator. This allows for measurements with soft ($100 - 2100$ eV) and hard x-rays ($2.1 - 20$ keV) of high intensity and brilliance. Photoelectrons were detected by a hemispherical EW4000 HAXPES analyzer purchased from Scienta Omicron. The analyzer had an acceptance cone of 56° and was mounted in the photon polarization plane [97, 98].

For the experiments of this thesis, synchrotron light was needed for two reasons:

1. The high intensity of the x-ray beam facilitates measuring XPS spectra with good statistics in less than 1 min. on a small spot of the sample. This allows the measurements to be repeated for multiple positions on the sample. Averaging the data from different sample spots significantly improves the signal-to-noise ratio, but keeps the effect of beam damage low.

2. The tunable beam energy, i.e., the tunable wavelength of the synchrotron light, is necessary for the NIXSW measurements. The reason for this is that the photoemission needs to be measured for a photon energy range of ± 4.5 eV around the Bragg energy of the chosen lattice plane.

The following sections give details about the experimental procedures and the parameters that were used for the XPS and NIXSW measurements. All measurements were performed at room temperature.

4.5.1. X-ray photoemission spectroscopy

For XPS measurements, soft x-ray radiation in a range of $120 - 700$ eV was used. Hence, measurements probed the valence band and the core levels of the Ag(100) sample and the adsorbed merocyanines. XPS measurements were performed under the following aspects: the characterization of the clean Ag(100) crystal, the validation of the coverage and stoichiometry of the adsorbate, and investigations of the adsorbate surface interactions.

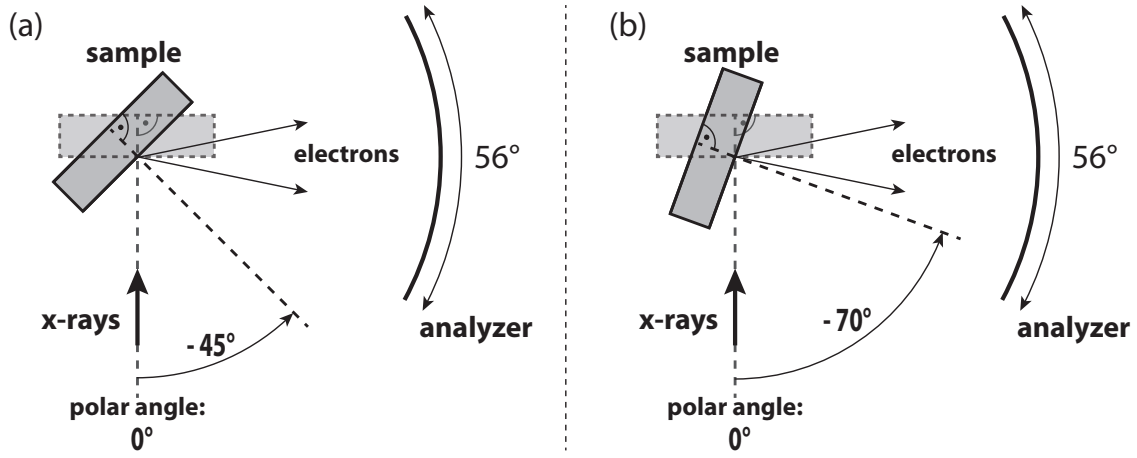

Figure 4.1.: Top view of the sample geometries used for XPS measurements at the I09 endstation of the DLS in Didcot, UK. (a) Sample geometry used for the XPS measurements of the merocyanine layers. (b) Sample geometry used for measurements with *quasi-normal* emission of the photoelectrons. The sample rotation around the vertical manipulator axis (polar angle) is indicated by the surface normal (dotted line). For comparison, the sample position for a polar angle of 0° (grazing emission geometry) is indicated by dotted lines. Arrows, indicating the photoelectrons, are arbitrary in their positions but visualize the shielding effect of the sample in the grazing emission geometry (overlap of the arrows with the sample).

Measurements were performed with the sample being rotated by −45° in the polar direction toward the analyzer, as displayed in Figure 4.1 (a). Hence, the surface sensitivity of the measurement was increased in comparison to measurements performed under *quasi-normal* emission of the photoelectrons (polar angle of −70°), as displayed in Figure 4.1 (b). However, compared to measurements with grazing emission of the photoelectrons (polar angle of 0°), signal intensities are higher, as the sample does not shield any photoelectrons from the analyzer. In Figures 4.1 (a) and (b), the sample geometry for grazing emission is indicated in light gray and with dotted lines.

Table 4.2 summarizes further experimental parameters used for the XPS measurements. Photon energies (E_γ) were chosen with respect to the binding energy range measured. To be most surface sensitive, the resulting kinetic energy (E_{kin}) of the photoelectrons was about 100 eV. The different kinds of spectra measured and their experimental purpose will be briefly described below.

Overview spectra

To exclude contamination of the sample, the Ag(100) crystal was characterized by XPS before the deposition of the adsorbates. The respective overview spectra were measured with a beam energy of 700 eV and a binding energy range of −15 to 600 eV. While for a clean sample only signals from Ag are detected, contamination would be observed by additional photoemission lines, e.g., C1s lines. In case of contamination, the sample cleaning was repeated.

Table 4.2.: Parameters used for XPS measurements. The time per spectrum results from the binding energy range of the spectrum, the step width, and the number of frames (repeats) measured. Please note that the number of frames varies for the measured overview spectra and the spectra of the Fermi edge. Accordingly, the number of frames is not given in the table. However, the number of frames was not altered for the photoemission spectra measured for the same orbital, thus that averaging of the spectra was allowed.

	photon energy (E_γ)	pass energy (E_{pass})	binding energy (E_{bind}) range	step width	time per spectrum
Overview spectrum:					
	700 eV	50 eV	$-15 - 600$ eV	500 meV	$\approx$ 5 min
Spectra for the line shape analysis:					
S2p	270 eV	20 eV	$163 - 173$ eV	40 meV	1 min
C1s	390 eV	20 eV	$285 - 294$ eV	20 meV	1 min
N1s	500 eV	20 eV	$398 - 408$ eV	40 meV	1 min
Spectrum of the Fermi edge for energy calibration:					
	E_γ	20 eV	$2 - 6$ eV	20 meV	$\approx$ 6 min

After the deposition, overview spectra were measured to control the coverage of the merocyanines. As a reference, an XPS spectrum of HB238-A with a coverage of less than 1 ML was used. The respective spectrum is displayed in Figure 4.2. The coverage of this sample was determined by LEED measurements beforehand [48, 70].

As the merocyanines HB238-A, HB238-B, HB238-C, and HB238-D, only differ in the length of the alkyl side chains, they exhibit the same number of S atoms. The comparison of the intensities of the S2p photoemission lines in the measured overview spectra thus provides information about the merocyanine coverages. For this purpose, overview spectra were normalized with respect to the Ag4d photoemission lines. To exclude multilayer effects in the photoemission spectra, XPS and NIXSW measurements were performed for coverages of less than 1 ML, if not stated otherwise.

Adsorbate characterization

Merocyanine layers were characterized by the line shape of the C1s, N1s, and S2p photoelectron lines. As already mentioned above, each photoemission line was probed with a different beam energy (E_γ). This was done on the background that the mean free path of electrons with a kinetic energy of about 100 eV is reduced to a minimum of about 5 Å [11]. Thus, the detected photoelectrons originate from the uppermost layers of the sample, and measurements are hence most surface sensitive.

Merocyanine layers are sensitive to beam damage. For long exposure times, i.e., when several spectra were measured on the same spot on the sample, dissociation of the molecules occurred. This was observed in the form of additional photoemission lines whose intensity increased at the expense of the molecular photoemission lines observed before.

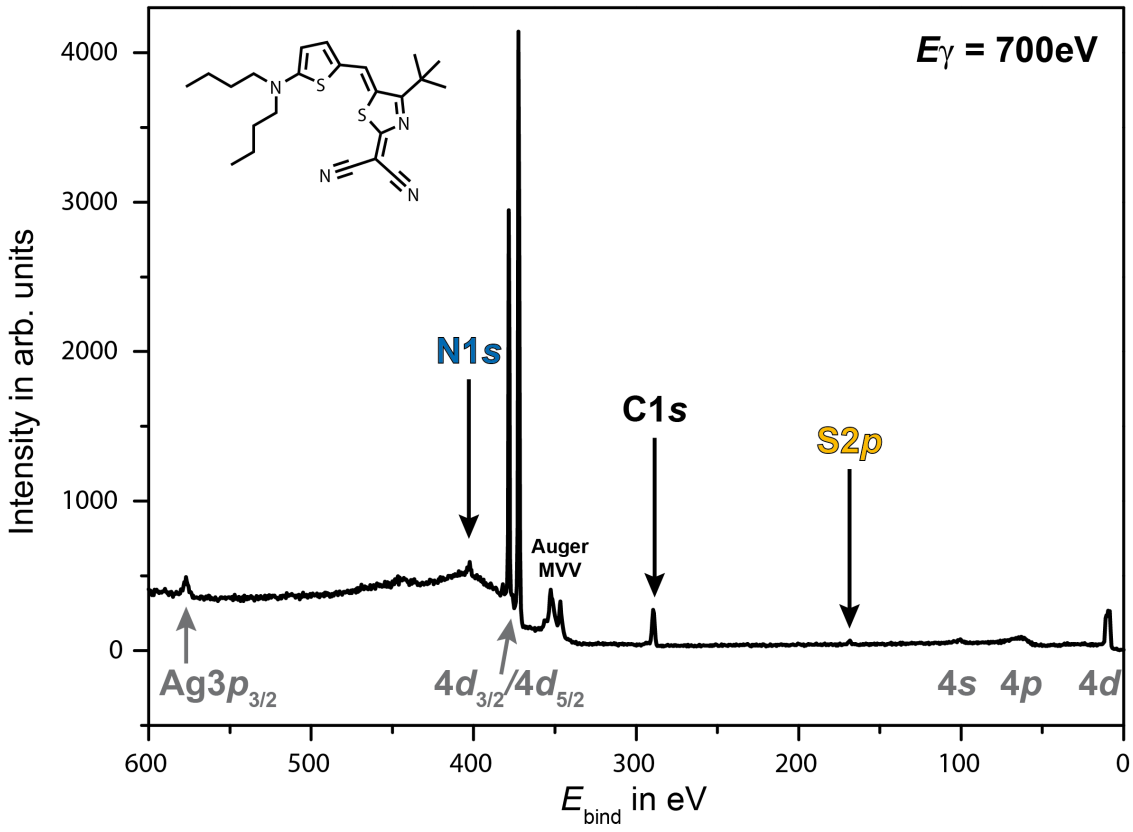

Figure 4.2.: XPS overview spectrum measured for HB238-A on the Ag(100) surface with a coverage of about 0.5 ML at a photon energy of 700 eV. Signals corresponding to the Ag surface are labeled in gray below the spectrum. Signals corresponding to adsorbed HB238-A molecules are labeled above the spectrum. The molecular structure of HB238-A is again displayed in the upper left corner of the spectrum.

To minimize the effect of beam damage on the data, the measurement time per spectrum was reduced to 1 min. for all photoemission lines. To improve the signal-to-noise ratio of the data, spectra of the same photoemission line were measured on different spots on the sample. For the displayed spectra of Chapters 6 and 7, 5 to 10 measurements were averaged.

Small inaccuracies of the monochromator were corrected by calibration measurements of the Fermi edge. Calibration measurements of the Fermi edge were performed after each movement of the monochromator and, thus, for every photon energy. The experimental parameters are listed in Table 4.2. As the Fermi edge is expected to be measured at a binding energy of 0 eV, the XPS spectra were corrected by the experimental binding energies determined for the Fermi edge. The error range of this photon energy calibration was dependent on the accuracy of the Fermi edge determination and hence in a range of ± 0.05 eV.

4.5.2. Normal incidence x-ray standing wave measurements

NIXSW measurements were performed to determine the adsorption heights of the C, N, and S atoms of HB238-A with respect to the extended Ag(200) Bragg planes parallel to the crystal surface (ref. to Chapter 8), and for the determination of the S adsorption sites in the observed monolayer phases of the merocyanines (ref. to Chapter 9).

Accordingly, the photoemission of the C1s, N1s, and S1s orbitals was measured for the Ag(200) and Ag(400) Bragg planes, parallel to the Ag(100) crystal surface. For the determination of the S adsorption sites, photoemission of the S1s orbitals was measured additionally, for two Bragg reflections inclined with respect to the crystal surface, i.e., for the Ag(111) and Ag(220) Bragg reflections. The respective Bragg planes are displayed in Figure 3.3 of Chapter 3. Table 4.3 summarizes the photon energies E^{hkl}_{Bragg} that fit the Bragg conditions of the above-named Bragg reflections. In addition, it specifies the order of harmonics of the undulator spectrum, which is required to access the Bragg energies.

Table 4.3.: Bragg energies E^{hkl}_{Bragg} for measurements of the Ag(200), Ag(400), Ag(111), and Ag(220) Bragg reflections. To access the respective photon energies, the correct order of harmonics of the undulator spectrum is required, as denoted in the table. Lattice spacings d_{hkl} refer to the distance between the Bragg planes at a temperature of 25°C and were calculate from the bulk lattice constant $a_{\mathrm{Ag}} = 4.0856 \pm 0.0020$ Å [74–77].

	Ag(200)	Ag(400)	Ag(111)	Ag(220)
Lattice spacing (d_{hkl})	2.043 Å	1.022 Å	2.360 Å	1.445 Å
Bragg energy (E^{hkl}_{Bragg})	3035.54 eV	6071.08 eV	2628.86 eV	4292.90 eV
Order of harmonics	3	5	3	5

Figure 4.3 illustrates exemplarily two sample orientations that were used for the NIXSW measurements. Panel (a) refers to measurements of the Ag(200) reflection, panel (b) to measurements of the Ag(220) Bragg reflection. The angle ξ denotes the angular deviation of the incident x-ray beam from normal incidence to the measured Bragg plane. ζ describes the angle between the Bragg plane and the surface of the Ag(100) surface. An overview of the ξ and ζ values used for the NIXSW measurements is presented in Table 4.4.

Table 4.4.: Important angles of the NIXSW measurements at the (200), (111), and (220) Bragg reflections. P is the polar angle and refers to the vertical manipulator axis at the I09 endstation at the DLS. ξ denotes the deviation of the incident photon beam from normal incidence. ζ describes the angle between the measured Bragg plane and the surface of the Ag(100) crystal. Please note that the merocyanines HB238-A to HB238-D are abbreviated in this table as A, B, C, and D. Columns corresponding to the same merocyanine are shaded in the same color.

	A(200)	B(200)	B(111)	B(220)	C(200)	C(111)	D(200)	D(111)	D(220)
P	0°	2.4°	-52.3°	-42.4°	2.4°	-52.3°	2.4°	-53.9°	-42.9°
ζ	0°	0°	54.7°	45.0°	0°	54.7°	0°	54.7°	45.0°
ξ	-2°	0.4°	0.4°	0.6°	0.4°	0.4°	0.4°	-1.2°	0.1°

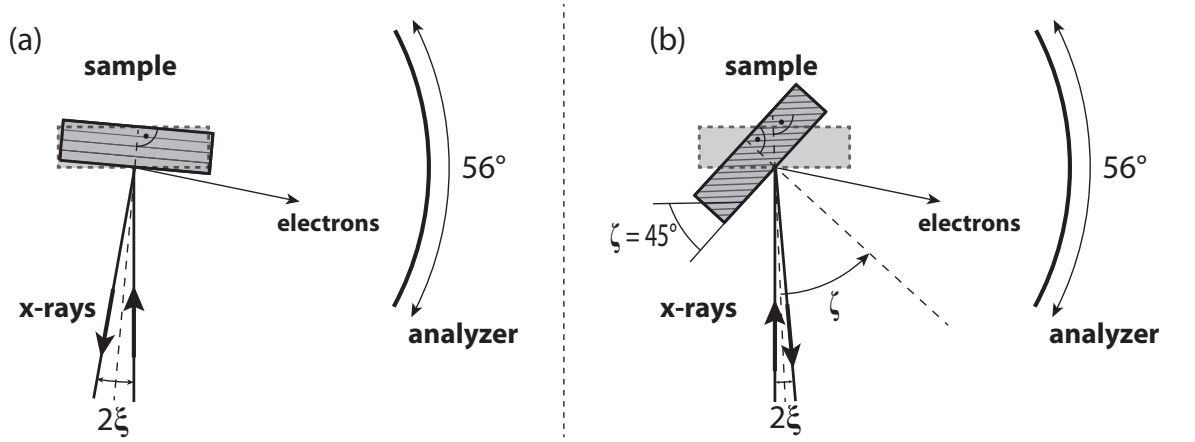

Figure 4.3.: Top view of the sample geometry used for the NIXSW measurements at the I09 endstation at the Diamond Light Source. The sketch applies to the used Ag(100) crystal and represents exemplarily the sample orientations for measurements at the Ag(200) and the Ag(220) Bragg reflection. (a) Sample orientation for measurements at the Ag(200) Bragg reflection. Here, the (200) Bragg planes are parallel to the surface of the Ag(100) crystal. (b) Sample orientation for measurements at the Ag(220) reflection. The angle ζ between the Ag(100) surface and the (220) Bragg planes is 45°. ξ denotes the angular deviation of the incident x-ray beam from the normal incidence with respect to the measured Bragg plane.

Comparable to the XPS measurements, NIXSW data measured for the same orbital, but on different fresh spots of the sample, were averaged to obtain a good signal-to-noise ratio of the data with a low impact of beam-induced damage of the organic layer. At each sample spot, a reflectivity curve was measured to ensure a low mosaicity. Typical FWHM values of the reflectivity curves were in a range of 0.7 to 0.8 eV for the (200) and (220) Bragg reflections and 0.9 to 1.0 eV for the (111) Bragg reflection. In case of bad mosaicity, i.e., in case of broader reflectivity curves, the sample spot was discarded, and the next sample position was approached.

During each NIXSW measurement, the energy of the x-ray beam was increased from $E_\gamma = E_{\mathrm{Bragg}} - 4.5$ eV to $E_\gamma = E_{\mathrm{Bragg}} + 4.5$ eV. The complete photon energy range was divided into three sections. The first section included a photon energy range of 3 eV and was measured for photon energies below E_{Bragg} in which no standing wave field was formed, yet. Accordingly, this region is called a *out-of-Bragg* region in the following. The same applies for the third section, in which a photon energy range of 3 eV above E_{Bragg} was measured, again for an energy range in which no standing wave field was formed. These two out-of-Bragg regions were probed by 6 data points (photoemission spectra) each. The respective spectra show the photoemission yield of the measured orbital without the influence of the standing wave field, i.e., the adsorption heights of the adsorbates. The section of the photon energy range in which the standing wave field was formed, was probed by 24 data points distributed over a range of $E_{\mathrm{Bragg}} \pm 1.5$ eV. Here, more data points were measured compared to the out-of-Bragg regions, to ensure a good description of the photon energy dependence of the measured photoemission yield. The reflectivity curve used for the data evaluation was measured stepwise in parallel to the photoemission spectra of the NIXSW scans.

4.5.3. Data processing

For a better signal-to-noise ratio of the data, measurements on different sample spots were averaged, for both XPS and NIXSW data.

Photoemission lines were fitted, using the software CasaXPS [62]. For all spectra, a linear background was subtracted. The slight asymmetry of the photoemission lines was described by a Gaussian/Lorentzian product combined with a blend function (TLA(3,6,8)) [62]. Comparable to the analysis of the soft XPS data, fit models for the NIXSW analysis were developed from the respective averaged out-of-Bragg spectra. For these fit models, certain fit parameters were constrained to ensure chemical consistency. This applies to the ratio of the line integrals that is known from the molecular stoichiometry, and the FWHM, which is expected to be the same for photoemission lines of the same orbital, e.g., the S1s orbital. The line positions of independent lines, however, were considered as a free fit parameter.

For the evaluation of the NIXSW data, line positions and the FWHM of the lines were constrained to the values of the fit model developed from the out-of-Bragg spectrum. Only the line integrals were not constrained to account for the changes in the photoelectron yield during the measurement. The propagation of the developed fit parameters to all photoemission spectra of the NIXSW measurement was performed in CasaXPS. The propagation included the calculation of the standard deviation of the photoemission yield. The fit results, i.e., the photoemission yield, the standard deviation, and the corresponding photon energies, also known as the photoelectron yield curve, were exported in ASCII files for further evaluation with the program Torricelli [68]. The scattering of the data points in the yield curve around the expected values strongly depends on the signal-to-noise ratio observed in the individual photoemission lines of the measurement. For the out-of-Bragg spectra of the here presented NIXSW data sets, the line integrals deviate by about 6% from the expected ratio.

For the data evaluation with Torricelli [68], the ideal reflectivity curves and phases of the Ag Bragg planes were calculated for a sample temperature of 300 K, with respect to the values of ζ and ξ, listed in Table 4.4. Non-dipolar correction parameters for the different photon energies, and hence, for the different kinetic energies of the photoelectrons, were imported from the NIST database [69] and are listed in Table 4.5. Normalized statistical errors of the photoemission yield were calculated by a Monte-Carlo analysis in Torricelli [68]. The p_c and f_c values and the respective statistical errors, obtained from the fits of the photoemission yield curves in Torricelli, were plotted in Argand diagrams as, e.g., displayed in Figure 8.4 of Chapter 8, below.

4.5.4. Binding energy corrections

Due to a hysteresis, i.e., a mispositioning, in the mechanics of the monochromator, small inaccuracies in the photon energies exist. In NIXSW measurements, the difference between the real and expected photon energies becomes noticeable in a binding energy shift of the photoemission line in the out-of-Bragg regions. As these artificial shifts lead to an under- or overestimation of the photoemission yield of individual photoemission lines during the NIXSW analysis, they need to be corrected.

Table 4.5.: Non-dipolar correction parameters of the S1s, the C1s, and the N1s orbitals, calculated for the different kinetic energies E_{kin} of the photoelectrons. Δ is the difference of δp and δd. The data was provided by the NIST database [69]. For better visibility, table entries corresponding to the same orbital are shaded by the same color.

Orbital	Bragg reflection	E_{kin} in eV	δp	δd	$\Delta = \delta d - \delta p$
S1s	(111)	152.35	0.38087	−1.37995	−1.76082
S1s	(200)	558.96	−0.46395	−1.51320	−1.04925
S1s	(220)	1816.08	−1.11820	1.39195	2.51015
S1s	(400)	3593.92	−1.44725	1.23105	2.67830
C1s	(200)	2748.74	0.76647	0.56969	−0.19678
N1s	(200)	2633.74	0.86944	0.63570	−0.23374

In case of chemical components with slightly different binding energies that are located at different adsorption heights, a binding energy shift of the experimental photoemission line is expected for the photon energy range in which the standing wave field exists. However, the binding energy of the experimental photoemission line should be constant for the out-of-Bragg photon energy regions. In Figure 4.4, the out-of-Bragg regions of the photon energy are shaded in light blue. Here, the binding energy of the experimental photoemission line was determined and plotted versus the expected photon energy at which the spectrum was supposed to be measured. As visible in Figure 4.4, here demonstrated for the S1s orbital of HB238-D and the (111) Bragg reflection, the binding energy decreases linearly during the NIXSW measurement. The same behavior of decreasing binding energies was observed for all evaluated NIXSW measurements of this thesis.

An evaluation of the individual (not averaged) NIXSW spectra revealed that the error in the photon energy is reproducible. All spectra that were measured for the same Bragg reflection and hence, the same binding energy range, exhibited the same error in the photon energy and, accordingly, the same shift in the binding energy. Thus, the binding energy correction could be applied to the averaged data. This correction of the binding energy shift was needed to allow for a robust separation of the S1s photoemission lines of the electron donor and the electron acceptor, as it will be described in Chapters 8. Without the correction, the photoemission yield curves of the separated donor and acceptor components were observed to show an increasing or decreasing background that deviated from the expected intensity of one.

For correcting the binding energy, the data of Figure 4.4 was fitted by a linear regression curve as indicated by the red line. The maximum difference in the binding energy observed between the first and the last scan of the measurement is indicated by a black arrow. Here, the binding energy difference amounts to about -0.06 eV. Without the photon energy error, the binding energy E_{bind} is expected to be constant for the out-of-Bragg regions.

For the NIXSW data evaluation in this thesis, the binding energy of the first photoemission spectrum, measured for the smallest photon energy E_{γ}^{0}, was assumed to be correct. Please note that the concrete value of the binding energy is not important, as it does not impact

the shape and the fit of the photoemission yield curve. To ensure a constant binding energy in the out-of-Bragg regions, the binding energies of all photoemission spectra E^i_{bind} were corrected manually in CasaXPS by the value of ΔE^i_{bind} that was determined according to

$$\Delta E^i_{\text{bind}} = b(E^i_\gamma - E^0_\gamma). \tag{4.1}$$

Here, E^i_γ depicts the expected photon energy of the spectrum i (x-axis of Figure 4.4) and b is the slope of the regression curve. The index $i = 0, 1, 2, .., 36$ refers to the individual spectra of the series, with $i = 0$ being the first spectrum.

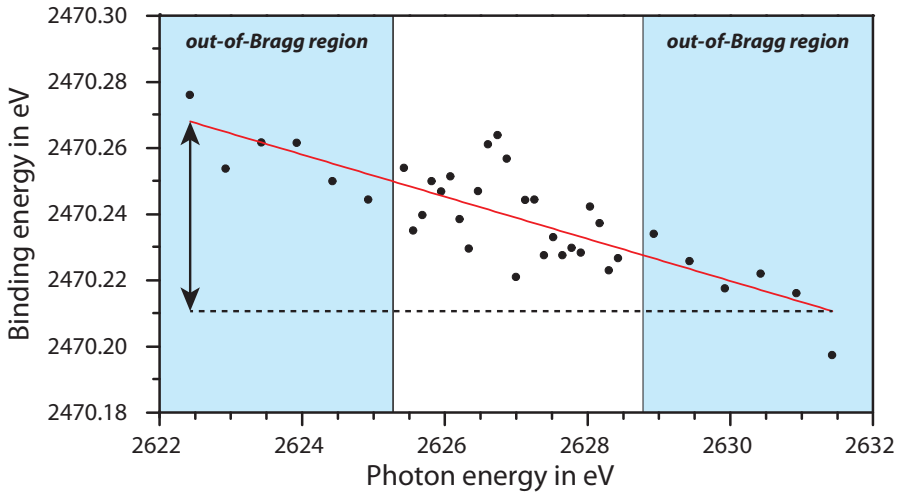

Figure 4.4.: Artificial decrease of the binding energy during the NIXSW measurements caused by inaccuracies of the monochromator. The data was measured for the S1s orbital of HB238-D and the Ag(111) Bragg reflection with a theoretical Bragg energy of 2628.86 eV. Please note that the Bragg energy of the measured data differs from the theoretical value by about 1.5 eV, due to temperature differences and the energy calibration of the monochromator. The data was fitted by a linear regression curve that is displayed in red. The black arrow indicates the maximum difference in the binding energies, due to the error in the photon energy.

5. Optimizing SPA-LEED measurements

The work described in this chapter was published in the Journal Review of Scientific Instruments 94, 064707 (2023): "Increasing the scan speed in high resolution, low energy electron diffraction measurements by presetting the gate time" by Anna J. Kny, Moritz Sokolowski, and Peter Kury.

A reprint of this publication can be found in Appendix A.1. The author's contribution to the publication of this paper included: measuring the experimental data, presenting the data scientifically (partly), data discussion, and revision of the manuscript.

This chapter introduces a speed-up data acquisition routine for SPA-LEED measurements. As reported in the author's master's thesis, HB238-A monolayers on the Ag(100) surface undergo a dewetting of the surface over time [70]. The layers are stable for only about one day before they show a decreasing coverage of the surface by ordered domains. This decrease in coverage is accompanied by an increase of bare Ag surface and the growth of three-dimensional clusters on the surface, which can be directly observed by STM measurements. In SPA-LEED measurements, the dewetting is observed as a decrease in the diffraction spot intensities. Electron beam-induced damage of the merocyanine monolayer during the SPA-LEED measurements is an additional factor for the decrease of the diffraction spot intensity with time. As a consequence, it is desirable to keep the measuring times of SPA-LEED patterns to a minimum. However, recording of two-dimensional SPA-LEED patterns is in particular for merocyanine monolayers time demanding, because these exhibit a high density of low-intense diffraction spots (due to large unit cells in real space) and thus require the collection of many data points and a good signal-to-noise ratio of the data.

In order to save time during measurements of two-dimensional SPA-LEED patterns without losing much information in reciprocal space, a speed-up routine was developed. Evidently, there are many other situations of recording SPA-LEED images, where a reduction of the measurement time is welcome. Some of these are mentioned in Appendix A.1 and the conclusion of this chapter. However, this chapter specifically focuses on the application of the routine for the analysis of merocyanine monolayers and hence, on the advantage of the speed-up routine for two-dimensional SPA-LEED scans.

5.1. Scientific context

Dewetting of molecular layers from surfaces is a frequently occurring phenomenon [12, 99, 100]. In the monolayer, often chemisorbed structures of flat-lying molecules are observed [48, 101, 102]. For some molecules, the arrangement in the monolayer equals the molecular arrangement in the crystallographic bulk lattice planes [102]. However, some molecular crystals do not exhibit lattice planes with an in-plane orientation of the molecules, but the molecules in one plane are tilted or shifted with respect to each other [12]. This is one reason why molecules are forced into different, bulk-unlike structures when they adsorb on a substrate surface in a flat-lying geometry. An adsorption geometry that is supported by the interfacial interactions. As a result, dewetting, i.e., a slow phase transformation of the monolayer to small crystal-like clusters, might occur. This is driven by a minimization of the surface free energy and the lattice energy of the organic structure [12, 103].

As already described in Chapter 3.2, a SPA-LEED instrument scans the intensity of the reciprocal space as a function of the momentum transfer parallel to the surface ($\mathbf{k}_{||} = (\mathbf{k}_x, \mathbf{k}_y)$). This is done by an electrostatic deflection system. The intensity of a pixel in the reciprocal space is measured by a channeltron detector in a point-by-point manner. Hence, the total acquisition time of a two-dimensional scan, i.e., an array of pixels, is given by the scan size in the reciprocal space (proportional to the number of pixels) and the acquisition time (gate time) of each pixel. Typical scans with a resolution of 600×600 pixels and sufficient gate times of $5 - 10$ ms require total acquisition times of 30 to 60 min per scan. Taking into account that a detailed analysis of an organic layer requires more than one scan, or scans with even higher resolution, it becomes apparent that long acquisition times result, which can be a major restriction of the SPA-LEED method, especially when metastable (only kinetically stabilized) organic layers are investigated.

5.2. The speed-up routine

To decrease the total acquisition times for two-dimensional SPA-LEED scans, a speed-up routine was developed. This section describes the general working principle of the speed-up routine. For more detailed information, the reader is referred to the publication in Appendix A.1.

The idea behind the routine was to adapt the user-set gate time τ_{set} during the recording of a scan to the information content at the pixel position, i.e., the specific $\mathbf{k}_{||}$ value. Pixels of the reciprocal space that correspond to diffraction spots exhibit high count rates (intensities) and are thus measured with the user-set gate time. For pixels of low intensity that correspond to the background of the diffraction pattern and for which the information content is low, the user-set gate time is reduced. Accordingly, pixels of low intensity are measured faster, and hence, the scan speed of the SPA-LEED pattern is increased.

The routine works according to the following principle. The user-set gate time τ_{set} is adjusted with respect to the count rate of a pixel f_{pre}. To determine the count rate, a pre-scan is performed for each pixel. This pre-scan is measured with a gate time τ_{pre} that is smaller than the user-set gate time. The value of τ_{pre} was 0.15 ms in the present thesis, but is adjustable by the user. The count rate f_{pre} of the pixel is determined from the

number of measured counts N_{pre} during the pre-scan by $f_{\mathrm{pre}} = N_{\mathrm{pre}}/\tau_{\mathrm{pre}}$.

By the value of f_{pre}, the routine accesses the relevance of the measured pixel. The relevance is classified in three count rate ranges: the irrelevant, fully relevant, or increasingly relevant count rate range. The user can control the assignment of the pixel to these ranges by the input of the threshold count rate values $f_{\mathrm{TH,low}}$ and $f_{\mathrm{TH,high}}$. These apply as follows:

- For $f_{\mathrm{pre}} < f_{\mathrm{TH,low}}$ the pixel is judged to be irrelevant, i.e., to be part of the background of the SPA-LEED pattern. In this case, the scan finishes and f_{pre} is assigned to the pixel intensity.
- For $f_{\mathrm{pre}} > f_{\mathrm{TH,high}}$ the pixel is judged to be fully relevant, i.e., to correspond to a diffraction spot. In this case, a second scan with a gate time $\tau_{\mathrm{post}} = \tau_{\mathrm{set}} - \tau_{\mathrm{pre}}$ is performed. Thus, the total gate time of the fully relevant pixels corresponds to the user-set gate time.
- For $f_{\mathrm{TH,low}} < f_{\mathrm{pre}} < f_{\mathrm{TH,high}}$ the pixel is judged to be increasingly relevant, i.e., pixel in this intensity range might correspond to weak diffraction spots or the wings of a diffraction spot. This range depicts a transition range. In this range, the gate time of the second scan is adjusted with respect to the measured count rate of the pre-scan.

In the present thesis, the gate time of the second scan τ_{req} with which a pixel in the increasingly relevant count rate range was measured, was determined from f_{pre} by a quadratic function according to

$$\tau_{\mathrm{req}} = \tau_{\mathrm{pre}} + \alpha^2(\tau_{\mathrm{set}} - \tau_{\mathrm{pre}}) \tag{5.1}$$

with

$$\alpha = \frac{f_{\mathrm{pre}} - f_{\mathrm{TH,low}}}{f_{\mathrm{TH,high}} - f_{\mathrm{TH,low}}}. \tag{5.2}$$

Finally, the count rates of the measured pixels are determined by the sum of the counts measured in the pre- and the second scan ($N_{\mathrm{pre}} + N_{\mathrm{post}}$) divided by the total gate time with which the pixel was measured ($\tau_{\mathrm{pre}} + \tau_{\mathrm{post}}$).

5.3. Experimental examples

Figure 5.1 shows two SPA-LEED patterns, both measured for the α-phase of HB238-A on the Ag(100) surface. Both patterns were measured on a fresh sample and for comparable coverages of about 1 ML. In addition, both patterns were measured with comparable total acquisition times. However, pattern (b) was measured with the speed-up routine and hence allowed for scanning with a higher resolution (1000×1000 pixels) compared to pattern (a) (320×320 pixels).

SPA-LEED patterns of organic structures that exhibit large unit cells in real space show many faint diffraction spots in the reciprocal space. As visible in Figure 5.1 (a), a resolution of 320×320 pixels is barely sufficient to distinguish between the diffraction spots in the pattern. However, a pattern with a resolution comparable to Figure 5.1 (b), i.e.,

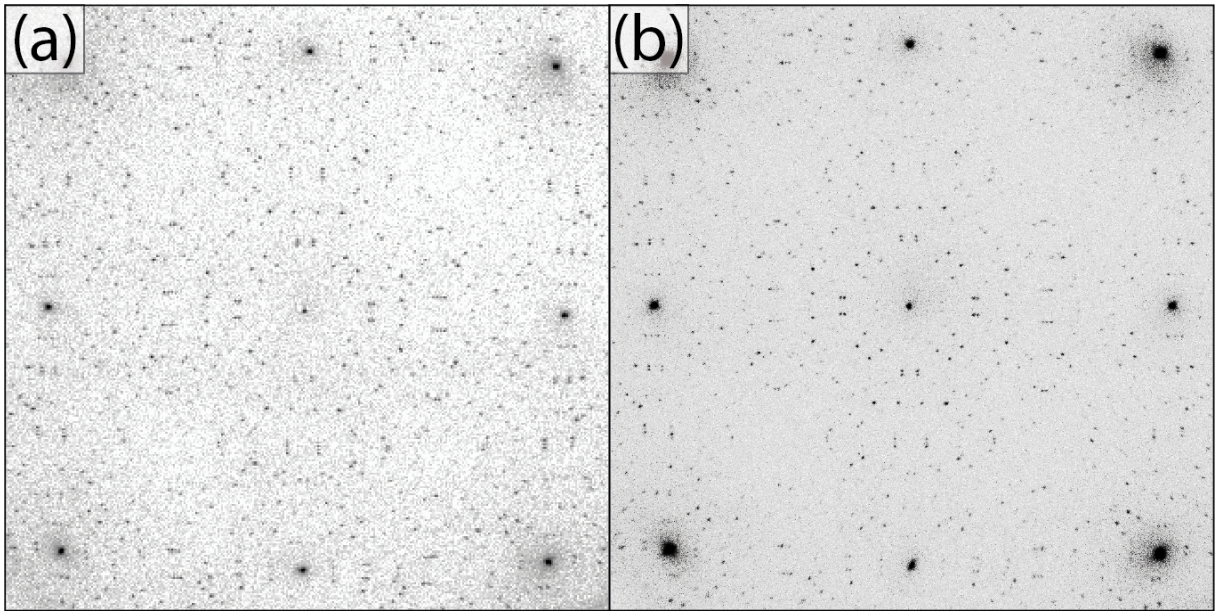

Figure 5.1.: SPA-LEED pattern measured for the α-phase of HB238-A on the Ag(100) surface and an electron energy of 80.9 eV. The pattern (a) was measured without applying the speed-up routine. The acquisition time of pattern (a) was 34 min (320×320 pixels, gate time of 20 ms). Pattern (b) was measured in a comparable time of 27 min with the speed-up routine. However, applying the speed-up routine allowed a measurement of the pattern with much higher resolution (1000×1000 pixels, gate time of 8 ms). The Figure was taken from ref. [82] and slightly adapted.

1000×1000 pixels, measured without the speed-up routine would require 133 min of acquisition time and is therefore not feasible for metastable structures.

The comparison of the patterns of Figure 5.1 demonstrates the advantage of the speed-up routine for two-dimensional SPA-LEED scans of merocyanine structures. Although, few very faint diffraction spots get lost during the measurement with the routine, the high gate times with which the diffraction spots are measured in combination with the high resolution, lead to a diffraction pattern of high contrast and with good spot intensities. The increased noise level of the background, which comes as a side effect of the gate time reduction, can be counteracted by a so-called *oversampling* of the pattern. Oversampling describes the process of summarizing the pixel intensities of successively measured patterns. As the noise of the pattern is arbitrary, but the positions of the diffraction spots are static, oversampling decreases the average noise level of the pattern.

In the present thesis, the speed-up routine was used for SPA-LEED measurements of known superstructures with which the temperature and the coverage dependence of the merocyanine layers were investigated. In addition, it was used to control the quality of the merocyanine layer for subsequent further measurements, i.e., one-dimensional SPA-LEED scans or TPD experiments.

5.4. Conclusion

This chapter presented an excursion on a data acquisition routine that was developed to increase the scan speed of SPA-LEED measurements. Even if the development of this routine is only indirectly related to the topic of this thesis, it has been shown that a detailed analysis of the merocyanine layers would not have been possible without the speed-up routine due to their limited stability [70].

The use of the speed-up routine has several advantages. The gate time reduction for pixels with low intensity allows to perform fast two-dimensional SPA-LEED scans with good resolution of the patterns. These can be used for preparatory characterizations of the sample, i.e., to verify the presence of the correct phase or to verify the correct coverage of the adsorbate before subsequent measurements are performed. In addition, the routine allows performing fast high-resolution SPA-LEED scans. This is explicitly helpful if metastable organic layers with large unit cells, and hence, a huge number of diffraction spots, are measured. However, the usage of the speed-up routine has to be considered with care if structures with low-intense diffraction spots are supposed to be analyzed, e.g., structures with azimuthal disorder, or weak features in the wings of the diffraction spots.

Although the speed-up routine was only used for two-dimensional SPA-LEED scans in the context of the present thesis, it can further be applied for measurements of two-dimensional or three-dimensional reciprocal space maps (data-cubes), which is otherwise not possible due to time restrictions. Thus, the routine may offer a way to use a SPA-LEED instrument for recording intensity versus energy curves of LEED spots in an indirect manner. Such curves (LEED-IV-curves) are of interest because they give access to quantitative structural data of the surface [50].

6. The structure formation of HB238-A on the Ag(100) surface

This chapter is based on the experimental investigations, published in the Journal Nanoscale 15, 10319 (2023): "Chiral self-organized single 2D-layers of tetramers from a functional donor-acceptor molecule by the surface template effect" by Anna J. Kny, Max Reimer, Noah Al-Shamery, Ritu Tomar, Thomas Bredow, Selina Olthof, Dirk Hertel, Klaus Meerholz, and Moritz Sokolowski.

A reprint of this publication can be found in Appendix A.2. The author's contribution to the publication of this paper included: the data acquisition and discussion, the scientific presentation of the data, and the writing of the manuscript, including the revision.

This chapter summarizes the most important results from the above-mentioned publication. Hereby, the structural properties of ordered HB238-A phases on the Ag(100) surface are discussed. The publication reports two ordered HB238-A phases, a thermodynamically metastable, low-temperature phase, called β-phase, and the α-phase that is stable at RT for about one day. The focus of this chapter is on the highly ordered α-phase, which is commensurate with the underlying Ag(100) surface.

The following sections describe the molecular arrangement in the α-phase as it was proposed from STM and SPA-LEED measurements. Furthermore, the interfacial interactions of the HB238-A molecules with the Ag(100) were investigated by XPS and UPS measurements. For further structural information regarding the adsorption heights and the adsorption sites of the HB238-A molecules in the α-phase, the reader is referred to Chapters 8 and 9.

Please note that the name of the investigated merocyanine is HB238 in the above-named publication. The suffix "A" has been added in this thesis with regard to the investigated derivatives of this merocyanine (ref. section 2.4).

6.1. Scientific context

This chapter presents the first structural investigation of HB238-A monolayers. Although HB238-A was already investigated in solution [1, 2], bulk crystals [2, 29] and spin-coated films [1, 2], structural information about monolayers, i.e., the wetting layers on substrate surfaces, was missing. Only recently, another paper on HB238-A monolayers was published [44]. This paper reports an edge-on arrangement of HB238-A molecules in the monolayer of a highly oriented pyrolytic graphite (HOPG) surface. The publication

derives this result from measurements of AFM height profiles combined with photoluminescence spectra.

As already explained in Chapter 2, monolayer structures often differ from the molecular arrangements in thick films or organic crystals, due to the interfacial interactions. While the interfacial interactions get lost for molecules in higher layers regarding the surface, the intermolecular interactions between the layers of different structures, e.g., between the second and the monolayer, still play a role. Hence, the monolayer structure has a significant impact on the further structural growth of the vacuum-deposited film. Knowledge and control about the structural growth of the molecules in the monolayer can thus be used to control the polymorphism of optoelectronically active layers, and thus to improve the device efficiencies.

Due to the complex molecular structure of the merocyanine HB238-A, i.e., the low symmetry of the molecule and non-planar, non-rigid alkyl side groups, the formation of ordered monolayer phases was not predictable. Hence, the investigations of HB238-A monolayers in this thesis were performed on the Ag(100) surface. The advantage of the Ag(100) surface is based on its unreconstructed surface structure and its low reactivity [104]. In addition, the four-fold symmetry of the Ag(100) surface limits the number of symmetry-equivalent domains, i.e., mirror and rotational domains, that might be formed by an adsorbate to a maximum of four.

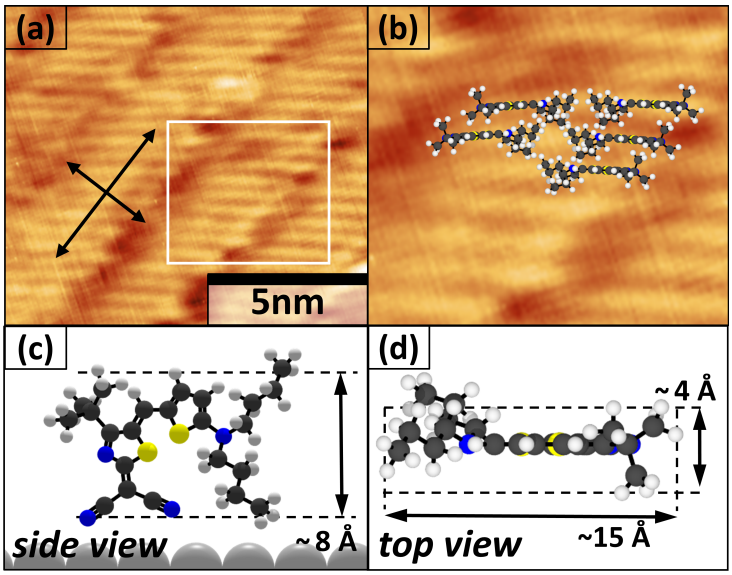

Figure 6.1.: STM image and hardsphere model of the β-phase. (a) STM image of the chain-like β-phase aggregates with indicated growth direction and width (long/short black arrows). The STM image of (b) shows a zoom-in of the image in (a) (white frame) that is superimposed by a hardsphere model of the edge-on oriented HB238-A molecules. For clarity, a side view and a top view of a single HB238-A molecule in edge-on orientation are given in (c) and (d). Color code: S yellow, N blue, C gray, H white. Van der Waals radii are reduced by a factor of 0.3. (40 K, $U_{\mathrm{bias}} = -0.29$ V, $I_{\mathrm{t}} = 5.4$ pA) The Figure was taken from the SI of the above-named publication [48].

6.2. Monolayer structures of HB238-A on the Ag(100) surface

HB238-A forms two different ordered monolayer phases on the Ag(100) surface. As already explained in Chapter 4, the HB238-A deposition was always performed for a sample temperature of 300 K. Subsequently, the HB238-A layers were investigated at different temperatures. This was initially done to increase the layer stability of the commensurate α-phase, as this phase was observed for the complete investigated temperature range of $25 - 350$ K. However, for a direct cooling of the samples to a temperature lower than 110 K, the metastable β-phase was observed in parallel to the commensurate α-phase. This section provides a brief overview of the structures of both phases.

6.2.1. The β-phase

The β-phase constitutes a kinetically stabilized phase. In the β-phase, the HB238-A molecules are in an edge-on orientation with respect to the Ag(100) surface. This adsorption geometry is displayed in Figure 6.1 (c) and (d) as a schematic side and top view. The adsorbed molecules form small aggregates with a coplanar π-stacking of the molecules. Hence, only the long molecular axis, as indicated in Figure 6.1 (d), is visible in the STM images of Figure 6.1 (a) and (b). In this *coin-roll*-like arrangement, the orientation of the molecules (long molecular axis) is inclined by 40° to 50° with respect to the growth direction of the aggregates.

Numerous of these small aggregates condense and form larger islands of irregular shape. Voids within the islands are avoided by lateral shifts between the molecules, leading to varying widths of the aggregates and changes in their growth direction. Due to the small sizes of the aggregates and the low structural order of the molecules, no diffraction spots of the β-phase are obtained in SPA-LEED measurements. For sample temperatures higher than 110 K, the β-phase transforms irreversibly into the thermodynamically more stable α-phase.

6.2.2. The commensurate α-phase

In the α-phase, the HB238-A molecules are arranged in a flat-lying, face-on adsorption geometry in which the π-system of the molecule is oriented parallel to the Ag(100) surface. As already mentioned above, the α-phase is directly observed after the deposition of HB238-A and was investigated in a temperature range between 25 K and 350 K. The domains of the α-phase are a few hundred nm in size and highly ordered. The space group of the α-phase is $P2$. Hence, the unit cells of the α-phase exhibit a twofold rotational symmetry. In combination with the fourfold symmetry of the Ag(100) surface, this leads to the existence of four symmetry equivalent domains, i.e., two rotational domains and two mirror domains, which can be observed in the respective SPA-LEED diffraction pattern. A SPA-LEED pattern of the α-phase measured for HB238-A is displayed in Figure 5.1 of Chapter 5. An additional SPA-LEED pattern of the α-phase can be found in Chapter 7. However, the SPA-LEED pattern of Figure 7.2 was measured for the merocyanine HB238-

B that forms the same phase, i.e., superstructure, on the Ag(100) surface as will be explained later.

The unit cell vectors of the α-phase can be expressed with respect to the unit cell vectors of the Ag(100) surface ($\mathbf{a}_1$ and $\mathbf{a}_2$) by a superstructure matrix according to

$$\begin{pmatrix} \mathbf{b}_1 \\ \mathbf{b}_2 \end{pmatrix} = \begin{pmatrix} 1 & -8 \\ 8 & 3 \end{pmatrix} \begin{pmatrix} \mathbf{a}_1 \\ \mathbf{a}_2 \end{pmatrix}. \tag{6.1}$$

The length of the Ag(100) lattice vectors can be derived from the Ag bulk lattice constant a_{Ag} by $a_1 = a_2 = 1/\sqrt{2} \cdot a_{\mathrm{Ag}}$. At 25°C, a_{Ag} is 4.0856±0.0020 Å [74–77] which results in a Ag(100) surface lattice constant of $a_1 = a_2 = 2.89$ Å. $\mathbf{b}_1$ and $\mathbf{b}_2$ are the lattice vectors of the merocyanine monolayer. For the α-phase of HB238-A, the lattice vectors result to $b_1 = 23.30$ Å and $b_2 = 24.69$ Å. The angle between the $\mathbf{b}_1$ and $\mathbf{b}_2$ results to $\gamma = 103.43°$.

Hence, the unit cell of the α-phase is large and contains 67 Ag atoms in the first Ag layer and four HB238-A molecules. The integer matrix elements of the superstructure matrix reveal the commensurate growth of the organic layer. For more detailed information regarding the commensurability of the layer, the reader is referred to the publication in Appendix A.2 and to the sections 3.2 and 4.2.3 of the present thesis.

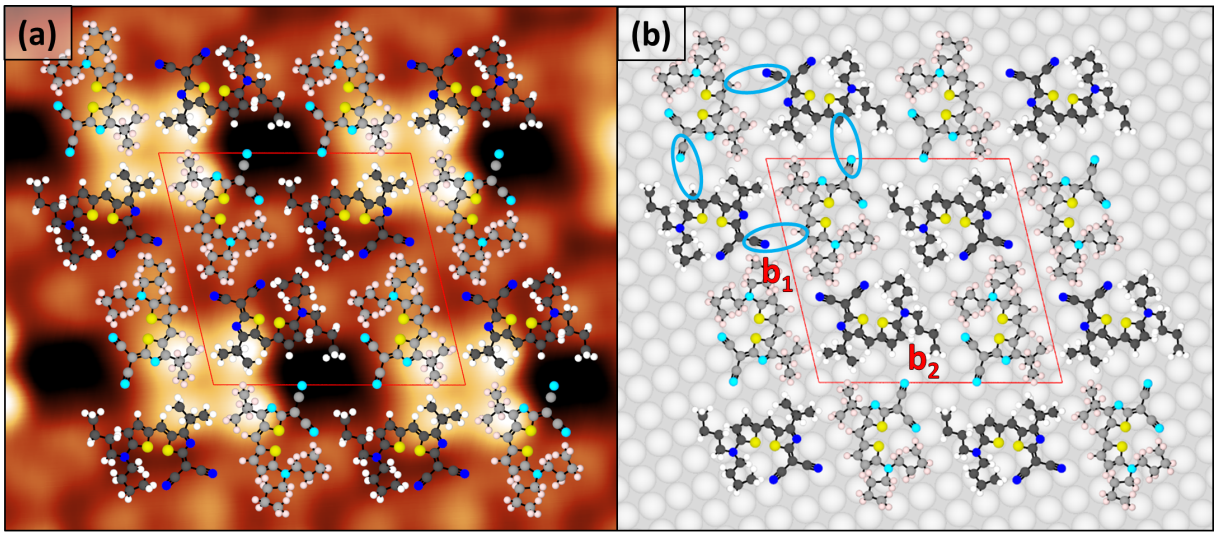

Figure 6.2.: STM image and hardsphere model of the commensurate α-phase of HB238-A on the Ag(100) surface. (a) STM image superimposed by a respective hardsphere model. (300 K, $U_{\mathrm{bias}} = -0.20$ V, $I_{\mathrm{t}} = 0.05$ nA) (b) Same hard-sphere model as displayed in (a) but on a hardsphere model of the Ag(100) surface. Please note that the lateral positions of the molecules on the Ag surface are (at this stage of information) arbitrary and do not indicate the correct adsorption sites. For further information about the adsorption sites, see Chapter 8. The color code is as in Figure 6.1 above. The unit cell is indicated in red. In (b), hydrogen bonds are indicated by lobes in light blue. The figure was taken and adapted from the above-named publication [48].

An STM image of the α-phase, superimposed by a hardsphere model, is displayed in Figure 6.2 (a). In the α-phase, the HB238-A molecules form enantiopure tetramers. These tetramers depict the primary building units of the α-phase. The existence of tetramers formed by four molecules of the same handedness was demonstrated by bias-dependent STM measurements. These revealed that the groups of four bright lobes, visible in the STM image of Figure 6.2 (a), correspond to four *t*Bu-groups of four neighboring molecules. This assignment was further supported by density functional theory (DFT) calculations that were performed for gas phase molecules and by STM measurements of monolayers for which the *t*Bu-group of the molecule was exchanged against an *i*Pr-group (HB238-E). The respective experimental data of the STM measurements can be found in Appendix C.

As HB238-A is a prochiral molecule, the existence of enantiopure tetramers is astonishing but can be explained by the intermolecular interactions. The tetramers are stabilized by hydrogen bonds between donor and acceptor groups of neighboring molecules. To be more precise, these hydrogen bonds are formed between the nitrile groups (CN groups) and hydrogen atoms located at the thiophene ring. In Figure 6.2 (b), these hydrogen bonds are exemplarily indicated by lobes in light blue. Within the same domain, only tetramers of the same handedness are found. Hence, the complete domain is formed enantiopure. Of course, tetramers and domains formed by the second enantiomer are found in the respective mirror domains.

Since the α-phase grows commensurate with the Ag(100) surface, each tetramer on the Ag(100) surface occupies the same adsorption sites. This is surprising as the $P2$ space group of the α-phase indicates that not all of the four merocyanine molecules of the tetramer occupy the same adsorption sites. These structurally different molecules are indicated by bright and dark colors in Figure 6.2. The reasons for the different adsorption sites of the merocyanines in the α-phase will be discussed later in Chapter 11 based on additional experimental data. Please note that the adsorption sites of the HB238-A molecules in the structural model of Figure 6.2 (b) are arbitrary, as the model does not consider later experimental data, yet. The commensurate growth of the α-phase indicates strong interfacial interactions of the HB238-A molecules with the Ag(100) surface that will be discussed in the following section.

6.3. Interfacial interactions in the α-phase

Strong interfacial interactions of the HB238-A molecules with the Ag(100) surface are also indicated by XPS and UPS spectra. This section describes the most important findings obtained from the spectra. For detailed information about the spectra, the reader is referred to the above-named publication that can be found in Appendix A.2. The spectra were measured for the α-phase of HB238-A with a coverage of less than one monolayer and for a thick film of several multilayers.

The respective UPS spectra show a nearly clean Fermi edge (no former lowest unoccupied molecular orbital (LUMO)). The highest occupied molecular orbital (HOMO) and the HOMO-1 of HB238-A show differential shifts for an increasing coverage which result in a larger binding energy difference between the two photoemission lines in the multilayer spectrum. For the two investigated coverages, this differential shift in binding energy

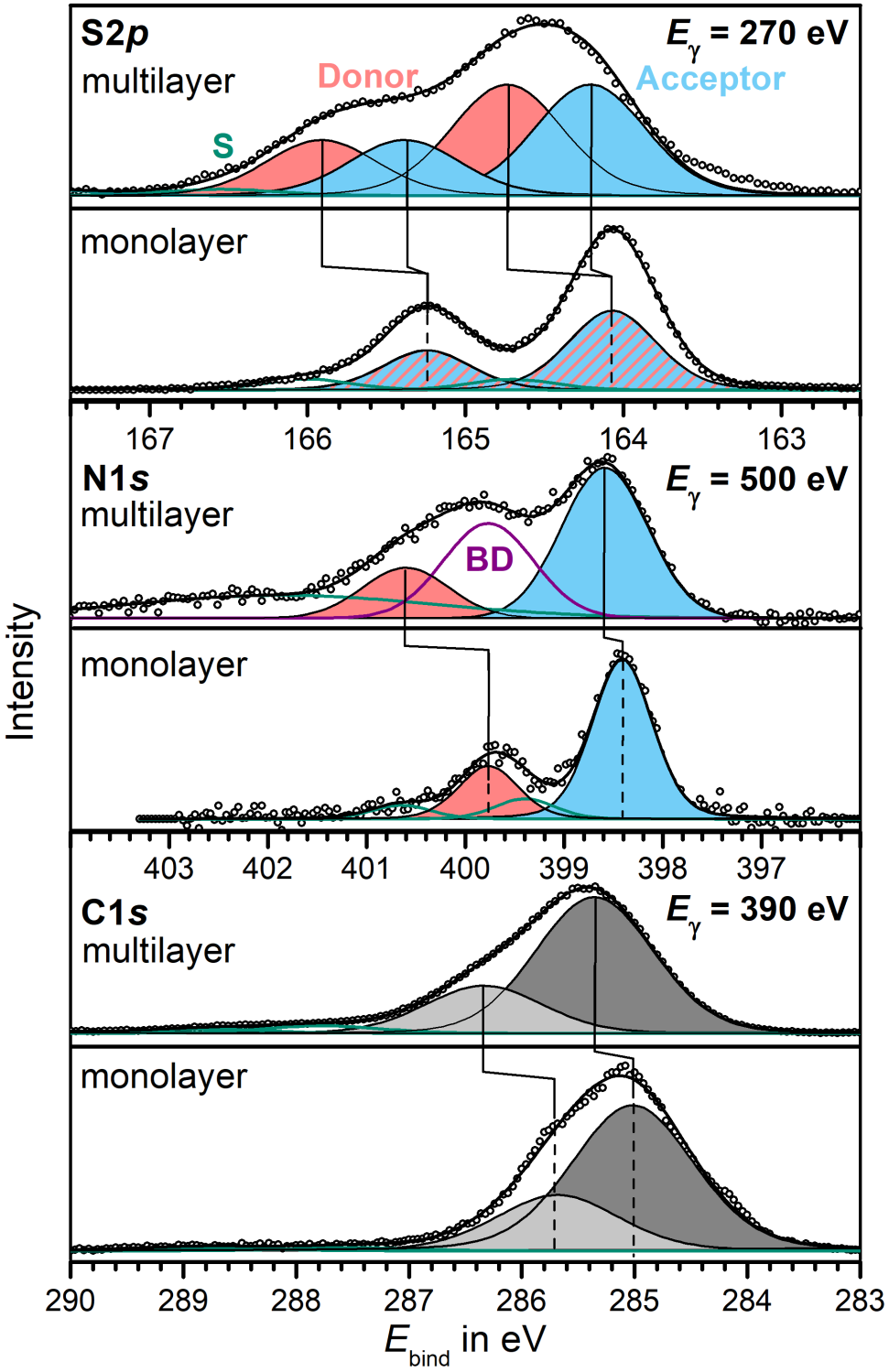

Figure 6.3.: XPS spectra measured for mono- and multilayers of the merocyanine HB238-A on the Ag(100) surface. The spectra show data of the S2*p*, the N1*s*, and the C1*s* photoemission lines. As indicated in the spectra, blue shaded lines correspond to the acceptor components, and red shaded lines correspond to the donor components. Differential shifts of the photoemission lines are indicated by vertical lines. Photon energies E_γ are denoted in the spectra. Taken from ref. [48]. For further details, see Appendix A.2.

amounts to 0.30 ± 0.05 eV. In addition, the HOMO of the monolayer is located at a higher binding energy (1.77 eV) compared to the multilayer (1.61 eV). Thus, the spectra indicate that both molecular orbitals, the HOMO and the HOMO-1, contribute to the binding of the HB238-A molecules to the Ag surface.

Differential shifts between the photoemission lines are also observed in the XPS spectra measured for the same HB238-A coverages as the UPS spectra. Photoemission lines were measured for all kinds of atoms of the HB238-A molecule, namely for the S2p, the N1s, and the C1s orbitals. The respective spectra are displayed in Figure 6.3.

The spectra measured for the multilayers show broader photoemission lines. This is expected, as the monolayer exhibits a smaller set of molecular adsorption geometries and molecular binding partners compared to the multilayer. In addition, the photoemission lines of the monolayer are shifted to lower binding energies. This shift is much larger for the donor components than for atoms located in or close to the electron acceptor of the HB238-A molecule. Although this is surprising at first glance, it indicates two things: a charge transfer between the Ag surface and the face-on adsorbed HB238-A molecules and a shielding of created photo holes by the electron density of the Ag surface.

These observations apply to all measured spectra. However, the largest changes in the spectra, concerning the binding energies of the donor and acceptor components, are observed for the S2p spectra. While the photoemission lines of the donor and the acceptor are located at different binding energies for HB238-A multilayers, they have the same binding energy for the monolayer.

In the molecular structure of HB238-A, the S atom of the electron donor is situated in the thiophene ring, and the S atom of the acceptor is in the thiazole ring. The fact that both components show the same binding energy in the S2p spectra strongly supports the proposed face-on adsorption geometry of the HB238-A molecules in the monolayer. In the face-on geometry, both S atoms are in close contact with the Ag(100) surface and hence in a similar chemical environment that allows for charge transfer between the S atoms and the Ag(100) surface. As both photoemission lines are located at exactly the same binding energy (with respect to the experimental accuracy of 0.05 eV) this further indicates a strong binding of the S atoms to the Ag surface.

6.4. Conclusion and outlook

The experimental investigations of this chapter revealed that HB238-A forms one thermodynamically dominant phase on the Ag(100) surface, the α-phase. The α-phase is commensurate with the underlying Ag(100) surface. Thus, the set of molecular adsorption sites is the same for every unit cell. Surprisingly, the unit cell of the α-phase is large and contains four HB238-A molecules of the same handedness in a face-on adsorption geometry. There are, however, different reasons that contradict the suggestion that all molecules in the unit cell occupy the same adsorption sites. These are, i.e., the fourfold symmetry of the Ag(100) surface in combination with the $P2$ symmetry of the α-phase unit cell, and the strong intermolecular interactions (hydrogen bonds). Therefore, the reasons for the commensurability of the α-phase are not yet identified.

The above-described XPS spectra, however, indicate a strong binding contribution of the S atoms. This allows for different ways to investigate the reasons behind the commensurate growth of the α-phase:

1. A variation of the alkyl-side groups of HB238-A. This changes the sterical demand of the molecules in the monolayer while the molecular backbone is not altered. As a result, molecules are forced to occupy different, or the next equivalent, adsorption sites. The respective changes in the molecular arrangement might allow for conclusions about the preferred molecular adsorption sites.
2. An investigation of the adsorption heights of the S atoms with respect to the Ag(100) surface by NIXSW measurements. This determines the binding distances of the S atoms to the Ag(100) surface, which is in direct correlation with the interfacial interactions.
3. The determination of the S adsorption sites on the Ag(100) surface by NIXSW.

The third point is, however, challenging, due to the four molecules (8 S atoms) per unit cell and the low symmetry of the structure. Still, all of these investigations were performed as part of this thesis and will be described in the following three chapters.

7. The influence of sterical demanding side groups on the molecular packing

In this chapter, the influence of the *n*Bu alkyl side groups of HB238-A on the molecular packing is determined. This is done by a length variation of the alkyl side groups. The resulting structural changes in the monolayer and their influence on the interfacial interactions are reported. They provide information about the preference of specific adsorption sites and the intermolecular interactions.

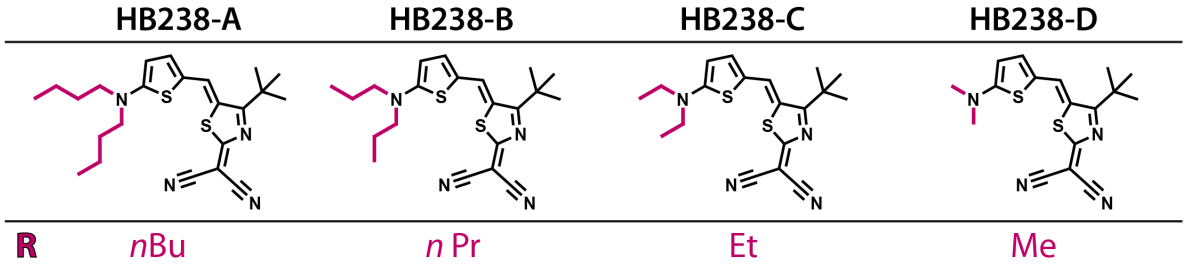

Figure 7.1.: Molecular structures of the investigated HB238-A derivatives. The altered alkyl side groups (R) are indicated in purple. The abbreviated names of the alkyl side groups are given below the structures. Names of the derivatives are displayed in bold letters above the molecular structures.

7.1. Scientific context

Intermolecular and interfacial interactions determine the molecular arrangement on a surface. As introduced in Chapter 6, the α-phase of the merocyanine HB238-A forms by an interplay of hydrogen bonds between the molecules and strong interactions with the underlying Ag(100) surface. Both interactions are balanced such that stable enantiopure tetramers are formed as primary building units of the α-phase. These tetramers assemble in commensurate domains on the Ag(100) surface.

Responsible for the commensurability of the α-phase are, therefore, the π-system and the functional groups of HB238-A. The sterically demanding and structurally flexible *n*Bu-groups only play a minor role, but act as spacers in the lateral structure formation. Changing the length of the alkyl side groups has only negligible effects on the electronic molecular structure and should, hence, not affect the principal binding motifs which are relevant for the formation of the α-phase. Thus, systematic variations of the alkyl side

groups probe the adsorption sites of the molecules on the surface, while the sterical demand and, hence, the packing of the molecules in the two-dimensional monolayer are altered. Similar investigations on the molecular packing have been reported for crystal-like structures of thick spin-coated merocyanine films [2].

In this context, three derivatives of varying alkyl side group lengths have been investigated by SPA-LEED, STM, and XPS. Their molecular structures are displayed in Figure 7.1. Purple color marks the altered alkyl side groups (R) which range from *n*Bu for HB238-A to Me-groups for HB238-D. Further information about the derivatives is provided in Chapter 2.4.

7.2. Commensurate phases

All monolayers were prepared under the same preparative conditions (see Chapter 4) as the α-phase of HB238-A introduced in Chapter 6. This ensured the comparability of the structures under kinetic aspects. Similar to HB238-A, the merocyanines HB238-B, HB238-C, and HB238-D form large ordered domains that were observable by STM measurements and sharp diffraction spots in the SPA-LEED patterns as visible in Figure 7.2. As anticipated above, the SPA-LEED data measured for monolayers of the three HB238-A derivatives reveal the growth phases that are also commensurate but partly structurally different from the α-phase of HB238-A.

The SPA-LEED patterns of HB238-B, HB238-C, and HB238-D are displayed in Figure 7.2. Simulations of the diffraction patterns result in information about the merocyanine unit cell, i.e., orientation and size, with respect to the unit cell of the Ag(100) surface. In Figure 7.2 the simulated patterns are displayed as a superposition with the experimental data on the right side of the SPA-LEED patterns. The reciprocal unit cell vectors of the Ag(100) surface and the merocyanine monolayer are displayed as yellow and red arrows, respectively. The superstructure matrices and the lattice parameters for the three merocyanine phases are summarized in Table 7.1. Please note, that the lattice parameters in Table 7.1 are calculated for a temperature of 300 K.

Again, the commensurability of a structure is indicated by integer elements of the superstructure matrix. Interestingly, HB238-B is found to form the identical phase as it was observed for HB238-A, namely, the α-phase. Thus, small changes of the alkyl side groups, i.e., by subtracting one CH_2 group, do not necessarily alter the molecular packing and hence the molecular adsorption sites. However, further decreasing the length of the alkyl side groups, i.e., for HB238-C and HB238-D, induces the formation of phases with smaller unit cells and, thus, a more condensed molecular packing. The surface area per molecule in units of Ag atoms is given in the last row of Table 7.1.

In contrast to HB238-A and HB238-B, the derivatives with shorter alkyl side groups, namely HB238-C (R=Et) and HB238-D (R=Me), form a phase with a quadratic unit cell of $P4$ symmetry. This phase is named Q-phase in the following. While the Q-phase is the only phase observed for HB238-C, the derivative with the shortest alkyl side groups, HB238-D, forms an additional commensurate phase. Due to the $P2$ symmetry of this phase, it is referred to as the small α-phase in the following (in contrast to the

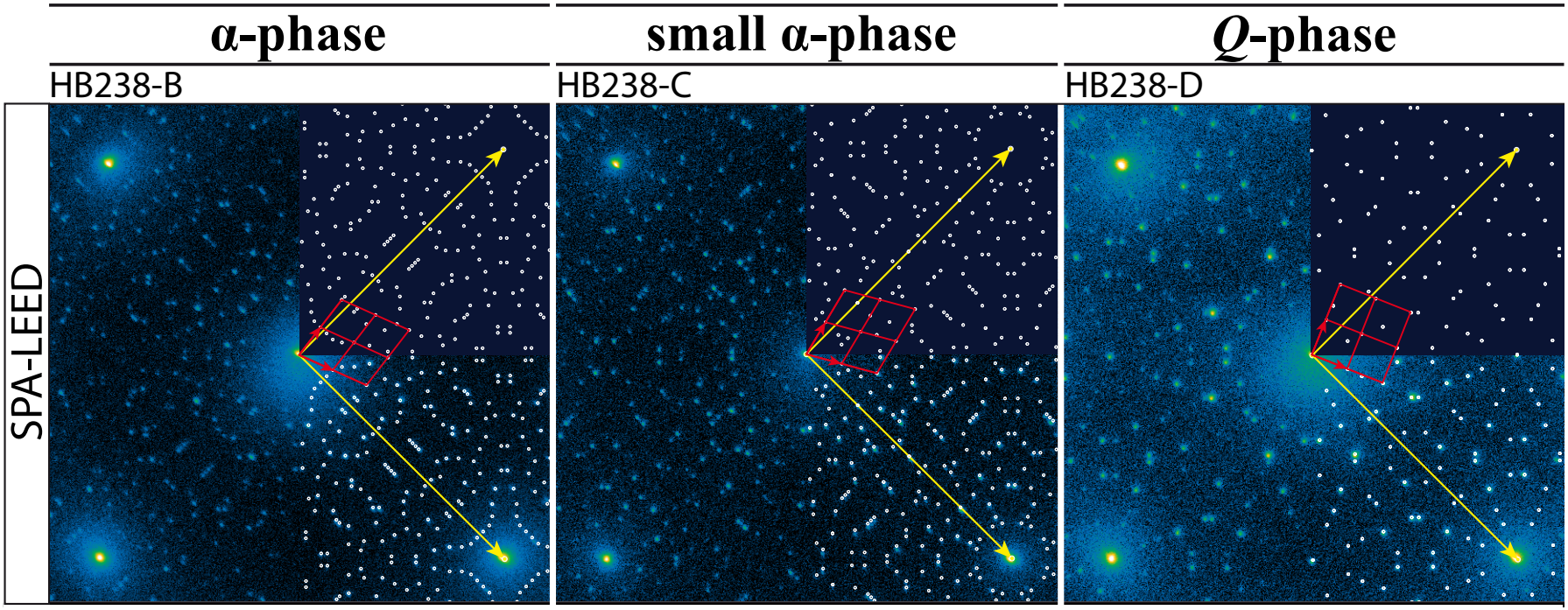

Figure 7.2.: SPA-LEED patterns measured for monolayers of the merocyanines HB238-B, HB238-C, and HB238-D on the Ag(100) surface. The HB238-A derivatives form three different structural phases as assigned. Measurements were performed with an electron energy of 81 eV for coverages of less than one monolayer and sample temperatures lower than 100 K. The right side of the SPA-LEED pattern is superimposed by a simulation of the diffraction spots (white dots). Here, the upper right quarter of the pattern shows only the simulation without the diffraction pattern in the background. This provides a better contrast and allows for a better comparison of the measured and simulated patterns. Reciprocal lattice vectors of the Ag(100) surface are indicated in yellow. They correspond to a length of 2.17 $Å^{-1}$. Four reciprocal unit cells of one merocyanine domain are indicated in red. The real space unit cell parameters are listed in Table 7.1.

Table 7.1.: Superstructure matrices and unit cell parameters of the monolayer phases formed by the merocyanines (MCs) HB238-A, HB238-B, HB238-C, and HB238-D on the Ag(100) surface. The phases are ordered by the size of the unit cells. Due to the commensurability of the phases, the error bars of the lattice parameters result from the uncertainty of the Ag crystal lattice constant $a_{\mathrm{Ag}} = 4.0856 \pm 0.0020$ Å [74–77]. Accordingly, the error bars are smaller than the numbers given in the table and apply to the third decimal place. $Z_{\mathrm{Ag}} : Z_{\mathrm{MC}}$ resembles the surface area per molecule given in units of Ag atoms. Z_{Ag} is the number of Ag atoms per unit cell, Z_{MC} the number of merocyanine molecules per unit cell.

	α-phase	**small α-phase**	**Q-phase**
MC	**HB238-A** **HB238-B**	**HB238-D**	**HB238-C** **HB238-D**
	$\begin{pmatrix} 1 & -8 \\ 8 & 3 \end{pmatrix}$	$\begin{pmatrix} 2 & -8 \\ 7 & 4 \end{pmatrix}$	$\begin{pmatrix} 3 & -7 \\ 7 & 3 \end{pmatrix}$
b_1	23.30 Å	23.82 Å	22.00 Å
b_2	24.69 Å	23.29 Å	22.00 Å
γ	103.43°	105.71°	90.00°
$Z_{\mathrm{Ag}} : Z_{\mathrm{MC}}$	$67 : 4 = 16.75$	$64 : 4 = 16$	$58 : 4 = 14.5$

α-phase). Monolayers of the small α-phase are prepared by deposition rates higher than 0.03 ML/min (Q-phase: $\leq$ 0.02 ML/min). The unit cell of the small α-phase is larger than the unit cell of the Q-phase and contains 64 Ag atoms (instead of 58 Ag atoms in the Q-phase). These aspects indicate that the Q-phase of HB238-D is thermodynamically more stable than the small α-phase. A fact that was confirmed by temperature-dependent SPA-LEED measurements that revealed a slow transformation of the small α-phase to the Q-phase with time.

7.3. Intermolecular interactions

The molecular arrangement of the three structural phases was derived from STM images. The data were measured for monolayers of HB238-A [48] and HB238-D at a sample temperature of 300 K and are displayed in Figure 7.3. The unit cells, obtained from SPA-LEED measurements, are indicated by blue arrows. For HB238-B and HB238-C, no STM data have been measured yet. However, due to the identical unit cells known from SPA-LEED, it can be assumed that their molecular arrangement is similar to that of HB238-A and HB238-D, respectively. As the molecular arrangement of HB238-A was already described in Chapter 6, this section focuses on the molecular arrangement in the small α-phase and the Q-phase.

Visible in the STM images of the small α-phase and the Q-phase are again characteristic groups of four bright lobes at the corners of the unit cells. For clarity, one of these groups is marked by a dotted blue square for each STM image. They indicate the positions of

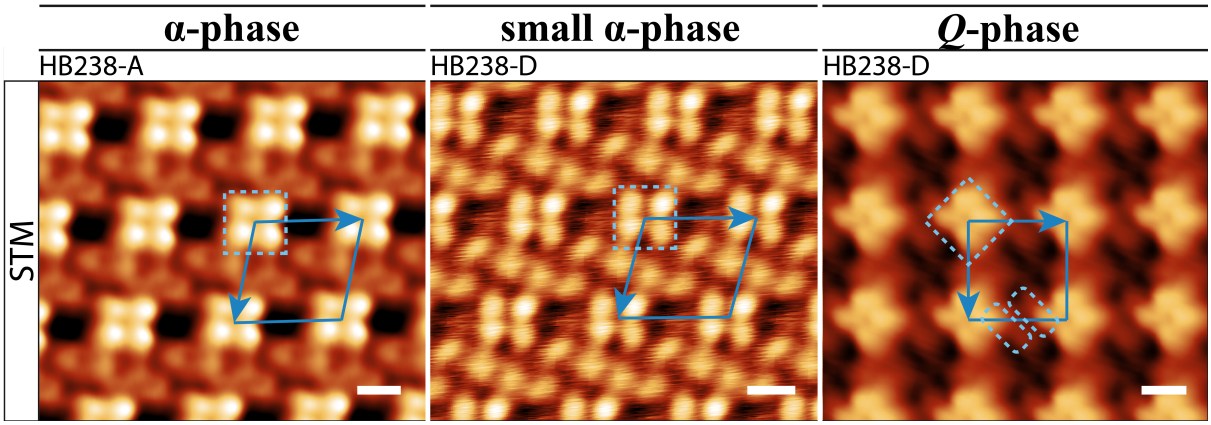

Figure 7.3.: STM images of the α-, small α-, and Q-phase measured for monolayers of HB238-A and HB238-D on the Ag(100) surface. The STM image of the α-phase was taken from ref. [48] (300 K, $U_{\text{bias}} = -0.3$ V, $I_{\text{t}} = 5$ pA) and was measured for HB238-A. The data of the small α-phase (300 K, $U_{\text{bias}} = -0.1$ V, $I_{\text{t}} = 20$ pA) and the Q-phase (300 K, $U_{\text{bias}} = -0.86$ V, $I_{\text{t}} = 8$ pA) were measured for the merocyanine HB238-D. The unit cell vectors are indicated by blue arrows. The unit cell parameters are listed in Table 7.1. The white scale bar equals a distance of 10 Å. Bias voltages were applied to the sample. For further details, see text.

four *t*Bu-groups and, hence, the presence of tetramers as explained in the last chapter (for experimental evidence, please refer to Appendix C). This is an important observation, as it demonstrates that the molecules form the same primary building units for all phases, independent of the alkyl side chain lengths. Hence, the hydrogen bonds between the nitrile groups and the thiophene ring of the neighboring molecules (see Chapter 6) are not altered significantly for the different unit cells.

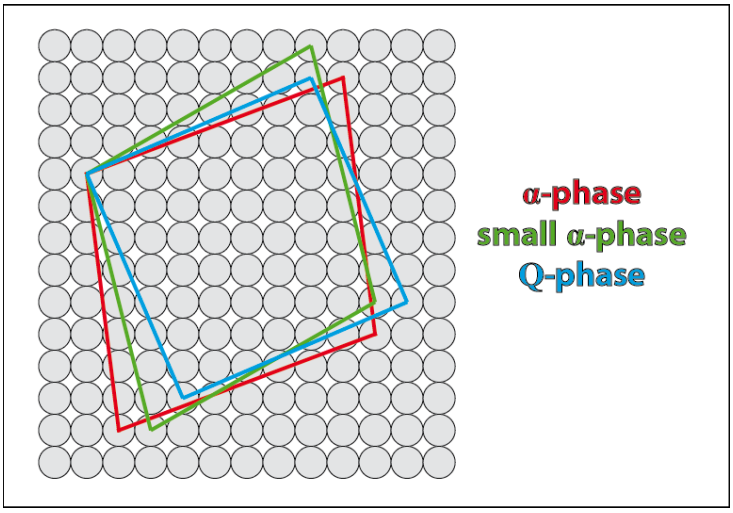

Figure 7.5.: Sketch of the unit cell orientations of the α-phase, the Q-phase, and the small α-phase with respect to the underlying Ag(100) surface. The sketch displays only one out of four symmetry equivalent domains, present on the Ag(100) surface. By comparing the positions of the unit cell corners, the sketch demonstrates the different symmetries of the lattice points with respect to the Ag(100) surface that are observed for the commensurate phases. Color code as indicated.

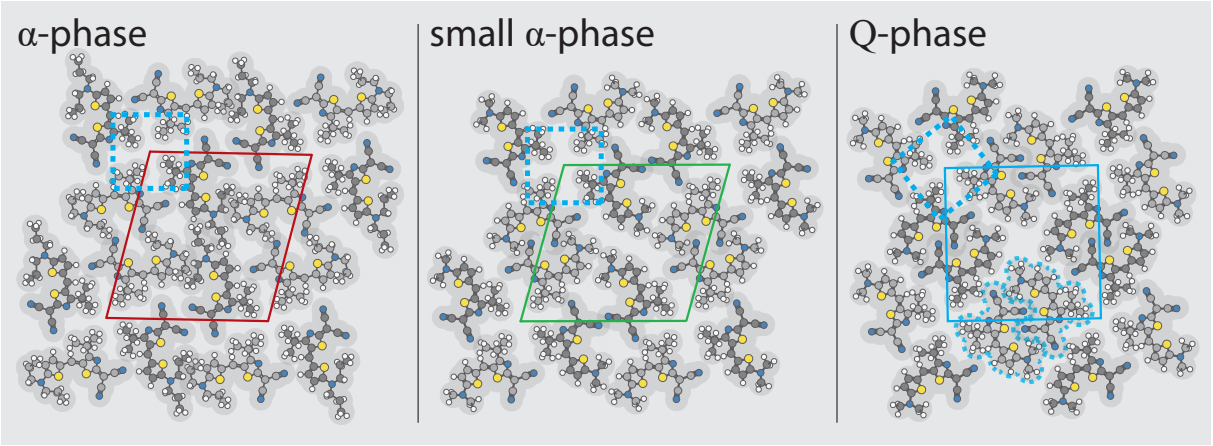

Figure 7.4.: Hardsphere models of the commensurate merocyanine phases, i.e., the α-phase, the small α-phase, and the Q-phase. The arrangement of the molecules with respect to each other and with respect to the lattice vectors is an anticipation from Chapter 9. Blue dotted squares mark the positions of the four *t*Bu groups for one tetramer, similar to Figure 7.3. Again, similar to Figure 7.3, one pair of dimer-forming molecules is indicated for the Q-phase by a blue dotted frame along the lower lattice vector. For further details, see text.

Comparing the STM images of the small α-phase of HB238-D with the data of the α-phase of HB238-A reveals a similar tetramer packing in the unit cell. This can be derived from the orientation of the groups of four bright lobes (indicated by blue dotted squares) with respect to the unit cell vectors. These blue dotted squares are also indicated in the respective structural models that are shown in Figure 7.4. Different from that, the tetramers appear to be rotated by about 45° in the Q-phase. This rotation might be driven not just by the smaller unit cell and thus by a decreased amount of uncovered Ag surface in the unit cell compared to the small α-phase, but in addition, a pairing of molecules between the tetramers might play a role, too. This pairing is observed along the unit cell vectors of the Q-phase. Here, two molecules come close together, as indicated by blue dotted frames in Figures 7.3 and 7.4, for the lower part of the unit cell. Due to the orientation of the enantiopure tetramers, this contact results in an anti-parallel orientation of the two molecules, favorable for an additional, strong hydrogen bond formation.

To summarize the most important aspects, the length of the alkyl side groups determines the packing of the tetrameric primary building units that are the same for all three phases. However, the enforced shift of the tetramers to new relative positions on the sample surface does not lead to a loss of the commensurability of the structure to the Ag(100) surface. Hence, the lateral shifts of the tetramers with respect to each other follow a grid of equal adsorption sites on the surface. This is also supported by the observation that no structural changes occur for small changes of the alkyl side group lengths, i.e., between HB238-A and HB238-B, which both form the α-phase. Interestingly, the changes in the unit cells are small concerning the substrate orientation. This can be derived from Figure 7.5 in which the unit cells of the three phases are indicated exemplarily for one domain. It demonstrates that only small changes in the positions of the unit cell corners are observed. For the α-phase and the small α-phase, this change implies a shift of the tetramers against each other by one Ag surface unit cell vector (2.89 Å).

For the Q-phase the rotation of the tetramers with respect to the unit cell vectors is observed additionally. However, in Chapter 11 we will show that this apparent rotation of the tetramers is only due to the different angle of the superstructure lattice vectors with respect to the substrate. In fact, it will be demonstrated in the following chapters that the position of the tetramers on the surface is similar for all phases.

7.4. Interfacial Interactions

To investigate the impact of the different tetramer packing on the interfacial interactions, XPS spectra were measured for all merocyanines and phases. Multilayer effects in the spectra were excluded by merocyanine coverages of less than one monolayer. The correct phases were ensured by LEED measurements. Information about the measurements and the data processing, including the fitting of the data, is given in Chapter 4.5.

The XPS spectra are displayed in Figure 7.6. The data of HB238-A are the same as the monolayer data presented in Chapter 6 and the corresponding publication [48]. The data of HB238-A and HB238-B represent the α-phase. The data of HB238-C was measured for the Q-phase, while HB238-D was measured for the small α-phase. Thus, the spectra represent all merocyanines and the three observed commensurate phases.

Comparable to Figure 6.3 of Chapter 6, photoemission lines were measured for the C1s, N1s, and S2p orbitals, to provide information on the interfacial interactions of all involved atoms of the merocyanines. The error of the determined binding energies is ± 0.05 eV and includes the calibration of the binding energy scale and the fit accuracy of the photoemission lines. Details about the fitting procedure can be found in Chapter 4.5.

Table 7.2.: Binding energies of the C1s components 1, 2, and 3, as indicated in the C1s spectrum of HB238-D. $E_{\text{bind}}^{\text{add. C atoms}}$ denotes the component shaded in dark red that represents additional C atoms. The spectra series was measured for the merocyanines (MCs) HB238-A to D for a photon energy of $E_\gamma = 390$ eV. The data of HB238-D refers to the small α-phase. The binding energies have an uncertainty of 0.05 eV due to the fit and the calibration of the binding energy scale.

C1s	HB238-A	HB238-B	HB238-C	HB238-D
C atoms per MC	23	21	19	17
$E_{\text{bind}}^{\text{comp. 1}}$	284.17 eV	284.26 eV	284.30 eV	284.30 eV
$E_{\text{bind}}^{\text{comp. 2}}$	284.85 eV	284.83 eV	284.91 eV	284.90 eV
$E_{\text{bind}}^{\text{comp. 3}}$	285.77 eV	285.82 eV	285.88 eV	285.82 eV
$E_{\text{bind}}^{\text{add. C atoms}}$	285.18 eV	285.23 eV	285.39 eV	$--$

Table 7.2 summarizes the binding energies of the C1s components, which can be distinguished in the spectra. In general, the C1s components are indicated in gray color as they cannot be assigned to individual, chemically different C atoms in the molecules. Correspondingly, they are labeled as components 1, 2, and 3 as indicated for the spectrum

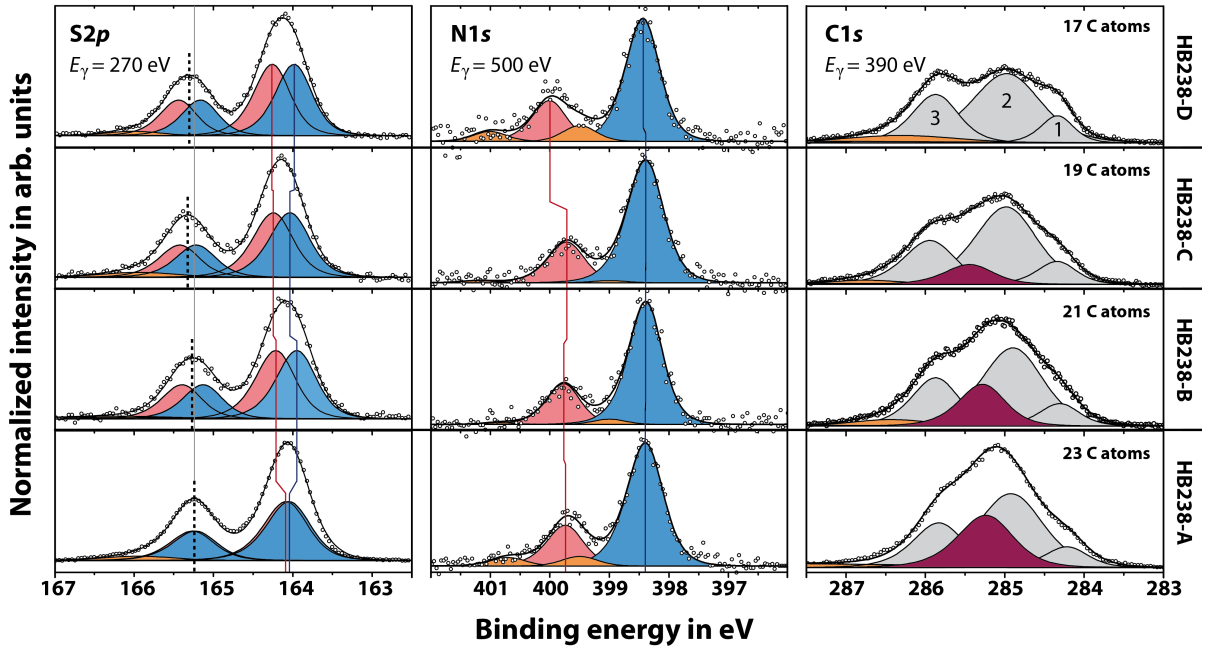

Figure 7.6.: XPS spectra of the merocyanines in dependence on the alkyl side group variation, measured for the merocyanines HB238-A to HB238-D (bottom to top). The data of HB238-D refers to the small α-phase. The S2p, N1s, and C1s photoemission lines were measured at RT for samples with merocyanine coverages of less than one monolayer. Photoemission lines of the same orbital are plotted in one column. In addition, fitted components are displayed. Their superposition, and hence, the spectrum fitted to the experimental data, is displayed by a black line.
The photon energies (E_γ) are indicated for the respective spectra series. Signal intensities for S2p and N1s photoemission lines are normalized to 1. Because of the different stoichiometry of the merocyanines, the C1s line intensities were normalized to the area of the HB238-A signal corresponding to 23 C atoms. The color code in the spectra is as follows: Red and blue shaded components correspond to the emission from atoms associated with the electron donor and the electron acceptor of the merocyanines, respectively. Orange-shaded components represent shake-up signals and signals due to beam damage. Components of the C1s lines, labeled with the numbers 1, 2, and 3, cannot be assigned to specific C atoms but represent groups of C atoms. The dark red shaded component in the C1s spectra of HB238-A, HB238-B, and HB238-C depicts the difference from the HB238-D spectra due to the increased number of C atoms in the alkyl side groups. Red and blue vertical lines indicate the binding energy differences of the donor and acceptor associated lines. For the S2$p_{1/2}$ lines, the overall shift in binding energy, i.e., the position of the maximum, is indicated by the black dotted line with respect to the position of the line maximum of HB238-A.

of HB238-D. Initially, the three components were fitted for HB238-D with respect to the shoulders visible in the peak shape of the overall C1s signal. They are located at binding energies of 284.30 eV, 284.90 eV, and 285.82 eV. As the other three merocyanines differ in the length of the alkyl side chains, their C1s signals were basically fitted with the same three components in a fixed area ratio.

The difference in the C1s spectra, due to the additional C atoms of the alkyl side chains, is given by an extra line that is shaded in dark red color. This component shifts slightly to lower binding energies for an increasing length of the alkyl side groups. This shift equals 0.21 ± 0.10 eV and can be explained by the effect that longer alkyl chains are less affected by the bond polarization of the adjacent tertiary amine and the corresponding loss of electron density.

On the other hand, the influence of the alkyl chains on the tertiary amine is also visible in the N1s spectra as will be discussed below. In general, the N1s spectra are described by two components. As the molecular backbone is not altered within the series of investigated merocyanines, the total number of N atoms is four for all four molecules. One N atom is located in the electron-donating part of the molecule (tertiary amine), and three N atoms are located in the electron-accepting part (thiazole ring and nitrile groups). Hence, we expect identical line integrals and similar line shapes for all N1s spectra of the series. In the XPS spectra of Figure 7.6, we can clearly distinguish between the tertiary amine of the donor and the other three N atoms of the electron-accepting group. This is expected, as the increased electron density in the electron-accepting group shifts the components to lower binding energies. The reverse is true for the N component in the electron-donating group. According to the number of N atoms in the electron-donating and -accepting groups, the resulting two photoemission lines are observed in an area ratio of 1:3 within a few percent. In Figure 7.6, the components are shaded in red and blue, respectively. The three N atoms of the electron-accepting group cannot be distinguished in their binding energies. The binding energies of all components are listed in Table 7.3.

Table 7.3.: Binding energies of the N1s components, measured for the merocyanines (MCs) HB238-A to D for a photon energy of $E_\gamma = 500$ eV. The data of HB238-D refers to the small α-phase. All investigated MCs include four N atoms in total. One N atom is located in the electron-donating, and three N atoms are located in the electron-accepting part of the molecule as indicated in Fig. 7.1. The binding energies have an uncertainty of 0.05 eV due to the fit and the calibration of the binding energy scale.

N1s	HB238-A	HB238-B	HB238-C	HB238-D
N atoms per MC	4	4	4	4
$E_{\text{bind}}^{\text{donor}}$	399.69 eV	399.72 eV	399.66 eV	399.95 eV
$E_{\text{bind}}^{\text{acceptor}}$	398.34 eV	398.34 eV	398.34 eV	398.39 eV

Electronically, the acceptor component is not altered by the variation of the alkyl side groups. Accordingly, the shifts observed in the binding energies of the acceptor exhibit a maximum value of 0.05 eV and are thus within the error range of the measurement ($\pm$0.10 eV). The same holds for the donor components of HB238-A, HB238-B, and HB238-C. Only the donor component of HB238-D is shifted to higher binding energies by, e.g., +0.29 eV in comparison to HB238-C. This can be explained by the inductive donating effect of the alkyl side groups. The first and second C atom of the alkyl side chains donate electron density to the tertiary amine. The respective component shifts to lower binding energies as the electron density increases with the length of the alkyl side groups. This explains the difference in the binding energies between HB238-D and HB238-C. However, the spectra show that the third and all subsequent C atoms in the alkyl groups (nPr for HB238-B and nBu for HB238-A) have no significant influence on the inductive electron-donating effect. Hence, for these spectra, the same binding energies are observed.

In the S2p spectra, we also observe two photoemission lines. However, the situation for these spectra is different, as the S2p orbital is subject to spin-orbit splitting. This leads to two photoemission lines, i.e., one S2$p_{3/2}$ and one S2$p_{1/2}$ line, per S atom which exhibit an area ratio of 2:1. Both, the S2$p_{3/2}$ and the S2$p_{1/2}$ photoemission line have a fixed binding energy difference of 1.18 eV [60].

For the above-described series of merocyanines, all molecules exhibit two S atoms. One S atom is located in the thiophene ring of the electron-donating part of the molecule, and one S atom is located in the thiazole ring of the electron-accepting part (see Fig. 7.1). The binding energies for the overall S2$p_{3/2}$ signals and the binding energies of the fitted components of the S2$p_{3/2}$ signals are summarized in Table 7.4. In Figure 7.6, the lines of the donor and acceptor components are again indicated by a red and blue shading. As both the S2$p_{3/2}$ and the S2$p_{1/2}$ photoemission lines have a fixed binding energy difference, they undergo the same shifts in binding energy within the series of merocyanines. Since the two S atoms are hardly affected by the variation of the alkyl side group from an electronic point of view, the shifts in the binding energy of the total photoemission lines are small and negligible, with a maximum value of 0.08 eV. Surprisingly, we observe changes in the line shape of the S2p photoemission lines of HB238-B, HB238-C, and HB238-D in comparison to HB238-A. This change in the line shape might be an artifact, as the data of HB238-A was measured during a different beam time and hence probably under slightly different experimental conditions. This would have possibly required a slightly different line profile for the fitting. However, the FWHM of the overall S2p lines does not change significantly within the spectra series as visible in Table 7.4, indicating that the splitting of the S components described below is real.

For HB238-A, the fitted donor and acceptor associated lines for the S2p signals are located at almost the same binding energy. This is different from the other merocyanines of the spectra series. Due to the different line shapes of the overall signals, the fitted donor and acceptor components are located at different binding energies, such that a splitting between them is observed. Please note that all spectra of the present XPS series were fitted with the same line shape as described in Chapter 4.5. The binding energies of the fitted donor and acceptor components are listed in the lower part of Table 7.4. The largest binding energy difference is observed for HB238-D. It comprises 0.28 eV. The rather similar splitting between the donor and acceptor components in the S2p spectra is

Table 7.4.: Binding energies of the S2$p_{3/2}$ components, measured for the merocyanines (MCs) HB238-A to D for a photon energy of $E_\gamma = 270$ eV. All investigated merocyanines exhibit two S atoms. One S atom is located in the electron-donating, and one S atom is located in the electron-accepting part of the molecule as indicated in Fig. 7.1. The binding energies have an uncertainty of 0.05 eV due to the fit and the calibration of the binding energy scale. (1) This data corresponds to the overall signal of the S2$p_{3/2}$ photoemission line. The corresponding values were determined from a fit of the S2$p_{3/2}$ peak with a single line.

S2$p_{3/2}$	HB238-A	HB238-B	HB238-C	HB238-D
S atoms per MC	2	2	2	2
$E_{\text{bind (1)}}$	164.06 eV	164.09 eV	164.14 eV	164.12 eV
FWHM $_{(1)}$	0.64 eV	0.66 eV	0.64 eV	0.63 eV
$E_{\text{bind}}^{\text{donor}}$	164.03 eV	164.17 eV	164.20 eV	164.22 eV
$E_{\text{bind}}^{\text{acceptor}}$	164.00 eV	163.91 eV	163.99 eV	163.94 eV
$E_{\text{bind}}^{\text{donor}} - E_{\text{bind}}^{\text{acceptor}}$	0.03 eV	0.26 eV	0.21 eV	0.28 eV

an important observation as it indicates that the interfacial interactions of the molecules are similar but still slightly different in the three phases.

In conclusion, it can be said that the absence of large differences in the PES spectra confirms a similar face-on geometry of all molecules in the commensurate phases. While no obvious changes related to the molecules or their phases are observed for the N1s and C1s spectra, the subtle changes in the S2p spectra indicate that the S atoms are more strongly involved in the interfacial interactions of the molecules with the Ag(100) surface than the C and N atoms.

7.5. Conclusion

From the variation of the alkyl side groups, the following conclusions can be derived. All investigated HB238-A derivatives form the same merocyanine tetramers as primary building units of the commensurate structures. This observation was expected, as the functional groups and the electronic structure of the molecules are not significantly altered by the alkyl side group variation. The latter was demonstrated by the absence of binding energy shifts in the measured series of XPS spectra. Only the donor electron density of HB238-D is slightly altered due to the decreased inductive effect of the methyl groups compared to the longer alkyl side groups.

The length of the alkyl side groups mainly alters the sterical demand of each molecule and thus also the sterical demand of the tetramers. This leads to the observation of three different phases on the Ag(100) surface, the α-phase, the small α-phase, and the Q-phase. All of these phases exhibit different tetramer packings. Most importantly, the SPA-LEED measurements revealed the commensurate growth of all three phases. Hence, the lateral positioning of the tetramers is not arbitrary but follows a grid of equal adsorption sites

on the Ag(100) surface.

On the other hand, the XPS data indicate that the interfacial interactions and hence, most likely also the positioning of the S atoms, are slightly different for the different merocyanines, even if the same phases are formed on the Ag(100) surface as it is the case for HB238-A and HB238-B. This indicates that the intermolecular interactions between the tetramers also play an important role in the layer formation. While the lateral arrangement of the tetramers is constrained by the defined adsorption sites on the Ag surface, the intermolecular interactions between the tetramers change. This change is caused by the altered relative tetramer arrangement and by the different sterical demands of the molecules. The intermolecular interactions between the tetramers might result in small molecular distortions, hence leading to slightly different molecular adsorption sites of the individual merocyanines within the tetramers as observed in the XPS spectra. This could be revealed from NIXSW measurements. Hence, these will be the subject of the next chapter.

8. The adsorption height of HB238-A

This chapter fathoms the specific contributions of the C, N, and S atoms to the interfacial interactions of the HB238-A molecules in the α-phase. This is done by determining the adsorption heights of the respective atoms to the Ag(100) surface by NIXSW. These measurements also provide information about the height distributions of the C, N, and S atoms.

The following people contributed to the experimental work performed at the I09 endstation of the DLS: Anja Haags, Sergey Subach, David A. Duncan, Moritz Sokolowski.

8.1. Scientific context

The adsorption height is defined as the distance between an atom or a specific group within a molecule and the substrate surface. For planar molecules in face-on adsorption geometry, it is typically related to the interfacial binding strength of the adsorbate [104, 105]. From the formation of commensurate phases and from the above presented XPS and UPS data (see Chapters 6 and 7), strong interfacial interactions between the merocyanine molecules and the Ag(100) surface can be expected. This chapter investigates the role of the functional groups in the binding of the molecules to the surface. This was done by NIXSW measurements, which provide information about the adsorption heights and the vertical order of the C, N, and S atoms in the monolayer. The functional groups responsible for the commensurate growth of the merocyanines are expected to occupy the same adsorption sites for symmetry-equivalent molecules. Hence, the respective N and S atoms in these groups should exhibit a high lateral and vertical order with respect to the underlying Ag(100) surface. The determined adsorption heights of the C, N, and S atoms represent average values that take all four molecules per unit cell and all atoms of the same kind (C, N, and S atoms, respectively) into account. However, as will be shown below, further analysis of the spectra allowed us to distinguish between the adsorption heights of the atoms related to the donor and acceptor components of HB238-A.

As the molecular backbone and the functional groups are the same for all investigated merocyanines, the adsorption heights on the Ag(100) surface are expected to be similar for the HB238-A derivatives. Changes in the adsorption heights should hence only be dependent on the different lateral arrangements of the tetramers on the surface, i.e., the formation of the α-phase, the small α-phase, and the Q-phase. These are investigated by NIXSW measurements and photoemission from the S1s orbital, in the second part of this Chapter.

8.2. Detailed Parameters of the NIXSW analysis

This section provides information about the analysis of the NIXSW data of this and the following chapter. It focuses on the details of the NIXSW measurements performed for the S1s orbitals of the merocyanines, as these will be used later to determine the lateral positions of the molecules on the Ag surface. However, the same principles apply to the evaluation of the C1s and the N1s data. Please note that further experimental parameters are reported in Chapter 4.5.2.

To obtain reliable fits of the NIXSW spectra with negligible contributions of beam damage, multiple NIXSW scans with short measurement times and hence low signal-to-noise ratio were averaged. Each NIXSW scan was performed on a fresh sample spot. Typical measurement times per spectrum were in the range of 30 s. For the S1s spectra, the number of averaged spectra (N) are listed in Tables 8.1, 8.2, and 8.3. Beam damage was frequently observed as an appearance of an additional, low-intensity line at lower binding energies, separated by about -2 eV from the overall line maximum of the S1s signal. Hence, beam damage was distinguishable from the merocyanine S1s signal and did not affect the data evaluation.

Each NIXSW measurement comprises a series of 36 photoemission spectra that were measured for the same binding energy range but with different photon energies. In this thesis, these spectra series are often referred to as NIXSW spectra. Each series of spectra was measured from low to high photon energies to obtain the best accuracy of the x-ray monochromator. The spectra of the NIXSW series were divided into three groups. 6 spectra were measured in a 3 eV wide range at lower photon energies, 24 spectra were measured in a range of 3 eV around the Bragg energy, and finally, 6 spectra were measured in a 3 eV range in the out-of-Bragg region at higher photon energies. Please note that the presented yield curves shown below do not show the whole measured photon energy range, but only the region of $E_{\mathrm{Bragg}} \pm 2$ eV, for presentation purposes.

Table 8.1.: Details of the fitted photoemission lines of the S1s NIXSW spectra measured for the (200) Bragg reflection. N denotes the number of individual NIXSW data sets that were averaged to obtain the displayed data. (1) This FWHM corresponds to that of the experimental S1s photoemission line obtained from averaging the first 6 out-of-Bragg spectra of each measurement. (2) These values correspond to the fit parameters of the individual donor and acceptor lines. They were constrained to be constant for all spectra of the NIXSW measurement. For more information, please refer to the text.

S1s (200)	HB238-A	HB238-B	HB238-C	HB238-D
N	16	11	25	5
FWHM $_{(1)}$ in eV	1.11 ± 0.01	1.00 ± 0.07	1.11 ± 0.02	1.01 ± 0.11
FWHM $^{\mathrm{donor}}_{(2)}$	0.95 eV	0.87 eV	0.92 eV	0.78 eV
FWHM $^{\mathrm{acceptor}}_{(2)}$	0.95 eV	0.87 eV	0.92 eV	0.78 eV
$E^{\mathrm{donor}}_{\mathrm{bind}} - E^{\mathrm{acceptor}}_{\mathrm{bind}}$ $_{(2)}$	0.37 eV	0.37 eV	0.37 eV	0.52 eV

Table 8.2.: As above, but for the (111) reflection.

S1s (111)	HB238-B	HB238-C	HB238-D
N	13	15	12
FWHM $_{(1)}$	1.05 ± 0.02 eV	1.08 ± 0.01 eV	1.06 ± 0.05 eV
FWHM $^{\text{donor}}_{(2)}$	0.87 eV	0.88 eV	0.78 eV
FWHM $^{\text{acceptor}}_{(2)}$	0.87 eV	0.88 eV	0.78 eV
$E^{\text{donor}}_{\text{bind}} - E^{\text{acceptor}}_{\text{bind}}$ $_{(2)}$	0.37 eV	0.37 eV	0.52 eV

Table 8.3.: As above, but for the (220) reflection.

S1s (220)	HB238-B	HB238-D
N	13	9
FWHM $_{(1)}$	1.12 ± 0.06 eV	1.08 ± 0.05 eV
FWHM $^{\text{donor}}_{(2)}$	0.87 eV	0.78 eV
FWHM $^{\text{acceptor}}_{(2)}$	0.87 eV	0.78 eV
$E^{\text{donor}}_{\text{bind}} - E^{\text{acceptor}}_{\text{bind}}$ $_{(2)}$	0.37 eV	0.52 eV

Photoemission lines for the NIXSW analysis were evaluated by using the software CasaXPS [62]. After systematically testing different line shapes, photoemission lines were fitted using the in CasaXPS implemented TLA(3,6,8) line shape. This line shape consists of a Gaussian/Lorentzian product combined with a blend function such that it accounts for the slight asymmetry of the photoemission lines.

To obtain a reliable fit of the donor and acceptor lines, the following constraints were applied to the fit parameters of the NIXSW spectra: Donor and acceptor lines were fitted with an identical FWHM that was not allowed to change within a series of NIXSW spectra. In addition, the binding energies of the donor and acceptor components, and hence, also the difference between them, were fixed. Thus, only the line integrals were left as free fit parameters. (For examples of fitted spectra, see Figure 8.2 below.)

The determined binding energy differences in combination with the respective FWHM values are listed in Table 8.1 for the data measured at the (200) Bragg reflection. The respective values for the (111) and (220) Bragg reflections are summarized in Tables 8.2 and 8.3. The parameters that were constrained to be constant for the fit of the NIXSW spectra, i.e., the FWHM of the components and their binding energy, were determined by initial, iterative fits of the spectra in the out-of-Bragg regions. Please note that soft XPS spectra were not available because of the high S1s binding energy.

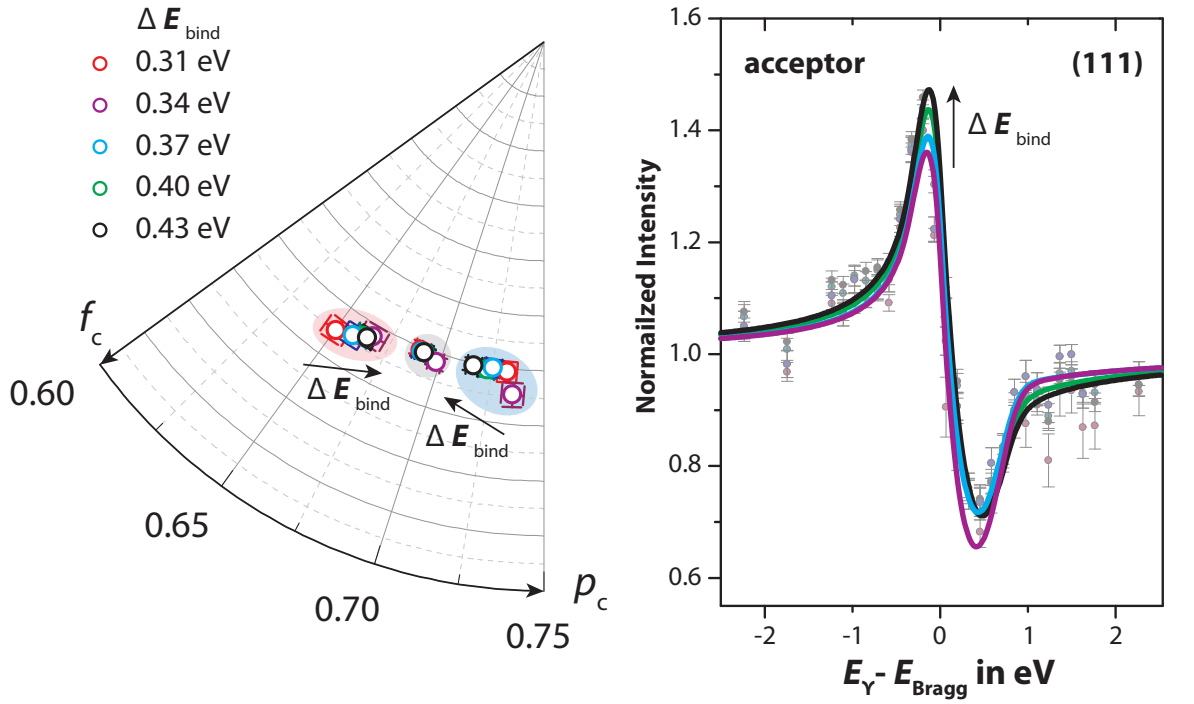

Figure 8.1.: Influence of the donor-acceptor binding energy splitting (ΔE_{bind}) on the NIXSW results. (a) Argand diagram displaying the resulting Argand vectors for different binding energy splittings. The data correspond to the data measured for HB238-C and the (111) Bragg reflection. As indicated by black arrows, the donor and acceptor components shift together for an increasing splitting. Red and blue shadings indicate Argand vectors that correspond to the donor and the acceptor, respectively. Argand vectors shaded in light gray correspond to the sum of the components. Please note that the Argand vectors overlap partly. Hence, not all data points are visible. (b) Photoemission yield curve of the acceptor component plotted for the different binding energy splittings. It demonstrates that mainly the increase of the photoemission intensity at lower photon energies (see arrow) is affected, which might lead to an underestimation of p_{c} for large ΔE_{bind} values.

During these iterations, the binding energy difference between the donor and acceptor components and their FWHM was systematically altered. The goal of this alteration was to obtain a stable fit of the donor and acceptor components in which the expected 1:1 area ratio for the out-of-Bragg spectra was fulfilled, although the line areas were left as free fit parameters. In combination with a good description of the experimental photoemission line shape, this criterion was fulfilled by a binding energy difference in a range of ± 0.06 eV from the here reported values.

Figure 8.1 illustrates the impact of different binding energy splittings (ΔE_{bind}) on the resulting acceptor photoemission yield curve and the corresponding Argand vectors of the donor and the acceptor components. This was done exemplarily for the data of HB238-C measured for the (111) Bragg reflection. As visible in Figure 8.1 (a), the Argand vectors shift together for an increasing value of ΔE_{bind}. Hence, the difference in p_{c} of the donor and acceptor components gets reduced.

For the data evaluation reported in this thesis, a splitting of $\Delta E_{\mathrm{bind}} = 0.38\ e\mathrm{V}$ was chosen. For this splitting, the smallest deviations of the Argand vectors from the vectors of the next, also acceptable values, are observed. Accordingly, the reported Argand vectors of the donor and acceptor components are subject to a p_{c} error of 0.01 and a f_{c} error of 0.04.

As the binding energy of the components is not influenced by the photon energy, the so determined values of ΔE_{bind} were constrained for the fit of the (200), (111), and (220) data. In addition to the donor and acceptor components, a broad, low-intensity satellite (gray line in Figure 8.2) was fitted to the higher binding energy edge of the overall S1s photoemission line. This improved the description of the background asymmetry of the spectrum and, hence, increased the fit stability of the donor and acceptor components.

Important for obtaining a good description of the photoemission lines by the donor and acceptor components was the correction of the binding energy scale for the error of the monochromator, as described in Section 4.5.4. An insufficient binding energy correction was indicated by an increasing or decreasing background in the donor and acceptor photoemission yield curves, which, in that case, deviated from the expected constant intensity with a value of one.

8.3. The adsorption height of HB238-A

To determine the adsorption height of HB238-A, NIXSW measurements were performed at the (200) Bragg reflection of the Ag single crystal. The (200) Bragg planes run parallel to the (100) crystal surface and describe all symmetry equivalent planes parallel to the surface obtained by translational symmetry operations. The (200) Bragg planes of the Ag crystal are located at a distance d_{200} perpendicular to the crystal surface, which equals $0.5 \cdot a_{\mathrm{Ag}} = 2.04$ Å [74–77]. The respective theoretical Bragg energy E^{200}_{Bragg} equals 3035.5 eV at $\Theta_{\mathrm{I}} = 90°$. Please note that the Bragg energies used in the performed measurements are slightly different. Deviations occur due to thermal expansion of the Ag crystal, inaccuracies of the monochromator, and deviations of Θ_{I} from 90°. Measurements were performed with photon energies E_γ from $E^{200}_{\mathrm{Bragg}} - 4.5\ e\mathrm{V}$ to $E^{200}_{\mathrm{Bragg}} + 4.5\ e\mathrm{V}$. The NIXSW analysis of HB238-A was based on the photoemission signals of the S1s, N1s, and C1s orbitals.

Exemplary photoemission spectra of the different orbitals are displayed in Figure 8.2. They show photoemission spectra that were measured at four different photon energies ($E_\gamma - E_{\mathrm{Bragg}}$), as labeled in the respective spectra. The spectra of the highest and lowest photon energies of each column correspond to an energy for which no reflectivity at the (200) plane is present and no standing wave-field effects apply. These are called *out-of-Bragg* energies in the following. Significant reflectivity is achieved for photon energies from about $E_{\mathrm{Bragg}} - 0.5\ e\mathrm{V}$ to $E_{\mathrm{Bragg}} + 0.75\ e\mathrm{V}$. Accordingly, these photon energies are called *in-Bragg* energies in the following. In Figure 8.2, the second and third spectrum of each column falls into this energy range. Exemplary reflectivity curves are displayed in the lower part of Figure 8.3, where the photon energies of the in-Bragg spectra displayed in Figure 8.2 are indicated by the vertical gray lines.

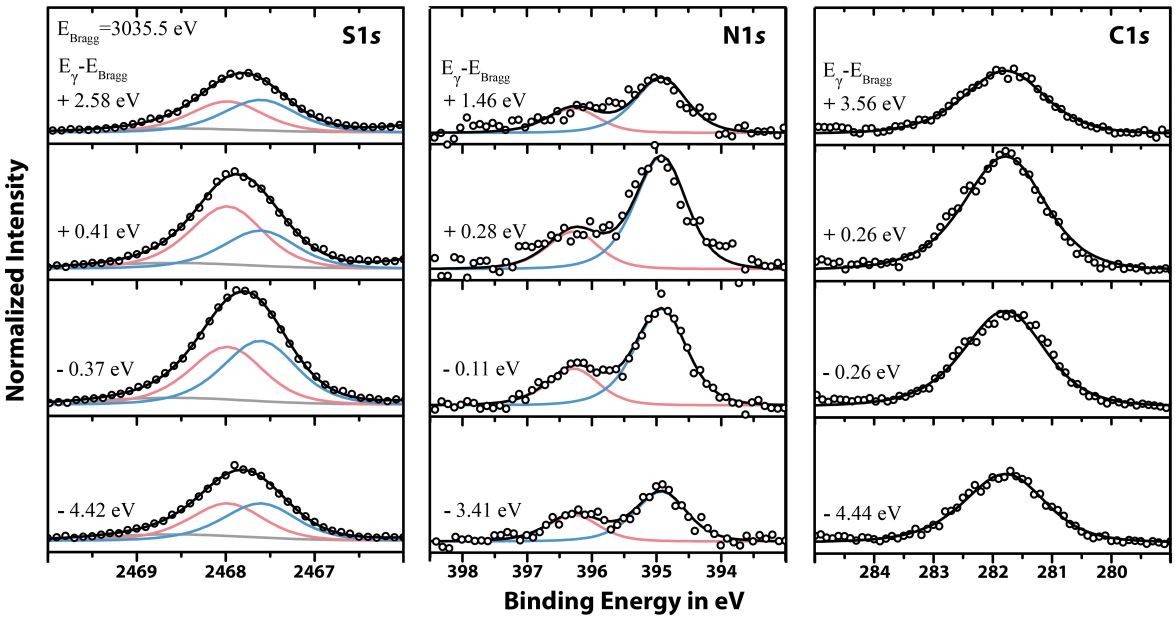

Figure 8.2.: Photoemission curves for the S1s, N1s, and C1s orbitals of HB238-A, measured during the NIXSW measurements at the Ag(200) Bragg plane. The photon energy E_γ of the x-ray beam is indicated for each spectrum with respect to the Bragg energy, E_{Bragg}, of 3035.5 eV. Experimental data points are fitted by different lines. Red lines refer to components in the donor part of the molecule, and blue lines to the acceptor part. Gray lines in the S1s spectra refer to shake-up signals. The C1s signal was fitted with one line, displayed in black.

For the out-of-Bragg spectra, the N1s and the C1s spectra are comparable to the measured soft XPS spectra of Chapters 6 and 7. However, the inaccuracies of the monochromator also impact the binding energies of the photoemission lines. Hence, the binding energies of the N1s and C1s lines differ from the measured soft XPS spectra by about 3 eV. However, this does not have a consequence for the analysis of the NIXSW data. Similar to the soft XPS spectra in Figure 7.6 of Chapter 7, the photoemission spectra were fitted by lines representing chemically different components of the molecule. Components corresponding to the electron-donating part of the molecule are represented by red lines, while blue lines correspond to photoemission from atoms that are associated with the electron-accepting part. For the C1s data, the chemically nonequivalent atoms in the molecule cannot be distinguished. Accordingly, the signal is described by a single line displayed in black. This black line describes the sum of all components. Similar black lines describe the sum of the components in the S1s and N1s spectra. Line shapes were developed from out-of-Bragg XPS spectra as described in the section above.

Concerning the stoichiometry and the line shapes, the measured N1s and the C1s spectra are in good agreement with the respective soft XPS data. For the S atoms, photoemission from the S1s orbital was measured instead of photoemission from the S2p orbital. This was done because of the better photoemission cross-section of the S1s orbital at the Bragg energy. Based on the S2p photoemission results of Chapter 7, the binding energy differences of the donor and acceptor components were assumed to be similar for the measured S1s spectra. However, as described above, a binding energy difference of 0.38 eV

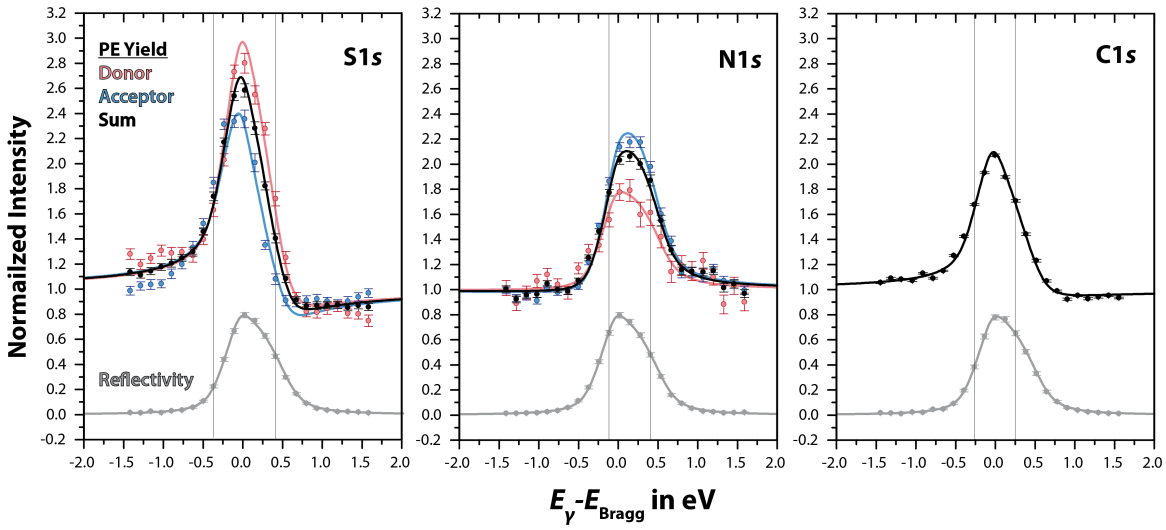

Figure 8.3.: Photoemission yield $Y(E)$ and reflectivity curves of the S1s, N1s, and C1s orbitals of HB238-A, measured at the Ag(200) Bragg plane. The photon energy was varied in a range of 4.5 eV around the Bragg energy of 3035.5 eV. Reflectivity curves are displayed in gray. The photoemission yield is normalized such that it is equal to one, for data points measured at out-of-Bragg conditions, i.e., for photon energies with a reflectivity value of zero. The photoemission yield of the donor components is displayed in red and the yield of the acceptor in blue. The black curve describes the sum of both components.

was used to fit the S1s photoemission spectra. Although this binding energy difference is much larger compared to that of the S2p spectra, it is still smaller than the binding energy difference of 0.55 ± 0.05 eV that is observed between the donor and acceptor components of HB238-A multilayers (S2p spectra, see Chapter 6).

As described above, the donor-acceptor architecture of HB238-A leads to different chemical environments of the S atoms of isolated molecules and multilayers [106]. Although the chemical environment of the donor and acceptor components becomes similar by the face-on arrangement of the molecules in the monolayer, as observed by similar binding energies in the respective S2p soft XPS spectra (see Chapters 6 and 7), the binding energy splitting is still observed for photoemission from the S1s orbital as mentioned above. This might be explained by final and initial state effects that contribute differently to the photoemission of the two orbitals. Hence, the S1s orbital might be less affected by the interfacial binding than the S2p orbital. As a result, we observe a larger binding energy difference for the donor and acceptor components of the S1s spectra (0.38 eV) than for the S2p spectra (0.03 eV).

For the out-of-Bragg spectra, the donor acceptor area ratio of the S1s and the N1s spectra is expected to be 1:1, and 1:3, respectively (see Chapter 7). This is different for the in-Bragg spectra. Here, the area ratios of the components change. This effect is more pronounced for the S1s lines of Figure 8.2 than for the N1s lines, as will be discussed below. The changes in the area ratios indicate that the donor and acceptor components are located at different adsorption heights with respect to the Ag surface. In Figure 8.3, the integrated intensities of the photoemission spectra are plotted against the Bragg-

centered photon energy ($E_\gamma - E_{\mathrm{Bragg}}$). In these yield curves, the color code is the same as in Figure 8.2. In addition, for reference purposes, the respective reflectivity curves are displayed in gray. The solid lines represent the fit of the photoemission yield $Y(E)$ according to Equation (8.1)

$$Y(E)_{hkl} = 1 + S_{\mathrm{R}} \sqrt{R(E)} + 2\,|S_{\mathrm{I}}|\,R(E)\,f_c \cos\left(\eta(E) - 2\,\pi\,p_c + \psi\right)\,. \tag{8.1}$$

Here, $R(E)$ is the reflectivity. S_{R}, S_{I}, and ψ are non-dipolar photoemission correction parameters that account for the systematic experimental over- and underestimation of the photoelectron intensity in NIXSW measurements related to the outgoing and incoming x-ray wave [64]. The photoemission yield curves are normalized to a value of one for out-of-Bragg photon energies [68]. For further information, see Chapter 3.

Similar to Figure 8.2, the black curves of Figure 8.3 are the sum of the donor and acceptor components, which describe the overall integrated intensity of the respective photoemission spectra. As expected from the different intensity versus photon energy behavior of the donor and the acceptor components in the S1s and the N1s spectra, we find that the respective yield curves deviate from each other and hence, also from the sum of the photoemission yield, indicating different coherent fractions, coherent positions, or both. The values of the coherent fraction f_{c} and position p_{c}, which are obtained from the fits of the photoemission yield curves, are listed in Table 8.4. In addition, the values are displayed in the Argand diagram of Figure 8.4. From the coherent position, the adsorption heights z_{200} of the respective components with respect to the (200) Bragg plane can be determined by $z_{200} = (n + p_{\mathrm{c}}) \cdot d_{200}$. Here, n is an integer number and equals $n = 1$ for reasonable adsorption heights. Please note that possible relaxations of the Ag surface are not considered, as the adsorption heights are determined with respect to the extended Ag(200) Bragg planes. However, for Ag(100), surface relaxation effects are usually within $0 - 2\%$ of the bulk lattice constant [107] and hence negligible for discussing the molecular adsorption heights with respect to the surface layer.

8.3.1. C atoms

HB238-A comprises 23 C atoms in total. The C1s signal of Figure 8.4 represents the average value of all C atoms. Hence, on average, the heights of the C atoms of HB238-A result in a coherent position of $p_{\mathrm{c}}^{\mathrm{C}} = 0.445 \pm 0.007$ and accordingly in an adsorption height of $z_{200}^{\mathrm{C}} = 2.952 \pm 0.014$ Å. As described above, HB238-A is non-planar and includes two nBu groups and one tBu group. These groups are expected to deviate in their adsorption heights from the height of the π-system. This is due to the structural flexibility of the nBu groups and the tetrahedral geometry of the tBu group. Thus, the C atoms of HB238-A are subject to a large adsorption height distribution that leads to a low coherent fraction of the average signal.

Expecting an (undistorted) arrangement of the tBu group in which the π-system of the molecule is preferably in closest contact with the surface, two of the three methyl groups are pointing towards the surface. Accordingly, the third methyl group would point away from the surface into the vacuum, resulting in an adsorption height of this group which

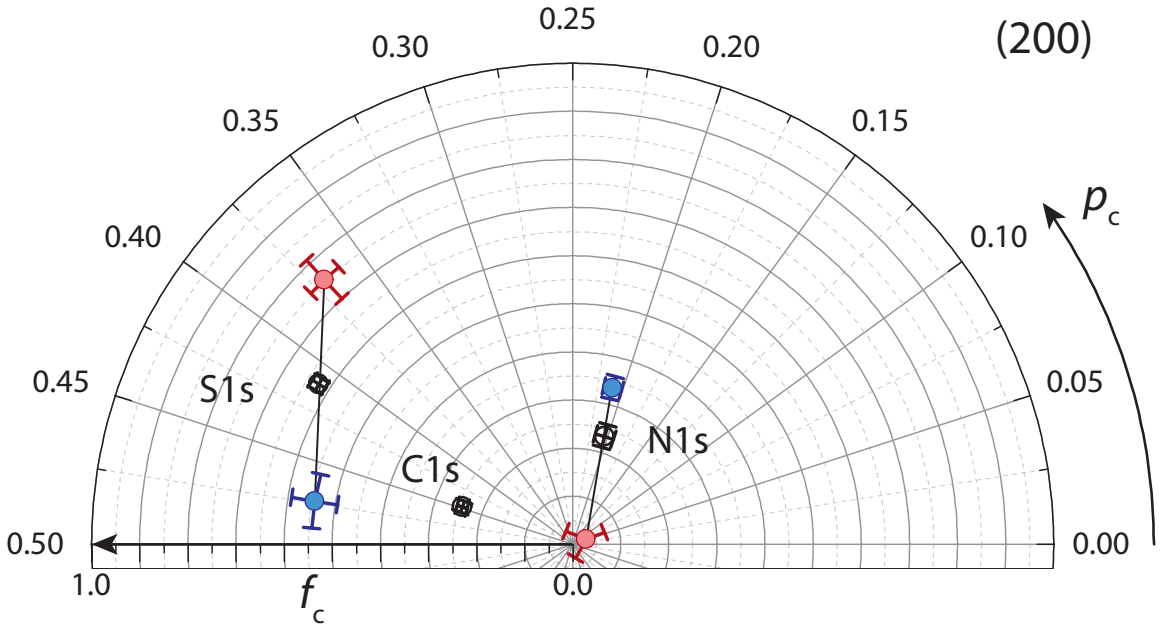

Figure 8.4.: Argand diagram displaying the results for the coherent positions (p_c) and the coherent fractions (f_c) for the different components and orbitals of HB238-A measured for the Ag(200) Bragg reflection. The respective values are summarized in Table 8.4. Error bars are given according to the fit of the photoemission yield curves displayed in Figure 8.3. Color code as above. For illustration purposes, the donor and acceptor components of the same orbital are connected by a line that is, hence, also running through the sum of the components (black data points).

Table 8.4.: Values of the coherent positions p_c and the coherent fractions f_c determined for the S1s, N1s, and C1s orbitals of the merocyanine HB238-A in the α-phase, and the (200) Bragg reflection. Hence, the z_{200} values are the (averaged) adsorption heights of the molecular S, N, and C atoms on the Ag(100) surface with respect to the extended Bragg plane. z_{200} is determined from the value of p_c by $z_{200} = (n + p_c) \cdot d_{200}$ with $d_{200} = 2.0428$ Å and $n = 1$.

		p_c	f_c	z_{200} in Å
	S_{A+D}	0.411 ± 0.004	0.623 ± 0.015	2.882 ± 0.008
S1s	S_D	0.370 ± 0.008	0.754 ± 0.054	2.799 ± 0.016
	S_A	0.474 ± 0.017	0.543 ± 0.048	3.011 ± 0.035
	N_{A+D}	0.204 ± 0.013	0.234 ± 0.024	2.460 ± 0.027
N1s	N_D	0.056 ± 0.271	0.030 ± 0.041	$--$
	N_A	0.210 ± 0.009	0.335 ± 0.025	2.472 ± 0.018
C1s	C	0.448 ± 0.008	0.242 ± 0.011	2.958 ± 0.016

would be by a maximum of 1.44 Å[1] larger than the adsorption height of the π-system. This geometry of the *t*Bu group is likely as the adsorption height of the molecule to the surface is quite small, as will be discussed below.

Thus, we expect the adsorption height of the π-system and the *n*Bu groups (averaged C height) to be smaller than the experimental average value of $z_{200}^{\mathrm{C}} = 2.958 \pm 0.014$ Å. This adsorption height can be estimated by a subtraction of the 1.44 Å height difference mentioned above that applies to one out of 23 C atoms in the molecule (2.958 Å−1.44 Å/23). Hence, the averaged adsorption height of the π-system and the *n*Bu groups results in 2.90 Å. However, as discussed above, the described height distribution of the C atoms is expected to lead to a rather small value of the coherent fraction, which is confirmed by the experimental value of $f_{\mathrm{c}}^{\mathrm{C}} = 0.248 \pm 0.011$.

8.3.2. N atoms

For nitrogen, the number of atoms per HB238-A molecule is four. As demonstrated in Chapters 6 and 7, photoemission from N atoms in the electron-donating part (1 atom) and N atoms in the electron-accepting part (3 atoms) of the molecule can be distinguished experimentally. Hence, together with the sum of the donor and acceptor components, three yield curves are obtained, which are displayed in Figure 8.3. Accordingly, these provide three points in the Argand diagram of Figure 8.4. The three points fall onto a line with the sum of both components being located such that it divides the line between the donor and the acceptor with a ratio of 1:3. This is expected as the sum rule for Argand vectors ($\mathbf{F}_{\mathrm{c}}$) applies. It can be expressed as

$$\mathbf{F}_{\mathrm{c}}^{\mathrm{sum}} = \sum_{j=1}^{K} \gamma_j \cdot \mathbf{F}_{\mathrm{c}}^{j}\,, \tag{8.2}$$

with j indexing one of K chemically different components which have molar fractions of γ_j [98]. A detailed explanation of the sum rule can be found in ref. [98]. The fact that we find the expected stoichiometric ratio between the two components supports that the effects of beam damage are small. This was safeguarded by performing several NIXSW measurements with short exposition times on different fresh spots on the sample as described in Section 8.2 and in Chapter 4.5.2.

We find for both N-components a low coherent fraction. For the acceptor component, the coherent fraction is $f_{\mathrm{c}}^{\mathrm{N_A}} = 0.335 \pm 0.025$ and thus significantly larger than the coherent fraction of the donor component which has a value of $f_{\mathrm{c}}^{\mathrm{N_D}} = 0.030 \pm 0.041$ and is hence close to zero. The small coherent fraction of the donor component is surprising because this states that the tertiary amine of HB238-A does not exhibit a vertical order in the α-phase.[2] Hence, the respective adsorption height $z_{200}^{\mathrm{N_D}}$ is not calculated since it would not have any physical meaning. For the acceptor component an adsorption height of

[1] This height was calculated under the assumption of a non-distorted tetrahedral geometry of the *t*Bu group and a C-C bond distance of 1.54 Å [74].

[2] Please note that effects due to a low statistic in the respective photoemission spectra cannot be excluded.

$z_{200}^{\mathrm{N_A}} = 2.472 \pm 0.018$ Å is determined. The also low coherent fraction of the acceptor component indicates different adsorption heights for the N atoms of the CN groups and the thiazole ring. This is expected, as the N atom of the thiazole ring is likely to be found in an adsorption height similar to that of the π-system. The N atoms of the CN groups, on the contrary, are most likely closer to the Ag surface. This might be due to charge transfer that was already indicated in the respective soft XPS spectra.

8.3.3. S atoms

The number of S atoms per HB238-A molecule is two. One S atom is located in the thiophene ring of the electron-donating part, and one S atom is located in the thiazole ring of the electron-accepting part of the molecule. In the Argand diagram of Figure 8.4, the two components fall onto a line that is split by the sum of the components in a 1:1 ratio. Hence, the splitting follows the expected stoichiometry according to Equation (8.1). Both components exhibit a rather high coherent fraction of $f_c^{\mathrm{S_A}} = 0.543 \pm 0.08$ and $f_c^{\mathrm{S_D}} = 0.754 \pm 0.054$. The higher coherent fraction of the donor component is surprising as it indicates that the adsorption height of the thiophene ring is better defined than the adsorption height of the adjacent tertiary amine that was discussed above. The S atoms are found at an adsorption height of $z_{200}^{\mathrm{S_A}} = 3.011 \pm 0.035$ Å and $z_{200}^{\mathrm{S_D}} = 2.799 \pm 0.016$ Å. Hence, the donor component (thiophene S atom) is about 0.3 Å closer to the surface than the acceptor component (thiazole S atom), but on average, the adsorption heights of the S atoms are found to be larger than the adsorption heights of the N atoms ($z_{200}^{\mathrm{N_A}} = 2.472 \pm 0.018$ Å). However, the higher coherent fractions of the S atoms may indicate that the S atoms contribute more strongly to the interfacial binding of the HB238-A molecules in the α-phase than the N atoms, which have less defined adsorption heights.

8.4. The adsorption heights of the HB238-A derivatives

The narrow height distribution of both the donor and the acceptor S atoms motivated us to investigate the differences in the adsorption heights of the merocyanines HB238-B, HB238-C, and HB238-D. These results may provide further information about differences in the interfacial interactions in the α-phase compared to those in the small α-phase and Q-phase. Thus, NIXSW data for the S1s orbitals were measured. Further measurements of the C1s and N1s orbitals were not performed due to the expected low significance of the results as discussed above.

The respective photoemission yield curves are displayed in Figure 8.5. Remarkably, the yield curves of the different merocyanines are very similar to each other, although all three merocyanines form different phases. The data of HB238-D were again measured for the small α-phase. The Argand diagrams of Figure 8.6 (a) and (b) display the respective f_{c} and p_{c} values, which are, in addition, summarized in Table 8.5. The data in Figure 8.6 (a) represents the sum of the donor and acceptor components. In addition, the Argand diagram in (b) shows the vectors of the respective donor and acceptor components. In the Argand diagram, each set of points is connected by a dotted line, with the sum

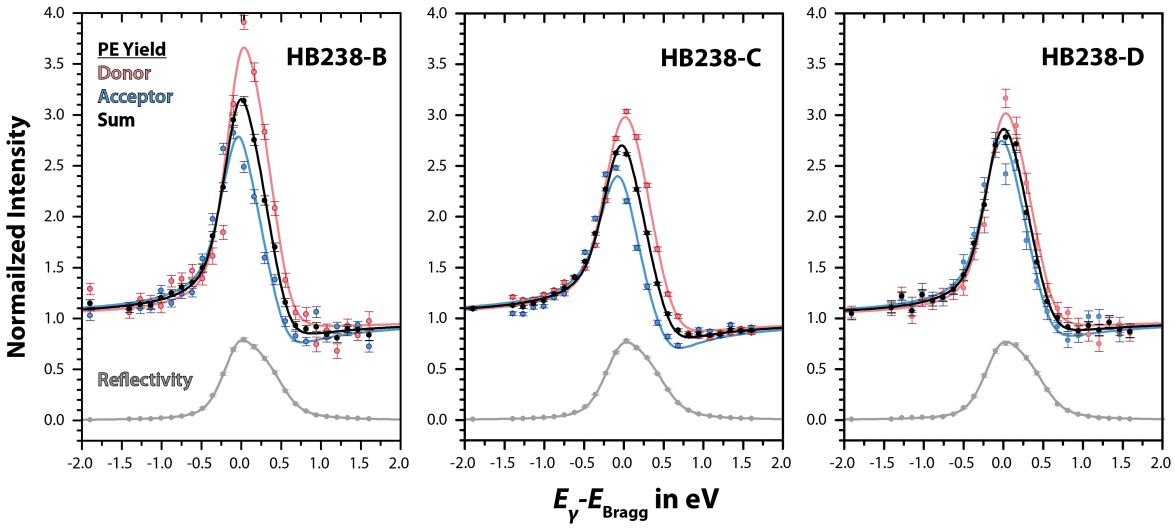

Figure 8.5.: Photoemission (PE) yield $Y(E)$ and reflectivity curves of the S1s orbitals of HB238-B, HB238-C, and HB238-D, measured for the Ag(200) Bragg reflection. The photon energy was varied in a range of $E^{200}_{\mathrm{Bragg}} \pm 4.5$ eV around the Bragg energy of 3035.5 eV. However, for presentation purposes, only a range of $E^{200}_{\mathrm{Bragg}} \pm 2$ eV is displayed. Reflectivity curves are displayed in gray. The photoemission yield is normalized such that it is equal to one for data points measured at the out-of-Bragg conditions, i.e., for photon energies for which the reflectivity has a value of zero. The photoemission yield of the donor components is displayed in red, and the yield of the acceptor in blue. The black curve corresponds to the sum of both components.

displayed as a white spot for reference purposes. Please note that Figure 8.6 also includes the data of HB238-A for comparison.

Interestingly, by comparing the sum (A+D) of the donor and acceptor S atoms displayed in Figure 8.6 (a), we find two pairs of p_{c} values. In Figure 8.6 (a), they are indicated by two solid lines in radial direction. The merocyanines HB238-A and HB238-C are found at an adsorption height of $z^{\mathrm{S_{A+D}}}_{200} = 2.88 \pm 0.01$ Å. The merocyanines HB238-B and HB238-D at $z^{\mathrm{S_{A+D}}}_{200} = 2.79 \pm 0.01$ Å which results in a difference of 0.09 ± 0.02 Å. Thus, the pairing does not correlate with the phase formation, because HB238-A and HB238-B both form the α-phase. The difference between the coherent fractions for both pairs is about 0.1 and, thus, not within the error range of the values.

In Figure 8.6 (b), the results for the respective donor (red error bars) and acceptor components (blue error bars) are displayed. Each set of components is connected by a dotted line. The signals of the summed components are added as open circles. As expected from the 1:1 stoichiometry, the signals that correspond to the sum of both components are found at about the middle of the dotted lines. Aberrations from that are in a range of $5 - 6\%$ and are most likely due to uncertainties in the fitting of the separated components. We find the donor components at adsorption heights of $z^{\mathrm{S_D}}_{200} = 2.71 \pm 0.02$ Å to 2.78 ± 0.01 Å. The coherent fractions of the donor components are high and range from $f_c^{\mathrm{S_D}} = 0.80 \pm 0.05$ to 0.96 ± 0.08. The acceptor components are, for all investigated merocyanines, located at larger heights. The respective values range from $z^{\mathrm{S_A}}_{200} = 2.86 \pm 0.02$ Å to 3.04 ± 0.02 Å and correspond to coherent fractions of $f_c^{\mathrm{S_A}} = 0.67 \pm 0.04$ to 0.74 ± 0.05.

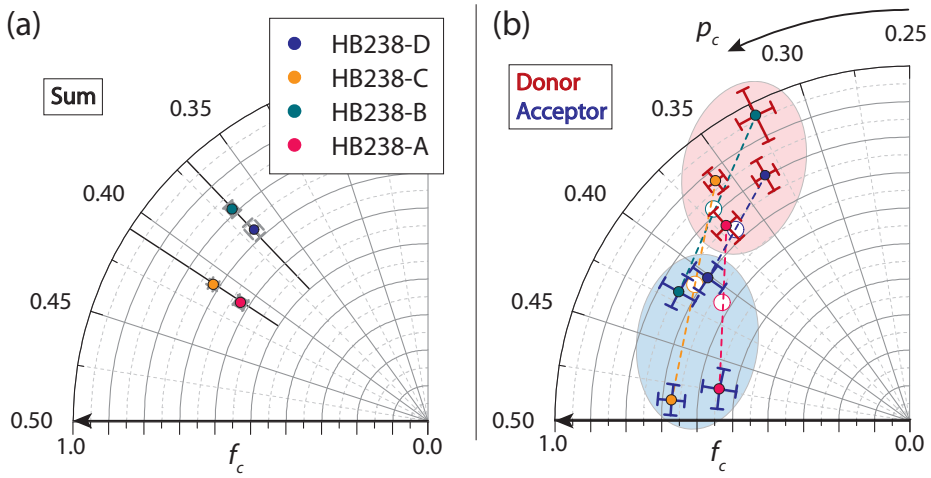

Figure 8.6.: Argand diagram displaying the results for the coherent positions (p_c) and the coherent fractions (f_c) determined for the S1s photoemission of the merocyanines HB238-A, HB238-B, HB238-C, and HB238-D. Measurements were performed for the Ag(200) Bragg reflection. In (a), the sum of both components is displayed. Identical p_c values are indicated by solid black lines. (b) displays the individual values of the donor (points with red error bars) and the acceptor (points with blue error bars). Error bars according to the fit of the photoemission yield curves. Color code as indicated. For illustration purposes, donor and acceptor components in (b) are connected by a line that is, hence, also running through the sum of the components, indicated in white.

Table 8.5.: Values of the coherent positions p_c and the coherent fractions f_c determined for the S1s orbitals of the merocyanines HB238-A (α-phase), HB238-B (α-phase), HB238-C (Q-phase), and HB238-D (small α-phase) and the (200) Bragg reflection. The adsorption heights z_{200} of the S atoms are determined with respect to the extended Bragg plane. z_{200} is determined from the value of p_c by $z_{200} = (n + p_c) \cdot d_{200}$ with $d_{200} = 2.043$ Å [74–77] and $n = 1$. The indices A, D, and A+D indicate values of the donor, acceptor, and the sum of both.

		p_c	f_c	z_{200} in Å
HB238-A	S_{A+D}	0.411 ± 0.004	0.623 ± 0.015	2.882 ± 0.008
	S_D	0.370 ± 0.008	0.754 ± 0.054	2.799 ± 0.016
	S_A	0.474 ± 0.017	0.543 ± 0.048	3.011 ± 0.035
HB238-B	S_{A+D}	0.369 ± 0.003	0.812 ± 0.018	2.796 ± 0.006
	S_D	0.324 ± 0.009	0.963 ± 0.081	2.705 ± 0.018
	S_A	0.419 ± 0.010	0.744 ± 0.054	2.899 ± 0.020
HB238-C	S_{A+D}	0.410 ± 0.002	0.715 ± 0.009	2.881 ± 0.004
	S_D	0.358 ± 0.005	0.869 ± 0.035	2.775 ± 0.010
	S_A	0.486 ± 0.010	0.673 ± 0.038	3.036 ± 0.021
HB238-D	S_{A+D}	0.367 ± 0.004	0.727 ± 0.027	2.793 ± 0.009
	S_D	0.335 ± 0.007	0.802 ± 0.049	2.726 ± 0.014
	S_A	0.402 ± 0.010	0.695 ± 0.052	2.864 ± 0.021

Hence, the donor components of all phases exhibit a smaller vertical height distribution compared to the acceptor components (seen from the larger $f_c^{S_D}$ with respect to the $f_c^{S_A}$ values). In addition, the observed heights of the acceptor components are by at least 0.08 Å larger than the adsorption heights of the donor components and span a larger range.

8.5. Discussion

In summary, the above-determined adsorption heights of the C, N, and S atoms of HB238-A in the α-phase lead to the structural model displayed in Figure 8.7. The hardsphere model shows a side view of the face-on adsorbed molecule. The model is drawn to scale regarding the adsorption heights of the molecule as determined by NIXSW. The spheres of the Ag atoms correspond to the full van der Waals radii of 1.72 Å [108]. The radii of the molecular C, N, and S atoms of HB238-A are reduced to 1/6 of the van der Waals radii. As the *n*Bu groups are structurally flexible due to their ability to rotate around their single bonds, their positions remain arbitrary. Hence, the two *n*Bu groups of the HB238-A molecule in Figure 8.7 were replaced by methyl (CH_3) groups for better visibility of the molecular backbone.

The adsorption heights determined for the C, N, and S atoms of HB238-A in the α-phase support the idea of strong interfacial interactions and a chemisorption of the molecules. This idea was already proposed from the binding energy shifts observed in the XPS spectra of Chapter 6. For classifying the interfacial interactions, the sum of the van der Waals radii of the HB238-A atoms and the Ag atoms can serve as a reference. For physisorbed molecules, adsorption heights are expected to be close to the sum of the van der Waals radii [110, 111], while the height of chemisorbed molecules is expected to be significantly smaller [112].

For HB238-A, the sum of the van der Waals radii are 3.42 Å for C/Ag, 3.27 Å for N/Ag, and 3.52 Å for S/Ag [108]. Therefore, comparing these values to the determined overall adsorption heights of the C, N, and S atoms of $z_{200}^{C_{\pi-\mathrm{system}}} = 2.90 \pm 0.02$ Å, $z_{200}^{N} = 2.46 \pm 0.03$ Å, $z_{200}^{S} = 2.88 \pm 0.01$ Å it results that the binding distances are 15% smaller than the sum of the van der Waals radii for C, 24% for N, and 19% for S. By that the adsorption height of HB238-A in the α-phase is comparable to the adsorption height of other π-conjugated molecules on the Ag(100) surface. One example is 3,4,9,10-perylenetetracarboxylic acid dianhydride (PTCDA) for which an adsorption height of 2.84 ± 0.02 Å was reported for the perylene carbon atoms [104].

Regarding the different adsorption heights determined for the donor and acceptor components of N and S, the data indicate a distorted, non-planar adsorption geometry of the adsorbed molecule. These distortions are caused by the interactions of the functional groups with the surface. The estimated maximum value for the intramolecular vertical distortion determined from the z_{200} values is about 0.44 Å ($z_{200}^{C_{\pi-\mathrm{system}}} - z_{200}^{N_{A+D}}$).

This molecular distortion is visualized in the model of Figure 8.7. However, the exact distortions of the molecular structure remain, to some extent, arbitrary. In general, the donor components show smaller adsorption heights compared to the atoms located in the

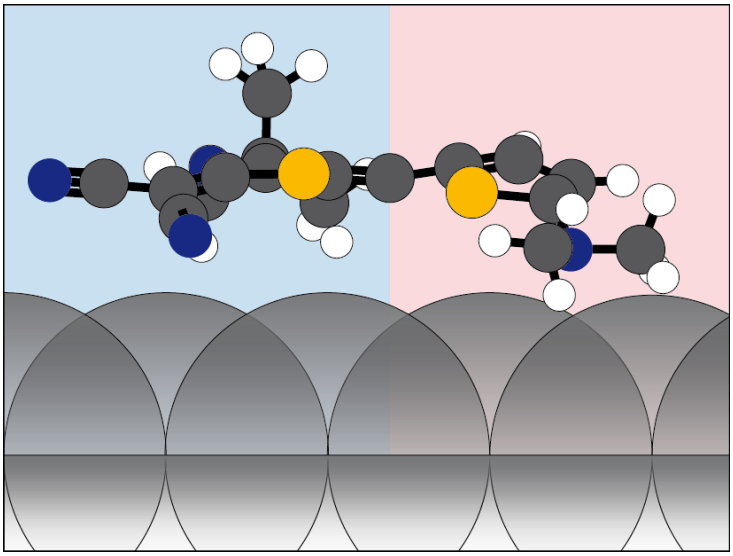

Figure 8.7.: Hardsphere model illustrating the adsorption heights of the C, N, and S atoms of HB238-A in the α-phase, on the Ag(100) surface. For better visibility of the molecular backbone, the nBu groups are not displayed but were exchanged by CH_3 groups (equal to the structure of HB238-D).
The topmost layer of the Ag(100) surface is indicated with circles representing the full van der Waals radii [108, 109]. For better presentation purposes, the radii of the HB238-A atoms are reduced to 1/6 of the full van der Waals radii [108]. Color code as above. The model is to scale with the adsorption heights determined by NIXSW, however, the corresponding distortion of the molecule and the resulting height distribution of the atoms are to some extent arbitrary. Please note that the tBu group of the molecule is only partly visible as it is located on the rear part of the molecule on the left (acceptor) side. However, the corresponding Me group that points away from the surface into the vacuum, as described in the text, is clearly visible. For further information, see text.

electron-accepting part of HB238-A. This most likely corresponds to a charge transfer between the Ag surface and the electron donor, as observed in the XPS spectra discussed in Chapter 6. However, as the coherent fraction of the N1s donor component is close to zero, the small adsorption height of the tertiary amine to the Ag surface as displayed in Figure 8.7 does not have a physical meaning. The low value of the coherent fraction is possibly related to a large vertical disorder, but might also be affected by the low statistics of the respective photoemission spectra.

In general, f_c values of one would only occur for a theoretical, perfectly ordered system with all atoms of a component being located at the same adsorption height. Hence, f_c values below one are expected due to disorder in the layer and lattice vibrations. In the case of the S components measured for the four investigated merocyanines, the f_c values of the acceptor components are in a range of 0.54 ± 0.05 to 0.74 ± 0.05. Hence, they are in a range typical for chemisorbed organic molecules [104, 113]. For the donor components, the coherent fractions are even higher and range from a minimum value of 0.75 ± 0.05 for HB238-A to a maximum value of 0.96 ± 0.08 for HB238-B. These values are extremely high and are comparable with coherent fractions observed for photoemission bands of the metal substrate, e.g., Ag3d [104]. This indicates a high vertical order of the donor

components, i.e., the S of the thiophene ring, which hence must correspond to defined lateral adsorption sites of the donor S atoms on the Ag(100) surface. Similar results were found for, e.g., thiophene adsorbed on Cu(111) for which a coherent fraction of 0.85 was determined [114] and for end-capped quarterthiophene on Ag(111), which shows a coherent fraction of 0.70 [115].

For further interpretation of the data, it needs to be considered that each unit cell of the three commensurate phases contains four molecules. While the $P4$ symmetry of the Q-phase allows for four symmetry equivalent molecules in the unit cell, this is not the case for the $P2$ symmetry of the α-phase and the small α-phase. Here, the unit cell contains two pairs of symmetry-equivalent molecules. Due to the strong interfacial binding, it is assumed that symmetry equivalent molecules occupy the same adsorption sites and, hence, have the same adsorption heights. Taking the donor and acceptor components into account, this leads for the α-phase and the small α-phase to a total number of eight S atoms per unit cell, which are distributed onto a maximum number of four different adsorption sites, i.e., two sites for S_A and two sites for S_D. Hence, the experimentally determined results, i.e., the results for the S1s donor and acceptor, are averaged values of two heights.

As the S atoms of the symmetry nonequivalent molecules cannot be distinguished experimentally, the following considerations are made to estimate the different adsorption heights. According to the sum rule introduced in Equation 8.2, the Argand vector defined by the experimental results can be described by a sum of the Argand vectors of the two underlying components. To fulfill the sum rule, at least one component is required to have a coherent fraction higher than the coherent fraction of the experimentally determined sum. Hence, two situations are possible. In the first one, both components have the same coherent fraction and different coherent positions (symmetrical splitting). In the second situation, the coherent fraction of one component is higher than the coherent fraction of the second component (asymmetric splitting). In this case, the higher coherent fraction may be expected for the component with the smaller coherent position, as the smaller adsorption heights indicate stronger interfacial interactions and hence a narrower height distribution. Both cases are illustrated schematically in the Argand diagram of Figure 8.8.

In the asymmetrical situation, the pair of points in the Argand diagram would follow the dark orange dotted lines for assuming that the component closer to the surface has a coherent fraction of one. This is indicated for some examples of coherent positions by light gray open points. Hence, two limiting cases can be considered for which their two components either have a maximum difference in the coherent positions or their coherent fractions. For this example, the maximum difference of the positions amounts to $\Delta p_c = 0.22$, which corresponds to a height difference of $\Delta z = 0.45$ Å. Respectively, the maximum difference of the coherent fractions results in $\Delta f_c = 0.49$. The real points of the components in the Argand diagram will be located somewhere in this marked area between the two limiting cases.

Due to the similar binding energies in the XPS spectra of the S atoms and the high coherent fractions of the donor and acceptor components, it can be expected that the differences in the adsorption heights of the symmetry nonequivalent molecules do not differ much. Hence, high coherent fractions are expected for all components, which favors a symmetric

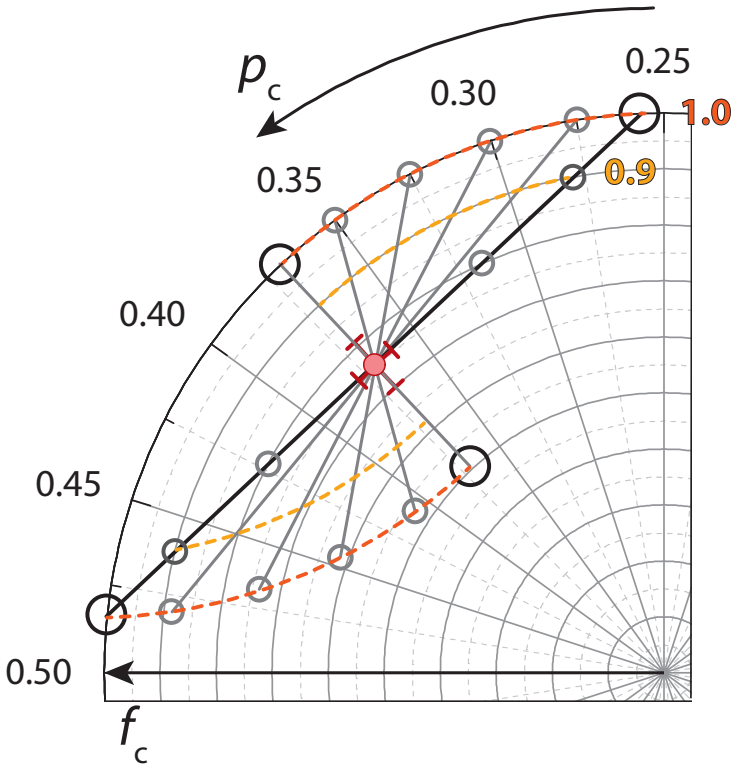

Figure 8.8.: Illustration of the theoretical splitting of the experimentally determined HB238-A donor component into two signals representing four donor S atoms of two nonequivalent molecules. Open circles indicate the limiting cases of the maximum difference possible for the coherent fraction and the coherent position. Each pair of points is connected by a gray solid line. In general, two cases can occur: a symmetrical case in which both components have the same coherent fraction, and an asymmetrical case in which one component has a larger coherent fraction than the other component. In the symmetrical case, the points follow the black line as indicated. For the asymmetrical case, dotted lines in orange color mark lines on which the points are located if the coherent fraction of the component closer to the surface is set to 1.0 or 0.9, respectively.

situation with similar coherent fractions. This is much more likely than a strongly asymmetrical situation with one component having a much lower coherent fraction than the other. However, as explained above, a coherent fraction of one is a theoretical assumption that does not apply to real experimental conditions. Hence, coherent fractions of 0.9 or lower are more realistic, which thus leads, in case of similar coherent fractions, to a small difference in the coherent positions. The same arguments, of course, also apply to the C and N components of HB238-A, but due to the large number of atoms per molecule underlying the experimental data and the much lower coherent fractions, the situation is much more complex there and cannot be solved without further experimental data.

8.6. Conclusion

The determination of the adsorption height of HB238-A in the α-phase on the Ag(100) surface revealed strong interfacial interactions of the molecules with the surface. These are observed by adsorption heights that are considerably smaller than the sum of the van der Waals radii, thus indicating a chemisorption of the molecules. The determined adsorption heights in combination with the small height distribution of the S atoms indicate that the S atoms also possess a high lateral order, which is most likely accompanied by the formation of covalent bonds to the Ag surface.

Similar adsorption heights of the S atoms were found for all investigated merocyanines, independent of the respective commensurate phase formed on the surface. Further theoretical considerations allow us to give an upper limit for the difference in the adsorption heights for the symmetrically nonequivalent molecules which are expected to be found in the α-phase of HB238-A and HB238-B, and the small α-phase of HB238-D.

9. Determination of the molecular adsorption sites

This chapter describes the determination of the adsorption sites of the merocyanine molecules in the α-phase of HB238-B and the small α-phase of HB238-D. The results are derived from NIXSW measurements performed at the I09 endstation of the DLS. They investigate why the interplay of the intermolecular hydrogen bonds and the strong covalent interfacial bonding of the molecules leads to two different molecular adsorption sites on the Ag(100) surface instead of one single adsorption site for all molecules.

The following people contributed to the experimental work performed at the I09 endstation: Anja Haags, Sergey Subach, David A. Duncan, and Moritz Sokolowski.

9.1. Scientific context

The unit cells of the α-phase and the small α-phase both exhibit a $P2$ symmetry and contain four merocyanine molecules in total. The previous chapters derived that the four molecules can be divided into two nonequivalent pairs, which most likely occupy different adsorption sites. Still, the question remains which driving force is behind the occupation of two different adsorption sites on the Ag(100) surface, which exhibits a four-fold symmetry. This question is addressed by NIXSW experiments, with which the adsorption sites of the four molecules in the unit cell are determined. In more detail, this determination again concentrates on the adsorption sites of the two S atoms per molecule, from which one can deduce the azimuthal orientation of the entire molecule for assumed molecular structures. The adsorption sites are used to derive structural models of the molecular arrangement in the unit cell. By comparing the resulting intramolecular S distances with the distances observed in the crystal structures, these models also provide first information about the lateral distortions of the adsorbed molecules. These are not only driven by the interfacial interactions but also by lateral intermolecular interactions. Hence, the observed lateral distortions of the molecules also allow insight into the strength of the intermolecular interactions.

This chapter is organized as follows. The following sections first introduce the experimental NIXSW data before the data is interpreted to find out about the adsorption sites of the molecules in the unit cell, a procedure also referred to as triangulation [67, 114, 116]. The results are used to develop structural models for the molecular arrangement in the α-phase of HB238-B and the small α-phase of HB238-D.

As HB238-A and HB238-B are expected to exhibit a similar molecular arrangement in the α-phase, HB238-B was measured exemplarily. To obtain a complete picture of the ordering of the here investigated merocyanines on the Ag(100) surface, the NIXSW results are also compared to data measured for the Q-phase of HB238-C, later in this chapter. In the Q-phase, the situation is in so far different from that of the α-phases that the square unit cell indicates a $P4$ space group of the structure and hence the existence of a four-fold rotation axis. Hence, the structure would allow for identical adsorption sites for all four molecules in the unit cell.

9.2. The principles behind triangulation

The principle behind the determination of adsorption sites by NIXSW is based on measurements performed for a set of three different and independent Bragg planes. In Chapter 8, the (200) Bragg reflection was used to determine the distance of the adsorbed S atoms of the merocyanines with respect to the extended Bragg planes. For the determination of the adsorption sites, the distance of the S atoms with respect to two additional Bragg planes was measured. These Bragg planes are required to be pairwise non-coplanar to the Ag(200) Bragg plane such that an intersection point of the three Bragg planes exists. Please note that in the case of highly symmetric molecular structures, i.e., in the presence of glide planes, it might be sufficient to measure a total number of two different Bragg reflections [67]. However, as the present structures are only of low symmetry, this is not the case here. Accordingly, data for the (111) and (220) Bragg reflections were measured.

For the theoretical case of a single adsorbed atom on the surface, the adsorption site would directly result from the intersection point of the three Bragg planes after shifting them by the determined value of $z^{hkl} = (n + p_c^{hkl}) \times d_{hkl}$ along the normal vector of the planes. n is an integer number and equals 1 for the (200) Bragg reflection and 0 for the (111) and (220) Bragg reflections. For many-atom-systems, however, the values of the coherent fractions need to be taken into account additionally, and the adsorption sites are, hence obtained by a fit of simulated values to the experimental f_c and p_c values. Detailed information about this fitting procedure is provided in Chapter 3.

As the molecules and the unit cell are of low symmetry, the following assumptions were made for the determination of the adsorption sites:

1. From the $P2$ space group and the corresponding C_2 symmetry of the tetramers, we assume that each unit cell contains two pairs of symmetry equivalent molecules which are located on diagonal positions relative to each other.

2. Symmetry equivalent molecules occupy the same adsorption sites and can be mapped onto each other by the two-fold rotation axes located in the center of the unit cell and in the center of each tetramer (corners of the unit cell).

3. The intramolecular distance between the two S atoms is similar to their distance in the bulk structures, which ranges from 3.1190(1) Å to 3.2203(3) Å (see Appendix B).

4. Each S component exhibits an ideal coherent fraction of one, which neglects any

thermal and statistical disorder in the positions of the S atoms. For more information concerning this approximation, please see Section 9.4, below.

However, as the molecular packing is rather dense in all considered phases, the derived models directly provide feedback about the reliability of the obtained molecular adsorption sites from the sterical overlap of the molecules. This feedback was further used to optimize the structural models, as, e.g., an overlap of neighboring molecules must be avoided. Finally, but very important, the models must also fit the topographic contrast observed in the respective STM images.

9.3. S adsorption with respect to the (111) and (220) Bragg planes

This section describes the NIXSW analysis performed for the determination of the S adsorption sites. It concentrates on the data obtained for the (111) and (220) Bragg reflections, which are, in combination with the (200) data discussed in Chapter 8, used for the triangulation and the modeling of the molecular arrangement on the surface.

9.3.1. Adsorption sites in the α- and the small α-phase

Figures 9.1 and 9.3 present the measured NIXSW spectra of HB238-B and HB238-D monolayers. The measurements were performed on the same sample as for the corresponding (200) data that was already discussed in Chapter 8. The displayed spectra were measured at four different photon energies and show the fitted line intensities for out-of-Bragg conditions (upper and lower spectra) and in-Bragg conditions (two spectra in the middle). The denoted photon energies are given with respect to E_{Bragg}. As E_{Bragg} depends on the distance between the Bragg planes, the Bragg energy is different for the (111) and the (220) Bragg reflections.[1] Here, the theoretical values result to $E^{111}_{\mathrm{Bragg}} = 2628.9\ e\mathrm{V}$ and $E^{220}_{\mathrm{Bragg}} = 4292.9\ e\mathrm{V}$. A sketch of the (200), (111), and (220) Bragg planes can be found in Chapter 3.

Similar to the data of the (200) Bragg reflection, which are displayed here again for completeness of the dataset, the donor and acceptor components are represented by red and blue lines in Figure 9.1. This assignment of colors holds for all the figures in this chapter. Again, the donor and acceptor lines show different behavior in their photon energy dependence of the intensities, indicating that the atoms contributing to the components differ in their distances to the (111) and (220) Bragg planes. However, by comparing the experimental intensities for the out-of-Bragg and in-Bragg spectra, it becomes clear that the increase and decrease of the signal intensity (bottom to top spectra) are more pronounced for the (111) Bragg reflection. This observation is also reflected by the resulting yield curves displayed as black lines in Figures 9.2 for HB238-B and 9.4 for HB238-D.

In addition, the (220) yield curves show a higher noise level than those of the (200) and the (111) data. The reason for this is based on the larger difference of E^{220}_{Bragg} to the

[1] Please note that the intensity of the (220) reflectivity curve is smaller due to the higher Bragg energy and related absorption effects.

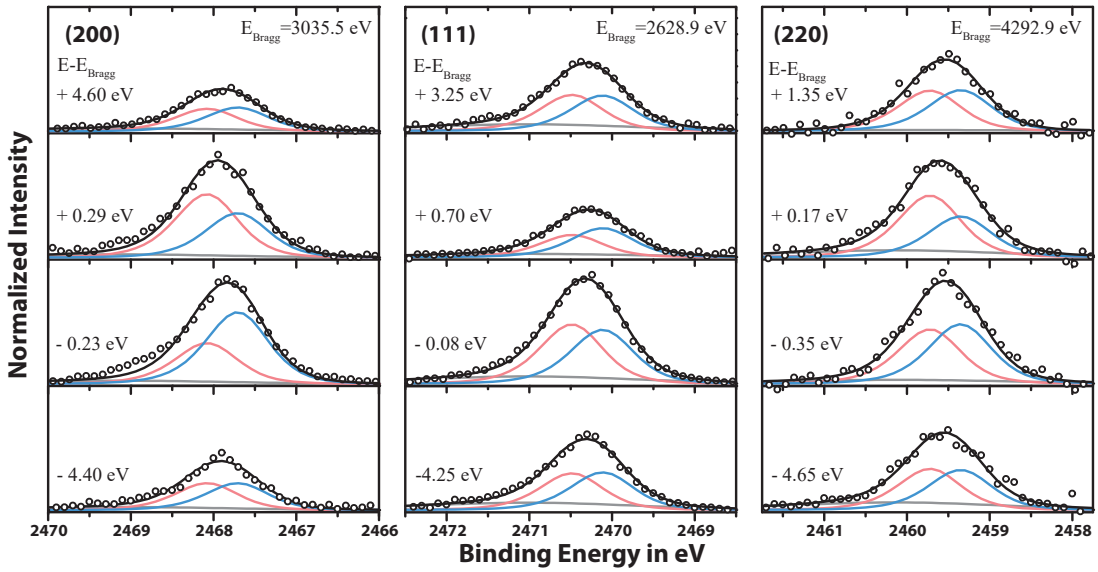

Figure 9.1.: Photoemission curves for the S1s orbitals of HB238-B, measured during the NIXSW measurements at the Ag(200), (111), and (220) Bragg reflections. The photon energy of the x-ray beam is indicated for each spectrum with respect to the Bragg energy E_{Bragg}. Experimental data points are fitted by different lines as described in the text. Color code: red (donor component), blue (acceptor component), gray (satellite), black (sum of the components).

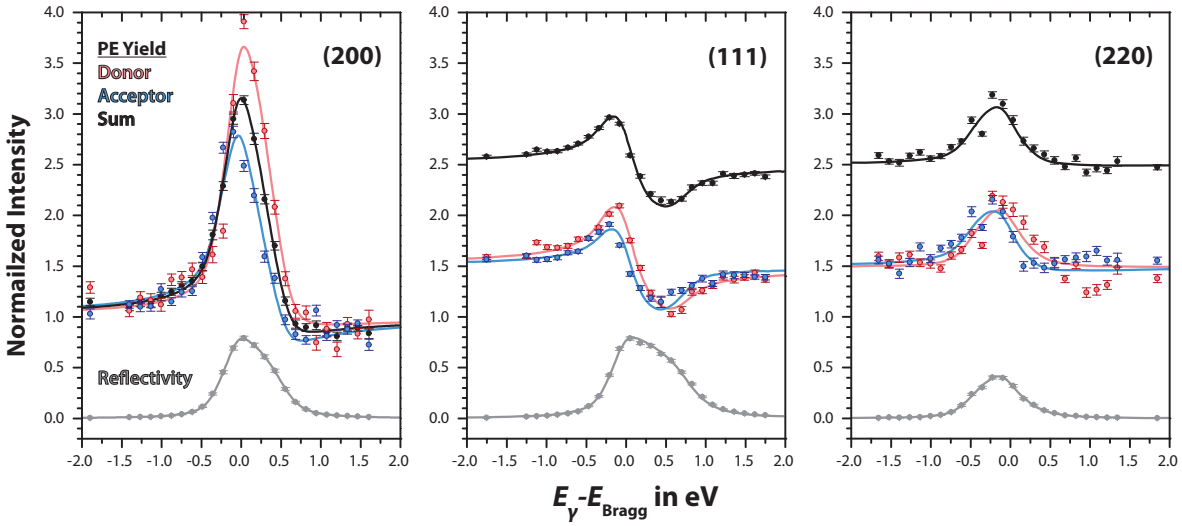

Figure 9.2.: Photoemission (PE) yield $Y(E)$ and reflectivity curves for the S1s orbitals of HB238-B, measured for the Ag(200), (111), and (220) Bragg reflections with corresponding fits. Color code as above. For better visibility, the yield curves measured at the (111) and (220) Bragg reflections are displayed with a vertical offset of +0.5 for the donor (red) and acceptor (blue) lines, and by +1.5 for the line representing the averaged sum of both components (black). Photon energies E_γ are given with respect to the Bragg energies, which are $E^{200}_{\mathrm{Bragg}} = 3035.5\ e\mathrm{V}$, $E^{111}_{\mathrm{Bragg}} = 2628.9\ e\mathrm{V}$, and $E^{220}_{\mathrm{Bragg}} = 4292.9\ e\mathrm{V}$.

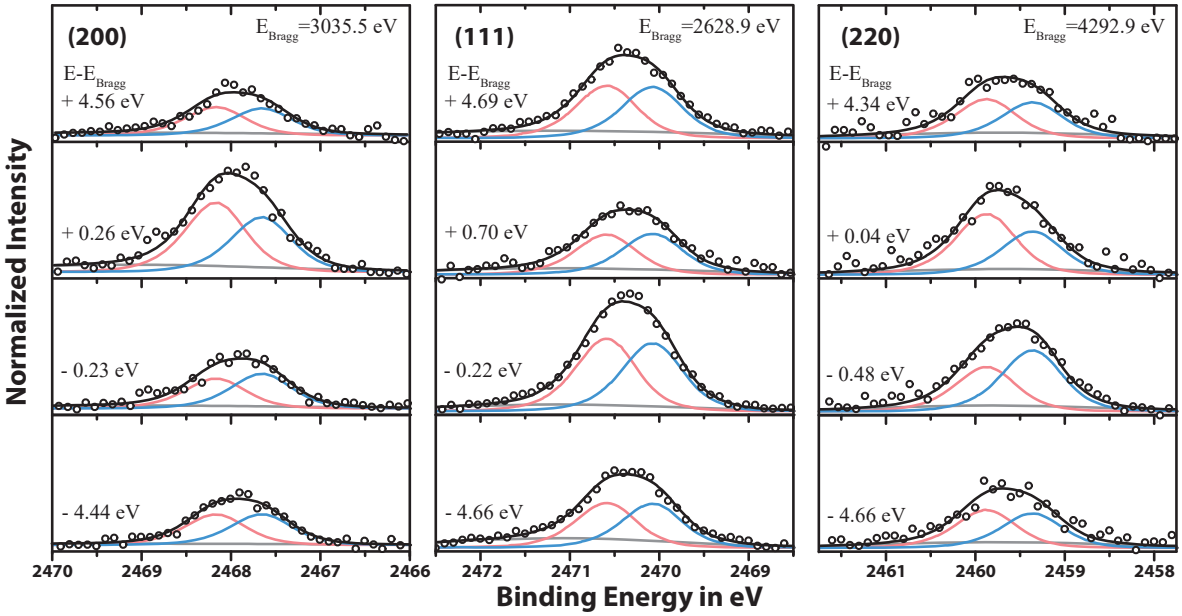

Figure 9.3.: As Figure 9.1 but for HB238-D.

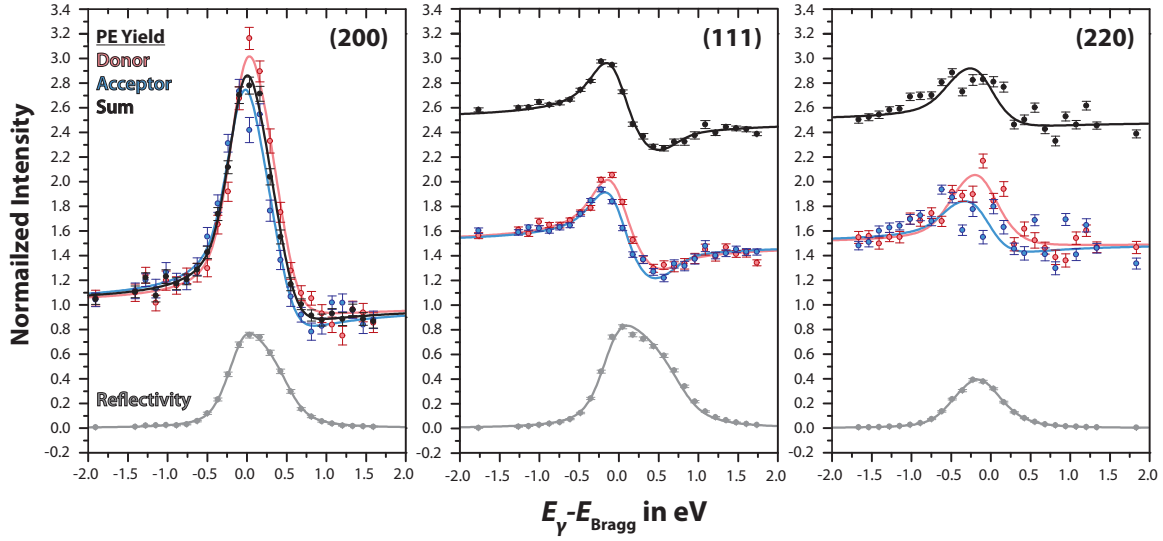

Figure 9.4.: As Figure 9.2 but for HB238-D.

Table 9.1.: Values of the coherent positions (p_c) and the coherent fractions (f_c) determined for the S1s orbitals of the merocyanines HB238-B and HB238-D and the (111) Bragg reflection. The values correspond to the α-phase and the small α-phase, respectively. z_{111} denotes the adsorption distance of the sulfur atoms of the molecule with respect to the (111) Bragg plane. z_{111} is determined from the value of p_c by $z_{111} = p_c \cdot d_{111}$ with $d_{111} = 2.360$ Å. The indices A, D, and A+D indicate values of the donor component, the acceptor component, and the sum of both components.

(111)		p_c	f_c	z_{111} in Å
HB238-B	S_{A+D}	0.712 ± 0.002	0.688 ± 0.009	1.679 ± 0.004
	S_D	0.692 ± 0.004	0.689 ± 0.016	1.632 ± 0.008
	S_A	0.732 ± 0.004	0.702 ± 0.021	1.726 ± 0.010
HB238-D	S_{A+D}	0.713 ± 0.002	0.587 ± 0.009	1.682 ± 0.006
	S_D	0.703 ± 0.004	0.559 ± 0.015	1.659 ± 0.010
	S_A	0.722 ± 0.003	0.619 ± 0.012	1.704 ± 0.007

Table 9.2.: Values of the coherent positions (p_c) and the coherent fractions (f_c) determined for the S1s orbitals of the merocyanines HB238-B and HB238-D and the (220) Bragg reflection. The values correspond to the α-phase and the small α-phase. z_{220} gives the adsorption height of the sulfur atoms of the molecule with respect to the (220) Bragg plane. z_{220} is determined from the value of p_c by $z_{220} = p_c \cdot d_{220}$ with $d_{220} = 1.445$ Å. The indices A, D, and A+D indicate values of the donor component, the acceptor component, and the sum of both components.

(220)		p_c	f_c	z_{220} in Å
HB238-B	S_{A+D}	0.413 ± 0.043	0.166 ± 0.043	0.597 ± 0.062
	S_D	0.31 ± 0.074	0.145 ± 0.082	0.478 ± 0.106
	S_A	0.488 ± 0.051	0.220 ± 0.060	0.704 ± 0.074
HB238-D	S_{A+D}	0.565 ± 0.044	0.193 ± 0.043	0.816 ± 0.064
	S_D	0.425 ± 0.042	0.201 ± 0.056	0.615 ± 0.061
	S_A	0.643 ± 0.048	0.274 ± 0.073	0.929 ± 0.070

S1s binding energy, leading to a smaller photoemission cross section and, accordingly, to a lower signal-to-noise ratio in the spectra. Counteracting this problem, 13 NIXSW data sets for HB238-B and 9 data sets for HB238-D were averaged, respectively (see Table 8.3). To avoid beam damage influencing the signal intensity, each NIXSW data set was measured at a fresh sample position.

The coherent fractions and coherent positions that result from the fit of the photoemission yield curves of Figures 9.2 and 9.4 are listed in Tables 9.1 for the (111) Bragg reflection and in Table 9.2 for the (220) Bragg reflection. Data of the Q-phase will be discussed in Section 9.3.2, below.

For the S atoms of both molecules, HB238-B and HB238-D, an adsorption distance of $z_{111}^{\mathrm{S_{A+D}}} = 1.68 \pm 0.01$ Å to the (111) Bragg plane was determined for the sum of the donor and acceptor components ($\mathrm{S_{A+D}}$). In contrast to that, the adsorption distances to the (220) Bragg plane are different (HB238-B $z_{220}^{\mathrm{S_{A+D}}} = 0.60 \pm 0.06$ Å, HB238-D $z_{220}^{\mathrm{S_{A+D}}} = 0.82 \pm 0.06$ Å). They differ by $\Delta z_{220}^{\mathrm{S_{A+D}}} = 0.22 \pm 0.06$ Å, indicating differences in the molecular adsorption sites in the α-phase and small α-phase.

It is striking that the coherent fractions of the (220) data are so small. With values of 0.17 ± 0.04 for HB238-B and 0.19 ± 0.04 for HB238-D, $f_{\mathrm{c}}^{\mathrm{S_{A+D}}}$ is by about $40 - 50\%$ lower than the respective values for the (111) Bragg reflection. This behavior is somehow expected, as the lattice spacing d_{hkl} between the (220) Bragg planes is about 38% smaller than the lattice spacing between the (111) Bragg planes. In general, f_{c} is an indication for the spread of the (sulfur) adsorption distances around the average adsorption distance z_{hkl} determined from the coherent position by $z_{hkl} = p_{\mathrm{c}} \cdot d_{hkl}$. A second factor leading to small f_{c} values is the existence of more than one distinct adsorption distance for the S atoms, as it is the case for the present structures due to the donor and acceptor components.

Although the separate fits of the donor and acceptor components in Figures 9.1 and 9.3 also results in low f_{c} values between 0.15 to 0.27, the data show that for both molecules the donor components are found at smaller (220) adsorption distances than the respective acceptor components. The difference in the adsorption distances with respect to the (220) Bragg plane between the acceptor and donor components results to $\Delta z_{220}^{\mathrm{A\text{-}D}} = 0.23$ Å for HB238-B and $\Delta z_{220}^{\mathrm{A\text{-}D}} = 0.31$ Å for HB238-C.

For the (111) Bragg reflection, the differences in the adsorption distances between the acceptor and donor components are smaller compared to the (220) data and result in 0.09 Å for HB238-B and 0.05 Å for HB238-D. Again, the donor components are found at smaller adsorption distances than the acceptor components. Coherent fractions between 0.56 and 0.70 indicate only small variations in the adsorption distances of the sulfur atoms with respect to the (111) Bragg plane.

Summarizing, the NIXSW data for the α-phase of HB238-B and the small α-phase of HB238-D indicate only minor differences in the molecular adsorption sites of the two phases. To obtain more information about how the two symmetrically nonequivalent pairs of molecules in the structures influence the f_{c} and p_{c} values by occupation of different adsorption sites, the Q-phase of HB238-C was measured for the (111) Bragg reflection. As the $P4$ space group of the structure requires identical adsorption sites for all four molecules, changes in the NIXSW data are expected in comparison to the data of HB238-B and HB238-D.

9.3.2. Comparison to the adsorption in the Q-phase

Figure 9.5 shows the photoemission yield curves of HB238-C in the Q-phase measured for the (200) and the (111) Bragg reflections. Please note that the (200) data was already discussed above (see Section 8.4). The corresponding f_c and p_c values for the (111) Bragg reflection are listed in Table 9.3. Data of the (220) reflection is missing for experimental reasons.

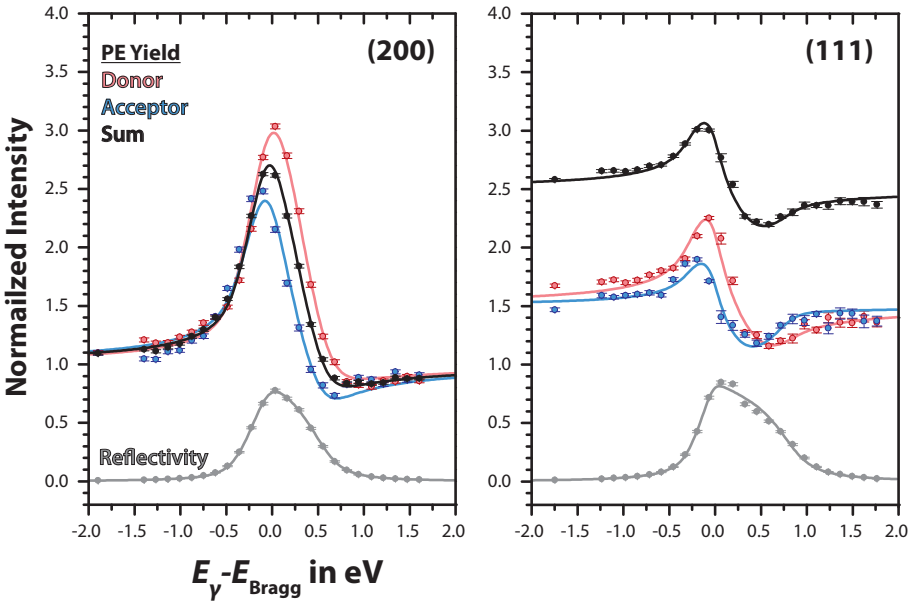

Figure 9.5.: Photoemission yield and reflectivity curves for the S1s orbitals of HB238-C, measured for the Ag(200) and (111) Bragg reflections with corresponding fits. Color code as above. For better visibility, the yield curves measured at the (111) Bragg reflection are displayed with a vertical offset of +0.5 for the donor (red) and acceptor (blue) lines and by +1.5 for the line representing the average sum of both components (black). Photon energies E_γ are given with respect to the Bragg energies, which are $E^{200}_{\mathrm{Bragg}} = 3035.5\ e\mathrm{V}$ and $E^{111}_{\mathrm{Bragg}} = 2628.9\ e\mathrm{V}$.

Table 9.3.: Values of the coherent positions (p_c) and the coherent fractions (f_c) determined for the S1s orbitals of the merocyanine HB238-C and the (111) Bragg reflection. The values correspond to the molecular arrangement in the Q-phase. z_{111} denotes the adsorption distance of the sulfur atoms of the molecule with respect to the (111) Bragg plane. Determination of z_{111} and explanation of the indices as above.

(111)		p_c	f_c	z_{111} in Å
HB238-C	S_{A+D}	0.691 ± 0.003	0.607 ± 0.013	1.631 ± 0.007
	S_D	0.658 ± 0.005	0.638 ± 0.019	1.553 ± 0.012
	S_A	0.725 ± 0.004	0.601 ± 0.015	1.711 ± 0.009

Surprisingly, the $p_c^{S_{A+D}}$ value of the (111) reflection for HB238-C differs by only $\Delta p_c = -0.02$ from the respective values of HB238-B and HB238-D. This corresponds to a difference in the adsorption distances of 0.05 Å. Also, the coherent fraction does not show a difference in the compared phases, because the value $f_c^{S_{A+D}}$ of 0.61 ± 0.01 for HB238-C lies in the range given by the values of HB238-B and HB238-D. A graphical representation of the (111) and (220) p_c and f_c values of the three molecules is given by the Argand diagrams of Figure 9.6. Here, Figure 9.6 (a) displays the values of $p_c^{S_{A+D}}$ and $f_c^{S_{A+D}}$, while Figure 9.6 (b) displays the data points of the respective donor and acceptor components. Pairs of donor-acceptor components of one molecule are connected by a dotted line in the same color as the data points. The sum of the components is displayed as a white circle.

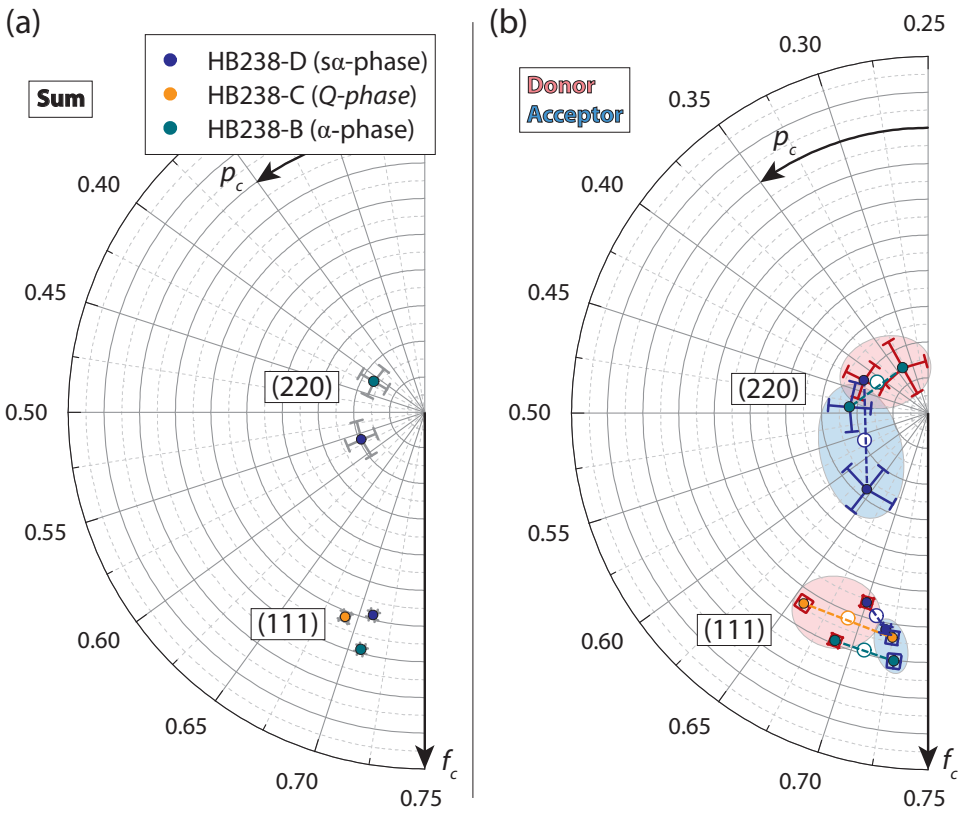

Figure 9.6.: Argand diagram displaying the results for the coherent positions (p_c) and the coherent fractions (f_c) determined for the S1s photoemission of the merocyanines HB238-B (α-phase), HB238-C (Q-phase), and HB238-D (small (s) α-phase). Color code as indicated. Measurements were performed for the (111) and (220) Bragg reflections. In panel (a), the sum of the donor and acceptor components is displayed. Panel (b) displays the individual values of the donor (points with red error bars) and the acceptor components (points with blue error bars). For better visibility, the respective components are marked by shaded backgrounds in red and blue colors. Error bars are given according to the fit of the photoemission yield curves. For illustration purposes, donor and acceptor components in (b) are connected by a line that is, hence, also running through the vector related to the sum of the components, indicated in white. The full radius of the Argand diagram corresponds to a coherent fraction of 1.

For the donor and acceptor components of HB238-C, we find a difference in the adsorption distance of 0.16 Å. The respective p_c values differ by $\Delta p_c^{A\text{-}D} = 0.07$. This splitting leads to a p_c^A value of HB238-C similar to the p_c^A values obtained for HB238-B and HB238-D. The respective coherent fraction of the acceptor component results in $f_c^A = 0.60 \pm 0.2$. For better visibility, the group of data points corresponding to the acceptor components of the molecules is marked by a blue shaded background in Figure 9.6. The respective groups of data points corresponding to the donor components are indicated by a red shaded background. While the data points of the acceptor components are similar for the three merocyanines, the difference in the donor components is larger and results to $\Delta p_c^D = 0.03$ and, hence, $\Delta z_{111}^D = 0.07$ Å.

Thus, the data indicate that the molecules occupy similar adsorption sites in all three phases, the α-phase of HB238-B, the Q-phase of HB238-C, and the small α-phase of HB238-D. Only minor deviations in the f_c and p_c values indicate small differences in the molecular arrangement with respect to the Ag(100) surface. These differences are most likely due to the presence of two different molecular adsorption sites in the structures of HB238-B and HB238-C. However, according to the NIXSW data, the differences in the molecular adsorption sites are most likely of minor nature.

9.4. The lateral molecular arrangement in the small α-phase

Using the data determined for the (200), (111), and (220) Bragg reflections, the lateral arrangement of the merocyanines HB238-B and HB238-D on the Ag(100) surface can be determined. This section begins with the triangulation of HB238-D, which forms the small α-phase. HB238-D features the shortest alkyl side chains in the explored series of merocyanines, consisting of two methyl groups. Hence, no flexible alkyl side chains have to be considered in the structural models of the lateral arrangement of the molecules.

9.4.1. General considerations

As already considered above, the unit cells of the α- and small α-phase include two pairs of symmetry nonequivalent molecules, i.e., two different pairs of molecular adsorption sites. The experimentally determined donor and acceptor components, thus, represent average values of the molecular adsorption sites. To distinguish between the two symmetrically nonequivalent molecules, the experimental vectors were split symmetrically according to the scheme displayed in Figure 8.8, above.

For the (200) data of HB238-D, the splitting is illustrated in the Argand diagram of Figure 9.7 (a). Assuming that all molecules in the unit cell are equivalent concerning their vertical order, the splitting was performed under the requirement that both of the resulting donor and acceptor components have the same coherent fraction f_c^{split}, which is, by at least 0.1 higher than the corresponding experimental value. This requirement is reasonable, as the experimental $f_c^{exp.}$ values, $f_c^{S_D} = 0.80 \pm 0.05$ and $f_c^{S_A} = 0.70 \pm 0.05$, are already rather high. An asymmetric splitting as described in Chapter 8 for Figure 8.8

was not considered here. However, it principally cannot be excluded.

The difference Δp_c between the coherent position of the experimental value and the split components was calculated by

$$\Delta p_c = \arccos\left(\frac{f_c^{exp.}}{f_c^{split}}\right)\frac{1}{2\pi}. \tag{9.1}$$

For the acceptor components, the splitting with $f_c^{split} = 0.8$ leads to a difference of $\Delta p_c^A = 0.08$ from the initial, experimental value and, hence, to an adsorption height difference of $\Delta z_{200}^{S_A} = 0.34$ Å between the two acceptor components. For a splitting with $f_c^{split} = 1.0$, the height difference in the acceptor components increases to $\Delta z_{200}^{S_A} = 0.52$ Å.

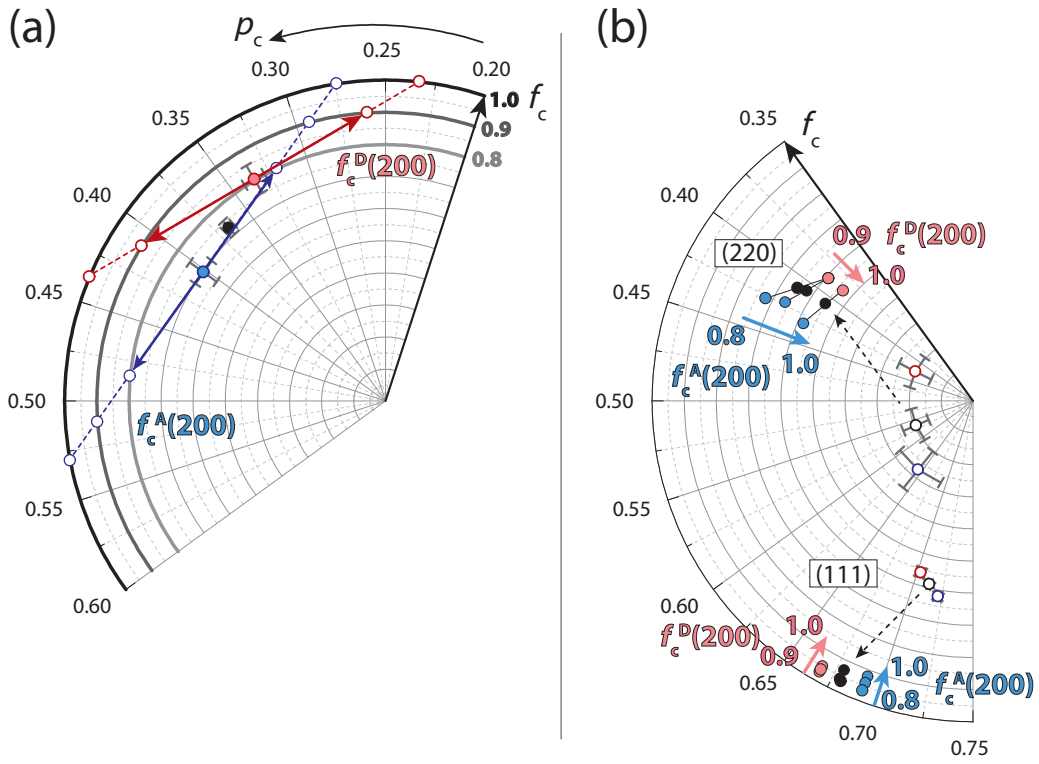

Figure 9.7.: Argand diagrams representing the principles behind the f_c and p_c estimation of the (200) donor (D) and acceptor (A) components. Panel (a) illustrates the splitting of the experimental donor (red color) and acceptor (blue color) components measured for the (200) Bragg reflection into two components, each (open circles in red and blue). The resulting two donor and two acceptor components describe the two symmetrically nonequivalent molecules per unit cell. It can be assumed that the split components have an equal coherent fraction ($f_c^A(200)$, $f_c^D(200)$), which is at least 0.1 higher than the experimental value. Panel (b) illustrates the effect of the different $f_c^A(200)$ and $f_c^D(200)$ values, and the resulting differences in the coherent positions, on the f_c and p_c values of the (220) and (111) Bragg reflections. The values for the (220) and (111) data were calculated for ideal atop positions of all S atoms. Data points with error bars represent the experimental data of HB238-D. Please note that some error bars are hidden behind the respective data points. In panel (a), the experimental data points are filled, following the color code used above. In panel (b), the experimental data are drawn as open circles, which are connected to the theoretical data by a dotted black arrow.

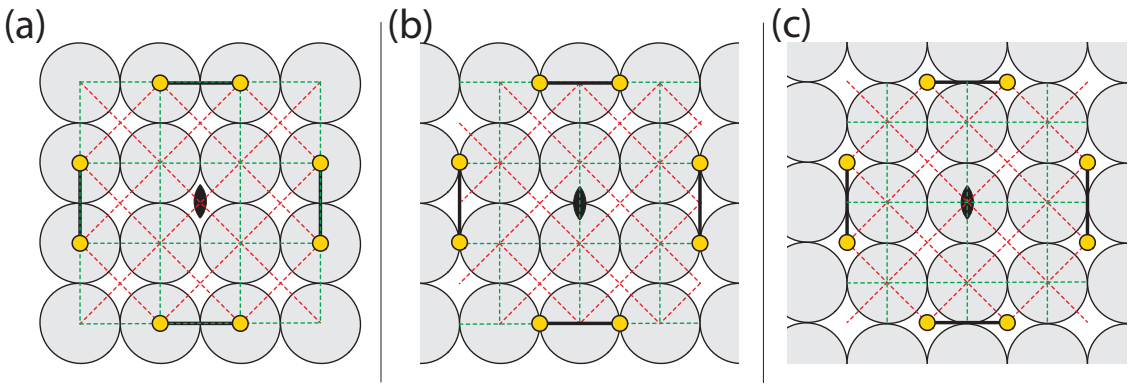

Figure 9.8.: Sketch of the high symmetry adsorption sites of the S atoms. Please note that only the S atoms (yellow spheres) of the four molecules within the tetramer are displayed. In addition, the lateral distances between the molecules are reduced by integer lattice distances, for representation purposes. The adsorption sites are sketched for the atop positions (a), the bridge positions (b), and the four-fold hollow positions (c). Pairs of S atoms that correspond to one merocyanine molecule are connected by a black line. Intersections of the (111) and (220) Bragg planes with the Ag(100) surface (gray spheres) are indicated by green and red colors, respectively. They are indicated for the symmetrically different Bragg planes used for the calculation of the theoretical f_c and p_c values. For further information regarding these Bragg planes or the calculation process, please see Chapter 3.

Accordingly, the splitting of the donor components results for $f_c^{\text{split}} = 0.9$ in a difference of $\Delta p_c^{\text{D}} = 0.07$ from the experimental value and, hence, in an adsorption height difference of $\Delta z_{200}^{\text{S}_\text{D}} = 0.31$ Å. Again, this difference increases for $f_c^{\text{split}} = 1.0$ to $\Delta z_{200}^{\text{S}_\text{D}} = 0.42$ Å. Thus, the maximum of the adsorption height difference, obtained for $f_c^{\text{split}} = 1.0$, is smaller for the donor components, as the coherent fraction of the respective experimental value is higher compared to the acceptor component.

For the determination of the S adsorption sites on the Ag(100) surface, the simulation was started with the high-symmetry adsorption sites as displayed in Figure 9.8. Here, the intersections of the (111) and (220) Bragg planes with the (100) surface are indicated by green and red colors, respectively. Accordingly, all eight S atoms were placed on the atop positions, the bridge positions, and the fourfold hollow positions, respectively. This is possible, due to the four-fold symmetry of the Ag(100) surface and the fact that the distance between two directly neighbored Ag atoms (2.89 Å [75, 76]) is in the range of the intramolecular S S distance (see Appendix B). For the adsorption heights of the S atoms to the Ag(100) surface, the above-determined $z_{200}^{\text{S}_\text{D}}$ and $z_{200}^{\text{S}_\text{A}}$ values of the split components were considered.

By calculating the corresponding p_c and f_c values for the (111) Bragg reflections, bridge positions of the S atoms result in a coherent fraction $f_c^{\text{sum}}(111)$ of zero. This is due to the presence of four symmetry equivalent domains. These are considered in the calculation of p_c and f_c as described in Chapter 3. As can be seen from Figure 9.8 (b), the p_c values of two domains (distance of the S atoms with respect to the green dotted lines, vertically and horizontally) would differ by 0.5. Accordingly, the respective Argand vectors of two domains would be rotated by $\pi/2$ with respect to each other and would thus mutually cancel each other.

Fourfold hollow positions, however, lead to a high coherent fraction but to a $p_c^{sum}(111)$ value of 0.18, which deviates significantly, by 0.53, from the experimental value. Hence, an adsorption of all S atoms at or close to the bridge and the fourfold hollow position can be excluded.

The calculated p_c and f_c values for the adsorption of the S atoms at atop positions of the Ag atoms are displayed in Figure 9.7 (b) as filled data points. Please note that these data points represent the average values of the donor and acceptor components, respectively, thus enabling a direct comparison with the experimental data points, displayed as open data points.

Although the calculated f_c values are significantly higher than the respective experimental values for both the (111) and the (220) Bragg reflections, a good agreement in the coherent positions is observed. For the (220) Bragg reflection, p_c^{sum} differs by only 0.16, while for the (111) Bragg reflection, the difference is 0.03 and thus even much smaller. According to the good agreement for the p_c values in Figure 9.7 (b), it can be concluded that the S atoms of HB238-D adsorb close to the atop positions of the Ag atoms. However, at least a few of the 8 S atoms per unit cell are expected to be located away from the atop positions, as the experimental f_c values are lower than the calculated ones.

In addition to the general positions of the atop-(220) and (111) values in the Argand diagram of Figure 9.7 (b), the diagram also illustrates the influence of $f_c^{split}(200)$ and accordingly $\Delta p_c(200)$ on the calculated data points. Here, $f_c^{split}(200)$ of the donor components is denoted as $f_c^{D}(200)$ and ranges from 0.9 to 1.0 according to Figure 9.7 (a). Equivalently, $f_c^{split}(200)$ of the acceptor components is denoted as $f_c^{A}(200)$ and ranges from 0.8 to 1.0. Increasing $f_c(200)$ values are marked by arrows in the same colors as used for the donor and acceptor components above. As one would expect from the increasing value of $\Delta p_c(200)$, the coherent fraction of the calculated (220) and (111) values decreases for increasing values of $f_c(200)$. As the angle ζ between the (111) Bragg plane and the Ag(100) crystal surface is 9.7° larger than the angle between the (220) Bragg plane and the crystal surface (see Figure 3.3 of Chapter 3), the calculated data points for the (111) Bragg reflection are less affected by $\Delta p_c(200)$.

As the calculated f_c values for the (220) and (111) Bragg reflections are closer to the experimental values for high coherent fractions of the split (200) components, the $f_c^{split}(200)$ values are assumed to be equal to one for the following further refinement of the adsorption sites in lateral direction. This is required, as the effects related to the splitting are not large enough to explain the experimentally observed small f_c values. Thus, the adsorption sites of the S atoms need to be considered in more detail.

9.4.2. Further refinement of the adsorption sites

The above considerations regarding the splitting of the experimental (200) donor and acceptor components allow us to distinguish between the adsorption heights of the two pairs of nonequivalent molecules per unit cell. As merocyanines are π-conjugated molecules, large vertical distortions of the molecules, i.e., large differences in $p_c^A(200)$ and $p_c^D(200)$ are unlikely. This leads to the assumption that the two low $p_c^{D,A}(200)$ values correspond to the same pair of molecules. The same holds vice versa for the two high $p_c^{D,A}(200)$ values. Hence, one pair of molecules is located at $z_{200}^D = 2.51$ Å and $z_{200}^A = 2.59$ Å, while the second pair of molecules is located at $z_{200}^D = 2.93$ Å and $z_{200}^A = 3.12$ Å. But up to now, this splitting is only a speculation.

In order to find the S adsorption sites matching the experimental NIXSW data, the S atoms were systematically shifted away from the atop positions of the Ag atoms. The results were transferred to structural models and compared to the experimental STM data. The respective results for the data of HB238-D and, hence, the small α-phase are displayed in Figures 9.9, 9.10, and 9.11.

Figure 9.9 shows the results of the systematic adsorption site variation as calculated p_c and f_c values. Following criteria for matching adsorption sites regarding the results of p_c and f_c were used:

1. Compared to the acceptor component, the Argand vector of the donor component of both the (111) and (220) Bragg reflection must exhibit a smaller value of p_c, as observed in the experimental results.

2. The (111) donor and acceptor components were allowed to differ by not more than 0.03 from the experimental value of p_c, and 0.15 from the experimental value of f_c.

3. For the (220) donor and acceptor components, the acceptable values of p_c and f_c were initially set slightly larger than the range of the respective error bars. However, it turned out that the experimentally observed splitting of the donor and acceptor components in combination with the low coherent fraction could not be reproduced by the simulation. Hence, for the (220) data, the focus was set to match the more reliable data point displayed in Figure 9.9 (a), representing the average of all S atoms in the unit cell.

In the Argand diagrams of Figure 9.9 (a) and (b), the individual calculated vectors of the triangulation process, i.e., the Argand vectors for all tested adsorption geometries with plausible results, are presented as small data points in black (panel (a), sum of all S atoms), light red (average of all donor S atoms), or light blue (average of all acceptor S atoms), respectively. The resulting groups of plausible data points are highlighted by backgrounds shaded in the same color. The center of mass for each group of data points is given as larger filled data points with a darker color. These values are used for the following comparison with the experimentally determined values of f_c and p_c.

The respective adsorption sites of the S atoms are displayed in Figure 9.10 (a) in a schematic top-view. Likewise, as in Figure 9.9, the lateral range of the donor and acceptor components is given by areas shaded in red and blue colors. The maximum variation in the S coordinates in one direction that is allowed by the size of the shaded areas

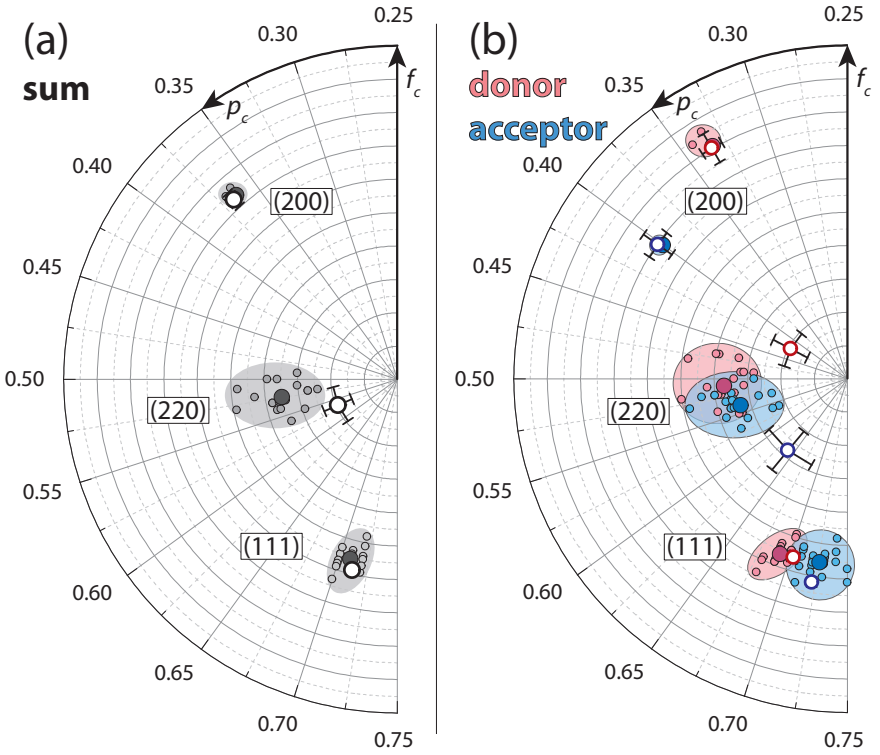

Figure 9.9.: Results of the adsorption site determination of the S atoms of the merocyanine HB238-D in the small α-phase on the Ag(100) surface. Panel (a) displays a scatter plot of the calculated p_c^{A+D} and f_c^{A+D} values in the Argand diagram. Panel (b) displays a scatter plot of the calculated $p_c^{A,D}$ and $f_c^{A,D}$ values of the donor and acceptor components in the Argand diagram. Color code as above. Small data points in panels (a) and (b) refer to average values that were calculated for a specific molecular arrangement in the unit cell, and hence, one set of molecular adsorption sites (individual results). The respective molecular adsorption sites are indicated in Figure 9.10. Large filled data points refer to the center of mass of the respective groups of individual results. These groups are indicated by a shaded background. Large open data points with error bars refer to the experimental results. Please note that the error bars of the experimental (111) data points are too small to be visible. The indicated f_c scale ranges from 0 to 1.

results in 0.33 Å and hence 11% of the Ag(100) surface lattice constant. Hence, the determined S adsorption sites are well localized on the Ag(100) surface. For any larger lateral deviations of these adsorption sites, significantly lower values for f_c^{111} and p_c^{111} are observed, accompanied by an increase of the f_c^{220} values or a decrease of p_c^{220}.

For the development of a structural model, the S adsorption sites were adjusted to fit the values determined for the center of mass of the lateral positions. These are displayed in Figure 9.10 (a) as large filled data points. Here, the lighter red and blue colors of the top and, accordingly, also of the bottom pair of S atoms correspond to the S atoms at a larger adsorption height with respect to the Ag(100) surface. Pairs of donor-acceptor S atoms, indicating a molecule, are connected by a solid black line.

In Figure 9.10 (b), the schematic presentation of the S adsorption sites is transferred into the molecular arrangement of the HB238-D tetramer. Here, the two pairs of symmetrically

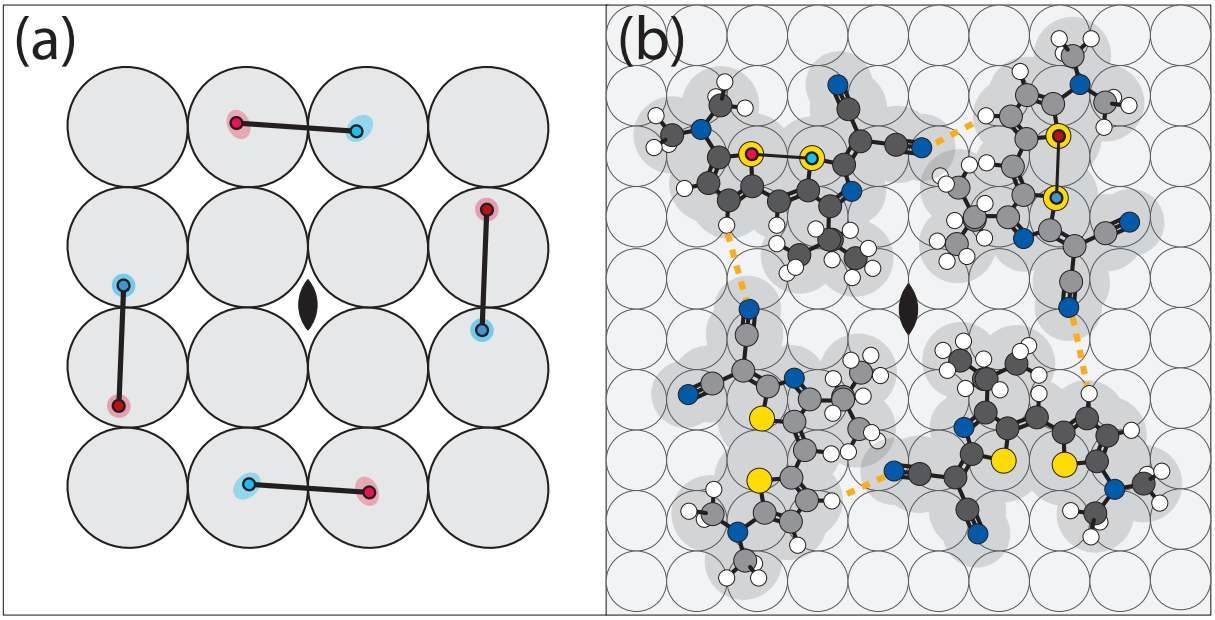

Figure 9.10.: Schematic presentation of the determined S adsorption sites of the merocyanine HB238-D on the Ag(100) surface. (a) Top view of the S adsorption sites on the Ag(100) surface with the indicated centered two-fold rotation axis. Pairs of donor and acceptor atoms connected by a solid black line belong to one molecule. Please note that the distances between the molecules are reduced in panel (a) to illustrate the small range of reasonable S adsorption sites. These are displayed as shaded areas in red (donor components) and blue (acceptor components) colors and include all adsorption geometries that led to the Argand vectors of the individual results displayed in Figure 9.9. Bright and dark colors represent higher and lower adsorption heights. Comparable to Figure 9.9, the filled data points indicate the center of mass of the individual positions.
(b) Hardsphere model of the molecular arrangement of HB238-D according to the determined S adsorption sites in (a). For clarity, the upper two molecules are superimposed by the schematic representation of the molecules in (a). Gray shaded areas around the molecules correspond to the respective full van der Waals radii. Please note that bright molecules correspond to smaller Ag-S distances.

nonequivalent molecules are indicated by lighter and darker colors. Please note that the dark molecules exhibit the larger Ag-S distances. The molecular arrangement is in agreement with the $P2$ symmetry of the structure as indicated by the twofold rotation axis. Hydrogen bonds between the CN groups and the thiophene rings of the neighboring molecules are indicated by orange dotted lines. Their length results in about 2.9 Å. Hence, the hydrogen bonds in this model are about 12% longer than the hydrogen bonds of the respective bulk structure (see Appendix B.1). However, please note that this model is based on molecular structures derived from general principles, i.e., established bond lengths [74], and does not include molecular distortions that might change the bond lengths during the adsorption process.

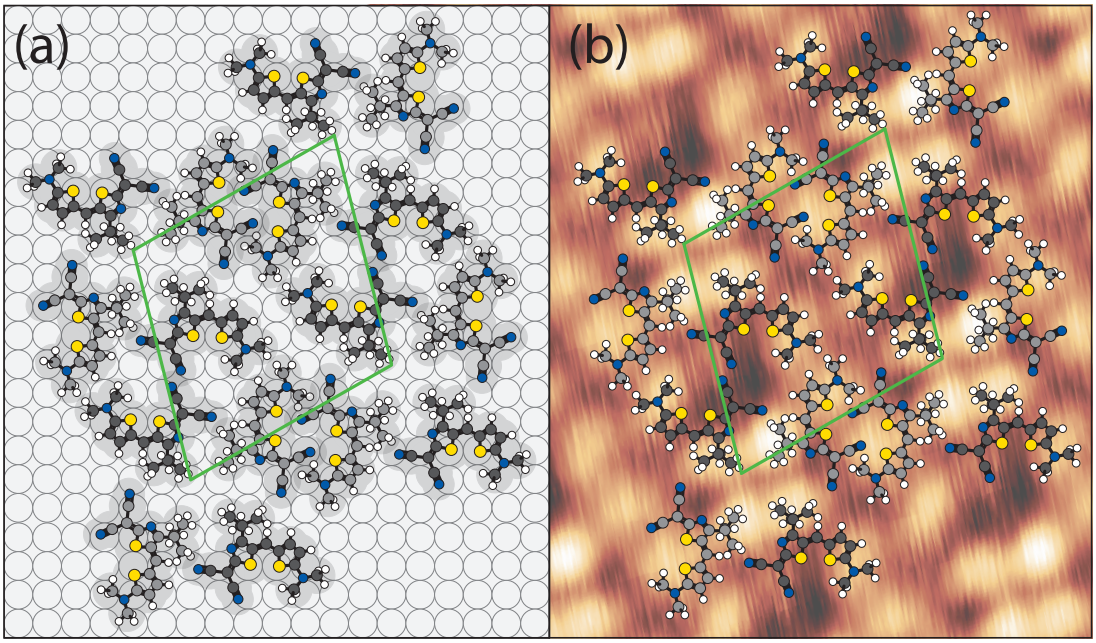

Figure 9.11.: Hardsphere model of the small α-phase of HB238-D on the Ag(100) surface (a) and superimposed with a respective STM image (b). The S adsorption sites correspond to the adsorption sites determined from the NIXSW analysis. The STM image is rotated compared to the identical STM image of the small α-phase that was displayed in Figure 7.3 (300 K, $U_{\mathrm{bias}} = -0.1$ V, $I_{\mathrm{t}} = 20$ pA). Pairs of bright molecules are located along the short vector of the superstructure. Gray shaded areas around the molecules correspond to the full van der Waals radii.

9.4.3. The unit cell packing

The resulting molecular arrangement of HB238-D in the small α-phase is displayed in Figure 9.11. Panel (a) shows the molecular adsorption sites as a hardsphere model on the Ag(100) surface. The unit cell, as obtained from the SPA-LEED measurements described in Chapter 7, is indicated in green. The molecular packing in the unit cell is compact. Especially along the short unit cell vector, the bright molecules of neighboring molecules are located close to each other and appear to form dimers of symmetry equivalent molecules. Again, please note that the molecules of this hardsphere model are not subject to molecular distortions as they might occur during adsorption on the Ag(100) surface. In addition, the intermolecular interactions, as observed by the hydrogen bond formation or the dimer formation, might lead to additional molecular distortions that were not considered here but might lead to a more favorable molecular packing.

However, as displayed in Figure 9.11 (b), the obtained molecular arrangement explains the topographic contrast observed in the STM data of the small α-phase of HB238-D. Please note that the STM image displayed here is rotated in comparison to the STM image of the small α-phase displayed in Figure 7.3. The *t*Bu-groups of the molecules that are centered in the tetramers are located at the corners of the unit cell, hence, creating the four bright lobes visible in the STM data. Furthermore, the presence of molecular dimers explains the intermediate contrast along the short lattice vectors while the dark areas in the STM image match with the positions of the CN groups.

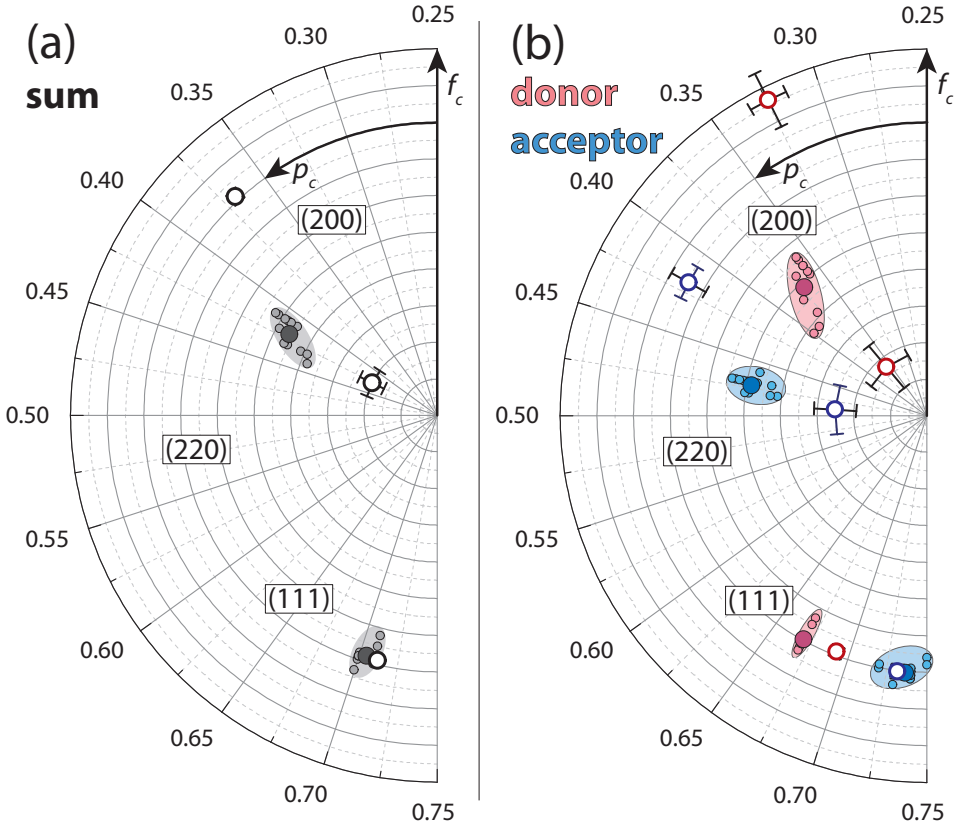

Figure 9.12.: Results of the adsorption site determination of the S atoms of the merocyanine HB238-B in the α-phase on the Ag(100) surface. Presentation and color code as in Figure 9.9, above. Please note that the error bars of the experimental (111) data points are too small to be visible. The respective lateral positions of the S atoms are indicated in Figure 9.13.

9.5. The lateral molecular arrangement in the α-phase

By an equivalent triangulation to that of HB238-D above, the adsorption sites of HB238-B on the Ag(100) surface were determined. The results are summarized in Figures 9.12, 9.13, and 9.14. The color code of the data points is the same as above. Again, the experimentally determined p_c^A and p_c^D values of the (200) Bragg reflection were split to obtain two sets of adsorption heights for the two pairs of nonequivalent molecules per unit cell. This splitting was performed for $f_c^{split} = 1.0$ and resulted in donor adsorption heights $z_{200}^{S_D}$ of 2.61 Å and 2.79 Å. The respective acceptor adsorption heights $z_{200}^{S_A}$ resulted to 2.65 Å and 3.14 Å. The difference $\Delta z_{200}^{S_A}$ is with 0.49 Å larger than for the donor components ($\Delta z_{200}^{S_D} = 0.18$ Å) as the experimental coherent fraction of the acceptor is by 0.22 smaller than the coherent fraction of the donor.

Variation of the adsorption sites led to a good agreement of the calculated p_c values with the experimentally determined values. Variations were found to be largest for the donor components for both Bragg reflections, with values of about $\Delta p_c = 0.05$. In this calculation, even the p_c^A and p_c^D values of the (220) Bragg reflection were reproduced. However, the coherent fractions of the (220) components were observed to be by about $\Delta f_c = 0.32$ higher than the experimental values.

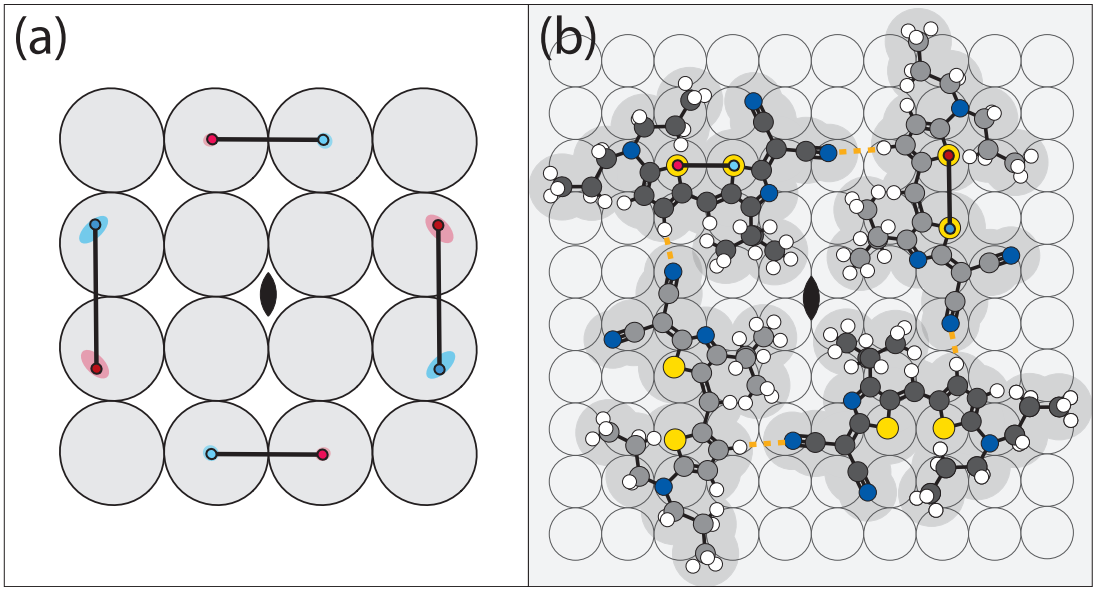

Figure 9.13.: Schematic presentation of the determined S adsorption sites of the merocyanine HB238-B on the Ag(100) surface. Presentation and color code as in Figure 9.9, above.

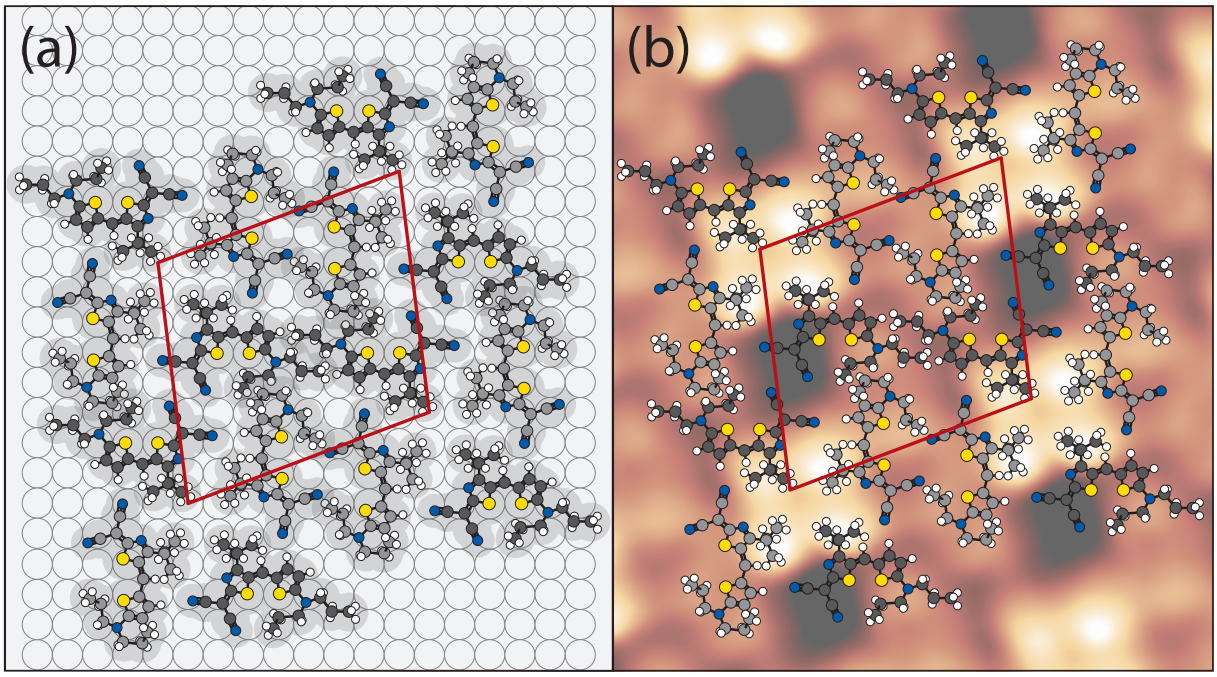

Figure 9.14.: Hardsphere model of the α-phase of HB238-B on the Ag(100) surface (a) and superimposed with a respective STM image (b). The S adsorption sites correspond to the results of the NIXSW analysis. The STM image is imaged and rotated compared to the STM image of the α-phase displayed in Figure 7.3 (300 K, $U_{\mathrm{bias}} = -0.3$ V, $I_{\mathrm{t}} = 5$ pA). Pairs of bright molecules are located along the long vector of the superstructure. Gray shaded areas around the molecules correspond to the full van der Waals radii.

The corresponding adsorption sites are displayed in Figure 9.13. Please note that the orientation of the alkyl side chains (nPr groups) remains arbitrary. Compared to the molecular arrangement of HB238-D in Figure 9.10, the HB238-B molecules are slightly rotated. Here, in the α-phase, the intramolecular axis of the molecules (black solid lines in Figure 9.13 (a)) are oriented nearly parallel to the Ag surface lattice vectors. The difference in the molecular rotation of the molecules in the two phases is about 4°. Due to the off-centered positions of one set of molecules (left and right molecule in Figure 9.13 (a)), the tetramer is slightly elongated in the horizontal direction. The molecular orientations in the α-phase lead to similar distances between the molecules of the tetramer. Stabilizing hydrogen bonds between neighboring molecules are of about 2.9 Å in length and, hence, comparable to the small α-phase.

The unit cell packing of the α-phase is illustrated in Figure 9.14. Again Figure 9.14 (a) displays the hardsphere model on a schematic Ag(100) surface while Figure 9.14 (b) demonstrates the agreement of the hardsphere model with the STM data presented in Chapter 7. Although the structures of the α-phase and the small α-phase seem to be quite similar, the unit cell of the α-phase is larger by 16% (ref. to Chapter 7). Hence, the spacing between the molecules along the longer unit cell vector is larger. However, a dimer formation of the two molecules along this vector, which are displayed in bright colors in Figure 9.14, might still be possible.

9.6. Conclusion

This chapter presents a complete analysis of the molecular adsorption sites of HB238-B and HB238D in the α-phase and the small α-phase, respectively. The adsorption sites of the S atoms were determined by NIXSW. As both structures contain a number of eight S atoms per unit cell, the individual adsorption sites had to be deduced by simulations from the average signal obtained from the measurements.

Experimentally, it could be distinguished between S atoms of the donor and acceptor parts of the merocyanines, i.e., the S atoms in the thiophene ring and the thiazole ring, respectively. This was possible due to the different binding energies of the S atoms in XPS, which are a result of the neighboring electron-donating and withdrawing groups and final state effects in the photoemission process. This binding energy difference was confirmed by the comparison of multilayer and monolayer soft XPS S2p spectra (see Chapter 6).

The models take the intramolecular S S distances determined for the crystal structures and the bond lengths expected for the H-bonds into account. The respective values obtained for the hardsphere models of the monolayer phases result in an intramolecular S S distance between 3 Å and 4 Å. Hence, the observed intramolecular S S distances are larger than the $3.12-3.22$ Å observed for the crystal structures at room temperature (ref. to Table B.1), which indicates a distortion of the molecules in contact with the Ag(100) surface caused by the interfacial interactions and intermolecular interactions.

The length of the hydrogen bonds in the tetramers was found to be about 2.9 Å for the monolayer phases. Respective values in the crystal structures result in 2.56 Å. Hence, the hydrogen bonds are longer and thus, weaker in the monolayer compared to the bulk

crystal structures. Still, STM measurements at domain boundaries revealed the tetramers to be the most stable unit of the structure.

10. The growth of thin KCl layers on the Ag(111) surface

The work of this chapter was published in the Journal of Physical Chemistry Letters 16, 696-702 (2025): "An Atomistic Analysis of the Carpet Growth of KCl Across Step Edges on the Ag(111) Surface" by Anna J. Kny, Adam Sweetman, and Moritz Sokolowski.

A reprint of this publication can be found in Appendix A.3. The author's contribution to the publication included: the measurement of the data, the analysis of the data, the scientific presentation of the data, and the writing and revision of the manuscript.

This chapter investigates the growth of thin KCl(100) layers on the Ag(111) surface. The publication focuses on the carpet growth behavior of the KCl layers, allowing for a seamless growth of KCl domains across monatomic steps of the Ag(111) surface. The following sections review the work of the above-mentioned publication.

10.1. Scientific context

Molecular orbitals in contact with a metal surface hybridize with the electronic states of the underlying metal surface. Hence, studies of electronically decoupled molecules are performed using a dielectric layer between the molecules and the metal surface [117–119]. For investigations of the molecules by STM, the respective dielectric layer should be thin enough to allow electrons to tunnel through [117, 119, 120]. Thus, a dielectric material with a wide band gap is required, which must allow for the controlled growth of closed films with large domains.

These properties are provided by thin alkali halide films. Accordingly, the growth of thin potassium chloride (KCl) films on the Ag(111) surface was studied in the context of the present thesis. These films allow for the study of merocyanine films that are electronically decoupled from the underlying Ag(111) surface. However, as the interfacial interactions between merocyanines and alkali halide films are weak, structural investigations of merocyanines on KCl films require time and are thus part of future investigations.

This work depicts the first investigation of KCl films on a Ag(111) surface. Like alkali halide layers on other metal surfaces [121–124], KCl layers on Ag(111) grow in a (100) orientation. Hence, a lattice mismatch in the form of the lattice geometry and the form of the lattice constants is present, which leads to a *carpet-like* growth mode across monatomic step edges of the Ag(111) surface. The carpet growth is defined as the seamless growth of domains across step edges of the underlying substrate surface that is accompanied by a lifting of the domain in the step region.

The carpet growth allows KCl domains to grow across step edges of the underlying Ag(111) surface and thus to form large domains of several hundred nm in size. This growth mode was already observed for many combinations of alkali halides and metal surfaces [125–129]. However, the exact ion arrangement at the edges of the steps, which compensates for the difference in height between the two terraces, has so far remained unresolved.

The existing model, proposed by Schwennike et al. for NaCl(100) layers on the semiconductor surface Ge(100) [125], uses a continuum description from elasticity theory. In this model, the ionic positions and the ionic interactions with the surface are neglected. However, for metal surfaces, the situation is more complicated. Due to the Smulochowski dipole, metal step edges exhibit local charges [130]. In addition, mirror charges are present at the dielectric/metal interface. The alkali halide ions are expected to interact with these charges, leading to distortions of the ionic layer in the carpet growth region. Thus, continuum models are only coarse approximations of the situations at the step edges. However, knowledge about the ionic arrangement and the growth modes is important to guarantee the aspired film properties. In this context, an atomistic model for the carpet growth over Ag(111) step edges was developed in this work.

10.2. The carpet growth of KCl on the Ag(111) surface

In the present publication, the ionic arrangement in the carpet growth region was analyzed by room-temperature STM measurements for KCl layers of 3 ML thickness. The high atomic resolution of the measurements, necessary for the analysis, was achieved by using Cl^- decorated W-tips [59]. Accordingly, Cl^- ions were displayed as bright protrusions [59].

Due to the Smulochowski dipole, the positive charge on the upper Ag step edge offers preferred adsorption sites for the Cl^- ions. This leads to a growth of the KCl domains with the polar $\langle\bar{1}10\rangle$ lattice lines parallel and perpendicular to the Ag steps. Due to the attractive interactions between the Cl^- ions and the Ag atoms at the upper Ag step edge, a straightening of the overgrown Ag steps occurs, as visible in the STM image of Figure 10.1 (a).

The STM image of Figure 10.1 (a) shows an example of carpet growth across a monatomic Ag step. The width of the carpet region is indicated by a solid line in light blue and equals four KCl unit cells. The carpet region describes the number of strained KCl unit cells in the direction perpendicular to the Ag step, necessary to adapt to the height of the next Ag terrace. On the next Ag terrace, the KCl domain continues seamlessly without lateral shifts, as highlighted by the blue dotted line. For an atomistic analysis of the ionic arrangement in the carpet region, line profiles were measured and analyzed.

In Figure 10.1 (b), the averaged line profile of carpet growth across the monatomic Ag step in Figure 10.1 (a) is displayed in red. It was used to develop a hard sphere model of the ionic arrangement in the carpet region as displayed in Figure 10.1 (b). Please note that the distance (z) between the Ag surface and the KCl layer in the model remains arbitrary. The strain that is induced in the KCl layer in the carpet growth region leads

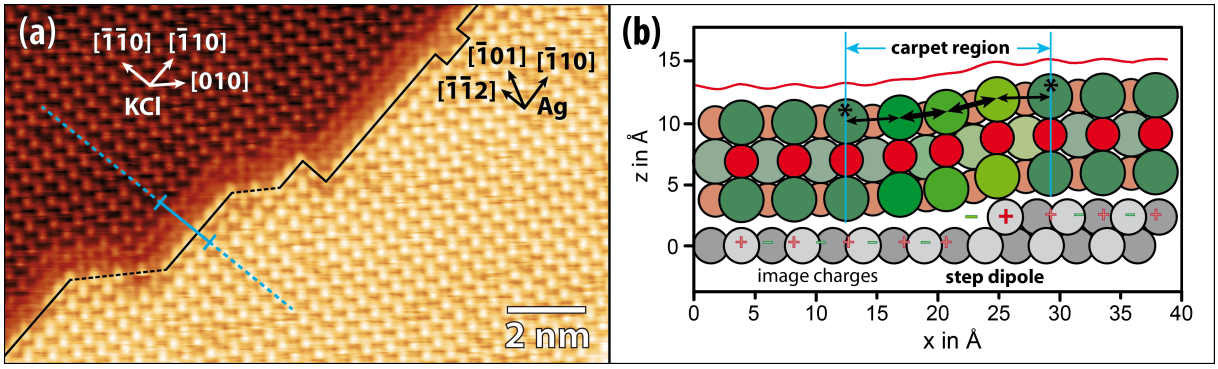

Figure 10.1.: STM image (a) and hard sphere model (b) of the carpet growth across a Ag step of monatomic height on the Ag(111) surface. The Cl^- ions are imaged as bright protrusions. The KCl layer is of 3 ML thickness. The figure is a reduced representation of Figures 1 and 3 from the above-mentioned publication [79]. The carpet width is indicated by a solid line in light blue. The hard sphere model in (b) was developed from an averaged height profile, displayed as a red line, which was measured along the polar KCl $[\bar{1}\,\bar{1}\,0]$, and accordingly the Ag $[\bar{1}\,\bar{1}\,2]$ direction, across the Ag step displayed in (a). Color code: green (Cl^-), red (K^+), gray (Ag). The step dipole (Smulochowski dipole) and the image charges are indicated. Thick and thin black arrows highlight the uneven strain distribution in the carpet region. Thicker arrows indicate a stronger strain. ($U_{bias} = -1.3$ V, $I_t = 0.56$ A)

to a distortion of the KCl lattice. However, as indicated by thick and thin black arrows, the strain in the carpet region is not distributed uniformly across the four KCl unit cells. Here, thick arrows indicate a stronger strain. The unit cell, marked by the upper thick arrow, should be pointed out at this point. This unit cell compensates for about 51%±3% of the height difference (Δz).

Although the lattice distortions are energetically unfavorable, the system gains energy by keeping the carpet region, in which the KCl film is lifted away from the surface, small. Moreover, the strong non-uniform distortion is most likely induced by the attempt of the KCl lattice to adapt to the local charges on the Ag surface, especially to the Smulochowski dipole, but also to the image charges.

For higher Ag steps, a step splitting results from the interactions of the Ag step with the KCl layer. This avoids an additional loss of energy, which would occur for higher Ag steps due to larger carpet widths or stronger lattice distortion. This step splitting is expected to occur during the KCl deposition at a sample temperature of 403 K. It creates micro-terraces with a minimum width of about 13 Å and Ag steps of monatomic height. Hence, carpet growth of KCl on the Ag(111) surface is only observed for monatomic Ag steps.

10.3. Conclusion

As a result of this work, we found that the interactions between the KCl layer and the Ag atoms strongly influence the arrangement at step edges of the Ag(111) surface. In particular, it was found that in contrast to models based on an elasticity theory, the

carpet region is formed by KCl unit cells that are locally distorted.

KCl layers prefer to grow with their polar $\langle\bar{1}10\rangle$ lattice lines parallel to the Ag step edges. This, in combination with the lattice mismatch of KCl and Ag, results in the appearance of carpet growth. KCl deposition at a sample temperature of 403 K leads to a straightening of overgrown Ag step edges along the KCl $\langle\bar{1}10\rangle$ lattice lines, a process which is influenced by attractive interactions of the Cl^- ions and the positive charges at the upper edge of the Ag steps.

In addition, the carpet growth induces a step splitting for Ag steps higher than a monatomic step. This leads to the formation of micro-terraces exhibiting a minimum width of 13 Å. Measurements of the ionic arrangement in the carpet growth regions for monatomic steps and the growth across multiple micro-terraces reveal that this minimum width is required for the carpet growth to proceed. The reason for this is encoded in the number of strained KCl unit cells (width of the carpet region), necessary for the KCl film to adapt to the height of the next terrace. Smaller Ag terraces or higher Ag steps than monatomic ones would induce a much higher strain on the KCl lattice due to the larger height difference which needs to be compensated. In addition, the system would lose interfacial binding energy for an increased width of the carpet region in which the KCl layer is lifted away from the Ag surface. Thus, carpet growth across higher Ag steps or micro-terraces smaller than 13 Å is not observed and the respective Ag steps constitute domain boundaries of KCl.

11. Discussion

This thesis presents a structural analysis of merocyanine monolayers on the Ag(100) surface. The general molecular structure of the investigated merocyanines is displayed in Figure 11.1. The whole series of investigated merocyanines is displayed in Figure 2.4 of Chapter 2. The molecules differ in the length of the alkyl side chains, denoted as R, that are attached to the tertiary amine. Hence, the merocyanines differ in the electron-donating group of the molecules.

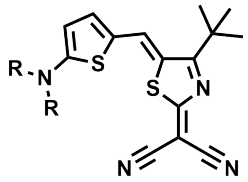

Figure 11.1.: General molecular structure of the investigated merocyanines. R denotes the alkyl side group. For the investigated merocyanines, R equals: *n*Bu (HB238-A), *n*Pr (HB238-B), Et (HB238-C), and Me (HB238-D).

11.1. The electronic structure

As it could be demonstrated by soft XPS data of the monolayer phases, the changes in the length of the alkyl side groups led to only minor changes in the electronic structure of the adsorbed molecules. This could be concluded from the presence of only small chemical shifts ($\Delta E_{\mathrm{bind}}^{\mathrm{S}2p_{3/2}} = 0.08$ eV, $\Delta E_{\mathrm{bind}}^{\mathrm{N}1s} = 0.05$ eV) of the S$2p_{3/2}$ photoemission line and the photoemission line of the N1s acceptor component within the series of investigated merocyanines. Although the inductive effect of the alkyl side chains is influenced by the higher polarizability of longer alkyl side chains [131], the chemical shifts of the donor components in the experimental N1s spectra show that this effect is only minor for alkyl groups with more than two C atoms in a row, i.e., *n*Pr (HB238-B) and *n*Bu (HB238-A) in the case of the investigated merocyanines. Here, from HB238-C to HB238-A, the donor component shifts by only $\Delta E_{\mathrm{bind}}^{\mathrm{N}1s} = 0.03$ eV. Furthermore, the similar binding energies that are obtained for the adsorbed merocyanines indicate similar bonding situations on the Ag(100) surface. Thus, from the similar electronic structures of the adsorbed molecules and the similar binding geometries, it can be concluded that any structural changes of the molecular adsorption sites are presumably related to the lateral sterical demands of the merocyanine molecules in the monolayer phases.

11.2. The primary building units of the monolayer

The circumstance that the molecular packing of the molecules in the monolayer phases can be altered by the length of the alkyl side groups was used to analyze the interplay of interactions of the molecules with the Ag surface and the molecule-molecule interactions in the structures. STM measurements, performed for different bias voltages, revealed that all of the merocyanines form tetramers on the Ag(100) surface as schematically displayed in Figure 11.2, below. These tetramers are the primary building units of all investigated commensurate merocyanine phases. This molecular arrangement is stabilized by hydrogen bonds that are formed between the CN groups and the H atoms, located at the thiophene ring. Hence, each molecule of the tetramer is connected by two hydrogen bonds to two neighboring molecules in the tetramer. Accordingly, the formation of tetramers implies an enantiopure arrangement of the molecules in the tetramers, as otherwise, less hydrogen bonds between neighboring molecules could be formed. As the alkyl side chains of the merocyanines are located on the periphery of the tetramer, pointing away from the center, they influence the lateral sterical demand of the merocyanine tetramers on the surface. The impact of the altered sterical demand was analyzed by SPA-LEED measurements of the merocyanine monolayers and revealed the formation of three distinct phases, formed by different arrangements of the tetramers.

Interestingly, all of the observed phases, i.e., the α-phase, the Q-phase, and the small α-phase, grow commensurate with the Ag(100) surface. The commensurability of the structures was proven by high-resolution scans in which diffraction spots were analyzed, which depict a superimposition of two or more diffraction spots of symmetry equivalent domains. The results, in combination with temperature-dependent measurements, verify the commensurability of the structures. Hence, the lattice parameters reported in Chapter 7 are only affected by the uncertainties of the Ag lattice constant that is at 25°C 4.08621 ± 0.00016 Å [74–76]. The SPA-LEED results also revealed the existence of four symmetry equivalent domains, i.e., mirror and rotational domains, on the Ag(100) surface. The information about the unit cell orientations to the underlying Ag surface constitutes one of the requirements for the later structure model development from the NIXSW data.

From the size of the unit cell and a unit cell content of four merocyanine molecules, it could be deduced that the respective footprints of the merocyanines decrease from 16.75 Ag atoms per molecule in the α-phase to 16 Ag atoms per molecule in the Q-phase and at least 14.5 Ag atoms per molecule in the small α-phase. The altered sterical demand of the tetramers causes the tetramers to adsorb on the next equivalent adsorption site on the surface to maintain the stability of the structure. This behavior led to the main question addressed in this thesis, namely, the reasons for the commensurate growth of the merocyanines regardless of the complex tetramer formation on the surface.

11.3. The molecular adsorption sites

The question about the commensurability of the structure and thus, about the molecular adsorption sites, was answered by NIXSW measurements. This was necessary, as STM measurements provide only a rough estimation of the molecular arrangement in the unit cells.

However, due to the large unit cell that includes a total number of four merocyanine molecules, the experimental S1s, N1s, and C1s photoemission lines denote average signals of 8 S atoms, 16 N atoms, and $68-92$ C atoms per unit cell. Accordingly, the arrangement of the molecules in the unit cell was investigated by photoemission of the S1s orbital. This is valid as the 2 S atoms of each molecule are sufficient to describe the lateral orientation of the molecules in the monolayer. In addition, photoemission of the S1s orbitals has the advantage of a higher photoemission yield compared to the C1s or N1s orbitals, as the binding energy of the S1s orbital is with 2472.0 ± 0.4 eV [74, 132] closer to the used Bragg energies of the (200), (111), and (220) Bragg reflections.

For the NIXSW measurements, the focus was set on the determination of the adsorption sites of the merocyanines in the α-phase and the small α-phase. As the merocyanines HB238-A and HB238-B both form the α-phase, it was expected that both molecules occupy the same adsorption sites on the Ag(100) surface. Hence, HB238-B was analyzed exemplarily for the α-phase. As a representative for the small α-phase, the HB238-D monolayers were measured. The presence of the correct phase was safeguarded by LEED data.

As already indicated above, the individual S adsorption sites had to be deduced from the average photoemission signal of the 8 S atoms per unit cell that was obtained from the measurements. Experimentally, it was possible to distinguish between S atoms of the donor and acceptor parts of the merocyanines, i.e., the S atoms in the thiophene ring and the thiazole ring, respectively. This was done by exploiting the different binding energies of the S atoms in the XPS spectra, which result from the neighboring electron-donating and withdrawing groups. This binding energy difference was already observed for the respective S2p spectra (see Chapter 7). However, there it is not resolved and can only be deduced from the broad peak shape of the S2p photoemission line of the merocyanine monolayer. The respective FWHM is 0.66 eV for the α-phase (HB238-B) and 0.63 eV for the small α-phase (HB238-D). The binding energy difference of the acceptor and donor components that were fitted to the S2p photoemission line results in only $\Delta E_{\mathrm{bind}} = 0.26 \pm 0.10$ eV for HB238-B and 0.28 ± 0.10 eV for HB238-D.

Accordingly, the same behavior was observed for the S1s spectra, albeit with a different binding energy difference between the donor and acceptor components. For the α-phase (HB238-B), the binding energy difference amounts to $\Delta E_{\mathrm{bind}} = 0.37 \pm 0.10$ eV and for the small α-phase (HB238-D) to $\Delta E_{\mathrm{bind}} = 0.52 \pm 0.10$ eV. The uncertainty in the resulting Argand vectors due to the unresolved binding energy difference of the donor and acceptor components is in a range of $\Delta p_{\mathrm{c}} = 0.01$ and $\Delta f_{\mathrm{c}} = 0.04$. Please note that the errors of p_{c} and f_{c} given in the summarizing tables, e.g., Table 8.4 refer only to those of the fit of the photoemission yield curves and do not include the systematic error related to the binding energy difference of the components. These errors specifically indicate the fit reliability.

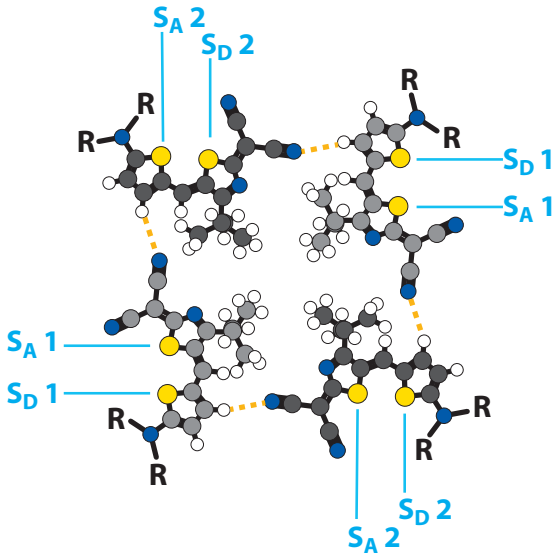

Figure 11.2.: Molecular structure of the merocyanine tetramer with indicated, symmetrically nonequivalent S atoms. For the electron-donating group of the merocyanine, these are denoted as S_D 1 and 2. Respectively, the S atoms of the electron accepting group are denoted as S_A 1 and 2. Color code: yellow (S atoms), blue (N atoms), gray (C atoms), white (H atoms), R (alkyl side groups). Orange dotted lines indicate the hydrogen bonds that lead to the formation of the enantiopure tetramers. Symmetry nonequivalent molecules are indicated by brighter and darker colors.

For the determination of the molecular adsorption sites, the C_2 symmetry of the structures was taken into account. The presence of the C_2 symmetry, i.e., the presence of two-fold rotation axes, in combination with the presence of molecular tetramers, indicates the existence of two pairs of symmetry nonequivalent molecules per tetramer, as indicated in Figure 11.2 by brighter and darker colors of the molecules. These symmetry nonequivalent molecules have different molecular adsorption sites. Thus, two nonequivalent donor S_D and two nonequivalent acceptor S_A adsorption sites contribute to the donor and acceptor photoemission lines obtained for each Bragg reflection. In Figure 11.2, these are denoted as S_D 1, S_D 2 and S_A 1, S_A 2. Due to the different adsorption sites, the respective S atoms, e.g., S_D 1 and S_D 2, exhibit different adsorption distances to the respective (111) and (220) Bragg planes. Thus, the experimentally obtained coherent fractions are decreased in contrast to the situation of only one donor and one acceptor adsorption site. This decrease in the coherent fraction was needed to explain the experimentally obtained Argand vectors.

To distinguish between the different adsorption sites of the nonequivalent S_D and S_A atoms, the donor and acceptor Argand vectors, i.e., F_c^{sum}, of the (200) Bragg reflection were split into two Argand vectors ($F_c^{S_D1}$, $F_c^{S_D2}$) under the assumption that each component itself has a higher vertical order (coherent fraction) compared to the average value. That high coherent fractions of the individual components are very likely to be the case has been indicated by Figure 9.7 of Chapter 9 for the example of ideal atop adsorption sites of the S atoms. Accordingly, the (200) donor and acceptor components were split for a

theoretical f_c value of 1. Because the real value of the coherent fraction will most likely deviate from 1, the adsorption heights of the S atoms resulting from the NIXSW analysis might be over- and underestimated, respectively, by up to 0.1 Å.

As all of the investigated merocyanines form four symmetry equivalent domains on the Ag(100) surface, these had to be taken into account for the Argand vector calculation for the (111) and (220) Bragg reflections. Equivalent to the existence of four domains, the Argand vectors were calculated as an average value for the adsorption of the S atoms with respect to four symmetry equivalent (111) and (220) Bragg planes, respectively. The calculations considered the donor and acceptor adsorption sites of the S atoms to be independent from each other, taking only the C_2 symmetry of the structure into account. The adsorption sites were determined from systematic lateral variations of the S positions starting from the atop positions on the Ag atoms, covering a broad range of adsorption sites and adsorption site combinations. These variations were performed manually. However, the calculations showed that, due to the four molecules per unit cell and the existence of four symmetry equivalent domains, the calculated Argand vectors are quite sensitive to lateral variations in the S positions. For the NIXSW data evaluation of HB238-B and HB238-D, the maximum difference of the lateral positions that were reasonable to explain the experimental data, was 34% and 11% of the Ag lattice constant, respectively (see Figures 9.13 and 9.10 of Chapter 9).

Including all four molecules in the calculation, it was not possible to fit one molecular arrangement perfectly to the experimental Argand vectors and to explain the other experimental data in parallel. Accordingly, regions of acceptable deviations were defined in the Argand diagrams. The finally resulting adsorption sites were defined as the average values of the lateral positions that correspond to the respective Argand vectors within these regions. The author of this thesis is aware that more precise results of the adsorption sites would possibly be obtained with an automated search of the S adsorption sites. However, due to the complexity of the structure, i.e., a required lateral variation of the 4 different S atoms in the structure (S_D 1, S_D 2, S_A 1, S_A 2) and a required agreement of the results with the other experimental data, e.g., those from STM and LEED, the development of such a routine is challenging and was not achievable within the time frame of this work.

The resulting adsorption sites were paired under the requirement of plausible intramolecular S S distances and hydrogen bonds. The reference data, used for defining the plausible bond lengths, were the corresponding distances from the crystal structures. These were also measured as part of this thesis and are documented in Appendix B. Further, the pairing was controlled and optimized by the feedback obtained from the structural models, which had to agree with the contrasts observed in the STM data.

The developed structure models of the small α-phase of HB238-D (a) and the α-phase of HB238-B (b) are again illustrated in Figure 11.3. At first glance, it is already apparent that the molecular packing in both phases is quite condensed. This fact made it possible to identify the correct enantiomer for the displayed domain because extensive overlaps of neighboring tetramers had to be avoided, as they would cause a loss of interfacial interactions. However, even though the α-phase of HB238-B exhibits the larger unit cell, the longer alkyl side chains lead to a decreased amount of uncovered Ag surface per unit cell compared to the small α-phase of HB238-D. This becomes especially true for the

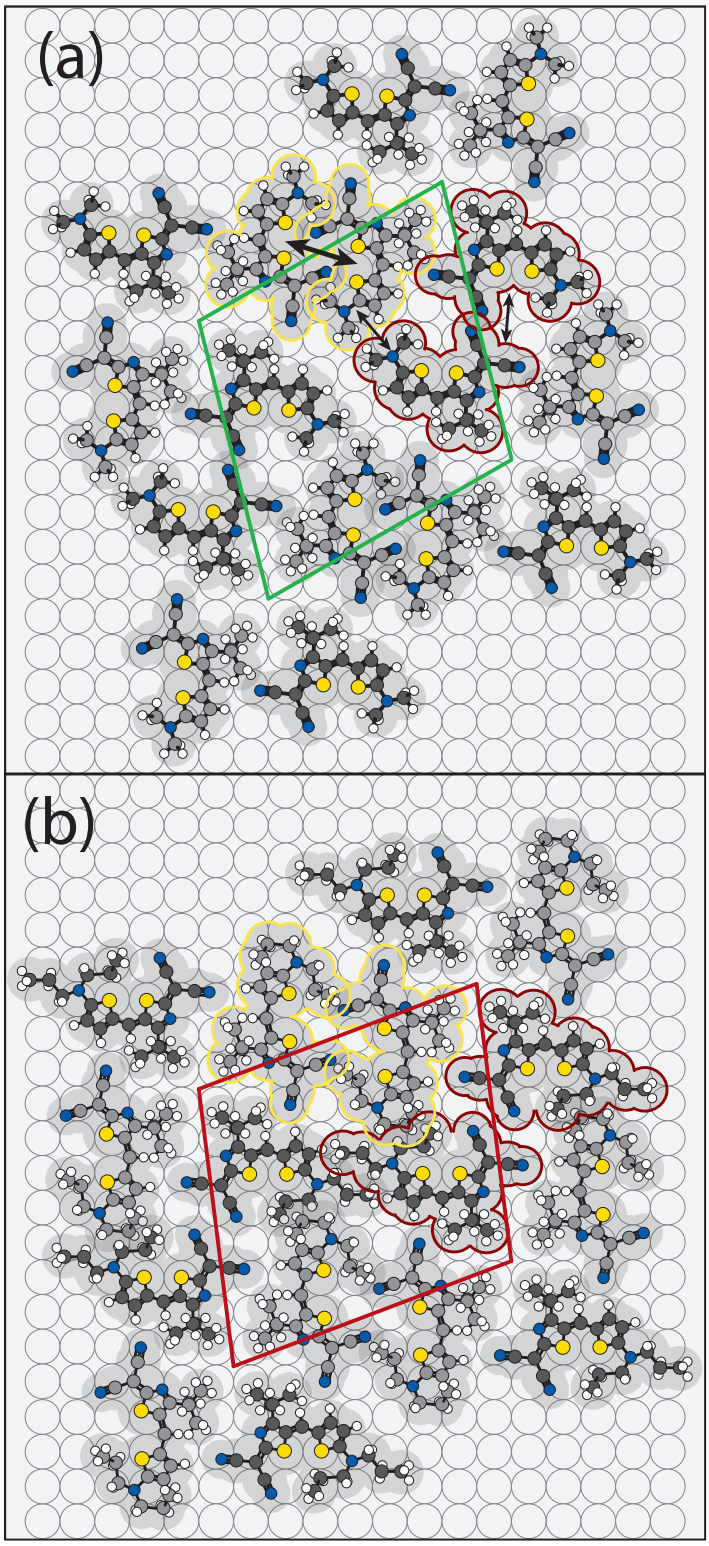

Figure 11.3.: Hard-sphere models of the small α-phase of HB238-D and the α-phase of HB238-B. Models were developed from the experimental data and are identical to the models displayed in Figures 9.14 and 9.11. Color code as in Figure 11.2, above. Molecules highlighted by a red or yellow frame are used to explain the interactions between the tetramers. Please note that the structure model of the α-phase describes a mirror domain compared to the HB238-A structures displayed in Chapter 6. Black arrows in (a) are described in the text. In (a), pairs of bright, yellow-framed molecules are located along the short superstructure lattice vector; in (b), these are located along the long superstructure lattice vector. Gray shaded areas correspond to the full van der Waals radii of the molecules.

region in the center of the unit cell, where the alkyl chains of four molecules come close to each other, stabilizing the structure by van der Waals interactions. Please note that the experimental results do not provide information about the orientation of the alkyl side chains. Thus, the orientations indicated in the structural models only show a plausible possibility that was chosen under steric aspects.

In both structure models, the adsorption sites of the S atoms are found to be either close to the atop positions of the Ag atoms or between the atop positions and the bridge positions. A detailed discussion of these adsorption sites will follow below. The two symmetry nonequivalent molecules per unit cell are, according to the experimental data, located at different adsorption sites. In the structure models, these are visible as bright and dark molecules. Apparently, as indicated by the molecules highlighted in yellow and red, the molecular arrangements of the structures suggest that the interactions between the tetramers might be more or less the same for both structures.

In the molecular arrangement derived for HB238-D (smaller alkyl side chains (Me groups)), the red highlighted molecules can mainly interact with the molecules of the neighboring tetramer by van der Waals interactions. These are exemplarily indicated in a simplified manner in Figure 11.3 (a) by thin black arrows. Thus, the intermolecular interactions between the two dark, red highlighted molecules are most likely much weaker than the hydrogen bonds that stabilize the tetramers. For the red molecules, adsorption sites very close to the atop positions are observed. The observed small deviations from the atop positions might be due to repulsive interactions that might occur between the CN groups of neighboring red molecules (also marked by a thin black arrow). This is supported by the fact that these deviations vanish for the α-phase (see the red highlighted molecules in Figure 11.3 (b)), in which the distance between the CN groups is larger.

Due to the molecular arrangement of the yellow molecules, their intermolecular interactions are expected to be stronger than the interactions between the red molecules. This can be deduced from the close contact of the donor and acceptor groups of the yellow molecules, indicating the formation of additional hydrogen bonds and holds for both phases. In Figure 11.3 (a), these possibly strong intermolecular interactions are indicated by a thick black arrow between the yellow molecules. The S atoms of these molecules were found to exhibit adsorption sites that deviate strongly from the atop positions on the Ag atoms, thus altering the intramolecular S S distance. Instead, the S atoms are shifted towards the bridge positions. These lateral shifts of the molecules might be a result of the strong attractive intermolecular interactions between the yellow molecules. Accordingly, the close contact of the yellow molecules might lead to an additional dimer formation. For the α-phase, displayed in Figure 11.3 (b), the intermolecular interactions between the yellow molecules can be expected to be weaker (compared to Figure 11.3 (a)) due to the sterical demand of the *n*Pr-groups of HB238-B. However, the distortion of the molecules that is noticeable in an increased intramolecular S S distances might also be driven by the hydrogen bonds between the molecules of the tetramer.

Accordingly, the lengths of the hydrogen bonds observed for the tetramers of the α-phase are close to the bond lengths observed for similar structural motifs of the crystal structures. The values obtained from the hard sphere models result in 3.0 Å (+18% deviation) and 2.4 Å (−6% deviation). For the small α-phase, the respective values result

in 3.2 Å (+25% deviation) and 2.3 Å (−10% deviation from 2.56 Å). For the values of the crystal structures, please refer to Table B.1. However, the determined hydrogen bond lengths only serve as a coarse reference, as changes in the ring structure were not considered in the structural models. Hence, the estimated errors of the hydrogen bond lengths determined from the structural models of the monolayer are in the range of 0.5 Å.

Only the S S distances were determined as absolute values as they are obtained from the NIXSW analysis. The S S distances result for the small α-phase in 3.0 Å (−4% deviation) and 2.9 Å (−7% deviation from 3.13 Å). For the α-phase, 3.0 Å (−4% deviation from 3.12 Å) was found for the S S distance of the red molecules, while the yellow molecules were observed to be distorted with an S S distance of 3.9 Å (+25% deviation).

11.4. The molecular arrangement in the Q-phase

At this stage, the reader might ask about the molecular arrangement in the Q-phase, which was experimentally observed as the only monolayer phase formed by HB238-C and the thermodynamically more stable phase of HB238-D. Transferring the binding motifs and adsorption sites found for the other two phases to the Q-phase, yields the molecular arrangement displayed in Figure 11.4. Different from the α-phase and the small α-phase, the tetramers must exhibit a four-fold symmetry as the Q-phase exhibits a $P4$ space group. Accordingly, all molecules in the Q-phase are symmetrically equivalent and occupy the same adsorption sites on the Ag(100) surface. However, for reasons of comparability with the other structural models, the molecules in Figure 11.4 are also displayed by bright and dark colors.

Please note that for obtaining this model, the adsorption sites of the dark molecules are the same as in the small α-phase. The fact that only the lateral positions of the bright molecules were adjusted is based on the following considerations, as the missing (220) data for this phase did not allow for a triangulation: For the (111) Bragg reflection an adsorption distance of $z_{111}^{\mathrm{A+D}} = 1.63 \pm 0.01$ Å with a coherent fraction of $f_{\mathrm{c}} = 0.61 \pm 0.01$ was obtained. Accordingly, the difference to the data of the α-phase and the small α-phase is small (max. $\Delta f_{\mathrm{c}} = 0.08$ and $\Delta z_{111}^{\mathrm{A+D}} = 0.05$ Å). The same holds for the data measured at the (200) Bragg reflection. However, here, the Q-phase of HB238-C is found to exhibit an adsorption distance to the extended (200) Bragg plane that is by $\Delta z_{200}^{\mathrm{A+D}} = 0.09$ Å larger in comparison to the other two phases. In the α-phase and the small α-phase, larger adsorption sites were found for S atoms located at the atop positions of the Ag atoms. Hence, the larger $z_{200}^{\mathrm{A+D}}$ indicates that, in the Q-phase, the S atoms of all molecules are located close to the atop positions. Accordingly, the bright molecules, which were shifted towards the bridge positions for the other phases, were placed on the same adsorption sites as the dark molecules for the structure model in Figure 11.4.

This molecular arrangement explains why the Q-phase is observed to be the more stable phase of HB238-D. Comparable to the small α-phase of HB238-D, the yellow-framed molecules are located such that they can form a hydrogen-bonded dimer. However, as all molecules in the Q-phase are structurally equivalent, the same is observed for the red molecules, making this structure more stable compared to the small α-phase. In addition, the molecular packing in the Q-phase leaves less Ag surface uncovered, which

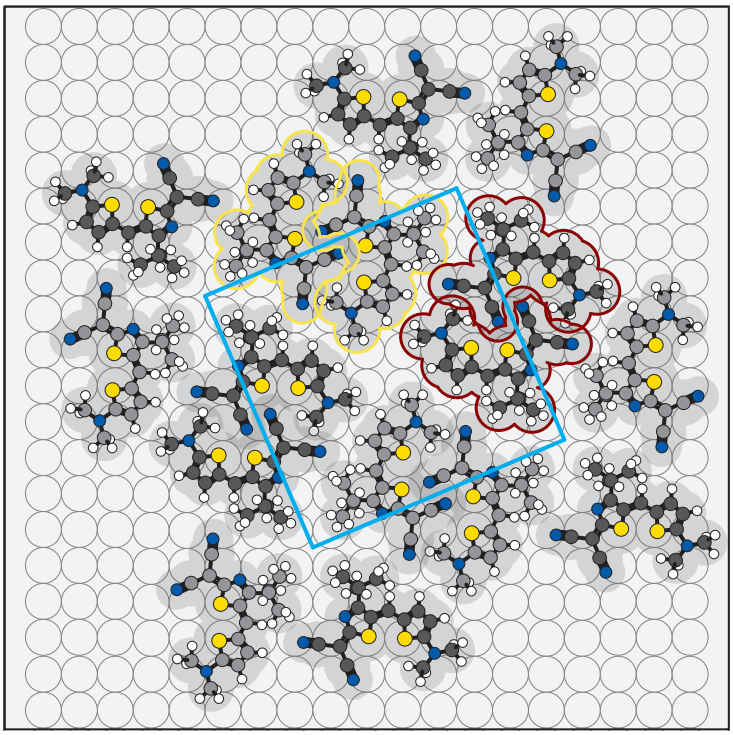

Figure 11.4.: Hard-sphere model of the Q-phase. The model was developed in agreement with the NIXSW data measured for HB238-C and the (200) and (111) Bragg reflections and the structural models developed for the small α-phase and the α-phase (see Figure 11.3). Although the same color coding was used as in Figure 11.3, the bright and dark molecules of the Q-phase are symmetry equivalent, hence, occupying the same adsorption sites on the Ag(100) surface. This is necessary to fulfill the C_4 symmetry of the $P4$ space group. This structural model was drawn for HB238-D to provide a better comparison to the structural models above. Please be reminded that the Q-phase is the more stable phase formed by HB238-D.

additionally increases layer stability by an increase of the van der Waals interactions. Still, STM measurements at domain boundaries revealed the tetramers to be the most stable building unit of the structure, as they showed no fragments of tetramers at the domain edges.

11.5. S adsorption sites of other organic molecules

Let us now come back to the discussion of the S adsorption sites. For the merocyanine structures, the S atoms located in the thiophene ring (donor component) and the S atom located in the thiazole ring (acceptor component) were found to adsorb close to atop sites of the underlying Ag surface. For laterally distorted molecules, a shift of the S adsorption sites from the atop sites towards the bridge positions is observed. The adsorption heights of the S atoms and hence the Ag-S distances were determined to be in a range between 2.5 Å and 3.3 Å. Accordingly, the Ag-S distances are by $6-29\%$ shorter than the sum of the van der Waals radii of Ag (1.7 Å) and S (1.8 Å), which is 3.5 Å [108]. This indicates that the bonding of the merocyanines in the monolayer has a chemisorptive character. However, for chemisorptive and hence localized Ag-S bonds, 2.5 Å to 3.3 Å appears to be

a broad spectrum of Ag-S binding distances. The explanation for this is possibly given by the correlation of the Ag-S distances with the adsorption sites of the S atoms determined by NIXSW.

For the example of the small α-phase (see Fig. 11.3), S atoms of red molecules that are located close to the atop positions were found to adsorb in larger Ag-S distances (i.e., 2.9 Å and 3.1 Å) than the yellow-framed distorted molecules (i.e., 2.5 Å and 2.6 Å). Due to the larger Ag-S distance for S atoms at the atop positions, it can be concluded that these S atoms bind more weakly to the Ag surface than the S atoms of the distorted molecules that sit between the atop and bridge positions and exhibit smaller Ag-S distances. If those values are compared to the literature, the following is found. Even the binding distances obtained for the S adsorption at the Ag atop sites are smaller than the binding distances of the weakly chemisorbed end-capped quarterthiophene (EC4T) for which Ag-S distances of 3.16 Å were observed [115]. As the S atoms of EC4T also adsorb at atop positions of the Ag atoms [115], however, on the less reactive Ag(111) surface, the adsorption distances are comparable and indicate that the merocyanines are more strongly chemisorbed than EC4T. In case of the atop-bridge S atoms of the merocyanines, the even smaller adsorption distances indicate a much stronger interfacial interaction that is definitely of chemisorptive nature. Covalent Ag-S bonds as present in the bulk structure of Ag_2S exhibit bond lengths of 2.5 to 2.7 Å [133] and are, hence, in the same range.

The reason that stronger Ag-S bonds are observed for those merocyanine molecules in the structures that are stronger distorted by intermolecular interactions might be found in exactly this detail. If the molecules are distorted, the π-system is weakened, which reduces the ability of intramolecular charge transport. Accordingly, the surface bonding of these molecules might get more pronounced to compensate for partial charges. The strong bonding of the S atoms close to the bridge sites would also explain why a dissociation of the merocyanine molecules in the monolayer is concluded from TPD experiments (see Appendix D). This idea is supported by the preferred adsorption of molecular S (S_2) at the higher coordinated adsorption sites of coinage metal surfaces [134, 135].

12. Summary and Outlook

The goal of the present thesis was to develop an understanding of the structure formation of merocyanine layers at a metal interface. This was achieved by systematic measurements studying the monolayer formation of a series of four structurally related, prototypical merocyanines. The general molecular structures of the merocyanines are displayed in Figure 12.1, which is a reprint of Figure 7.1 of Chapter 7. Here, R denotes the alkyl side chains that were altered in length, ranging from Me groups (HB238-D) to *n*Bu groups (HB238-A). As the metal substrate, the Ag(100) surface was chosen, a non-reconstructed surface of intermediate reactivity that limits the number of possible symmetry equivalent domains to four.

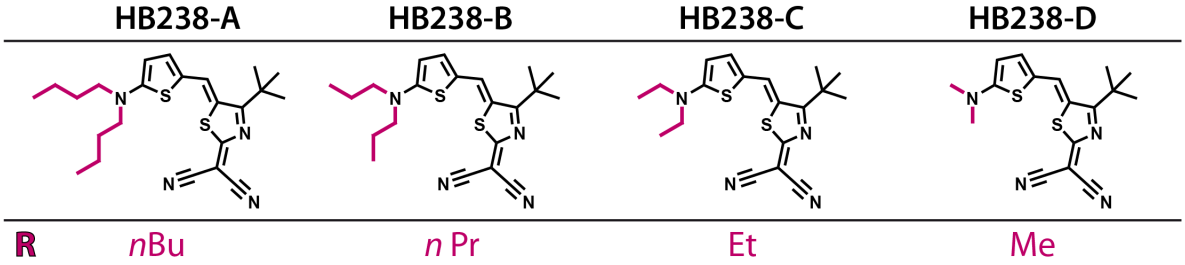

Figure 12.1.: Molecular structures of the merocyanines investigated in this thesis. R denotes the alkyl side chains that were varied symmetrically from Me groups to *n*Bu groups. Reprint of Figure 7.1 of Chapter 7.

The molecular arrangement in the monolayer is dependent on the interplay between the interfacial and the intermolecular interactions. Thus, both kinds of interactions were experimentally investigated. STM and SPA-LEED measurements provided information about the unit cell size, the unit cell orientation with respect to the Ag(100) surface, and first information about the molecular arrangement. XPS and UPS measurements for monolayers and multilayers delivered insights into the changes in the electronic structure of the molecules in contact with the Ag surface. The data set was completed by NIXSW measurements that determined exemplarily the adsorption height of HB238-A (R: *n*Bu) from the Ag(100) surface. Furthermore, for HB238-B (R: *n*Pr) and HB238-D (R: Me), the adsorption sites of the S atoms, and through this also the lateral arrangement of the molecules, were investigated.

Due to the different alkyl side chains, the investigated merocyanines exhibit different sterical demands and footprints on the Ag(100) surface. The different sterical demand causes the formation of three different phases. All of these phases grow commensurate with the underlying Ag(100) surface. Their structural information can be described as follows:

- **α-phase:**
  The α-phase is formed by the merocyanines HB238-A and HB238-B, respectively.
  Unit cell parameters: $b_1 = 23.30$ Å, $b_2 = 24.69$ Å, $\gamma = 103.43°$, $Z = 4$
  Space group: $P2$
  Number of domains: 4

- ***Q*-phase:**
  The Q-phase is formed by the merocyanines HB238-C and HB238-D, respectively.
  Unit cell parameters: $b_1 = 22.00$ Å, $b_2 = 22.00$ Å, $\gamma = 90°$, $Z = 4$
  Space group: $P4$
  Number of domains: 2

- **small α-phase:**
  The small α-phase is the thermodynamically less stable phase of the merocyanine HB238-D.
  Unit cell parameters: $b_1 = 23.82$ Å, $b_2 = 23.29$ Å, $\gamma = 105.71°$, $Z = 4$
  Space group: $P2$
  Number of domains: 4

The molecular arrangement in the three phases is similar and dominated by the formation of tetramers as the primary building blocks. These tetramers are enantiopure. However, tetramers of the other enantiomer are found in the respective mirror domains. The tetramers are formed by hydrogen bonds between four molecules that are adsorbed in face-on orientation. To be more precise, the hydrogen bonds are formed between the CN groups and the hydrogen atoms located on the neighboring molecule as indicated in Figure 12.2. These hydrogen bonds are comparable to those of the binding motifs in the bulk structures. In the α-phase of HB238-B and the small α-phase of HB238-D, the lengths of the hydrogen bonds in the tertramers are in a range of 2.3 to 3.2 Å (±0.5) Å (d(H$\cdots$N)). Comparison of these values to the reported values in literature indicates that these hydrogen bonds are likely weak, as the typical range of strong hydrogen bonds is $1.6 - 2.5$ Å [136].

Due to intermolecular interactions with the molecules of the neighboring tetramers, the tetramers of the α-phase and the small α-phase are slightly distorted and exhibit a C_2 instead of a C_4 symmetry. Accordingly, the molecules, indicated in Figure 12.2 by bright and dark colors, occupy different adsorption sites on the Ag(100) surface. For the Q-phase, the C_4 symmetry of the tetramer is maintained, and all molecules of the tetramers occupy the same adsorption site.

These adsorption sites of the investigated merocyanines are significantly determined by the Ag-S bonds. Laterally, the two S atoms prefer to adsorb at atop positions of the Ag atoms. Intermolecular interactions with the neighboring molecules lead to molecular distortions noticeable in intramolecular S S distances that are thus at most 31 % larger than the reference distances obtained from the crystal structures. The respective S adsorption sites of the distorted molecules are shifted symmetrically away from the atop positions in the direction of the bridge positions by a distance of 0.93 ± 0.02 Å (α-phase) and 0.70 ± 0.04 Å (small α-phase), respectively.

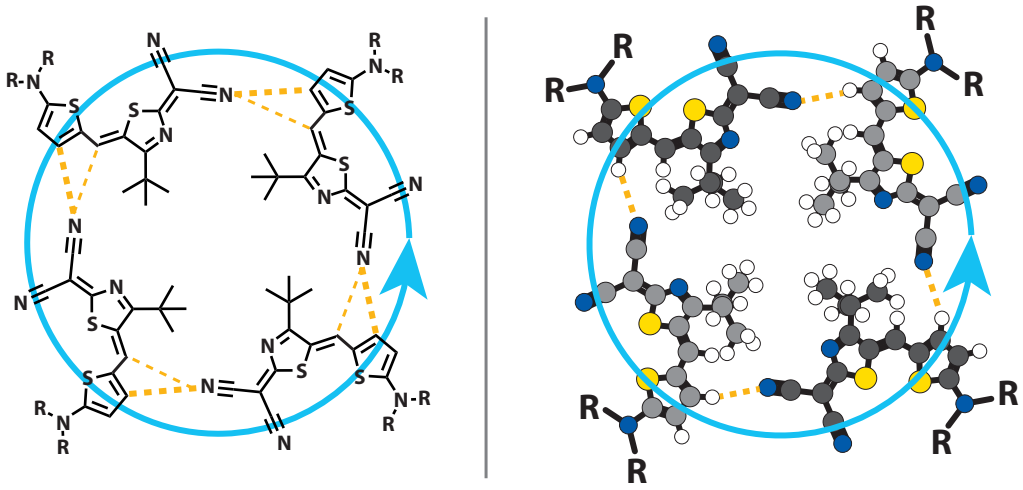

Figure 12.2.: Structure model of the tetramers (L enantiomer) formed as primary building units of the three merocyanine phases mentioned above. R denotes the alkyl side chains of different lengths. In the hard-sphere model on the right side, bright and dark colors indicate molecules that adsorb, in the case of the α-phase and the small α-phase, on different adsorption sites on the Ag(100) surface. Thus, for these phases, the tetramer exhibits a C_2 symmetry. Presumably, stronger and weaker hydrogen bonds are indicated by thick and thin orange dotted lines. Please note that only the stronger (thick) hydrogen bonds are discussed in this thesis. The blue cycle indicates the handedness of the tetramer.

The adsorption height of the S atoms, and hence the Ag-S distance, was determined to be smaller for the atop-bridge S atoms ($2.5-2.7$ Å) than for the atop S atoms ($2.8-3.1$ Å). These Ag-S distances are far below the sum of the Ag and S van der Waals radii (3.5 Å) and are in the range of the covalent Ag-S bonds ($2.5-2.7$ Å in Ag_2S [133]). Consequently, the strong Ag-S bonding is one of the main structure-determining bonding motifs of the here investigated merocyanine structures.

Between the tetramers, the molecules interact by van der Waals interactions and by further hydrogen bonds that are, however, considered to be weaker than the hydrogen bonds stabilizing the tetramers. Still, these hydrogen bonds between the tetramers are apparently strong enough to induce the above-mentioned molecular distortions, resulting in the stretched S S distances. These interactions between the tetramers result in an enantiopure tetramer arrangement and, further, in large domains. The arrangement of the tetramers with respect to each other can be altered by the length of the alkyl side chains, as already mentioned above, leading to the observation of the three distinct phases.

Let us now conclude the results of the present thesis. This thesis addressed the question of the structure-determining interactions, interfacial and intermolecular, of the investigated merocyanines on the Ag(100) surface. The results can be summarized as follows:

1. The strong interfacial interactions of the S atoms with the Ag surface are of covalent character and determine the face-on orientation of the molecules in the monolayer and the preferred adsorption sites. The Ag-S bonds are responsible for the commensurate growth of the investigated phases.

2. Strong intermolecular interactions, i.e., hydrogen bonds between the molecules, lead to the formation of enantiopure tetramers as primary building units of the structures.

3. Additional intermolecular interactions, given by additional hydrogen bonds and van der Waals interactions, lead to the observed enantiopure tetramer arrangement forming large ordered and commensurate domains.

Accordingly, the strong interfacial interactions of the S atoms and the hydrogen bond formation between the molecules are essential for the present merocyanine monolayer structures. This knowledge might be used in further studies to modify the molecular packing for tuning the layer properties, e.g., the charge-conducting behavior or the resulting optical properties.

Furthermore, the monolayer formation of merocyanines on dielectric layers such as KCl could be investigated. As thin KCl layers are sufficient to decouple the molecules from the underlying metal surface [117–119], they would allow for measuring, e.g., absorption and fluorescence spectra of the monolayers in dependence on the molecular arrangement. However, the results of this thesis strongly indicate that the presumably much weaker interfacial interactions between the merocyanines and the KCl layer are not sufficient for the formation of ordered merocyanine layers.

A. Publications

A.1. "Increasing the scan speed in high resolution, low energy electron diffraction measurements by presetting the gate time"

by Anna J. Kny, Moritz Sokolowski, and Peter Kury.

The research article is published in *Review of Scientific Instruments* 94, 064707 (2023).

Review of Scientific Instruments ARTICLE scitation.org/journal/rsi

Increasing the scan speed in high resolution, low energy electron diffraction measurements by presetting the gate time

Cite as: Rev. Sci. Instrum. **94**, 064707 (2023); doi: 1 0.1 063/5.01 37991
Submitted: 7 December 2022 • Accepted: 1 0 May 2023 •
Published Online: 9 June 2023

Anna J. Kny,[1] Moritz Sokolowski,[1,a)] and Peter Kury[2]

AFFILIATIONS

[1] Clausius-Institut für Physikalische und Theoretische Chemie, Universität Bonn, Wegelerstr. 12, 53115 Bonn, Germany
[2] out-of-the-box systems GmbH, Breddebuschhang 5c, 45257 Essen, Germany

[a)] Author to whom correspondence should be addressed: sokolowski@pc.uni-bonn.de. Telephone: +49 (0) 228/73-2507. Fax: +49 (0) 228/73-9358

ABSTRACT

We report on a speed-up data acquisition routine for recording intensities in reciprocal space (*k*-space) with increased scan speed by a single point detector. It is designed for recording low energy electron diffraction (LEED) data with high resolution by a spot profile analysis LEED instrument. It counteracts the problem of long acquisition times that are encountered when larger areas in the reciprocal space are scanned. It exploits the fact that in typical LEED images of ordered surfaces, more than 90% of the data points in *k*-space belong to the low-intense background, which is often not of interest. Only about 10% of the data points are related to the relevant diffraction features, namely, the LEED spots. Often it is not necessary to measure the background with the same statistical significance as measuring those points that contain information. The data points belonging to the LEED spots can be discriminated from those of the background by their higher intensities. An acquisition routine that sets an increased gate time for the counting in response to higher intensities thus safeguards good statistics for data points of the LEED spots and saves measurement time when recording data points of the background with small gate times. For typical LEED images, a reduction of the total acquisition time by a factor of about 10 is obtained. We give examples of one- and two-dimensional scans from current experiments, recorded with and without the speed-up routine. We further discuss how the routine supports the measurement of energy dependent reciprocal space maps.

INTRODUCTION

Low energy electron diffraction (LEED) is a widely applied method for the determination of the crystallographic properties of surfaces.[1–5] The large majority of LEED instruments are based on a spherical phosphorescent screen that is used for the detection of the electron diffraction pattern.[4,6] Today, the image on the screen is usually recorded by a camera located on the rear side of the transparent screen (back view LEED). In the following, we name this version of the instrument "optical LEED." These LEED instruments serve for the routine control of surface structures in surface science experiments. In addition, they are used for recording the intensities of LEED diffraction spots as a function of the electron energy for a quantitative determination of the atomic coordinates at surfaces.[7] A major advantage of optical LEED instruments is that they allow very fast data acquisition, because the entire diffraction image is recorded at once. One of their disadvantages, among others, is that the lateral resolution in the diffraction space (*k*-space) is rather limited.

For obtaining high resolution in *k*-space, a specialized LEED instrument, called spot profile analysis LEED (SPA-LEED), was developed by Henzler and co-workers.[8] For a general overview on the construction of the SPA-LEED, we refer the reader to the review by Horn von-Hoegen.[9] This type of instrument was first sold by Leybold GmbH, and then for many years by Omicron Nanotechnology GmbH, and it is a widely used instrument in the surface science community. Different from an optical LEED, a SPA-LEED instrument deflects the incoming and scattered electrons by an electrostatic deflection system. By varying the deflection voltages, the diffraction pattern can be scanned in a point by point mode across a small, circular aperture of 100 μm (or sometimes

Review of Scientific Instruments ARTICLE scitation.org/journal/rsi

300 μm) in diameter. Behind the aperture, the scattered electrons are detected by a channel electron multiplier (CEM). Due to a large sample-to-aperture distance of ~30 cm and the smallness of the aperture, the angular and, hence, the k-space resolution of the SPA-LEED instrument is much larger than that of an optical LEED. For SPA-LEED instruments, the parameter that characterizes the k-space resolution, the so-called *transfer width*, can reach – under ideal conditions – values of up to 2000 Å, while only a value of 150 Å is typical of optical LEED instruments.[9]

The use of a CEM for counting the electrons in a single pulse mode is very important because its high dynamic range from 0.1 to more than 10^6 counts per second (cps) allows a correct determination of the intensity profiles of diffraction spots as a function of the momentum transfer parallel to the surface ($k_\parallel$). The intensities typically drop from the center of the spots to the background over many orders of magnitude. In combination with the high k-space resolution, a quantitative determination and subsequent analysis of the spot profiles is thus possible. Under these advantages, the SPA-LEED technique has been used for the investigation of a very wide range of topics. Earlier work concerned, for example, surface defect structures, long-range order, dislocation networks, and the high precision determination of small changes of surface lattice constants, as reviewed in Refs. 9–11. Recently, SPA-LEED has been applied to the investigation of organic mono- and multilayers,[12–14] nanostructures on surfaces,[15,16] and different 2D materials.[17–19]

Over about the last 30 years, a number of technical improvements on the SPA-LEED instrument were made.[20] To name are, for example, the conical front end of the instrument for optimized sample access and for *in situ* deposition during data acquisition,[21] a pulsed direct current heating for quasi field-free diffraction measurements at high sample temperatures,[22] and a program-controlled setting of the electron energy for recording of reciprocal space maps (RSMs).[23,24] However, one major drawback of the SPA-LEED method was not overcome yet. As the SPA-LEED instrument is based on a single point detector, the recording of the intensity distribution in reciprocal space requires scanning, which leads to long data acquisition times. This aspect is addressed here.

For a typical 2D SPA-LEED diffraction pattern of 400 × 400 data points and a gate time of typically 0.5–5 ms per data point, a total data acquisition time up to 15 min is required. For higher resolution (more data points) and longer gate times, this may increase to even a few hours for a single diffraction pattern. Obviously, the acquisition of a series of 2D patterns, e.g., for varying electron energies, is, therefore, not only impractical but also often impossible because changes in the surface structure occur during the data acquisition. For spot profile analysis, the limitations are smaller because usually only 1D sections of the reciprocal space (line scans) are recorded, which allow acceptable measurement times.

In the following, we present an approach to increase the speed of measurements by SPA-LEED (with emphasis on 2D data acquisition). By employing a routine that sets a variable gate time of the counting process during scanning, we are able to speed up the counting process by a factor of about 10, while we observe only a minor or even negligible loss in the information content of the data. The routine exploits the fact that, for an ordered surface, typically more than 90% of the data points of the LEED image belong to the background between the diffraction spots. The intensity of the background is typically a factor of 10^2–10^5 smaller and exhibits only a small lateral variation with $k_\parallel$, compared to the diffraction spots. In most cases, one is not interested in the background, and the related data points are considered to contain little information. The diffraction spots that bear valuable information typically comprise only 1%–10% of the data points of a 2D diffraction pattern, depending on the width and density of the diffraction spots. Therefore, it may be favorable to spend significant acquisition time on the relevant data points and spend little time on data points of the background. The price that is paid for the saved acquisition time is an increased noise level for signals of low intensity, an aspect that we will discuss in detail.

The described approach can be interpreted as a special case of Shannon's information entropy: the least frequently occurring data points contain most of the information.[25,26] While this approach appears to be straightforward, the main difficulty, as known from algorithms for lossy data compression, is usually to decide which data points are more relevant than others. In retrospective, this can be decided from a cumulative distribution function (CDF). However, to do so, the data have to be recorded first, before unimportant data points may be discarded. Fortunately, for SPA-LEED data, the count rate observed at each data point is *per se* a direct measure of the relevance of this respective data point within the diffraction image, because, as said above, data points belonging to the information containing spots exhibit significantly higher count rates than the background. Thus, the data acquisition for a specific point of the diffraction image can be modified instantaneously as soon as the intensity of the point is known. This is done by the described speed-up routine. Of course, due to its design, the routine is not useful for all kinds of measurement. It may, in particular, fail when structures with lower intensity with respect to the background have to be discriminated or even be measured quantitatively.

DESCRIPTION OF THE SPEED-UP ROUTINE

In the following, we describe the details of the speed-up routine. A corresponding flow chart is given in Fig. 1. The speed-up routine was implemented in the SPA-LEED acquisition software Win-SPA, developed by one of the authors (P.K.).[27] We suppose, although we do not have firm evidence, that similar speed-up routines are user-implemented in the data acquisition routines of other scanning diffraction techniques (e.g., X-ray diffraction).

Prior to the scan, the user sets a gate time τ_{set} that is valid for all data points of the scan. However, after the software has set the deflection voltages of the SPA-LEED to the values corresponding to the specific point in the k-space, the counter is not started with the gate time τ_{set}. Instead, as a first step, a short "pre-scan" with a gate time τ_{pre} is performed. We found τ_{pre} = 0.15 ms to be useful, but other values are, of course, possible. In a second step, from the measured number of counts (N_{pre}), the count rate $f_{pre} = N_{pre}/\tau_{pre}$ is calculated. From f_{pre} the relevance of the data point is judged, and on that basis a "required" gate time τ_{req} is assigned. Because the algorithm assigns a gate time τ_{req} that is smaller than τ_{set} to the data points of the background, the total acquisition time for a scan is reduced. The detailed algorithm for this assignment of τ_{req} will be explained further below.

Review of Scientific Instruments ARTICLE scitation.org/journal/rsi

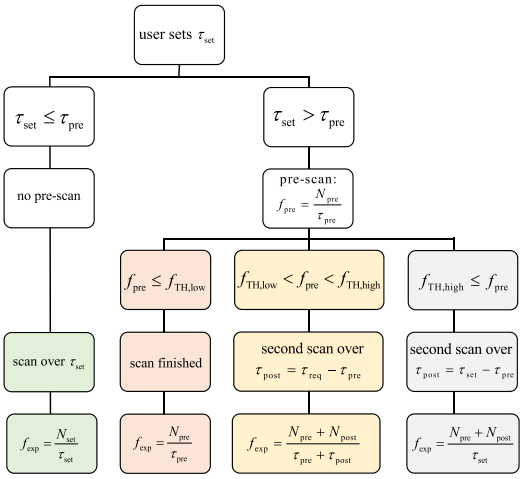

FIG. 1. Flowchart of the speed-up routine. The right branch represents the standard case. For details see text.

If $\tau_{req} > \tau_{pre}$, the program performs counting over a second interval of $\tau_{post} = \tau_{req} - \tau_{pre}$, wherein N_{post} counts are measured. Finally, the count rate (f_{exp}) is calculated as

$$f_{exp} = (N_{pre} + N_{post})/\tau_{req} = N_{true}/\tau_{req} \quad (1)$$

and stored as one data point $[f_{exp}(k_\parallel)]$. We note that the overhead for starting and stopping the counter, as well as for performing the calculations, is negligible in comparison to the gate times τ_{req} that are typically ≥0.1 ms, since the counter operation of the presently used 16 bit counter (compatible to intel 8254) is based on a 1 MHz clock, thus allowing gate times in 1 μs increments.

The algorithm for the assignment of the required gate time τ_{req} from the count rate of the pre-scan (f_{pre}) uses the following rules:

1. The required gate time τ_{req} depends on two input variables, the gate time τ_{set} set by the user and the measured count rate f_{pre}.
2. In addition, two threshold count rate values, $f_{TH,low}$ and $f_{TH,high}$, are predefined, but can be altered by the user. A data point with f_{pre} below $f_{TH,low}$ is considered to be *irrelevant*; a data point with f_{pre} above $f_{TH,high}$ is regarded as *fully relevant*.
3. *Fully relevant* data points are always measured with the full user set gate time τ_{set}.
4. *Irrelevant* data points are measured with a small gate time, given by the smaller one of the two values, τ_{set} and τ_{pre}.
5. Data points with count rates f_{pre} between $f_{TH,low}$ and $f_{TH,high}$ are considered to be of *increasing relevance*. In this transition range, the required gate time τ_{req} is assigned by a monotonic increasing function $[\tau_{req}(f_{pre})]$ that computes τ_{req} for a given value of f_{pre}. The value of τ_{req} increases from τ_{pre} to τ_{set} when f_{pre} varies from $f_{TH,low}$ to $f_{TH,high}$.
6. For the unlikely case of $\tau_{set} < \tau_{pre}$, the required gate time is equal to τ_{set}, and no pre-scan is carried out.

For defining the function $\tau_{req}(f_{pre})$, which describes the transition range, it is useful to define the normalized count rate α of f_{pre}:

$$\alpha = \frac{f_{pre} - f_{TH,low}}{f_{TH,high} - f_{TH,low}}, \quad (2)$$

which varies from 0 to 1 when f_{pre} varies from $f_{TH,low}$ to $f_{TH,high}$. Obviously, the choice of the function $\tau_{req}(\alpha)$ is not unique; the simplest choice would be a step function that increases τ_{req} from τ_{pre} to τ_{set} at one threshold value f_{TH}. However, as the relative width of the *noise band* (see below) depends on the absolute number of counts $(1/\sqrt{N} = 1/\sqrt{f_{exp}\,\tau_{req}})$, and, hence, on τ_{req}, a smooth variation of τ_{req} yields a smooth and continuous widening of the noise band when scanning away from the center of the diffraction spots into the background.

In Fig. 2, three examples of the function $\tau_{req}(f_\alpha)$ are illustrated, which we describe below. At present, we have implemented a quadratic increase of τ_{req} according to

$$\tau_{req} = \tau_{pre} + \alpha^2(\tau_{set} - \tau_{pre}). \quad (3)$$

This function yields a large reduction of the gate time at low count rates. Alternatively, a linear function

$$\tau_{req} = \tau_{pre} + \alpha(\tau_{set} - \tau_{pre}), \quad (4)$$

or a smooth step-like function

$$\tau_{req} = \begin{cases} \tau_{pre} + 2\alpha^2(\tau_{set} - \tau_{pre}), & \text{if } \alpha \le 0.5, \\ \tau_{pre} + (1 - 2(\alpha - 1)^2)(\tau_{set} - \tau_{pre}), & \text{if } \alpha > 0.5, \end{cases} \quad (5)$$

is possible. This latter function yields a differentiable transition from τ_{pre} to τ_{set}. However, the quadratic function [Eq. (3)] yields a larger

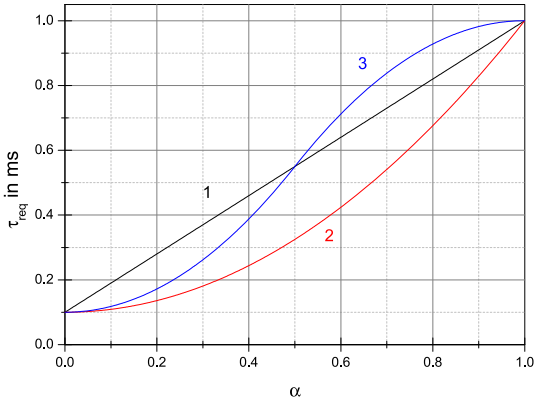

FIG. 2. Total gate time calculated for a data point as a function of the normalized count rate α in the transition range for τ_{set} = 1 ms and τ_{pre} = 0.1 ms. The numbers on the curves correspond to the different possibilities of varying τ_{req} as a function of α that are described in the text.: (1) linear increase [Eq. (4)], (2) quadratic increase [Eq. (3)], and (3) smooth transition [Eq. (5)]. For the examples presented here, we used the quadratic increase.

Review of Scientific Instruments ARTICLE scitation.org/journal/rsi

reduction of the measurement time. Roughly, one can infer that the speed-up routine reduces the total acquisition time by a factor of $1 - x \times (1 - \tau_{pre}/\tau_{set})$, where x denotes the percentage of irrelevant data points. In more detail, the reduction of the acquisition time depends also on the CDF of the specific diffraction pattern. In practice, a small value of τ_{pre} has to be chosen such that at points of low intensities the number of counts during τ_{pre} is of the order of one ($\tau_{pre} \times f_{exp} \approx 1$). We experienced that for the quadratic dependence of τ_{req} [Eq. (3)] the acquisition time reduction in 2D scans ranges from 60% to well over 90%, depending on the choice of $f_{TH,low}$ and $f_{TH,high}$, as well as the sharpness of the diffraction spots.

EXPERIMENTAL EXAMPLES

We start with an analysis of the impact of the speed-up routine on the noise in a 1D scan for didactic reasons. This information helps to understand the role of the control parameters ($f_{TH,low}$ and $f_{TH,high}$). We note ahead that, while the speed-up routine is most useful for 2D scans, it is of less use for 1D scans because, there, the reduction of the acquisition time is limited, and unwanted changes in profile wings may result.

1 D SPA-LEED scans

Figure 3 compares two 1D scans that were recorded on the specular spot, i.e., the (0,0) spot of the Ag(100) surface without and with the speed-up routine, i.e., for constant and for variable gate times, calculated from Eq. (3), respectively. Both scans comprise 1000 points and were recorded for τ_{set} = 10 ms. Thus, a ratio τ_{set}/τ_{pre} = 67 applies. The region of high count rates, where no gate time reduction is performed, is marked as gray-shaded in Fig. 3.

The inverse full width at half maximum (FWHM) of the spot (0.58% of the surface Brillouin zone, 100% = $2\pi/2.89$ Å) corresponds to a length of about ~500 Å in real space, which is a typical value for a well-prepared metal surface. When measuring 1D spot profiles, not too much acquisition time can be saved by the speed-up routine, because the scans extend only over a limited area of the background. Recording the scan using the speed-up routine took 4 s [Fig. 3(b)], while it took 16 s without it [Fig. 3(a)].

It is common to plot the intensity (f_{exp}) on a logarithmic scale, as this helps visualizing changes in the shoulder regions of the spots. We also use the logarithmic scale for our profiles, but we display the number of counts N instead of f_{exp}, in order to discuss discrete counting events. Importantly, both scans in Fig. 3 display N for the gate time τ_{set}, independent of the fact that data points of scan (b) were partly recorded under varying gate times ($N = f_{exp} \times \tau_{set}$). Thus, the data points in scan (b) are upscaled when the gate time reduction is effective.

This has an important consequence. If we define the factor for reducing the gate time by $\varepsilon = \tau_{req}/\tau_{set}$, the number of truly measured counts (N_{true}) is $N_{true} = \varepsilon \times N$, or, equivalently, as $N_{true} = \varepsilon \times f_{exp} \times \tau_{set}$ [cf. Eq. (1)]. Hence, when the gate time reduction is effective, the truly measured number of counts is smaller by the factor ε (<1) with respect to the number of counts N displayed in Fig. 3(b). This aspect explains the increase of the noise level for the scan recorded with the speed-up routine.

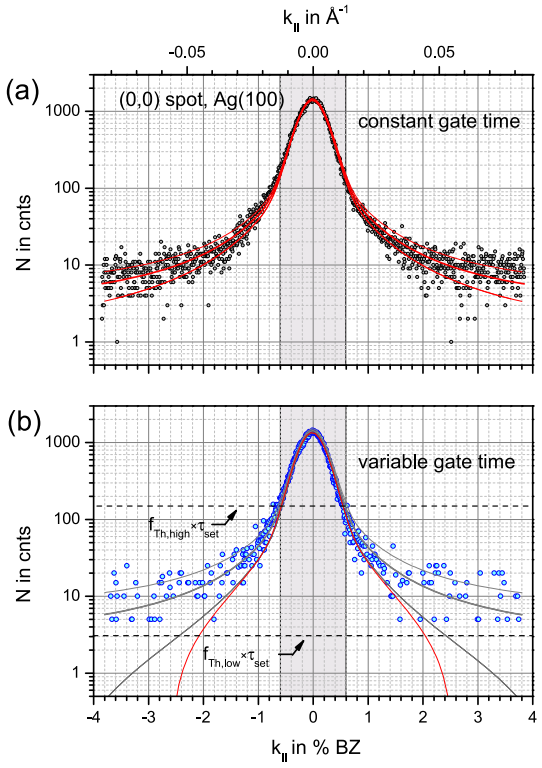

FIG. 3. 1D SPA-LEED scans of the specular, i.e., (0,0) spot of the Ag(100) surface with a scan range comprising 1000 data points. E_{kin} = 95.4 eV. This energy corresponds to a scattering phase S = 3.25 with respect to monoatomic steps. The gate time τ_{set} was 10 ms. The upper scan (a) was recorded with a constant gate time, the lower scan (b) with a variable gate time using the speed-up routine. The maximum count rate was 2×10^5 cps for both scans. For the speed-up routine, threshold rates of $f_{TH,low}$ = 300 cps and $f_{TH,high}$ = 15 000 cps were used. In the gray-shaded region, the full gate time τ_{set} is used; outside this region, the gate time is reduced to $\tau_{req} = \varepsilon \times \tau_{set}$, where ε decreases from 1 to 0.2 from higher to smaller count numbers. The full line represents a fit by a pseudo-Voigt function to the data in (a) (N_{Voigt}). This fit is used for both scans to calculate the noise band: The thin lines indicate the upper and lower edges of the noise band at $N_{Voigt} \pm 1/\sqrt{\varepsilon} \times \sqrt{N_{Voigt}}$ with ε = 1 and 0.2 in (a) and (b), respectively. The thin red line in (b) represents a fit by a pseudo-Voigt function to the data in (b). Note that under the gate time reduction, the displayed count number N is calculated from the number of truly counted events, $N = \varepsilon^{-1} N_{true}$. For further details, see text.

Noise in SPA-LEED scans

Before considering this effect in detail, we make a general remark on the statistics. As the arrival of scattered electrons at the detector constitutes a series of uncorrelated events of low frequency ($f_{exp} \lesssim 1 \times 10^6\ s^{-1}$) relative to the inverse temporal duration of the counting event ($1/10$ ns = $100 \times 10^6\ s^{-1}$), the number of electrons N that are detected within a given gate time follows a *Poisson*

Review of Scientific Instruments ARTICLE scitation.org/journal/rsi

distribution. This implies that the mean value ($\overline{N}$) and the variance (σ_N^2) of N are equal ($\overline{N} = \sigma_N^2$). Hence, the width of the "noise band", which can be estimated by the range between $\overline{N} - \sigma_N$ and $\overline{N} + \sigma_N$ is proportional to $\sqrt{\overline{N}}$.

However, when the data are displayed on the logarithmic scale, the apparent width of the noise band is proportional to $1/\sqrt{\overline{N}}$. This can be understood as follows: The upper and lower border of the noise band around $\overline{N}$ can be estimated by $\overline{N} \pm \sigma_N = \overline{N} \pm \sqrt{\overline{N}}$, and, hence, on the logarithmic scale, by $\log(\overline{N} \pm \sqrt{\overline{N}}) = \log(\overline{N}(1 \pm 1/\sqrt{\overline{N}})) = \log(\overline{N}) + \log(1 \pm 1/\sqrt{\overline{N}}) \approx \log(\overline{N}) \pm 1/\sqrt{\overline{N}}$. Thus, the width of the noise band on the logarithmic scale is larger for smaller values of N. This effect is clearly seen in the data displayed in Fig. 3(a).

For a quantitative discussion, we have fitted the data in Fig. 3(a) by a pseudo-Voigt profile (N_{Voigt}), i.e., by a sum of a Lorentzian and a Gaussian of equal FWHM. We further indicated the upper and lower borders of the noise band by thin lines at $N_{\mathrm{Voigt}} \pm \sqrt{N_{\mathrm{Voigt}}}$. This calculated noise band describes the experimentally observed noise well. Its width increases for smaller count numbers as expected. We note that the same aspect holds when the intensities f_{exp} are displayed, as long as these are calculated from the counts for a fixed gate time τ_{set}, i.e., $f_{\mathrm{exp}} = N/\tau_{\mathrm{set}}$.

Increase of noise due to the speed-up routine

If now, due to the speed-up routine, the gate time is reduced by a factor $\varepsilon < 1$, the average of the (true) number of counts is reduced by the same factor, and, as a consequence, the width of the noise band on the logarithmic scale increases by a factor $1/\sqrt{\varepsilon} > 1$. This effect can be observed in Fig. 3 from the comparison of the noise bands of the two scans outside the gray-shaded region where $\varepsilon < 1$ applies. There, the width of the noise band of the scan recorded with variable gate times [Fig. 3(b)] increases stronger than that for the scan recorded with constant gate time [Fig. 3(a)] due to the additional factor of $1/\sqrt{\varepsilon}$.

For a further quantitative discussion, the threshold values that determine the transition range need to be considered. For the present example, these were set to $f_{\mathrm{TH,low}} = 300$ cps and $f_{\mathrm{TH,high}} = 15\,000$ cps. These values correspond to 0.15% and 7.5% of the maximal intensity. For the used value $\tau_{\mathrm{set}} = 10$ ms, these threshold intensities translate into threshold count values of $N_{\mathrm{TH,low}} = 3$ cnts and $N_{\mathrm{TH,high}} = 150$ cnts. These values are represented by horizontal dashed lines in Fig. 3. The upper threshold defines the gray region, where no gate time reduction is effective ($N > N_{\mathrm{TH,high}}$, $\varepsilon = 1$). As expected, the two scans and the respective noise are identical there.

For data points of smaller count rates (outside the gray-shaded area), which fall into the transition range, the noise in the scan measured with variable gate time is increased vs that in the scan measured with the constant gate time by the factor $1/\sqrt{\varepsilon}$. Hereby, it seems as if the number of data points in the scan measured with variable gate time is reduced when N approaches the background level. This is however, not true. The missing data points exhibit zero counts and are thus not displayed on the logarithmic axis in Fig. 3. When using the speed-up routine, the probability of such data points with zero counts is strongly increased, due to the small value of the prescan time τ_{pre}.

The increase of the noise for reduced gate times can also be understood quantitatively to some extent. For the scan with reduced gate time [Fig. 3(b)], ε varies from 1 to 0.2. The lower, but still significant value of 0.2 in this example, results from the fact that already a single count ($N_{\mathrm{true}} = 1$) during τ_{pre}, yields a significant intensity value of $f_{\mathrm{pre}} = 1/\tau_{\mathrm{pre}} = 1/0.15$ ms = 6667 cps. This leads to a calculated count value of $N_1 = f_{\mathrm{pre}} \times 10$ ms = 67 cnts in Fig. 3(b), and N_1 is thus located well above the lower dashed line at $N_{\mathrm{TH,low}} = 3$ cnts. As a consequence of the small value of τ_{pre}, a value of f_{exp} well above $f_{\mathrm{TH,low}} = 300$ cps is already obtained for a single count. According to Eq. (2), a value of $\alpha = 0.433$ of the normalized count rate is received, and a gate time $\tau_{\mathrm{req}} = 2$ ms is calculated by Eq. (3). This minimal value of gate time τ_{req} (and hence the minimal value of ε, namely, $\varepsilon_{\mathrm{min}} = \tau_{\mathrm{req}}/\tau_{\mathrm{set}} = 0.2$) is a consequence of the small value of τ_{pre}, which yields a significant value of f_{pre}. Smaller values of τ_{req} are achieved for larger values of the lower threshold $f_{\mathrm{TH,low}}$ closer to f_{pre}. However, too small values of τ_{req} are impractical, because they lead to a statistically unmeaningful too large scaling of the $N_{\mathrm{true}} = 1$ events by a large factor of ε^{-1} ($N = N_{\mathrm{true}} \cdot \varepsilon^{-1}$).

The lower threshold value $N_{\mathrm{TH,low}} = 3$ cnts affects those data points where zero counts are recorded during the prescan. These data points fall below $f_{\mathrm{TH,low}}$ and are thus considered as irrelevant. As a consequence, no further acquisition time is spent ($\tau_{\mathrm{post}} = 0$). For small intensities, the probability to record zero counts during τ_{pre} increases, and an increasing fraction of the data points is considered as irrelevant. As said above, these data points are not displayed on the logarithmic scale, and the density of data points thus only seems to be reduced at small intensities in Fig. 3(b), which is not the case. However, the assignment of data points as irrelevant contributes significantly to the reduction of the total acquisition time.

From the minimal gate time $\tau_{\mathrm{req}} = 2$ ms and $\tau_{\mathrm{set}} = 10$ ms, a minimal value of $\varepsilon_{\mathrm{min}} = \tau_{\mathrm{req}}/\tau_{\mathrm{set}} = 2$ ms/10 ms = 0.2 results. Hence, the largest broadening of the noise band with respect to that of the scan, recorded for constant gate time is given by a factor of $1/\sqrt{\varepsilon} = \sqrt{5.0} = 2.2$ for small count numbers. The agreement of the theoretically expected noise band with the experimentally observed one is illustrated in Fig. 3(b). There, the same pseudo-Voigt profile as in Fig. 3(a) is shown, and the respective boarders of the noise band at $N_{\mathrm{Voigt}} \pm 2.2 \times \sqrt{N_{\mathrm{Voigt}}}$ are indicated. We note that the value of $\varepsilon^{-1} = 5.0$ also explains why small N values are given by multiples of 5 [$N = \mathrm{integer}(5.0 \times N_{\mathrm{true}})$] in Fig. 3(b).

Influence on fitted profiles

Finally, we comment on the influence of the speed-up routine on the fitting of the profile. For this purpose, the data in Fig. 3(b) were also fitted by a pseudo-Voigt profile (red line). In the gray shaded region, the fit comes very close to the one performed for the scan recorded at constant gate time (gray full line). Only small differences are seen, e.g., at the apex of the peak. However, in the wings of the profile, outside the gray-shaded region, the fitted curve falls significantly below the displayed data points. This is a consequence of the high number of data points with $N = 0$ cnts recorded at low intensities (not displayed on the logarithmic scale) when using the speed-up routine. In principle, these data points exhibit a too high statistical weight. [For this reason, the pseudo-Voigt profile derived from the scan in Fig. 3(a) was used to calculate the noise band in

Review of Scientific Instruments ARTICLE scitation.org/journal/rsi

Fig. 3(b)]. Quantitative peak fitting of profiles recorded with the speed-up routine thus requires care when features in the wings of the profiles are of interest. However, the spot positions and the FWHM are robust.

2D SPA-LEED patterns

As a second example, we show a 2D SPA-LEED pattern of an ordered phase of a large aromatic molecule on the Ag(100) surface in Fig. 4. We selected this example because the unit cell of the superstructure is very large (covering 67 Ag atoms), leading to many weak superstructure spots in the pattern. The pattern covers the reciprocal space up to the diffraction spots of second order [e.g., (1,1)] of the Ag(100) surface. For the details of this adsorbate, we refer to Ref. 28.

The superstructure spots are sharp, but are partly faint, and, often, two or even three spots are very close to each other. The pattern on the left side (a) was recorded with a fixed gate time of τ_{set} = 20 ms, while the one on the right side (b) of Fig. 4 with a variable gate time and τ_{set} = 1 ms. Due to the saved acquisition time, an increased number of points in k-space (by factor of 6.25) could be measured. Furthermore, it was possible to oversample the pattern by recording it over eight subsequent iterations. Hence, the intensity of the data points in Fig. 4(b) corresponds to the total number of counts recorded during the eight iterations. The threshold rates were $f_{TH,low}$ = 200 cps and $f_{TH,high}$ = 200 000 cps, i.e., they differed by a factor of 1000, which is also the ratio between the intensities of substrate spots and superstructure spots. The right pattern (b) (recorded with variable gate time) was measured within about 27 min; the left one (a) required 34 min.

The comparison of the two patterns reveals nearly no loss of details by the use of variable gate times for (b) with respect to (a), although some differences in the intensity distribution are visible for the very weak diffraction spots of the superstructure due to statistical reasons. In addition, the integer order spots appear to be broader. This is, however, only due to the settings of the gray scale of the image that were optimized for the visibility of the faint superstructure spots. These have intensities of the order of 2000 cps, corresponding to an average of 2 cnts during τ_{set} = 1 ms. Single counting events correspond to f_{pre} = 6667 cps (as above), leading to α = 3%, and, hence, $\tau_{req} \approx \tau_{pre}$ applies according to Eq. (3). Hence, single counting events are displayed as $N = f_{exp} \times \tau_{set} = 1$ cnts/$\tau_{req} \times \tau_{set} \approx 1$ cnts/$\tau_{pre} \times \tau_{set}$ = 6.7 cnts. Remarkably, the pattern recorded with the variable gate time is not missing the fainter superstructure spots. We explain this by a combination of two effects that increase the probability for recording counts at a position in k-space with low intensity, namely, the eight-fold oversampling of the pattern, and the higher density of the data points in k-space. Together, with the scaling of the single counting events by a factor of 6.7, this yields a high probability that the small intensity of the superstructure spots leads to significant counts in the pattern.

Notably, the increased number of data points proves to be beneficial for the quality of the diffraction pattern because it yields a higher spatial resolution and a better visibility of all diffraction spots. In addition, the oversampling by iterative recording of the pattern leads to a reduced noise of the background and a better contrast of the weaker spots, independent of the aspect whether the speed-up routine is used or not. Without the use of the speed-up routine scanning such a high number of data points as was done here

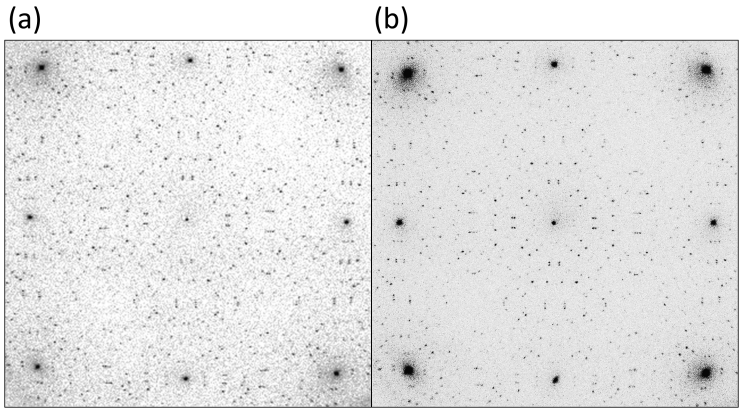

FIG. 4. SPA-LEED patterns of the highly ordered commensurate α-phase of a merocyanine molecule on the Ag(100) surface. For the full details of this phase, we refer to Ref. 28. Both patterns were recorded at 110 K and for an electron energy of E_{kin} = 80.9 eV. Due to experimental reasons, the coverages (θ) were slightly different, i.e., θ = 1.0 and 1.2 monolayers for the left and right pattern, respectively. The intensities are plotted on a logarithmic gray scale. The left pattern (a) was recorded for reference purpose without the speed-up routine, using a fixed gate time τ_{set} = 20 ms and 320 × 320 data points (no oversampling). The total acquisition time was 34 min. The right pattern (b) was recorded using the speed-up routine ($f_{TH,low}$ = 200 cps and $f_{TH,high}$ = 200 000 cps). Reflection range was 80 × 80 V^2, with 1000 × 1000 data points, gate time τ_{set} = 1 ms, with eight-fold oversampling. Without the speed-up routine, the total acquisition time for this pattern would have amounted to 133 min; due to the speed-up routine, an acquisition time of only 27 min was needed. The contrast and the brightness of both images were slightly optimized for better visibility. The comparison demonstrates that the speed-up routine records nearly all of the superstructure spots. This is, in part, due to the eight-fold oversampling and the higher number of data points underlying the scan. However, some loss of intensity occurs for the weaker diffraction spots, and the intensity profile of some substrate spots is modified.

Review of Scientific Instruments ARTICLE scitation.org/journal/rsi

would require a non-acceptable acquisition time of several hours, and, is, hence impossible to use. Therefore, the speed-up routine can advantageously be used for scanning 2D patterns when the focus is mainly on the positions of the spots and not on details of the spot profiles. In the latter case, the routine is not appropriate for the same reason as for 1D profiles.

Reciprocal space maps

As the final example for the use of the speed-up routine, we consider a reciprocal space map (RSM). In short, RSMs are 2D intensity maps in the $\mathbf{k}_{\parallel}$–$\mathbf{k}_{\perp}$ plane that comprise the reciprocal lattice rods of the surface for appropriate orientations of $\mathbf{k}_{\parallel}$. Figure 5 illustrates an RSM for the Ag(100) surface. An RSM is measured by recording a series of 1D line scans for a stepwise computer-controlled increase of the kinetic energy E_{kin}.[23] The smaller curvature of the *Ewald* sphere of the SPA-LEED instrument, compared to that of an optical LEED, is advantageous here and permits that, at not too small energies, RSMs with negligible distortions are obtained after converting the E_{kin} axis to the $\mathbf{k}_{\perp}$ axis. For the details, we refer to the article by Meyer zu Heringdorf and Horn-von Hoegen.[23]

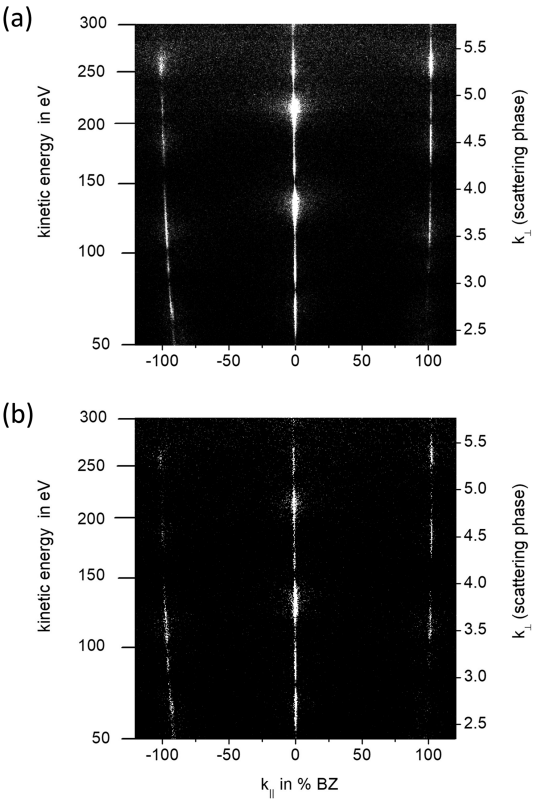

FIG. 5. Reciprocal space maps (RSMs) of the Ag(100) surface along the [100] = $\overline{\Gamma}\,\overline{\mathrm{M}}$ direction, with a scan range comprising 400 data points from −120% to 120% of the Brillouin zone. E_{kin} was varied from 50 to 300 eV in 400 steps. The gate time τ_{set} was 4 ms. The upper RSM (a) was recorded with a fixed gate time, while the lower (b), with variable gate times, using the speed-up routine. The maximum count rate was 4.5×10^5 cps. For the speed-up routine, threshold rates of $f_{TH,low}$ = 500 cps and $f_{TH,high}$ = 3000 cps were used. The total data acquisition times were about 15 and 1 min for (a) and (b), respectively. The intensities are plotted on a logarithmic, inverted gray scale. We note that there is a small, residual barrel distortion due to an imperfect deskewing of the $k_{\parallel}$ axis.

The recording of RSMs suffers from the same restrictions by the acquisition time as 2D scans. Figure 5 demonstrates that the reciprocal lattice rods, and, in particular, the intensity variation in the direction of the E_{kin} axis, can be observed when the speed-up routine is used, although the statistics are less good. This is, however, expected because the discussion of the statistics that we gave for the 1D scans above also applies here. The speed-up routine will thus be advantageous whenever an RSM serves for checking for surface quality, facetting, or simply the surface orientation, and will facilitate the acquisition of RSMs in general.

In addition, we have successfully tested that the reduction of the acquisition time also allows one to measure 3D data cubes in reciprocal space, which are obtained by stacking 2D scans for a series of kinetic energies. Recording such large datasets was prohibited so far by the necessary acquisition times. The recording of data cubes is attractive because from a subsequent integration of the intensities in cylinders around the reciprocal lattice rods, intensity vs energy curves (I–V curves) can be computed. Such I–V curves differ from those that are recorded by optical LEED due to the difference in the scattering geometries in SPA-LEED and optical LEED. This aspect would have to be addressed in quantitative LEED-IV calculations that simulate these I–V curves extracted from SPA-LEED data. Nevertheless, the possibility of measuring I–V curves by SPA-LEED is attractive, since its higher *k*-space resolution with respect to that of an optical LEED is advantageous when data for large superstructures where the spots are very close to each other, e.g., as in Fig. 4, are recorded.

CONCLUSIONS

We have introduced a speed-up routine in the SPA-LEED acquisition software that can save about 90% of the acquisition time when scanning 2D patterns or reciprocal space maps. We expect it to be useful for fast preparatory or alignment scans. In addition, it supports time critical data acquisition and permits recording 3D data cubes within an acceptable time. Due to its nature, the routine is less suited when quantitative scans of the wings of spot profiles are considered. A similar restriction applies to the situation where features of large and small intensity are of interest in parallel. Critical testing and adapting of the control parameters of the routine are unavoidable then.

ACKNOWLEDGMENTS

The authors thank Florian Schneider, Morris Mühlpointner, and Lukas Grönwoldt for the experimental support and Georg Held (Diamond Light Source, GB) and Rudolf Merkel (Jülich) for the helpful comments. The project was supported by the Deutsche

Review of Scientific Instruments ARTICLE scitation.org/journal/rsi

Forschungsgemeinschaft (DFG), under the Project No. SO-407/6-3, and through the Research Training Group 2591.

AUTHOR DECLARATIONS

Conflict of Interest

The authors have no conflicts to disclose.

Author Contributions

Anna J. Kny: Conceptualization (equal); Data curation (equal); Formal analysis (equal); Investigation (equal); Supervision (equal); Validation (equal); Visualization (equal); Writing – original draft (equal); Writing – review & editing (equal). **Moritz Sokolowski**: Conceptualization (equal); Data curation (equal); Formal analysis (equal); Funding acquisition (equal); Investigation (equal); Methodology (equal); Project administration (equal); Resources (equal); Supervision (equal); Validation (equal); Visualization (equal); Writing – original draft (equal); Writing – review & editing (equal). **Peter Kury**: Conceptualization (equal); Investigation (equal); Software (equal); Supervision (equal); Validation (equal); Visualization (equal); Writing – original draft (equal); Writing – review & editing (equal).

DATA AVAILABILITY

Data available on request from the authors.

REFERENCES

[1] R. K. Gehrenbeck, "Electron diffraction: Fifty years ago," Phys. Today **31**(1), 34–41 (1978).
[2] W. Moritz and M. Van Hove, *Surface Structure Determination by LEED and X-Rays* (Cambridge University Press, 2022).
[3] F. Jona, J. A. Strozier, Jr., and W. S. Yang, "Low-energy electron diffraction for surface structure analysis," Rep. Prog. Phys. **45**, 527 (1982).
[4] M. G. Lagally, "The present status of low-energy electron diffraction," Appl. Surf. Sci. **13**(1–2), 260–281 (1982).
[5] H. Sakama and A. Kawazu, "Recent progress in low-energy electron diffraction: Theory and application to semiconductor surfaces," Mater. Sci. Eng., R **14**(6), 255–317 (1995).
[6] M. G. Lagally and J. A. Martin, "Instrumentation for low energy electron diffraction," Rev. Sci. Instrum. **54**(10), 1273–1288 (1983).
[7] K. Müller and K. Heinz, *The Structure of Surfaces*, Springer Series in Surface Sciences Vol. 2 (Springer Verlag, 1985), p. 105.
[8] U. Scheithauer, G. Meyer, and M. Henzler, "A new LEED instrument for quantitative spot profile analysis," Surf. Sci. **178**(1–3), 441–451 (1986).
[9] M. Horn-von Hoegen, "Growth of semiconductor layers studied by spot profile analysing low energy electron diffraction—Part I," Z. Kristallogr. **214**(10), 591–629 (1999).
[10] M. Henzler, "Measurement of surface defects by low-energy electron diffraction," Appl. Phys. A **34**, 205–214 (1984).
[11] J. Wollschläger, J. Falta, and M. Henzler, "Electron diffraction at stepped homogeneous and inhomogeneous surfaces," Appl. Phys. A **50**, 57–68 (1990).
[12] C. Stadler, S. Hansen, I. Kröger, C. Kumpf, and E. Umbach, "Tuning intermolecular interaction in long-range-ordered submonolayer organic films," Nat. Phys. **5**, 153–158 (2009).
[13] L. Fernández, S. Thussing, A. X. Brión-Ríos, D. Sánchez-Portal, and P. Jakob, "Lateral interactions and order–disorder phase transitions of metal phthalocyanines on Ag(111)," J. Phys. Chem. C **125**(28), 15623–15635 (2021).
[14] L. Kilian, E. Umbach, and M. Sokolowski, "Molecular beam epitaxy of organic films investigated by high resolution low energy electron diffraction (SPA-LEED): 3,4,9,10-perylenetetracarboxylicacid-dianhydride (PTCDA) on Ag(111)," Surf. Sci. **573**(3), 359–378 (2004).
[15] C. Tegenkamp, "Vicinal surfaces for functional nanostructures," J. Phys.: Condens. Matter **21**, 013002 (2009).
[16] B. Hafke, C. Brand, T. Witte, B. Sothmann, M. Horn-von Hoegen, and S. C. Erwin, "Thermally induced crossover from 2D to 1D behavior in an array of atomic wires: Silicon dangling-bond solitons in Si(553)-Au," Phys. Rev. Lett. **124**, 016102 (2020).
[17] C. Brülke, T. Heepenstrick, N. Humberg, I. Krieger, M. Sokolowski, S. Weiss, F. S. Tautz, and S. Soubatch, "Long vertical distance bonding of the hexagonal boron nitride monolayer on the Cu(111) surface," J. Phys. Chem. C **121**(43), 23964–23973 (2017).
[18] S. Chen, P. A. Thiel, E. Conrad, and M. C. Tringides, "Growth and stability of Pb intercalated phases under graphene on SiC," Phys. Rev. Mater. **4**, 124005 (2020).
[19] K. Omambac *et al.*, "Non-conventional bell-shaped diffuse scattering in low-energy electron diffraction from high-quality epitaxial 2D-materials," Appl. Phys. Lett. **118**, 241902 (2021).
[20] W. Moritz, in G. Chiarotti and P. Chiaradia (Eds.) *Physics of Solid Surfaces - 5.4 SPA-LEED* (Springer Materials, 2015).
[21] P. Zahl and M. Horn-von Hoegen, "Third-generation conical spot profile analyzing low-energy electron diffraction," Rev. Sci. Instrum. **73**(8), 2958–2962 (2002).
[22] P. Kury, P. Zahl, M. Horn-von Hoegen, C. Voges, H. Frischat, H.-L. Günter, H. Pfnür, and M. Henzler, "Chopped sample heating for quantitative profile analysis of low energy electron diffraction spots at high temperatures," Rev. Sci. Instrum. **75**, 4911–4915 (2004).
[23] F.-J. Meyer zu Heringdorf and M. Horn-von Hoegen, "Reciprocal space mapping by spot profile analyzing low energy electron diffraction," Rev. Sci. Instrum. **76**(8), 085102 (2005).
[24] F.-J. Meyer zu Heringdorf, K. L. Roos, C. Wiethoff, M. Horn-von Hoegen, and K. R. Roos, "Growth of Ag nanowires on Au-pre-facetted 4° vicinal Si(001)," Surf. Sci. **602**, 1852–1857 (2008).
[25] C. E. Shannon, "A mathematical theory of communication," Bell Syst. Tech. J. **27**(3), 379–423 (1948).
[26] C. E. Shannon and W. Weaver, *The Mathematical Theory of Communication* (University of Illinois Press, 1963).
[27] P. Kury, WinSPA Software V2.x, http://winspa.de/index.htsml, 2022.
[28] A. J. Kny, M. Reimer, N. Al-Shamery, R. Tomar, T. Bredow, S. Olthof, D. Hertel, K. Meerholz, and M. Sokolowski, "Chiral self-organized single 2D-layers of tetramers from a functional donor-acceptor molecule by the surface template effect," Nanoscale (published online) (2023).

A.2. "Chiral self-organized single 2D-layers of tetramers from a functional donor-acceptor molecule by the surface template effect"

by Anna J. Kny, Max Reimer, Noah Al-Shamery, Ritu Tomar, Thomas Bredow, Selina Olthof, Dirk Hertel, Klaus Meerholz, and Moritz Sokolowski.

The research article is published in the Journal *Nanoscale* 15, 10319 (2023).

Nanoscale

PAPER

Cite this: *Nanoscale*, 2023, **15**, 10319

Chiral self-organized single 2D-layers of tetramers from a functional donor–acceptor molecule by the surface template effect†

Anna J. Kny, [a] Max Reimer,[b] Noah Al-Shamery, [a] Ritu Tomar, [a] Thomas Bredow, [a] Selina Olthof, [b] Dirk Hertel, [b] Klaus Meerholz [b] and Moritz Sokolowski *[a]

The ability to control the structural properties of molecular layers is a key for the design and preparation of organic electronic devices. While microscopic growth studies of planar, rigid and symmetric π-conjugated molecules have been performed to a larger extent, this is less the case for elongated donor–acceptor molecules with flexible functional groups, which are particularly interesting due to their high dipole moments. Prototypical molecules of this type are merocyanines (MCs), which have been widely studied for the use as efficient absorbers in organic photodetectors. For maximized light absorption and optimized electronic properties the molecular arrangement which is affected by the initial assembly of the films at the supporting substrate interface is decisive. The situation deserves special attention, when the surface nucleation leads to so far not known and bulk-unlike aggregates. Here, we report on the growth of a typical MC (**HB238**) on the Ag(100) surface, serving as the substrate. In the energetically preferred phase, the molecules adsorb in a face-on geometry and organize in tetramers with a circular dipole arrangement. The tetramers further self-order in large, enantiopure domains with a periodicity that is commensurate to the Ag(100) surface, likely due to a specific bonding of the thiophene and thiazol rings to the Ag surface. Using scanning tunneling microscopy (STM) in combination with low energy electron diffraction we derive the detailed structure of the tetramers. The center of the tetramer, which is most prominent in STM images, consists of four upward pointing *tert*-butyl groups from four molecules. It is encircled by a ring of four hydrogen bonds between terminal CN-groups and thiophene rings on neighboring molecules. In parallel, the surface interaction modifies the intramolecular dipole, which is revealed from photoemission spectroscopy. Hence, this example shows how the surface template effect leads to an unforeseen molecular organization which is considerably more complex compared to that in the bulk phases of **HB238**, which feature paired dipoles.

Received 17th February 2023,
Accepted 10th May 2023

DOI: 10.1039/d3nr00767g

rsc.li/nanoscale

Introduction

Merocyanine (MC) molecules are presently in the focus of research for applications in organic photodetectors and organic field effect transistors (OFETs).[1–4] The MC **HB238** (2-[5-(5-dibutyl-amino-thiophene-2-yl-methylene)-4-*tert*-butyl-5*H*-thiazol-2-ylidene]-malononitrile), which we report on, constitutes a prototypical MC.[5–7] Its molecular structure is shown in Fig. 1. Like other MCs, **HB238** comprises an electron donor and an electron acceptor group which are connected by a conjugated (poly-)methine bridge.[8] These groups and their corresponding sidegroups are marked in the structure **A** of Fig. 1(a). As the methine bridge allows for charge transfer that leads to a zwitterionic resonance structure **B**, MCs in general exhibit significant electrostatic dipole moments and high oscillator strengths.[9,10] Concerning their application in optoelectronics, the interest in MC films is based on the resulting high absorption coefficients combined with adjustable optical and charge conducting properties.[11] However, these properties are not only a consequence of the molecular structure, in particular the π-system, alone, but are also strongly related to the molecular packing. The latter can be altered, for instance, by a variation of the peripheral substituents (marked in gray in Fig. 1(a)) and determines whether the optical properties correspond to those of J- or H-aggregates.[6,7]

MC films can be prepared by spin coating or vacuum deposition on solid substrates. In the latter case, the details of the interfacial nucleation of the first layer and the subsequent film

[a]*Clausius-Institut für Physikalische und Theoretische Chemie, Universität Bonn, Wegelerstraße 12, 53115 Bonn, Germany. E-mail: sokolowski@pc.uni-bonn.de*
[b]*Department Chemie, Universität zu Köln, Greinstraße 4-6, 50939 Köln, Germany*
†Electronic supplementary information (ESI) available. See DOI: https://doi.org/10.1039/d3nr00767g

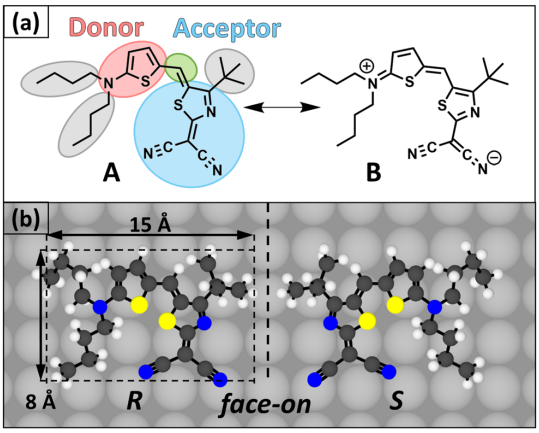

Fig. 1 Molecular structure of **HB238** and schematic hard sphere model of the molecule on the Ag(100) surface. (a) Neutral molecular structure of **HB238**, **A** and its zwitterionic resonance structure **B**.[8] Note that the negative charge of structure **B** is delocalized across both of the CN-groups. The red and blue colors indicate the donor and acceptor group, respectively. Both are connected by a methine bridge which is marked in green color; respective alkyl-side groups are marked in gray. (b) Top-view of the two enantiomers (*R* and *S*) of **HB238** due to the adsorption in face-on orientation on the Ag(100) surface, with indicated geometric dimensions (van der Waals radii reduced by a factor of 0.3). Structural details of the molecule and of the lateral and azimuthal orientation on the Ag(100) surface are chosen according to the later proposed structure model of the condensed phase (white: H, dark gray: C, blue: N, and yellow: S atoms).

growth are of importance for the resulting molecular packing, and thus the device properties. So far, this aspect has only been investigated to a limited extent, although the structure formation of MCs has been well studied for single crystals and spin coated films of several nm thickness.[5,6,12] Only few growth studies on self-assembled MC monolayers at substrate interfaces have been published,[13–15] possibly, because MCs are rather complex molecules, compared to other standard organic semiconductor molecules, for which the adsorption on surfaces has been thoroughly investigated.[16–19] In particular, MCs are non-planar, of low symmetry, and exhibit non-rigid side-groups with structural freedom. Thus, at first glance MCs are less evident candidates for generating ordered structures on surfaces. However, scanning tunneling microscopy (STM) investigations on vacuum deposited MC layers revealed that these may bear interesting aspects, *e.g.*, dimer formation.[20,21]

This work presents an STM study on the adsorption and ordering of the MC **HB238** on the Ag(100) surface. Additional low energy electron diffraction (LEED) data demonstrate that the Ag(100) surface impressively acts as a template for the lateral ordering, leading to a commensurate structure. This is related to an interfacial interaction that we characterized by UV- and X-ray-photoelectron spectroscopy (XPS/UPS).

Under kinetically hindered growth conditions, we find a phase of **HB238** with an edge-on orientation on the Ag(100) substrate, which is similar to structures seen for bulk phases.[6,7] However, the thermodynamically favored phase is one where the **HB238** molecules adsorb in a face-on orientation (Fig. 1(b)). The structure of this phase is unique, as it differs considerably from those observed in the bulk phases. There, the molecules arrange in antiparallel, *non* centro-symmetric dimers, which lead to a partial compensation of the electrostatic dipole moments.[6,7] On a second level, these dimers form characteristic structures like *quasi* 1D columns or 2D brickwall patterns.[6,7]

Quite differently, on the Ag(100) surface, the **HB238** molecules order in a structure of tetramers that are composed of four molecules of one single handedness. This ordering yields a circular arrangement of the dipoles (α-phase). This fact is interesting as **HB238** is only a *prochiral* molecule, meaning that upon adsorption on the surface in face-on orientation, *i.e.*, flat lying, it can have two different chiralities (*R* and *S*), as illustrated in Fig. 1(b).[22] The adsorbed molecules form enantiopure domains which are found for both chiralities, *i.e.* a 2D conglomerate. The growth of these requires the attachment of molecules with the same chirality as it is preset by the growing domain. The molecular arrangement in the surface layer is determined by the molecule/surface interaction and intermolecular hydrogen bonds.

Experimental and computational methods

The sample preparation and all subsequent experiments were carried out under ultra high vacuum (UHV) conditions. The **HB238** molecules were deposited from a Knudsen cell onto the clean Ag(100) single crystal surface. For the structural characterization we used low energy electron diffraction (LEED), in particular utilizing a special instrument, a so-called spot profile analysis LEED instrument (SPA-LEED)[23] which provides a high resolution in diffraction space and low electron beam currents. Furthermore, the layers were imaged by a scanning tunneling microscope operated at deliberate low tunneling currents (I_t). UPS and XPS measurements, were performed to monitor the molecular orbitals and for the chemical characterization of the adsorbed **HB238**. Coverages (θ) are given in numbers of monolayers (ML) as defined in the ESI.† Additional details concerning the sample preparation, the SPA-LEED method, the recording and evaluation of the STM data, and the photoemission spectra are also described in the ESI.†

For an assignment of the molecular orbitals we performed density functional theory (DFT) calculations. For this purpose, the minimum energy structure for an isolated **HB238** molecule was obtained by performing DFT calculations for a large set of conformers (few hundreds) which were obtained by using the conformer-rotamer ensemble sampling tool (CREST).[24] The DFT calculations were performed with the program ORCA 4.2.1.[25] Further details are given in the ESI.†

Results and discussion

Growth start and layer formation

Fig. 2(a) shows an overview STM image of the Ag(100) surface with a submonolayer coverage of **HB238**. After deposition at room temperature, the sample was immediately cooled down to 34 K. Numerous domains of two different ordered phases are seen, which we call the α- and β-phase in the following. Domains of the α-phase are large (some hundreds of Å in diameter) and show a long-range ordered structure in STM images of higher magnification, as for instance presented in Fig. 2(b). In this phase the molecules are adsorbed in a face-on orientation with respect to the surface (see Fig. 1(b)).

On the contrary, the domains of the β-phase are rather small (only a few tens of Å in diameter). They exhibit a short-range ordered structure, as can be seen in the STM image of Fig. 2(c). Differently to the α-phase, the domains of the β-phase nucleate at step edges or at defects, such as small clusters of impurities or **HB238** itself. This can be seen in Fig. 2(a).

Molecular orientation in the β-phase

The β-phase is composed of elongated aggregates of different widths. These exhibit a striped fine-structure with a periodicity of 4.7 ± 1.0 Å, which fits to the intermolecular distance typical for π-stacked MC molecules.[5] This fine structure is visible in Fig. 2(c), and at higher magnification in Fig. S2 in the ESI.† From this finding we propose that, in the β-phase the molecules are in an edge-orientation of the π-system with respect to the surface. In the ESI,† we show an overlay of the β-phase and a tentative structure model, and side/top views of the molecule in the proposed adsorption geometry. As the β-phase is less in the focus of this work, we only report some of its details here. In particular those, which set it apart from the α-phase.

The packing of the β-phase can be described as a *coin-role*-like arrangement of coplanar π-stacked molecules, possibly related to a coordination of the CN-groups to the Ag surface.[26] The orientation of the molecules (given by the edge side of the molecular plane), with respect to the growth direction of the aggregates (axis of the coin-roles) is inclined, with an angle varying from 40° to 50°. Hence, there are shifts between neighboring molecules in the direction of the molecular planes and parallel to the surface, which allow the aggregates to form compact domains without leaving voids. These shifts lead to the varying widths of the aggregates (perpendicular to the long axis). The exact molecular arrangement within the aggregates is experimentally unresolved, yet, because the STM tip only sees the edge sides of the molecules and not the complete π-systems (as for the α-phase, see below), and because no LEED pattern is received as a consequence of only short range order. However, from the above, we deduce that the packing in the β-phase follows a structural motif similar to those observed for some of the bulk structures of **HB238**.[6,7] For further details of the β-phase we refer to the ESI.†

The β-phase is thermodynamically less stable than the α-phase and exists only for temperatures below 110 K; at higher temperatures it transforms into the α-phase. The latter phase can be observed in the whole investigated temperature range of 25 to 350 K. However, prolonged annealing of the α-phase initiates the formation of small three dimensional clusters of **HB238** at step edges or domain boundaries. This reveals that the interfacial bonding to the surface is reversible, and that both phases are thermodynamically unstable, but are kinetically stabilized. However, for the α-phase the interfacial bonding to the Ag(100) surface makes it a template that induces a non-bulk-like molecular arrangement. This is described now.

Commensurability of the α-phase

Fig. 2(d) shows a section of the LEED pattern of the α-phase.[27] The specular spot is located in the lower left corner of the pattern. The green vectors ($\mathbf{a}_1^*$, $\mathbf{a}_2^*$) indicate the reciprocal lattice vectors of the substrate. Due to the four fold symmetry

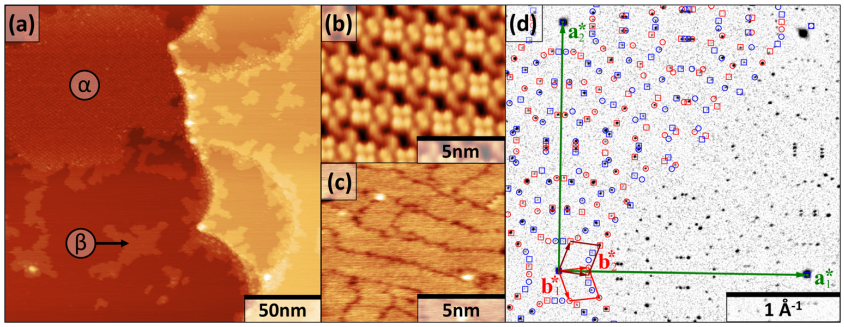

Fig. 2 STM images of **HB238** on Ag(100) and LEED pattern of the commensurate α-phase. The color code of the STM images represents the topographic height profile at constant current. (a) Overview of a submonolayer. The image shows two large terraces of the surface with two different ordered phases (α, β). One domain of each phase is marked exemplary (T = 34 K, U_{bias} = −0.51 V; I_t = 9.0 pA). (b) Small scale image of the α-phase with face-on orientation of the molecules (T = 300 K, U_{bias} = −1.51 V; I_t = 5.5 pA). (c) Small scale image of the β-phase with edge-on orientation (tunneling conditions as in (a)). (d) Upper right quadrant of the deskewed α-phase LEED pattern (110 K; θ = 1 ML; electron energy: 80.9 eV) including a simulation of the diffraction spots. The reciprocal lattice vectors of the substrate are indicated in green. The LEED pattern results from four symmetry equivalent domains which can be transferred into each other by a mirror operation (circles and squares of same color (red/blue)) or rotation (same symbol, but different colors). The unit cell of one domain and its respective mirror domain are indicated in red and dark red color.

of the Ag(100) surface, one quarter of the LEED pattern already contains all information.

The diffraction spots caused by the α-phase superstructure are sharp and well resolved, which agrees with the conclusion from STM that the domains of the α-phase extend over several hundreds of Å. The spots are very numerous such that the diffracted intensity is strongly distributed in reciprocal space. This effect leads to low intensities of the individual spots.

In one half of Fig. 2(d), the diffraction spots are overlain by a kinematic simulation of the superstructure according to the matrix given below. The simulated spots are marked by squares and cycles in red and blue color in order to indicate their origin from four symmetry equivalent domains. These are due to the symmetry of the Ag(100) substrate and can be transferred into each other by mirroring on the substrate vectors or by rotations of 90°. As an example, the unit cells of two domains related to each other by a mirror operation on the $\mathbf{a}_1$* vector are indicated in red and dark red color. The red unit cell is described by the reciprocal vectors $\mathbf{b}_1$* and $\mathbf{b}_2$*. The corresponding matrix which denotes the vectors $\mathbf{b}_1$ and $\mathbf{b}_2$ of the superstructure in real space with respect to the unit cell vectors of the substrate ($\mathbf{a}_1$, $\mathbf{a}_2$) is obtained as

$$(\mathbf{b}_1\ \mathbf{b}_2) = \begin{pmatrix} 1 & -8 \\ 8 & 3 \end{pmatrix} \begin{pmatrix} \mathbf{a}_1 \\ \mathbf{a}_2 \end{pmatrix}. \quad (1)$$

The integer numbers of the matrix elements identify the α-phase to be *commensurate*, which implies that the translational periodicity of the MC layer is controlled by the templating Ag (100) surface. This result is firm, because due to the large unit cell in real space and the resulting high number of close together lying diffraction spots, even small deviations from these integer numbers cause significant deviations of the simulated spot positions from the experimental ones, such that non-integer matrix elements that are only close to integer numbers can be excluded. The commensurability of the structure is a remarkable finding, because it guarantees a unique set of adsorption sites for all molecules in the complete layer. It reveals that the bonding potential between **HB238** in the α-phase and the Ag(100) surface exhibits a lateral corrugation leading to preferred adsorption sites of the molecule. This points to a *chemisorptive* character of the interfacial bonding which will be discussed further below.

The length of the unit cell vectors of the α-phase in real space result to b_1 = 23.30 Å and b_2 = 24.69 Å at a temperature of 300 K. We note that the two vectors differ by 6% in length and include an angle of 103.43°. Hence, the unit cell is not quadratic but oblique. The point group of the unit cell is identified as *P*211 (*P*2), and is given by the rotational symmetry of the molecular arrangement (tetramers with a two-fold rotational axis) that is described below. The unit cell covers 67 atoms of the Ag surface. From the size of the footprint of the face-on oriented molecule (~15 Ag atoms, see Fig. 1(b)) we can estimate that four face-on oriented **HB238** molecules fit into one unit cell. Due to the prochirality of **HB238** a mirror operation between two domains is accompanied by a change of the molecular chirality. Hence, two of the four symmetry equivalent domains contain molecules of one chirality while the opposite chirality is found in the two other domains. As we will show by STM images, the domains of the α-phase are enantiopure, *i.e.*, all molecules are of the same handedness.

Surface bonding of HB238 to Ag(100)

For understanding the interfacial bonding we have performed X-ray photoelectron spectroscopy. Two data sets are compared. One has been acquired for a thick disordered film (multilayer) that led to a complete attenuation of the photoelectrons from the substrate. The other one probes a submonolayer (~0.5 ML) of the α-phase for discerning the interfacial bonding. The respective spectra of the S2p, N 1s, and C1s orbitals are displayed in Fig. 3. The use of a submonolayer safeguards that

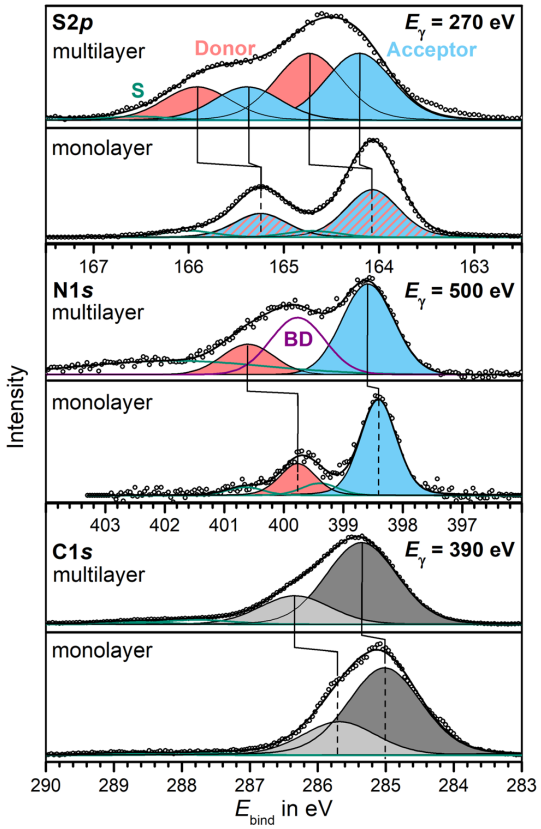

Fig. 3 XPS spectra of a multilayer and a monolayer (~0.5 ML) of **HB238** on Ag(100) showing the core levels of S2p, N1s, and C1s. Photon energies are denoted by E_γ. In addition fitted components and their sum (black solid line) are shown. The vertical lines indicate the chemical shifts of the components from the multilayer to the monolayer. The blue and red color shading of the components indicates the assignment of the peaks to the atoms (S and N) in the acceptor and donor groups, respectively. Fitted shake-up satellites are represented by the lines in turquoise color. For further details see text. S: satellite, BD: peak due to beam damage.

multilayer effects are absent in the respective spectra. However, for brevity we use the term "monolayer" in the following.

We have fitted all spectra by consistent sets of principal peaks, which resemble spectroscopically inequivalent atoms. The fitted peaks are linear combinations of Lorentzian and Gaussian peaks and were chosen on a basis of a semi-empirical approach in which some of the peaks comprise contributions from several chemically different atoms which cannot be separated spectroscopically, *e.g.*, for the C1s orbital. For an accurate fitting of the spectra it was necessary to include additional shake-up satellites on the high binding energy side of the principal peaks, marked by turquoise color in Fig. 3. Such shake-up satellites are typical for π-conjugated molecules.[28] Errors bars of the fitted binding energies are ±0.05 eV (including systematical errors of the peak fitting).

In principle, all spectra are composed of two components. One at higher binding energy and one at lower binding energy. For the S2p and the N1s orbitals these are related to the donor group (red shaded) and the acceptor group (blue shaded). In the case of the S2p orbital both components correspond to a doublet ($S2p_{3/2}$/$S2p_{1/2}$) with a fixed spin–orbit splitting of 1.18 eV and an internal area ratio of 2 : 1. For the C1s orbital, the assignment of the components to the acceptor and donor group is not strictly possible, hence they are marked as two different gray shades in Fig. 3. The reason for this is that there are numerous different chemical environments of the C atoms, like they are occurring in, *e.g.*, the aliphatic *n*-butyl and *tert*-butyl groups, and the π-conjugated system.

The binding energy difference between the donor and acceptor components can be explained as an *initial state* effect partly related to the reduced and increased electron densities on the respective groups. Therefore, this donor–acceptor splitting in the XP spectra can be seen as an indication for the presence of an unbalanced charge distribution, resulting in an electrostatic dipole, oriented from the negatively charged acceptor to the positively charged donor group for the molecules in the multilayer.

The area ratios of the two S2p doublets (1 : 1) and the principal lines of the N1s orbital (1 : 3) are in agreement with the expectations as they fit the number of respective atoms in the donor and acceptor groups (*cf.* Fig. 1(a)) for the multilayer and the monolayer. (We note that the three different N-atoms in the acceptor group cannot be discerned.) However, for the N1s orbital a consistent fit of the multilayer spectrum requires an additional peak located between the donor and the acceptor peak at 399.76 eV, marked by "BD" (violet line in Fig. 3). This peak increases with time of exposure to synchrotron radiation at the expense of the two principal peaks and is related to photoinduced modifications of **HB238** (beam damage, BD). The effect is more pronounced for the multilayer. For the monolayer it could be avoided by using small intensities and short exposure times (30 s). The fact that the monolayer is much less affected is explained by fast interfacial transfer of electrons from the Ag surface to the photoholes on all four N atoms. Therefore, in accordance with the derived face-on orientation in the monolayer, both the donor and acceptor group of the **HB238** are close to the Ag surface.

In comparison to the multilayer, the binding energies of all components in the monolayer shift to smaller binding energies as indicated by the vertical lines in Fig. 3. For the donor related peaks the shifts amount to −0.67 eV and −0.83 eV for the S2p and N1s orbitals, respectively. Interestingly, the acceptor shifts are systematically smaller compared to the donor shifts, and the respective values are −0.14 eV and −0.18 eV. For the C1s orbitals the shifts of the high and low binding energy components amount to −0.44 eV and −0.29 eV, respectively. The much smaller ratio of the shifts for the C1s orbital (only ∼1.5 instead of ∼4 as for the S2p and N1s) is conceivable, as many chemical different environments of the C atoms exist, as described above. For the S2p orbital, the donor and acceptor peaks of the monolayer even coincide and cannot be discriminated (marked by a red/blue hatching). This points to a similar local chemical environment of the donor and acceptor S atoms on the Ag surface. Within the spectral resolution both peaks are located at 164.07 eV. This binding energy is well compatible with that observed for other S containing π-conjugated molecules, *e.g.*, thiophenes in face-on orientation on Ag surfaces (164.5 eV on Ag(111)[29]).

The shifts can be explained by a combination of two effects. Screening of the photohole by the metallic Ag substrate (*final state* effect) leads to smaller binding energies of both components in the monolayer. Again, this implies a face-on orientation of the molecules that brings both the acceptor and the donor group close to the surface. The second effect is related to charge transfer between the Ag surface and the donor and acceptor groups, decreasing the absolute charges on the positively charged donor and the negatively charged acceptor group. The effect reduces the donor–acceptor splitting present for the multilayer, by shifting the donor and acceptor peaks in opposite directions on the binding energy scale (*i.e.*, to smaller and higher binding energies, respectively). As a result of both effects, smaller shifts (in the direction of smaller binding energies) of the acceptor than of the donor peaks result. These differential shifts seen for the S2p, N1s, and C1s orbitals, hence reveal that the internal electrostatic dipole is reduced, or even removed, upon adsorption on the surface. This finding is important because the so deduced underlying charge transfer indicates that the interfacial bonding of **HB238** to Ag(100) is not only due to van der Waals interactions, but also of *chemisorptive* nature involving charge transfer and possibly site specific bonds. This is in agreement with the noted commensurability of the structure.

Electronic structure and tunneling contrast

In order to get further insight into the adsorption geometry, we explain the contrast in the STM images of the α-phase in more detail. To this end, we display a sequence of STM images recorded at different bias voltages (U_{bias}) from −0.10 to −1.51 V in Fig. 4(a–c). All images were taken at constant tunneling current. Hence, they display the apparent topographic height. The used $U_{bias} < 0$ V corresponds to a tunneling out of

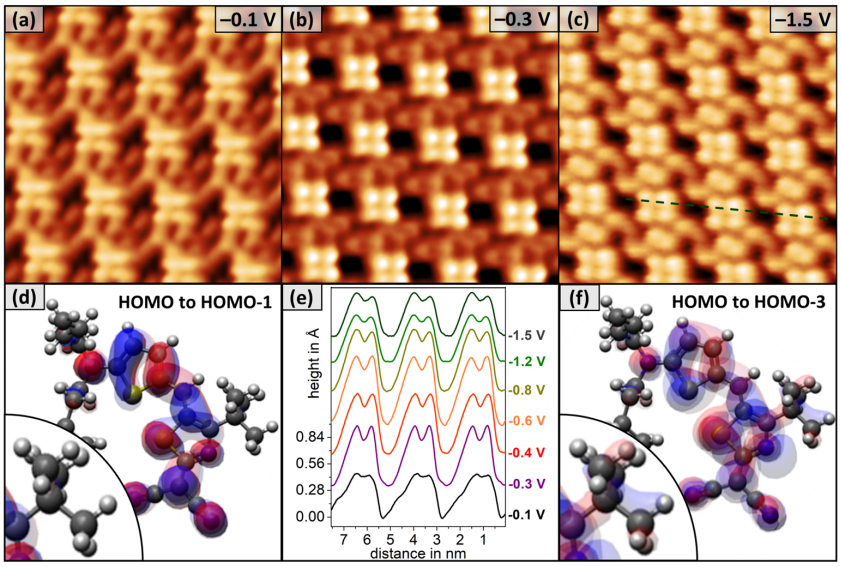

Fig. 4 Comparison of bias voltage dependent STM images in constant current mode and DFT calculated orbitals. (a)–(c): STM images of the α-phase as a function of the bias-voltage (100 Å × 100 Å). (d) and (f): **HB238** molecule in gas phase with superimposed selected orbitals which are considered for the explanation of the tunneling contrast. The *tert*-butyl group enlarged in the inserts of (d) and (f) contributes most to the tunneling contrast due to its exposed position at a larger distance to the surface. (e) Height profiles recorded at different bias voltages and constant tunneling current of 5 pA measured in horizontal direction crossing two of the four bright lobes (*tert*-butyl groups) and the dark areas of the above STM images as indicated exemplary by the dashed line in (c). The profiles are vertically shifted against each other for clarity.

occupied states. The most prominent feature is a tetramer with C_2 symmetry consisting of four bright lobes per unit cell that is seen for all bias voltages. The structural assignment of these four prominent lobes is a key to the understanding of the entire structure. One lobe corresponds to one molecule which was revealed from point defects in the periodic structure where one or even two lobes were missing. From the small spatial extension of the lobes we deduce that they cannot stem from the extended π-system of **HB238**. Instead they must be related to electronic states on the functional groups that are located further away from the surface and face towards the vacuum. Obvious candidates are the *tert*-butyl and the *n*-butyl groups which are bonded to the molecular backbone by bonds with rotational degrees of freedom (see Fig. 1 and S1†).

This assignment can be further probed by varying U_{bias} and taking height profiles across the tetramers. Fig. 4(e) compares height profiles as a function of U_{bias} for a constant tunneling current of 5 pA. The apparent topographic height of the lobes with respect to the positions of minimal height between the tetramers (dark areas) varies only moderately, *i.e.*, between 0.45 Å and 0.71 Å for a variation of U_{bias} from −0.10 to −1.50 V. This reveals that the lobes are related to occupied states further below the Fermi energy (E_F), but do not belong to an orbital with an energy close to E_F (as expected for frontier orbitals of the π-system), since no significant resonance effect is seen in the tested range of U_{bias}. In parallel, the more extended structures between the tetramers, which we assign to the rest of the molecule, also change in shape and contrast under the variation of U_{bias}.

To support this interpretation we consider additional information on the valence band states from ultra violet photoelectron spectroscopy (UPS) and density functional theory (DFT). Fig. 5 shows UPS data of the monolayer (α-phase) and, for comparison, also of a multilayer, and the clean Ag(100) surface. The binding energies of all spectra are referenced *versus* E_F. For both the monolayer and the multilayer spectrum we observe two distinct peaks in the range from 4 eV to E_F (0 eV). The peak closest to E_F is located at 1.77 eV and 1.61 eV for the monolayer and the multilayer, respectively. We assign theses peaks to the HOMO of the respective layers. A second well-resolved peak, which we relate to the HOMO−1, is found at 2.71 eV and 2.85 eV. There is a differential shift of the binding energies of the HOMO and HOMO−1 of 0.30 eV from the multilayer to the monolayer that brings the peaks closer to each other. It indicates a chemical interaction between the **HB238** and the Ag(100) surface involving the HOMO and HOMO−1. However, from comparison with the spectrum of the clean surface we find no significant additional density of states between the HOMO peak and E_F. This is dissimilar to the situation of other, more strongly bonded π-conjugated molecules,[30] where additional intensity close to E_F indicates occupied hybrid states related to the former LUMO and the Ag states. At binding energies above 3.5 eV, the strong intensity of the Ag4d band hides the molecular states of the monolayer

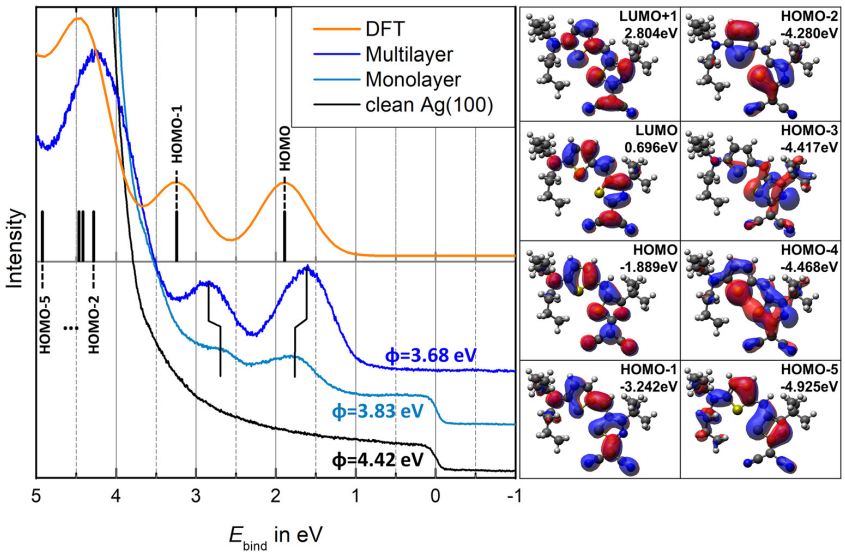

Fig. 5 UPS spectra of a multilayer and a monolayer of **HB238** on Ag(100). In addition, the spectrum for the clean Ag(100) surface is shown. The spectra were recorded at normal emission using HeI radiation (21.2 eV). Experimentally determined work functions are given (Φ). The data are compared to results obtained from DFT calculations. Energy levels of the orbitals of **HB238** in the gas phase were calculated and are indicated by sticks at the respective binding energies. For this purpose, the binding energies from DFT (with respect to the vacuum level) were corrected by the experimentally determined work function of the **HB238** multilayer spectrum (3.68 eV). The corresponding occupied orbitals and the LUMO and LUMO+1 are illustrated on the right hand side. The isosurface value corresponds to 0.02 per electrons per Å^3. Vertical lines indicate chemical shifts between the multilayer and the monolayer.

that are expected in this energy range from the DFT calculation (HOMO−2 to HOMO−5). In the multilayer spectrum, all these latter states together form a broad and strong peak.

The orbital assignment is supported by DFT calculations which were performed on isolated **HB238** molecules for the optimized structure of the molecule in the gas phase. In Fig. 5, the DFT calculated energies of the six highest occupied orbitals are given as a stick spectrum and, for better comparison with the experimental data, as a spectrum where all levels are represented by Gaussian peaks of a width fitted to that of the experimental peaks (0.75 eV FWHM). Hereby, the vacuum level of the DFT spectra was aligned to that of the multilayer, and is located at $E_F + \Phi$, whereby Φ denotes the work function of the multilayer. For comparison with STM data the calculated isospheres of the HOMO to the HOMO−5, the LUMO and LUMO+1, and the corresponding energies are given on the right hand side of Fig. 5.

Coming back to the interpretation of the STM contrast, we propose that the lobes in the tetramers stem from the *tert*-butyl groups that are, due to the tetrahedral bonding geometry, located at a larger distance to the surface compared to the rest of the molecule. The lobes are thus present due to a topographic contrast related to the *tert*-butyl groups although the related orbitals are at rather large binding energies. The amplitudes of the molecular orbitals as a function of increasing binding energy are displayed in Fig. 5. The amplitudes on the *tert*-butyl group are generally low, however they increase significantly from the HOMO to the HOMO−3/HOMO−4 (only 0.051 eV apart), which indicates the role of these orbitals for the tunneling contrast.

The significant contribution of the HOMO−2 and particular the HOMO−3 to the orbital amplitudes on the *tert*-butyl group can be derived from a comparison of Fig. 4(d) and (f), where the isospheres of the HOMO to HOMO−1 (d) and HOMO to HOMO−3 orbitals (f) have been superposed. This contribution explains the tunneling on the *tert*-butyl group resulting in a high topographic contrast at its position. We note that the discussed orbitals, HOMO−2 (−4.280 eV) and HOMO−3/HOMO−4 (−4.417 eV/−4.68 eV), of the monolayer are all hidden by the Ag4d states and cannot be discerned in the UPS spectrum.

Another argument for the *tert*-butyl group as the group responsible for the tetramers is that, in the only plausible alternative case of the *n*-butyl groups, we would have expected to see two lobes per molecule, one for each *n*-butyl group. This was, however, not the case. In addition, the related orbitals on the *n*-butyl groups are located at significantly larger binding energies (HOMO−5, −4.925 eV), making them inefficient for tunneling.

The Tersoff–Hamann interpretation[31] of STM explains why orbitals at rather high binding energies and outside the tunneling gap can contribute to the tunneling contrast measured at small bias voltages. The apparent height profile is given by a constant local density of states (LDOS), whereby the LDOS has to be integrated over the effective tunnel gap, *i.e.*, between

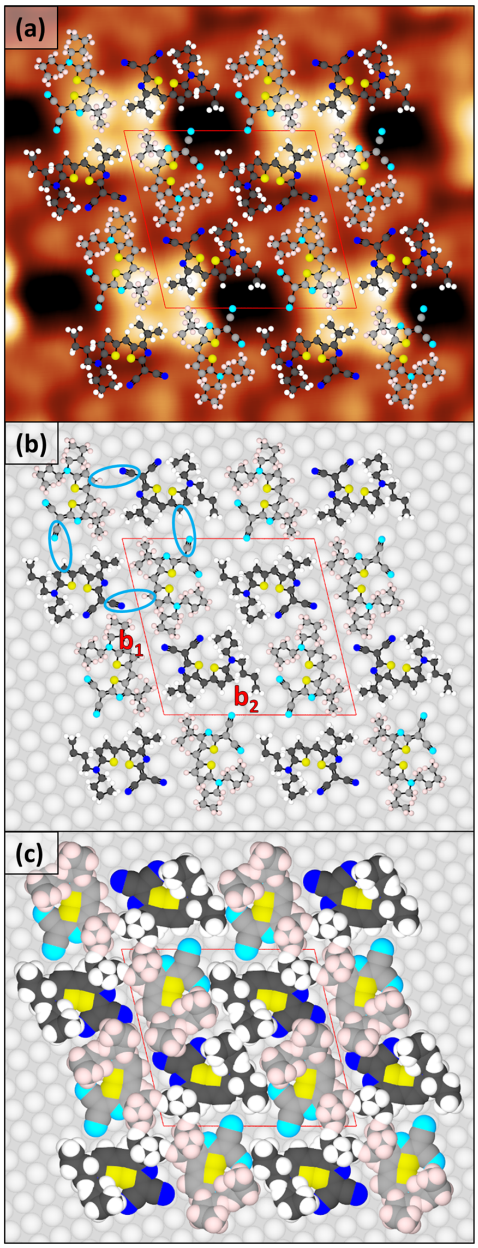

Fig. 6 Hardsphere model of the adsorption geometry of the *R* enantiomer of **HB238** within the unit cell of the α-phase on Ag(100). The two pairs of symmetry equivalent molecules are distinguished by different color shadings. (a) Hardsphere model and small scale STM image (T = 300 K; U_{bias} = −0.20 V; I_t = 0.05 nA). (b) Same structure model on the Ag (100) substrate with indicated intermolecular hydrogen bonds stabilizing the tetramers (lobes in light blue color). (c) Space-filling model. The displayed unit cell corresponds to the dark red colored unit cell given in Fig. 2(d). For the translational position of the adsorbate unit cell with respect to the substrate we refer to the text. van der Waals radii of (a) and (b) are reduced by a factor of 0.3. Color code as in Fig. 2.

U_{bias} and E_F. The small tunneling currents used in our experiments imply that the tip is at a large height with respect to the surface, where the upward standing *tert*-butyl groups contribute dominantly to the LDOS compared to the rest of the molecule. Hence, they strongly determine the tunneling contrast. Hereby, the energetic broadening of molecular states due to the interaction with the Ag states is important because it provides tails of the LDOS reaching further away from the orbital energies into the tunnel gap. Due to this effect the LDOS on the HOMO−1 to the HOMO−3/HOMO−4 on the *tert*-butyl groups contributes to the tunneling, although from Fig. 5 the positions of the related orbitals are found significantly below the applied range of bias voltages of −0.10 V to −1.51 V.

Formation of the tetramers due to hydrogen bonds

Based on the location of the *tert*-butyl groups in the STM images and the conclusions from the other spectroscopic techniques, we propose a model for the molecular arrangement in the α-phase, which is presented in Fig. 6. In panel (a) the model is superimposed on a respective STM image, in panel (b) on a hardsphere model of the Ag surface in order to illustrate the registry with respect to the surface and the intermolecular hydrogen bonds (light blue lobes). Finally, in panel (c) the structure is shown as a space filling hardsphere model. The interatomic distances and bonding angles of the **HB238** were approximated by literature values.[32] Modifications of these by the interfacial interaction are possible, but are likely small.[33] Rotations between the molecular groups (*e.g.*, between the *n*-butyl chains and the tertiary N-atom on the donor) were allowed for optimizing the structure in order to obtain the best spatial arrangement and explanation of the STM contrast.

As discussed above and demonstrated again by Fig. 6(a) the *tert*-butyl groups are located on the lobes of the tetramers. The thiophene and the thiazole rings are in contact to the surface in a face-on geometry, in agreement with XPS. Of course, small tilts of the ring planes *versus* the surface are compatible with the data. The tetramers are formed by four molecules of the same handedness, leading to a circular arrangement. Any hypothetic changes in the handedness would lead to repulsive electrostatic interactions between the CN-groups of neighboring molecules, and, in addition, to arrangements that are incompatible with the STM images. The positions of the four molecules in a tetramer can approximately be obtained by 90° rotations around the central lattice point. However, small lateral offsets have to be taken into account, too. These cause that the rotational symmetry of the tetramer is C_2, instead of C_4 (see Fig. 6(b)), and a $P211$ space group applies. Thus, the tetramers consist of two pairs of symmetry equivalent molecules which are marked by different color shadings in Fig. 6. Besides the explanation of the prominent lobes by the *tert*-butyl groups, the structure model explains further details in the STM images. The dark areas with low topographic contrast between the tetramers in the direction of the longer lattice vector $\mathbf{b}_2$ in Fig. 6(a) comply with areas of uncovered Ag surface. Furthermore, the extended structures of intermediate

topographic contrast in the middle of the unit cell can be related to the molecular backbone including the terminal CN-groups and the *n*-butyl chains.

For explaining the lateral packing we propose two types of intermolecular bonds, which we denote as primary and secondary bonds. Both can be identified in the space filling hard-sphere model of Fig. 6(c) from the contact points between the molecules. In Fig. 6(b) the primary and presumably stronger bonds are indicated by lobes of light blue color. These are formed between one of the CN-groups of a **HB238** molecule and the close lying hydrogen atom located on the thiophene ring of the neighboring molecule. The primary bonds stabilize the tetramers and mark them as the building blocks of the α-phase. We note again, that this attractive interaction between oppositely charged groups of the molecules would be impossible, if not all molecules within a tetramer had the same handedness. The secondary weaker bonds connect the tetramers along both lattice vectors ($\mathbf{b}_1$, $\mathbf{b}_2$) by interactions between the CN-groups and the *n*-butyl groups. Here, for the *n*-butyl groups the situation is as follows. Due to strong polarization of the carbon nitrogen bond, the strongest hydrogen bond can be expected for the hydrogen atoms which are bound to the carbon atom connected directly to the tertiary amine. For the other hydrogen atoms of the *n*-butyl group considerably weaker hydrogen bonds are expected.

Along the shorter lattice vector $\mathbf{b}_1$, the tetramers are closer (~5%) to each other, resulting in presumably stronger bonds compared to the $\mathbf{b}_2$ direction. Both, primary and secondary bonds are related to interactions between the acceptor and donor groups of **HB238**. Supposing that the molecular electrostatic dipole moment still exists to some, although reduced, extent in the adsorbed layer, it provides an explanation for the circular arrangement within the tetramers. The circular arrangement leads to a mutual compensation of the electrostatic dipole moments which is energetically favored. The formation of the tetramers for dipole compensation is thus an alternative to the formation of molecular dimers in bulk structures.[5,7]

The lateral position of the monolayer with respect to the Ag(100) surface has not been determined experimentally, yet. However, our structure model suggests a registry wherein all four molecules within the unit cell occupy similar adsorption sites. As seen in Fig. 6(b), the two S atoms of the donor and acceptor group are located on two very similar positions (~bridge positions) around the four-fold hollow sites of the Ag(100) surface. This fits to the conclusion from XPS and may indicate that the sulfur atoms indeed play a important role for the bonding of **HB238** to the surface.

Conclusions

The observed β-phase of **HB238** on the Ag(100) surface with a coin-role-like arrangement of molecules is dominated by intermolecular interactions. This arrangement corresponds to the structures found for some of the bulk phases of **HB238**.[6,7] The bonding of the edge-on oriented molecules to the surface plays a lesser role here; short range ordered aggregates and domains of only small size are found.

The existence of the second phase, the α-phase, with the molecules in a face-on orientation is remarkable. Very differently to the β-phase, it is long range ordered and forms large and nearly defect free domains. Due to entropical reasons, it was unexpected that such a large and non-planar molecule, of low symmetry and with rotatable side groups forms an ordered structure on the Ag(100) surface. However, a highly ordered and complex structure with chiral tetramers and enantiopure domains containing molecules of one single handedness was observed. The fact that only enantiopure domains are formed, indicates that the molecules can change their handedness by flipping when they bind to the rim of a growing domain on the surface.

The lateral arrangement of the tetramers on the Ag(100) surface constitutes a second aspect of interest, because the structure is commensurate with the Ag(100) surface periodicity. As a consequence, all tetramers exhibit identical adsorption sites on the Ag(100) surface. This is also somewhat unexpected because commensurate structures of large organic molecules typically contain only one or two molecules per unit cell.[34,35] In those situations, the commensurability of the structure can be understood from the preferential adsorption site of the individual molecule. In the present situation, the site is related to a minimum in the interfacial interaction energy of all four constituting **HB238** molecules under the restriction of their lateral arrangement within the tetramer. As explained above, we speculate that the sulfur atoms in the thiophene and thiazole rings contribute to the preference of these distinct adsorption sites. This makes the surface to act as a template.

Finally, we come back to the functionality of ordered MC layers and films. One aspect is given by the structure related optical properties.[6] The arrangement of the **HB238** molecules in tetramers implies circular aggregates of the transition dipole moments which may lead to interesting optical properties.[11,36] Evidently, using such tetramers for optical or electronic purposes requires to prepare them on wide-band gap, non-metallic interfaces that do not strongly perturb or even quench the molecular states. It is presently an open question whether the interfacial bonding to non-metallic surfaces (by van der Waals interactions) in combination with specific kinetic growth conditions will also provide the growth of MC tetramers. Besides the noted possibility to achieve a growth of tetramers, this knowledge is important for the growth of MC films, as it may reveal that the first layers of this type of molecules generally exhibit interface controlled and bulk-unlike structures.

Author contributions

A.J.K. performed the experiments, including data analysis and visualization, and wrote the manuscript. M.R. performed (XPS/

UPS) experiments. N.A.-S. performed supporting STM experiments. R.T. did the DFT calculations, supervised by T.B., S.O. supervised the XPS/UPS experiments and took part in writing the manuscript. D.H. provided the molecular materials. K.M. conceptualized the project and contributed to the writing of the manuscript. M.S. conceptualized and administrated the project, supervised the LEED, STM, and XPS measurements at the synchrotron and wrote the manuscript.

Conflicts of interest

There are no conflicts to declare.

Acknowledgements

The work was supported by Deutsche Forschungsgemeinschaft (DFG) through the research training group 2591. The XPS data was measured at the Diamond Light Source (beamline I09) *via* proposals SI25739 and SI28742. We thank N. Humberg, A. Haags, S. Subach, D. Duncan, and T.-L. Lee for experimental support.

References

1 A. Arjona-Esteban, J. Krumrain, A. Liess, M. Stolte, L. Huang, D. Schmidt, V. Stepanenko, M. Gsänger, D. Hertel, K. Meerholz and F. Würthner, Influence of Solid-State Packing of Dipolar Merocyanine Dyes on Transistor and Solar Cell Performances, *J. Am. Chem. Soc.*, 2015, **137**(42), 13524–13534.

2 J. Vanderspikken, W. Maes and K. Vandewal, Wavelength-Selective Organic Photodetectors, *Adv. Funct. Mater.*, 2021, **31**(36), 2104060.

3 D. Bialas, A. Zitzler-Kunkel, E. Kirchner, D. Schmidt and F. Würthner, Structural and quantum chemical analysis of exciton coupling in homo- and heteroaggregate stacks of merocyanines, *Nat. Commun.*, 2016, **7**, 12949.

4 A. Liess, L. Huang, A. Arjona-Esteban, A. Lv, M. Gsänger, V. Stepanenko, M. Stolte and F. Würthner, Organic Thin Film Transistors Based on Highly Dipolar Donor–Acceptor Polymethine Dyes, *Adv. Funct. Mater.*, 2015, **25**(1), 44–57.

5 H. Bürckstümmer, E. V. Tulyakova, M. Deppisch, M. R. Lenze, N. M. Kronenberg, M. Gsänger, M. Stolte, K. Meerholz and F. Würthner, Efficient Solution-Processed Bulk Heterojunction Solar Cells by Antiparallel Supramolecular Arrangement of Dipolar Donor–Acceptor Dyes, *Angew. Chem., Int. Ed.*, 2011, **50**(49), 11628–11632.

6 A. Liess, A. Arjona-Esteban, A. Kudzus, J. Albert, A.-M. Krause, M. S. A. Lv, K. Meerholz and F. Würthner, Ultranarrow Bandwidth Organic Photodiodes by Exchange Narrowing in Merocyanine H- and J-Aggregate Excitonic Systems, *Adv. Funct. Mater.*, 2019, **29**(21), 1805058.

7 N. Gildemeister, G. Ricci, L. Böhner, J. M. Neudörfl, D. Hertel, F. Würthner, F. Negri, K. Meerholz and D. Fazzi, Understanding the structural and charge transport property relationships for a variety of merocyanine single-crystals: a bottom up computational investigation, *J. Mater. Chem. C*, 2021, **9**(33), 10851–10864.

8 A. V. Kulinich and A. A. Ishchenko, Merocyanine dyes: synthesis, structure, properties and applications, *Russ. Chem. Rev.*, 2009, **78**(2), 141–164.

9 F. Würthner, R. Wortmann and K. Meerholz, Chromophore Design for Photorefractive Organic Materials, *ChemPhysChem*, 2002, **3**(1), 17–31.

10 F. Würthner, G. Archetti, R. Schmidt and H.-G. Kuball, Solvent Effect on Color, Band Shape, and Charge-Density Distribution for Merocyanine Dyes Close to the Cyanine Limit, *Angew. Chem.*, 2008, **120**(24), 4605–4608.

11 F. Würthner, T. E. Kaiser and C. R. Saha-Möller, J-Aggregates: From Serendipitous Discovery to Supramolecular Engineering of Functional Dye Materials, *Angew. Chem., Int. Ed.*, 2011, **50**(15), 3376–3410.

12 S. V. Shishkina, V. V. Dyakonenko, A. A. Ishchenko and A. V. Kulinich, Ideal polymethine state of merocyanines in the crystal, *Struct. Chem.*, 2022, **33**, 169–178.

13 L. Wolthaus, A. Schaper and D. Möbius, Brickstone arrangement in J-aggregates on an amphiphilic merocyanine dye, *Chem. Phys. Lett.*, 1994, **225**(4–6), 322–326.

14 R. W. Owens and D. A. Smith, STM Imaging of Cyanine Dye J-Aggregates Formed on Carboxyl-Terminated Self-Assembled Monolayers, *Langmuir*, 2000, **16**(2), 562–567.

15 A. Lohr, S. Uemura and F. Würthner, Trimeric Cyclic Assemblies of Calix4arene-Tethered Bismerocyanines, *Angew. Chem.*, 2009, **121**(33), 6281–6284.

16 G. Witte and C. Wöll, Organic Surface Science: Creating Order And Complexity Using Self-Assembly, *Phase Transitions*, 2003, **76**(4–5), 291–305.

17 D. P. Goronzy, M. Ebrahimi, F. Rosei, Arramel, Y. Fang, S. De Feyter, S. L. Tait, C. Wang, P. H. Beton, A. T. S. Wee, P. S. Weiss and D. F. Perepichka, Supramolecular Assemblies on Surfaces: Nanopatterning, Functionality, and Reactivity, *ACS Nano*, 2018, **12**(8), 7445–7481.

18 A. G. Slater, L. M. A. Perdigão, P. H. Beton and N. R. Champness, Surface-Based Supramolecular Chemistry Using Hydrogen Bonds, *Acc. Chem. Res.*, 2014, **47**(12), 3417–3427.

19 F. S. Tautz, Structure and bonding of large aromatic molecules on noble metal surfaces: The example of PTCDA, *Prog. Surf. Sci.*, 2007, **82**(9–12), 479–520.

20 M. Piantek, G. Schulze, M. Koch, K. J. Franke, F. Leyssner, A. Krüger, C. Navío, J. Miguel, M. Bernien, M. Wolf, W. Kuch, P. Tegeder and J. I. Pascual, Reversing the Thermal Stability of a Molecular Switch on a Gold Surface: Ring-Opening Reaction of Nitrospiropyran, *J. Am. Chem. Soc.*, 2009, **131**(35), 12729–12735.

21 A. Riemann, L. Browning and H. Goff, Conformational behavior of naphtho-merocyanine dimers on Au(111), *Surf. Sci.*, 2021, **709**, 121837.

22 R. Raval, Chiral expression from molecular assemblies at metal surfaces: insights from surface science techniques, *Chem. Soc. Rev.*, 2009, **38**, 707–721.

23 M. Horn-von Hoegen, Growth of semiconductor layers studied by spot profile analysing low energy electron diffraction - Part I, *Z. Kristallogr.*, 1999, **214**, 591–629.

24 P. Pracht, F. Bohle and S. Grimme, Automated exploration of the low-energy chemical space with fast quantum chemical methods, *Phys. Chem. Chem. Phys.*, 2020, **22**(14), 7169–7192.

25 F. Neese, F. Wennmohs, U. Becker and C. Riplinger, The ORCA quantum chemistry program package, *J. Chem. Phys.*, 2020, **152**(22), 224108.

26 B. H. Loo, Y. G. Lee and D. O. Frazier, Enhanced Raman spectroscopic study of the coordination chemistry of malononitrile on copper surfaces: Removal of ν(CN) degeneracy through π-coordination, *Chem. Phys. Lett.*, 1985, **119**(4), 312–316.

27 A. J. Kny, M. Sokolowski and P. Kury, Increasing the scan speed in high resolution, low energy electron diffraction measurements by presetting the gate time, *Rev. Sci. Instrum.*, 2023, DOI: **10.1063/5.0137991**.

28 A. Schöll, Y. Zou, M. Jung, T. Schmidt, R. Fink and E. Umbach, Line shapes and satellites in high-resolution x-ray photoelectron spectra of large π-conjugated organic molecules, *J. Chem. Phys.*, 2004, **121**(20), 10260–10267.

29 K. M. Baumgärtner, M. Volmer-Uebing, J. Taborski, P. Bäuerle and E. Umbach, Adsorption and Polymerization of Thiophene on a Ag(111) Surface, *Ber. Bunsenges. Phys. Chem.*, 1991, **95**(11), 1488–1495.

30 M. Willenbockel, D. Lüftner, B. Stadtmüller, G. Koller, C. Kumpf, S. Soubatch, P. Puschnig, M. G. Ramsey and F. S. Tautz, The interplay between interface structure, energy level alignment and chemical bonding strength at organic–metal interfaces, *Phys. Chem. Chem. Phys.*, 2015, **17**(3), 1530–1548.

31 J. Tersoff and D. R. Hamann, Theory of the scanning tunneling microscope, *Phys. Rev. B: Condens. Matter Mater. Phys.*, 1985, **31**(2–15), 805–813.

32 *Handbook of Chemistry and Physics*, ed. R. C. Weast, CRC Press, Cleveland, 55th edn, 1974.

33 H. L. Meyerheim, T. Gloege, M. Sokolowski, E. Umbach and P. Bäuerle, Adsorption-induced distortion of a large π-conjugated molecule studied by surface X-ray diffraction: End-capped quaterthiophene on Ag(111), *Europhys. Lett.*, 2000, **52**, 144–150.

34 J. Ikonomov, O. Bauer and M. Sokolowski, Highly ordered thin films of perylene-3,4,9,10-tetracarboxylic acid dianhydride (PTCDA) on Ag(100)., *Surf. Sci.*, 2008, **602**(12), 2061–2068.

35 N. Humberg, R. Bretel, A. Eslam, E. Le Moal and M. Sokolowski, Hydrogen-Bonded One-Dimensional Chains of Quinacridone on Ag(100) and Cu(111): The Role of Chirality and Surface Bonding, *J. Phys. Chem. C*, 2020, **124**(45), 24861–24873.

36 K. A. Kistler, C. M. Pochas, H. Yamagata, S. Matsika and F. C. Spano, Absorption, Circular Dichroism, and Photoluminescence in Perylene Diimide Bichromophores: Polarization-Dependent H- and J-Aggregate Behavior, *J. Phys. Chem. B*, 2012, **116**(1), 77–86.

Chiral self-organized single 2D-layers of tetramers from a functional donor-acceptor molecule by the surface template effect

Anna J. Kny,[†] Max Reimer,[‡] Noah Al-Shamery,[†] Ritu Tomar,[†] Thomas Bredow,[†] Selina Olthof,[‡] Dirk Hertel,[‡] Klaus Meerholz,[‡] and Moritz Sokolowski[*,†]

†*Clausius-Institut für Physikalische und Theoretische Chemie, Universität Bonn, Wegelerstraße 12, 53115 Bonn, Germany*
‡*Department Chemie, Universität zu Köln, Greinstraße 4-6, 50939 Köln, Germany*

E-mail: sokolowski@pc.uni-bonn.de

Additional Information on Experimental Details and DFT Calculations

Sample Preparation and Low Energy Electron Diffraction (LEED)

All experiments were carried out under ultra high vacuum (UHV) conditions at a base pressure of 3×10^{-10} mbar. The Ag(100) surface was prepared by sputtering with Ar ions for 20 min (1×10^{-5} mbar Ar, 1 keV, 5 μA, 300 K) and subsequent annealing at 600 K for ∼30 min. The surface quality was controlled by LEED. A multi-channel plate (MCP) LEED manufactured by OCI Vacuum Microengineering was used for verifying the structural order of the samples for the XPS/UPS and STM measurements. A SPA-LEED manufactured by Omicron NanoTechnology was used for detailed structural analysis. The sample preparation was optimized to yield large terraces. As a consequence of prolonged annealing, the monoatomic Ag steps are partly pinned at segregated surface impurities. This causes that long step edges exhibit a curved shape as it can be seen in Figure 2(a).

The **HB238** was synthesized and purified following the route of Bürckstümmer et al.[1] Photos of a three dimensional model are shown in Figure S1 in order to illustrate its steric structure. A homebuilt Knudsen cell was used for the deposition of the **HB238** using a crucible temperature of 310 °C. During the deposition, the Ag(100) sample was kept at room temperature. Notably, at low sample temperatures of about 110 K, no ordered structures were obtained due to kinetic reasons. The deposition was controlled by a quadrupole mass spectrometer, 200 Prisma of the company Balzer/Pfeiffer. Because the molecular mass of **HB238** (426.19 g/mol) exceeds the range of this mass spectrometer, we monitored m/z = 57 amu/e. Given coverages refer to the coverage of one monolayer (1 ML) which resembles a closed layer of face-on adsorbed molecules in the α-phase. Typical deposition rates were about 0.4 ML/min.

The SPA-LEED instrument was operated at beam currents of about 1 nA. In order to minimize the thermal background, the sample was cooled by liquid nitrogen to 110 K. The brightness and the contrast of the image shown

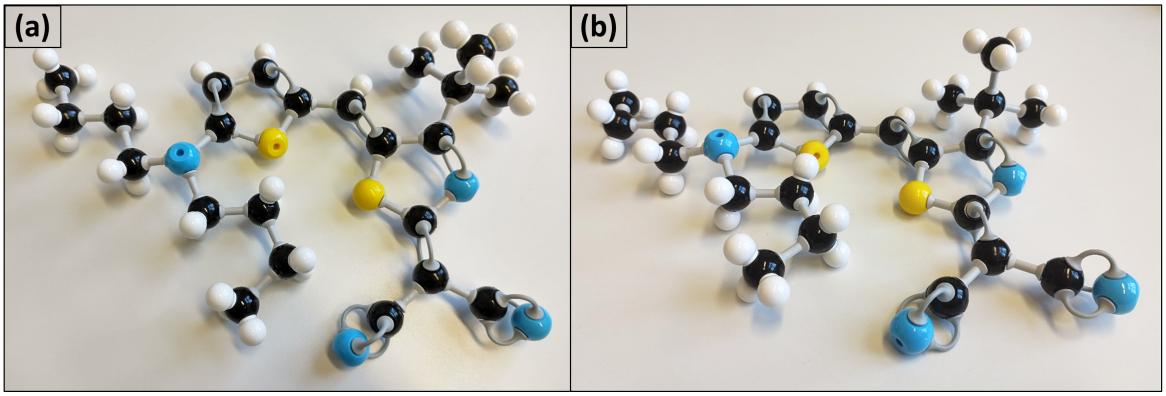

Figure S1: Three dimensional model of **HB238** (*R* enantiomer). The upward pointing *tert*-butyl group which is responsible for the prominent lobes observed in the STM images of the α-phase, is located in the upper right corner of each image. (a) Top view. (b) Inclined view. Color code: white: H, black: C, blue: N, and yellow: S atoms.

in Figure 2(d) were adjusted, and an additional background subtraction was performed. Prior to evaluation, the LEED patterns were deskewed using a software package developed by F. Sojka.[2] The parameters for the deskewing were obtained from recording a SPA-LEED pattern of the commensurate monolayer of PTCDA on Ag(100).[3] The kinematic simulations of the measured patterns were performed with the programs Spot-Plotter[4] and LEEDLab.[2,5]

Scanning Tunneling Microscopy

STM-measurements were done with an UHV 300 STM built by the company RHK Technology and self-cut Pt/Ir-tips (90:10) in constant current mode. Given bias voltages U_{bias} refer to the sample. The sample was cooled by a reduced flow of liquid He to obtain sample temperatures between 34 and 300 K. We had to use very low tunneling currents I_{t} of the order of 5 to 10 pA to obtain stable imaging conditions. At higher currents the molecules were easily displaced by tip sample interactions that are enhanced at smaller tip sample distances required for larger tunneling currents. Routinely, we measured at negative bias voltages. Measurements performed at positive bias voltages were less stable, but provided comparable structural information. For corrections and evaluation of the STM data the software Gwyddion[6] was used. For better visibility of the molecular structures, the brightness and contrast of the STM images were corrected. Error lines, caused by noise, were removed by the fractal correction of the Gwyddion program.[6] The STM images were deskewed such that the lattice fitted to the SPA-LEED data. This procedure corrects the distortions caused by the creep (drift caused by the piezoelectric elements) and thermal drift. STM images of the α-phase at high magnification were finally processed by the correlation averaging tool of the software WSxM.[7]

Photoemission Spectroscopy

UPS measurements were conducted with a helium discharge lamp (He-I, 21.22 eV, at a bias voltage of -8 V) at a pass energy of 2 eV, with an energy resolution (as determined by the width of the Fermi edge) of 110 meV, using a Phoibos 100 hemispherical analyzer (manufactured by Specs) under normal emission. The electron binding energy scale was calibrated using the Fermi edge of a cleaned gold substrate. X-ray photoemission spectroscopy (XPS) measurements were performed with synchrotron light at the beamline I09 at the Diamond Light Source. A hemispherical analyzer was used

and electrons were collected within an emission cone of 56° and an average angle of 45° with respect to the surface normal in the plane of the polarization of the synchrotron light. Photon energies (E_γ) were chosen such that the kinetic energies of the photoelectrons were about 100 eV. Indications for dissociation of molecules upon adsorption were only marginal, i.e., a small peak of about 6% of the total intensity of the S2$p_{3/2}$ peak is observed at 161.75 eV for the monolayer (outside the displayed range of Figure 3). It is presumably related to a small fraction of dissociated molecules at surface defects.[8]

DFT Calculations

The minimum energy structure for an isolated **HB238** molecule was obtained by performing density functional theory (DFT) calculations on 356 conformers which were obtained by using the conformer-rotamer ensemble sampling tool (CREST).[9] DFT calculations were performed with the program ORCA 4.2.1[10] using the Perdew-Burke-Ernzerhof (PBE)[11] functional and the def2-TZVPP basis sets.[12]

Additional information concerning the structure of the β-phase

The information content of STM data of the β-phase is more limited, compared to the α-phase, likely due to the edge-on orientation of the molecules in this phase and makes structural conclusions more speculative. However, here we amend some aspects that can be derived from the spatial demand of the molecules already.

Figures S2(a) and (b) display an STM image of the β-phase and a respective zoom-in, which is overlain by a model comprising five molecules. Notable is the striped fine structure of the aggregates (in vertical direction of Figs. S2(a)/(b)) with a periodicity of 4.7±1 Å,

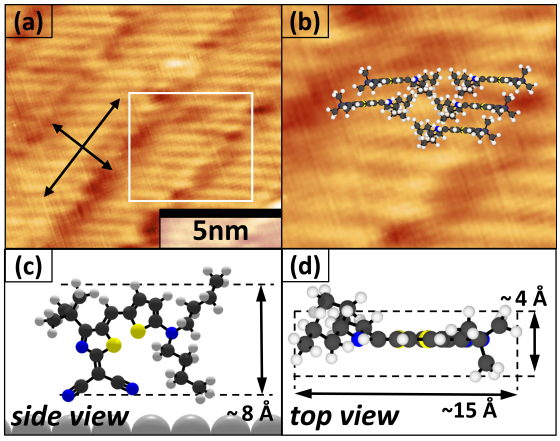

Figure S2: Small scale STM image of the β-phase and hardsphere model. (**a**) STM image of the β-phase (T=40 K, U_{bias}=−0.29 V; I_{t}=5.4 pA). The black arrows indicate the long and short axes of the aggregate. (**b**) Zoom-in of the region marked by the white frame in (a) superimposed by a proposed model showing five molecules. (**c, d**) Side- and top-view of a hardsphere model of **HB238** showing the molecule in edge-on orientation with respect to the Ag surface with indicated geometric dimensions (van der Waals radii reduced by a factor of 0.3). Structural details of the molecule, in particular of the flexible side groups, and the adsorption site on the Ag(100) surface are experimentally unconfirmed (white: H, dark gray: C, blue: N, and yellow: S atoms).

which was already mentioned in the main text. From comparison with the steric demand of a molecule in an edge-on orientation with respect to the surface, we conclude that this fine structure is related to a coplanar π-stacking of the molecules. The geometric dimensions of one molecule in this orientation are indicated in the side- and top-views of the hardsphere model in Figures S2(c) and (d). The estimated thickness of the molecule in the direction perpendicular to the π-system of $\sim$ 4 Å fits to the measured spacing of 4.7±1 Å. The molecule is oriented with its CN-groups to the surface, which is plausible from a chemical point of view.

In the direction of the stripes (horizontal direction in Fig. S2(a)) the aggregates exhibit a

width of ∼15 or ∼30 Å which corresponds to the length of one or two molecules in edge-on orientation. An example for the former case is given by the aggregates shown in Figure 2(c) in the main text, whereas an example for the latter is shown in Figure S2(b) (above). Hence, we propose that the aggregates are stacks of monomers or dimers. A clear topographic separation of the two molecules forming a dimer, which is expected at about the middle of the aggregate, is not seen (s. Fig. S2(b)). On the other hand, the aggregates can be clearly distinguished from each other. A possible explanation could be that the dimer formation is caused by the intertwining of opposing *n*-butyl groups from two molecules in tail-to-tail arrangement, leading to a constant apparent height in the STM image. Differently, the *tert*-butyl groups pointing to the edges of the aggregate cause a topographic separation from the neighboring aggregates that is imaged. This is illustrated in the tentative model in Figure S2(b).

The electrostatic interactions between neighboring molecules and the sterical demand of the *tert*-butyl-groups are the likely reasons that disfavor a simple coin-role-like stacking of the **HB238** molecules. Thus, lateral shifts between the molecules in the direction of the molecular axis and parallel to the surface occur. These varying shifts between the molecules cause changes in the direction of the long axis of the aggregates, which also lead to an inclination of the molecules with respect to the short axis of the aggregate (e.g., by 40° to 50° in Fig. S2(a)/(b)). As a result, the length of the short axis of the aggregate (perpendicular to the long one) can vary, which promotes a dense packing of the aggregates into larger domains (for examples cf. Fig. 2(c) in the main text).

References

(1) Bürckstümmer, H.; Tulyakova, E. V.; Deppisch, M.; Lenze, M. R.; Kronenberg, N. M.; Gsänger, M.; Stolte, M.; Meerholz, K.; Würthner, F. Efficient Solution-Processed Bulk Heterojunction Solar Cells by Antiparallel Supramolecular Arrangement of Dipolar Donor–Acceptor Dyes. *Angew. Chem. Int. Ed.* **2011**, *50*, 11628–11632.

(2) Sojka, F.; Meissner, M.; Zwick, C.; Forker, R.; Fritz, T. Determination and correction of distortions and systematic errors in low-energy electron diffraction. *Rev. Sci. Instrum.* **2013**, *84*, 015111.

(3) Ikonomov, J.; Bauer, O.; Sokolowski, M. Highly ordered thin films of perylene-3,4,9,10-tetracarboxylic acid dianhydride (PTCDA) on Ag(100). *Surf. Sci.* **2008**, *602*, 2061–2068.

(4) Bayersdorfer, P. "Spot-Plotter Version 1.2.1.4", Universität Würzburg. 2008.

(5) Sojka, F.; Fritz, T. "LEEDLab 2018 Version v1.2", Fritz & Sojka GbR, Apolda. 2019.

(6) Necas, D.; Klapetek, P. Gwyddion: an open-source software for SPM data analysis. *Cent. Eur. J. Phys.* **2012**, *10*, 181–188.

(7) Horcas, I.; Fernández, R.; Gómez-Rodríguez, J. M.; Colchero, J.; Gómez-Herrero, J.; Baro, A. M. WSXM: A software for scanning probe microscopy and a tool for nanotechnology. *Rev. Sci. Instrum.* **2007**, *78*, 013705.

(8) Moulder, J. F.; Stickle, W. F.; Sobol, P. E.; Bomben, K. D. In *Handbook of X-ray Photoelectron Spectroscopy*; Chastain, J., Ed.; Perkin-Elmer Corporation, 1992.

(9) Pracht, P.; Bohle, F.; Grimme, S. Automated exploration of the low-energy chemical space with fast quantum chemical methods. *Phys. Chem. Chem. Phys.* **2020**, *22*, 7169–7192.

(10) Neese, F.; Wennmohs, F.; Becker, U.; Riplinger, C. The ORCA quantum chemistry program package. *J. Chem. Phys.* **2020**, *152*, 224108.

(11) Perdew, J. P.; Burke, K.; Ernzerhof, M. Generalized Gradient Approximation Made Simple. *Phys. Rev. Lett.* **1996**, *77*, 3865–3868.

(12) Weigend, F.; Ahlrichs, R. Balanced basis sets of split valence, triple zeta valence and quadruple zeta valence quality for H to Rn: Design and assessment of accuracy. *Phys. Chem. Chem. Phys.* **2005**, *7*, 3297–3305.

A.3. "An Atomistic Analysis of the Carpet Growth of KCl Across Step Edges on the Ag(111) Surface"

by Anna J. Kny, Adam Sweetman, and Moritz Sokolowski.

The research letter is published in the *Journal of Physical Chemistry Letters* 16, 696-702 (2025).

THE JOURNAL OF PHYSICAL CHEMISTRY LETTERS
A JOURNAL OF THE AMERICAN CHEMICAL SOCIETY

pubs.acs.org/JPCL Letter

An Atomistic Analysis of the Carpet Growth of KCl Across Step Edges on the Ag(111) Surface

Anna J. Kny, Adam Sweetman, and Moritz Sokolowski*

Cite This: J. Phys. Chem. Lett. 2025, 16, 696–702 Read Online

ACCESS | Metrics & More | Article Recommendations | Supporting Information

ABSTRACT: The carpet growth of alkali halide (AH) layers across step edges of substrates enables the growth of seamless and continuous large domains. Yet, information about how the AH layer adapts continuously to the height difference between the terraces on the two sides of a step is only described by continuum models, which do not give details of the ionic displacements. Here, we present a first study of thin epitaxial KCl(100) layers grown on the Ag(111) surface by scanning tunneling microscopy that provides atomistic details for the first time. Measurements were performed at room temperature. Using a Cl^--decorated tip, we resolved the ionic arrangement and hence the KCl lattice distortion in the carpet growth region, in some cases even by imaging both types of ions. Our findings demonstrate the ability of the KCl lattice to distort locally over a short distance of four KCl unit cells as a result of the attractive interaction between the ions and the Ag atoms at and close to the steps. For Ag step edges covered by the KCl carpet, we observe a tendency to straighten along the ⟨110⟩ direction of the KCl layer. In addition, the carpet growth induces the formation of Ag microterraces, i.e., the splitting of higher Ag steps into multiple Ag steps of monatomic height during the KCl deposition at elevated temperatures. These microterraces have a minimum width determined by an energetically preferred fitting to the KCl lattice and allow for the carpet growth, while growth across higher Ag steps is not observed.

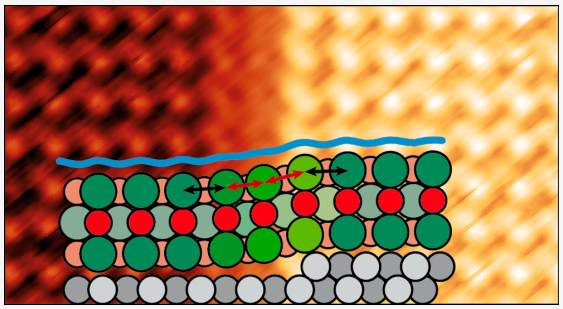

Due to their wide bandgap, alkali halides (AH) offer the opportunity to grow epitaxial, super thin dielectric layers on metal surfaces. While layers of usually just two to three monolayer thickness are still thin enough to allow for electrons to tunnel through, they successfully prevent a hybridization of orbitals of adsorbed molecules with the electronic states of the underlying metal substrate.[1−3] For this reason, AH films are widely used to study the properties of electronically decoupled molecules and their aggregates by scanning tunneling and also by atomic force microscopy.[3−7] A controlled growth of the AH layers is important in order to achieve sufficiently closed and ordered films and hence the aspired properties. However, the lattice mismatch between the AH and the substrate surface causes a non trivial growth situation which strongly depends on the specific material combination. For many combinations of AH and substrates, a growth behavior called *carpet* growth is observed that allows for a seamless growth of AH domains across steps of the substrate.[8−15] Existing models for the carpet growth use a continuum description from elasticity theory for the AH layers in which the specific ionic positions are unresolved.[8,10] However, as AH ions interact with local charges at metal step edges,[14,16,17] distortions of the AH films at step edges are likely. Hence, a continuum model is expected to provide only a coarse approximation of the situation.

In this Letter, we present a detailed atomistic model for the carpet growth of KCl(100) on the Ag(111) surface, which shows that a lattice distortion is indeed present and that it is concentrated in two out of four KCl unit cells in the carpet region at the steps. The ion positions were derived from STM measurements with extremely high atomic resolution. We describe the growth across single, double, and triple steps of the Ag substrate. Two surprising features are seen for Ag step edges which are overgrown by KCl: (i) Higher Ag steps (e.g., double or triple steps) split into monatomic steps and (ii) step edges rearrange in their direction such that they follow the polar ⟨$\bar{1}$10⟩ KCl lattice lines on a local scale. The originally energetically unfavorable situation at the step edge hence changes to one in which both the KCl lattice and the Ag surface adapt to each other, favoring attractive interactions between the ions and the step dipoles.

Received: September 26, 2024
Revised: December 16, 2024
Accepted: December 20, 2024
Published: January 10, 2025

https://doi.org/10.1021/acs.jpclett.4c02809
J. Phys. Chem. Lett. 2025, 16, 696−702

The major reason for the occurrence of carpet growth is that the AH film exhibits a different height for a monatomic layer (ML) than the substrate material. Thus, for AH films thicker than 1 ML, the vertical offset caused by a monatomic substrate step leads to repulsive Coulomb interactions between the ions on the upper and lower terrace at the step. This offset is avoided by continuous carpet growth. It was first observed for the growth of NaCl(100) layers on the semiconductor surface Ge(100) by Schwennike et al.[8] Using a continuum model for the AH layer, it was explained how the AH film grows seamlessly across substrate steps and adapts to the new terrace height like a uniform carpet.[8] In this model, the strained carpet regions connect the undistorted domains on the upper and lower substrate terraces and extend laterally and vertically over many unit cells.[8] This keeps the unfavorable vertical bending of the AH layer, which would otherwise create repulsive Coulomb forces, small, but only at the expense of a loss of interfacial binding energy in the areas close to the steps in which the AH film is detached from the Ge surface.[8]

STM measurements on AH films of thicknesses up to three atomic layers have reported widths for the strained carpet region of 25 Å for NaCl/Ge(100),[18] 15.7 Å for NaCl/Ag(100),[10] and 8 Å for NaCl/Ag(111).[14] Assuming a surface lattice constant of $a_{NaCl} = 1/\sqrt{2} \cdot a_{bulk} = 3.99$ Å,[19] this implies that the strain in the AH layer is distributed over a length of two to six surface unit cells in the direction perpendicular to the substrate step edge. Furthermore, a strain in the direction parallel to the step edge could also be present but was not resolved yet. A film thickness dependent width of the carpet region was found by low energy electron diffraction measurements for NaCl/Ge(100)[8] and NaCl/Ag(100).[10] The increase in the width of the carpet regions with the layer thickness indicates a gradient of the lattice distortion of the AH layers in the vertical direction.

Considering the carpet growth on metal surfaces, the "smearing out" of the electron density at step edges, leading to the Smulochowski dipole, also needs to be considered. It can influence the ionic arrangement at the step edge. The electron density excess at the lower step edge site and the depletion at the upper one[20] promote a growth mode with the polar $\langle \bar{1}10 \rangle$ direction of AH domains parallel to the step edge.[17] This is evidenced by the observation that domains often nucleate at step edges,[14,15,21] either on the upper or the lower step edge site, although this does not rigorously exclude a growth starting at defects on terraces. A growth starting at steps is also found for AH layers growing on-top of a 2 ML thick wetting layer as, e.g., reported for KCl/Ag(100).[11,21] Due to the favored adsorption sites created by the Smulochowski dipole and the resulting ion arrangement on the upper and lower step edge sites, multilayer AH domains have the same azimuthal orientation on the upper and lower terrace. This promotes the seamless overgrowth of the steps and induces carpet growth.

For the present reported experiments, sample preparation and measurements were performed in ultra high vacuum at a base pressure of 2×10^{-10} mbar. The Ag(111) crystal was cleaned by sputtering with argon ions (10^{-5} mbar argon, 1 kV beam energy, 5 mA emission current) and subsequent annealing at about 820 K. The KCl (purchased from VWR, >99.5%, degassed in UHV) was deposited from a Knudsen cell at 853 K while the sample was kept at an elevated temperature of 403 K (±5 K). Mühlpointner et al. found that this temperature is the optimal one for gaining a minimum of remaining bare Ag surface for a growth of KCl on Ag(100).[22] All measurements were performed at room temperature using a tungsten tip on a ScientaOmicron VT-STM/AFM instrument with a Nanonis controller. Given bias voltages (U_{bias}) refer to the sample. Images were recorded in constant current (I_t) mode.

We start by giving some general details about the growth of KCl on Ag(111) before we focus on the carpet growth. Monolayer thick wetting layers are rare for AH,[16,23] as these would require stronger compensation of the ionic charges by the respective mirror charges of the metal surface, compared to AH bilayers. We exclusively observed two layer thick wetting layers of KCl on Ag(111) for an overall coverage of about 2.5 ML that was chosen for our experiments. In addition, we observed partly a third layer on top of the wetting layer. Examples for 3 and 2 ML KCl layers are shown in Figure 1 (a) and (b), respectively. The KCl domains were of up to few hundreds of nm in size. Rare patches of uncovered Ag(111) surface were used to determine the layer thickness. Although the geometric single layer thickness derived from the 3D bulk unit cell is 3.15 Å,[19,24−27] measured layer heights are far below the geometrically expected one due to the dielectric character of KCl. For measurements in constant current mode, this causes the tip to be less retracted from the surface for every additional KCl layer. As will be discussed later, this leads to different image contrasts for different layer heights of the AH film. We obtain 2.94 ± 0.04 Å for the height of KCl bilayers with respect to the Ag surface, while we measure a height of 1.66 ± 0.01 Å for a third monatomic layer grown on top of a bilayer. This is in agreement with earlier reports for KCl on Ag(100).[28]

As mentioned above, an atomistic analysis of the carpet growth requires knowledge about the ionic positions in the carpet region and hence a very high resolution of the STM measurements. Thus, we now comment on the STM resolution and contrast that we achieve using decorated W-tips. Figure 1 (a) shows an overview STM image with two monatomic Ag steps, which are overgrown by a KCl domain of 3 ML height. For better visibility, Figure 1 (c) shows a magnification of the ion arrangement at the Ag step edge. From STM measurements reported for metallic and Cl^- decorated W-tips,[29] we conclude that the bright protrusions observed in our STM images correspond to the positions of the Cl^- ions. Interestingly, for one set of tunneling parameters, we were able to image both the K^+ and the Cl^- ions simultaneously, for KCl bilayers, as shown in Figure 1 (b), and partly for the carpet growth regions of 3 ML domains as it is visible in Figure 1 (c). In our measurements, this type of image contrast was reproducible and stable.

To date, the simultaneous imaging of anions and cations was only observed in rare cases, e.g., by Lauwaet et al.[13] for NaCl/Au(111), and only for low temperatures of 4 K. To the best of our knowledge, we report the first measurements of this kind at room temperature. The difficulty for imaging both type of ions is that tunneling with a metallic W-tip through its $d_{x^2-y^2}$-, p_z-, or s-orbitals, which all interact with the Cl^- p_z-orbitals of the KCl layer, does not offer the spatial resolution needed.[29] This suggests that the W-tip in our measurements was decorated with an adsorbed Cl^- anion. This type of tip decoration was analyzed for NaCl/Au(111) by Li et al.[29] who found that the imaging of either Na^+ or Cl^-, or of both ions simultaneously can be achieved for different tip−sample distances and hence by an appropriate choice of the tunneling parameters. We

https://doi.org/10.1021/acs.jpclett.4c02809
J. Phys. Chem. Lett. 2025, 16, 696−702

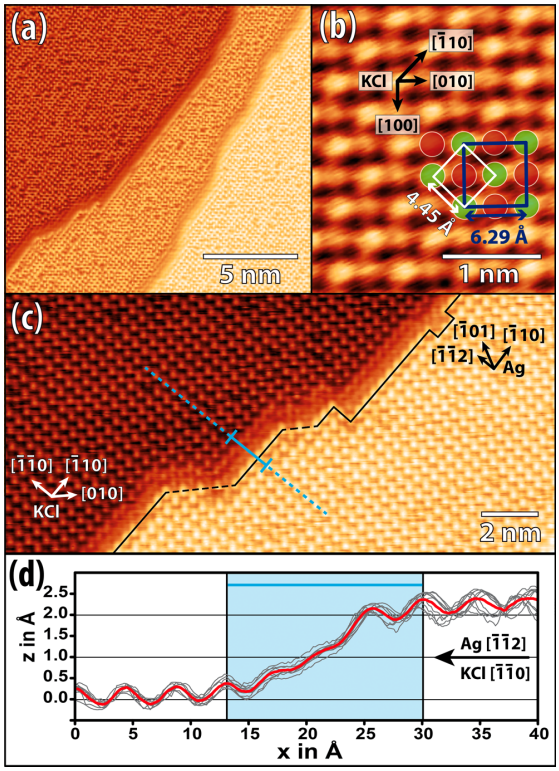

Figure 1. (a) Overview STM image of a KCl layer of 3 ML height which grows across two Ag steps of monatomic height. (b) STM image of a 2 ML KCl layer showing the positions of both ions superimposed by a hard sphere model (U_{bias} = −1.684 V, I_t = 3 nA). The STM image was measured at a different sample region than images (a) and (c). The projected KCl bulk unit cell (dark blue), the smaller KCl surface unit cell (white), and the lattice directions of KCl are indicated. Color code: Cl^- (green spheres), K^+ (red spheres). (c) Magnification of the step edge area of (a) and indicated lattice directions for KCl and Ag. Higher terraces are indicated by a brighter color. As demonstrated by the dotted line in light blue, no lateral shifts are observed between the domains on the upper and lower Ag terrace. (d) Scatter plot (gray) and averaged line profile (red) measured along the KCl [1̄10] lattice direction across the monatomic Ag step visible in (c). In (c) and (d), the width of the carpet region is indicated by the solid line in light blue. U_{bias} = −1.3 V, I_t = 0.56 nA. For further details, see text.

achieve the same variation of the contrast when we keep the tunneling parameters constant but measure AH films of different thicknesses. This can be derived from line profiles extracted from the image of Figure 2 (c) (displayed in Figure S1 of the Supporting Information (SI)). These show a much higher atomic corrugation for the Cl^- ions of the third layer (52.7 ± 2.6 pm) compared to those in the KCl bilayer (14.7 ± 1.8 pm). The reason for this is that the overlap between the Cl^- p_z-orbital of the tip and the p_z-orbitals of the ionic layer increases when the tip−sample distance is decreased, as it occurs for tunneling on the third layer for the same I_t set point.[29] Because of this increased contrast for 3 ML KCl domains, we focus on these to study the carpet growth.

In Figure 1 (c), sections of the step edge following the polar ⟨1̄10⟩ and nonpolar ⟨010⟩ KCl lattice lines mentioned above are indicated by solid and dotted black lines, respectively. As expected from the orientation effect related to the Smulochowski dipole, we find that the domains on the different terraces displayed in Figure 1 (a) and (c) have the same orientation, and we observe large sections in which the Ag steps run parallel to the polar ⟨1̄10⟩ lattice lines of the KCl layer. The AH layer thickness of 3 ML on both sides of the monatomic Ag step is hence an example of a situation in which carpet growth is expected to occur. An experimental evidence for this is that we find Cl^- ions of intermediate height contrast for four unit cells, marked by the light blue solid line in Figure 1 (b), in the region attached to the Ag step. A respective line profile is displayed in Figure 1 (d). This shows that the KCl film is vertically lifted from the lower terrace in a region close to the step edge, which we consider as the carpet region in the following. We note that we describe the exact positions of the ions in the carpet region below.

Before this, we discuss the fact that the KCl lattice is laterally strained due to the carpet growth and its possible impact. From the values of the bulk structure unit cells which are at 25 °C 4.0856 ± 0.0020 Å for Ag[19,30−32] and 6.2915 ± 0.0036 Å for KCl,[19,24−27] we expect the KCl(100) surface lattice constant ($1/\sqrt{2}\cdot a_{KCl}$ = 4.45 Å) to be 1.54 times larger than the Ag(111) surface lattice constant ($1/\sqrt{2}\cdot a_{Ag}$ = 2.89 Å). For clarity, the on the KCl(100) surface projected KCl bulk unit cell (dark blue) and the KCl(100) surface unit cell (white) are indicated in Figure 1 (b). For the KCl(100) lattice on the terrace but in a range of 15 nm adjacent to the strained carpet growth region, we obtained lattice constants of 4.29 ± 0.06 Å parallel to the Ag step edges and a lattice constant of 4.34 ± 0.07 Å perpendicular to the Ag step edges. For a detailed description of the determination method and comments about the errors, we refer to the SI. The difference of 1% between the two lattice constants is within the error range of our measurements and should be considered with care. However, the contraction of about 3% compared to the bulk derived lattice constant (4.45 Å) is beyond the error range, and hence, we consider this to be a result of a lateral distortion of the KCl lattice on the Ag(111) surface. The contraction is surprising as it causes stress in the ionic layer.

In the following, we draw some conclusions on a possible commensurability of the KCl lattice to the Ag(111) surface in the directions parallel and perpendicular to the Ag steps. The discussion of a possible commensurability is motivated, because it may be partly the driving force for the observed lateral contraction of the KCl lattice. Parallel to the steps, the polar KCl [1̄10] lattice direction is parallel to the Ag ⟨1̄10⟩ lattice line. In this direction, a commensurate growth of second order would be possible for a KCl lattice constant of 4.33 Å, which is within the error range of the measured lattice constant (4.29 ± 0.06 Å). This would favor a straightening of the Ag step edges along the KCl [1̄10] direction, as observed in our measurements. For a respective model, we refer to Figure 3 (c), below.

In the direction perpendicular to the Ag steps, the [1̄1̄0] direction of the KCl lattice is parallel to the Ag ⟨1̄1̄2⟩ lattice line (Figure 1 (c)). As the periodicity of the Ag lattice in the ⟨1̄1̄2⟩ direction can be described by a lattice constant of $\sqrt{\frac{3}{2}}\cdot a_{Ag}$ = 5.00 Å (cf. Figure 3 (c)), a commensurate KCl growth of eighth order could occur on the terraces for a KCl [1̄1̄0] lattice constant of 4.38 Å. This would be within the error range of our measurements, but due to the high order of

https://doi.org/10.1021/acs.jpclett.4c02809
J. Phys. Chem. Lett. 2025, 16, 696−702

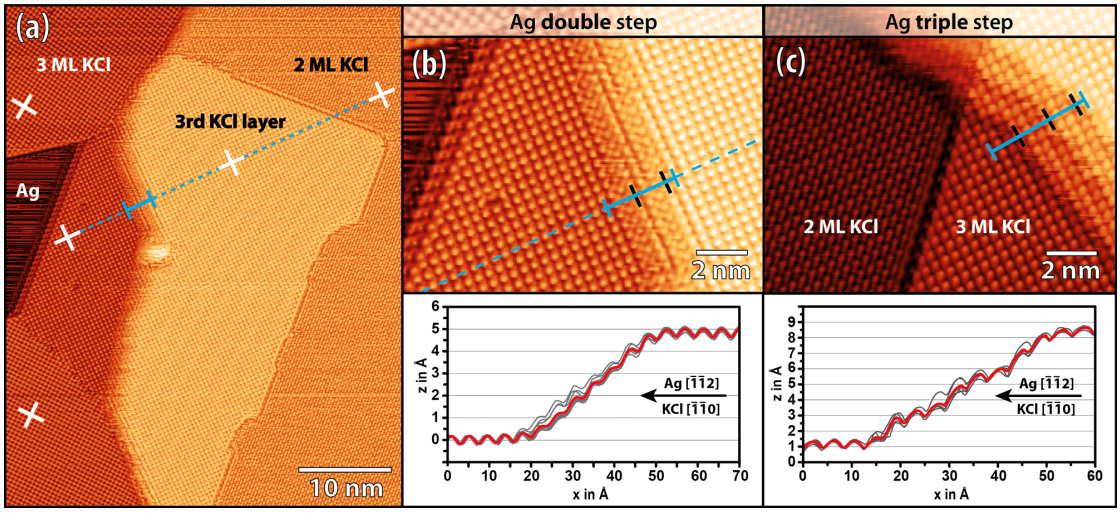

Figure 2. (a) Overview STM image showing different rotational domains of KCl beside bare Ag patches on the lower terrace (left side) and a KCl layer of 3 ML height growing from the upper terrace across the Ag double step in a carpet like growth mode. Domain orientations are indicated by white crosses, whose lines follow the polar lattice lines of KCl. In (a), (b), and (c), the carpet width is indicated by a blue solid line. (b) STM image and line profiles showing the carpet growth across the split Ag double step displayed in (a). The KCl layer is of 3 ML thickness. (c) STM image and line profiles showing the growth of a KCl layer across a Ag triple step. The image was taken in a different sample region than (a). The KCl layer on the left side is of 2 ML, the layer on the right side of 3 ML thickness. Step and height indication are as above. In (b) and (c), microterraces are indicated by black markers along the blue solid line indicating the carpet width. Line profiles are given as a scatter plot, with the averaged data displayed in red. $U_{bias} = -1.684$ V, $I_t = 3$ nA.

commensurability, we expect only a low impact on the orientation of the KCl domains.

However, a monatomic Ag step causes a shift between the Ag terraces which equals one row of Ag atoms in the $\langle\bar{1}12\rangle$ direction. This shift $(0.5\cdot\sqrt{\frac{3}{2}}\cdot a_{Ag})$ decreases the order of commensurability perpendicular to the steps from eighth to fourth, but only for the carpet growth region, connecting both Ag terraces. This might hence explain why the width of the carpet region equals four KCl unit cells in our experiments. Furthermore, it might be an additional reason for the lateral distortion in the carpet growth region, which we report below. As an interim summary, we state that a commensurate growth parallel to and to some extent also perpendicular to the Ag steps may play a role in the observed lattice contraction and width of the carpet region.

Beside the growth across Ag single steps discussed so far, the carpet growth also proceeds across higher Ag steps, which we will discuss now. As an example, Figure 2 (a) and (b) shows a Ag double step which is partly overgrown by a KCl layer of 3 ML height. Figure 2 (c) shows a Ag triple step overgrown by both a KCl bilayer (left side) and a KCl triple layer (right side). In Figure 2 (a), we observe a wetting layer of 2 ML thickness on the upper terrace, which is partly covered by a third layer. The white crosses in Figure 2 (a) indicate the polar directions of the KCl lattice and thus the domain orientations. The third layer grows in registry with the wetting layer, and no change in the orientation is observed. Furthermore, as indicated by the dotted line in light blue, this domain grows across the Ag double step and continues on the lower Ag terrace without a lateral shift. The carpet region is indicated by a solid line in light blue. The two adjacent KCl domains on the lower Ag terrace of Figure 2 (a), on the other hand, do not overgrow the Ag double step as evident from their different orientations. As most KCl domains start growing at Ag steps, which are in $\langle\bar{1}10\rangle$ orientation, angles between KCl domains on Ag(111) are found to be multiples of 30°.

Figure 2 (b) shows a magnification of the carpet growth region of Figure 2 (a) and the respective line profiles given as a scatter plot. As Figure 2 (a) reveals, we observe that the double step is maintained as a (not split) double step for those regions where it is not overgrown by a KCl carpet but where it only constitutes a boundary of the KCl domains. This is important because higher Ag steps which are overgrown by a coherent KCl domain generally split into multiple single steps. This splitting is indicated by the black markers on the light blue lines indicating the carpet region in (b) and (c). The so formed microterraces between two monatomic Ag steps are of about 13 Å in width. This equals the width of three KCl unit cells and hence also the number of KCl unit cells in the carpet region of a single step minus one (see above). An example of the growth across a Ag triple step and respective line profiles are shown in Figure 2 (c). Although, we observe kink sites and hence changes in the course of the step, the microterraces never have a width of less than 13 Å. Thus, we can conclude that a carpet growth on Ag(111) only exists for monatomic Ag steps. In case of higher Ag steps, i.e., double and triple steps, the Ag steps split and form microterraces which allow for the carpet growth. We assume that this step splitting occurs during the KCl deposition at the elevated sample temperature (403 K).

To obtain an atomistic structure model for the strained carpet region, we analyzed profiles measured along the polar KCl $\langle\bar{1}10\rangle$ direction perpendicular to Ag single and triple steps. These are shown in Figures 3 (a) and (b). The data are displayed as averaged profiles (red lines) of at least six individual scans and compared to hard sphere models. The respective scatter plots are displayed in Figure 1 (d) and 2 (c).

https://doi.org/10.1021/acs.jpclett.4c02809
J. Phys. Chem. Lett. 2025, 16, 696−702

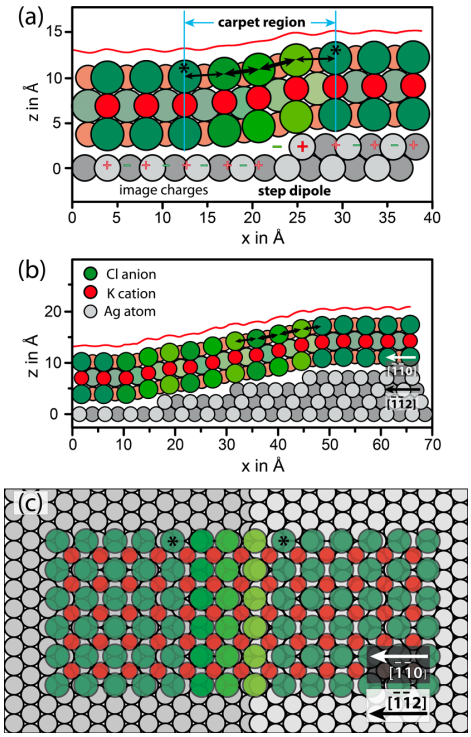

Figure 3. Averaged STM height profiles (red line) and hard sphere models of the carpet growth of a 3 ML KCl layer measured along the KCl $[\bar{1}10]$, and accordingly the Ag $[\bar{1}12]$, direction across a monatomic Ag step (a) and across a Ag step of 3 layer height with induced microterracing (b). Color code as indicated. Atoms in the background are indicated by fainter (K/Cl) or darker (Ag) color. Different green shades highlight Cl^- ions in structurally similar positions within the carpet region. Thick and thin black arrows indicate exemplary stronger and less strained unit cells in the carpet region, respectively. In (a), the step dipole and the image charges are indicated. $U_{bias} = -1.684$ V, $I_t = 3$ nA. The vertical offset of the profiles with respect to the models is subject to some arbitrariness. The top view (c) refers to the monatomic Ag step illustrated in (a) on a reduced scale. The star symbol marks rows of Cl^- ions with similar adsorption sites adjacent to the carpet region.

Coordinates (x, z) of the Cl^- ions are directly derived from the maxima in the profiles. This assumes that electronic effects at the step edge have only a minor influence on the height profile. Cl^- ions on the terraces are displayed by a dark green color. For better visibility, the Cl^- ions in the carpet region are indicated by different green shades. As we cannot derive the positions of the underlying Ag step edges from the STM profiles, the structure models show Ag positions that are compatible with those of the KCl ions. Furthermore, when we compare the carpet growth for a 2 and 3 ML thick KCl layer, we can exclude a coverage dependent broadening of the carpet regions (s. Figure 2 (c)). From this, we can conclude that, to adapt to the height of the next terrace, the ions in a KCl film shift vertically against each other (z direction) but that we do not have a gradient of the lattice distortion between the individual KCl layers.

As already described above, we observe a width of the carpet region of four KCl unit cells for the growth across a Ag single step, as shown in Figure 3 (a). Surprisingly, we find that the strain, induced on the KCl layer when it needs to adapt to the new terrace height, is not distributed uniformly across the KCl unit cells in the carpet region. A monatomic Ag(111) step has a height of 2.36 Å which needs to be overgrown. The unit cells adjacent to the upper and lower terrace compensate for 11% and 16% (±4%) of the height difference Δz (thin arrows in Figure 3 (a)), while the two unit cells marked by thick arrows compensate 51% and 23%, respectively (±3%). This height difference of the Cl^- ions is accompanied by a lateral distortion Δx of the KCl unit cells in $[\bar{1}10]$ direction. Again, the distortion is not distributed uniformly across the carpet region. The minimum next neighbor distance of the Cl^- ions is $a = 3.86 \pm 0.15$ Å and is observed for the unit cell marked by the lower/left thick arrow in Figure 3 (a). This corresponds to a contraction of 11 ± 4% with respect to the lattice constant observed on the terraces, while the other unit cells differ by only 1−2% (±3%). Thus, the main distortion (Δx and Δz) in the carpet region is concentrated on only two of the four KCl unit cells in the carpet region. For the growth across Ag triple steps, as illustrated in Figure 3 (b), we observe the same behavior because the step splitting leads to the growth across three distinct monatomic Ag steps. In order to visualize the arrangement, similar ion positions with respect to the carpet region in (a) and (b) are indicated by same colors.

Due to the adaption of the width of the Ag microterraces discussed above, the Cl^- ions are always close to Ag step edges. Otherwise, we would not be able to interpret the contrast observed in the STM images. For the split triple step in Figure 3 (b), we can describe the situation by three directly adjacent carpet regions. Here, on average, the unit cells marked exemplarily by thick arrows for the upmost carpet region compensate for 42 ± 9% and 38 ± 12% (top to bottom), of the height of a monatomic Ag step. The two peripheral unit cells marked by the thin arrows contribute with 19 ± 5%, and hence, again less to the adaption of the KCl lattice to the height difference of the step. Thus, the situation is very similar to the situation observed for the carpet growth across the monatomic Ag step discussed above. However, as the carpet growth directly continues across the next step edge, the distributions of the lateral distortion (Δx) is more balanced and the unit cells only differ by a maximum of ±6% from the lattice constant found on the terraces. In both of these situations of carpet growth, across monatomic and higher Ag steps, we do not observe a distortion of the unit cells in the direction parallel to the Ag step. However, perpendicular to the step, the projection of the distorted unit cells within the carpet region onto the Ag $\langle\bar{1}12\rangle$ direction leads to shorter distances. This might allow for the Cl^- ions which are on the upper and lower terrace adjacent to the carpet growth region (marked by stars), to occupy the same and energetically preferred adsorption sites with respect to the underlying Ag surface as it is visible in Figure 3 (c).

Thus, we are able to present the first atomistic model for the carpet growth of KCl on Ag(111) from which we learn the following: The ionic arrangement of the KCl lattice at the Ag step appears to be related to the step dipole and leads to preferred growth with the polar KCl $\langle\bar{1}10\rangle$ lattice lines parallel and perpendicular to the step edge. The distortion of the KCl lattice in the carpet region, necessary to adapt to the height of the next terrace, is, however, not distributed uniformly across the width of the four involved KCl unit cells. A possible reason for this could be the attempt of the KCl lattice to adapt to the charge distribution related to the step dipole on the upper and

https://doi.org/10.1021/acs.jpclett.4c02809
J. Phys. Chem. Lett. 2025, 16, 696−702

lower sides of the Ag step edge. This is different from the continuum model for the carpet growth developed by Schwennike et al., who considered a uniform distortion for the NaCl unit cells in the carpet regions on Ge(100).[8] The distortion of the KCl lattice in the x and z direction, which is strongest for the two KCl unit cells indicated by thick arrows in Figure 3, costs energy. On the other hand, the strong, nonuniform distortion of the KCl layer gains energy as the range in which the KCl layer is lifted away from the metal surface is decreased. In particular, the strong vertical distortion is favored by the attractive interactions between the step dipole related charges at the lower part of the Ag step edge and the K^+ ions in the KCl layer. In addition, the KCl layer is always attracted by the mirror charges on the Ag terraces. Finally, the strong bending of the carpet growth region resulting in the width of four unit cells favors the occupation of equal adsorption sites for the Cl^- ions which are on the upper and lower terrace adjacent to the carpet growth region.

For higher Ag steps, an additional loss of energy is avoided by a step splitting of the Ag steps into steps of monatomic height. The width of the created microterraces is determined by the width of the carpet region and cannot fall below it. This step splitting and the azimuthal reorientation of steps is expected to occur during the deposition and is supported by the elevated sample temperature of 403 K. The increased diffusion of Ag and KCl at this temperature, allowing for the step splitting but still low enough to avoid a dewetting of the Ag surface, thus might be the reason that sample temperatures of about 400 K are ideal for growing closed KCl films on Ag surfaces.[22] By these mechanisms, the Ag(111) surface adapts to the KCl layer. This is supported by the high mobility of Ag atoms located at steps or kink sites.[33,34] The system gains energy by step splitting of the higher Ag steps and by straightening of the overgrown Ag steps. A similar straightening of Ag(111) step edges was observed for the carpet growth of NaCl/Ag(111) by Matthaei et al., who performed the deposition at 293−303 K.[14] However, the KCl carpet region observed in our measurements is twice as large as for NaCl (four instead of two AH unit cells)[14] and differently, we also do not observe a reconstruction or a buckling of the KCl layer induced by kink sites of the step edges.[35]

In summary, our studies of epitaxial KCl(100) layers on the Ag(111) surface demonstrate that the ion arrangement in the carpet growth region of AH films on metal surfaces is nonuniform and of a defined, short width of, in our case, four KCl unit cells. Hence, the continuum model for the carpet growth of AH as introduced by Schwennike et al.,[8] is not appropriate here. Instead, models that provide an atomistic description of the ionic arrangement are needed to account for the interactions between the ionic layer and the metal surface, related to the step dipoles, the image charges of the surface, and the possible commensurate arrangement of the AH ions with respect to the metal surface. As these interactions are relevant for all combinations of AH and metal surfaces, although to a different extent, this conclusion applies for all AH films on metal surfaces which show a carpet growth behavior. The KCl induced splitting of higher Ag steps into monatomic steps, made possible by elevated sample temperatures during the deposition, favors the continuous AH growth across the step edges. A direct overgrowth of higher Ag steps does not occur, but the step splitting allows for the growth of the AH domains to continue such that the growth of large domains is enabled. This example of carpet growth also demonstrates that there is a minimum step width of about 13 Å which is needed for the carpet growth to occur. This is of special importance when the growth on vicinal surfaces with small terrace widths is considered, possibly with the aim to further tune growth modes of organic adsorbates on AH decoupling layers.

■ ASSOCIATED CONTENT

Supporting Information

The Supporting Information is available free of charge at https://pubs.acs.org/doi/10.1021/acs.jpclett.4c02809.

It includes additional experimental details concerning the layer corrugation and the determination of the KCl lattice constants (PDF)

■ AUTHOR INFORMATION

Corresponding Author

Moritz Sokolowski − *Clausius Institut für Physikalische und Theoretische Chemie, Universität Bonn, Bonn 53115, Germany;* orcid.org/0000-0001-5991-3910; Email: sokolowski@pc.uni-bonn.de

Authors

Anna J. Kny − *Clausius Institut für Physikalische und Theoretische Chemie, Universität Bonn, Bonn 53115, Germany;* orcid.org/0000-0002-7868-0531

Adam Sweetman − *School of Physics and Astronomy, University of Leeds, Leeds LS2 9JT, United Kingdom;* orcid.org/0000-0002-7716-9045

Complete contact information is available at: https://pubs.acs.org/10.1021/acs.jpclett.4c02809

Notes

The authors declare no competing financial interest.

■ ACKNOWLEDGMENTS

We thank Callum Hayward, Dylan S. Barker, Martin Specht, and Morris E.L. Mühlpointner for experimental support. The work was funded by the German research foundation (DFG) through the research training group 2591. A.S. thanks the Royal Society for funding via a University Research Fellowship, and the ERC for funding under Grant Agreement number 757720 3DMOSHBOND.

■ REFERENCES

(1) Repp, J.; Meyer, G.; Stojković, S. M.; Gourdon, A.; Joachim, C. Molecules on Insulating Films: Scanning-Tunneling Microscopy Imaging of Individual Molecular Orbitals. *Phys. Rev. Lett.* **2005**, *94*, 026803.

(2) Gross, L.; Schuler, B.; Pavliček, N.; Fatayer, S.; Majzik, Z.; Moll, N.; Peña, D.; Meyer, G. Atomic Force Microscopy for Molecular Structure Elucidation. *Angew. Chem., Int. Ed.* **2018**, *57*, 3888−3908.

(3) Kaiser, K.; Lieske, L.-A.; Repp, J.; Gross, L. Charge-state lifetimes of single molecules on few monolayers of NaCl. *Nat. Commun.* **2023**, *14*, 4988.

(4) Imai-Imada, M.; Imada, H.; Miwa, K.; Tanaka, Y.; Kimura, K.; Zoh, I.; Jaculbia, R. B.; Yoshino, H.; Muranaka, A.; Uchiyama, M.; Kim, Y. Orbital-resolved visualization of single-molecule photocurrent channels. *Nature* **2022**, *603*, 829−834.

(5) Illarionov, Y. Y.; Knobloch, T.; Jech, M.; Lanza, M.; Akinwande, D.; Vexler, M. I.; Mueller, T.; Lemme, M. C.; Fiori, G.; Schwierz, F.; Grasser, T. Insulators for 2D nanoelectronics: the gap to bridge. *Nat. Commun.* **2020**, *11*, 3385.

(6) Hoffmann-Vogel, R. Imaging prototypical aromatic molecules on insulating surfaces: a review. *Rep. Prog. Phys.* **2018**, *81*, 016501.

https://doi.org/10.1021/acs.jpclett.4c02809
J. Phys. Chem. Lett. 2025, 16, 696−702

(7) Bombis, C.; Ample, F.; Lafferentz, L.; Yu, H.; Hecht, S.; Joachim, C.; Grill, L. Single Molecular Wires Connecting Metallic and Insulating Surface Areas. *Angew. Chem., Int. Ed.* **2009**, *48*, 9966−9970.
(8) Schwennicke, C.; Schimmelpfennig, J.; Pfnür, H. Morphology of thin NaCl films grown epitaxially on Ge(100). *Surf. Sci.* **1993**, *293*, 57−66.
(9) Bennewitz, R.; Barwich, V.; Bammerlin, M.; Loppacher, C.; Guggisberg, M.; Baratoff, A.; Meyer, E.; Güntherodt, H.-J. Ultrathin films of NaCl on Cu(111): a LEED and dynamic force microscopy study. *Surface Science* **1999**, *438*, 289−296.
(10) Kramer, J.; Tegenkamp, C.; Pfnür, H. The growth of NaCl on flat and stepped silver surfaces. *J. Phys.: Condens. Matter* **2003**, *15*, 6473.
(11) Loppacher, C.; Zerweck, U.; Eng, L. M. Kelvin probe force microscopy of alkali chloride thin films on Au(111). *Nanotechnology* **2004**, *15*, S9.
(12) Repp, J.; Meyer, G. Scanning tunneling microscopy of adsorbates on insulating films. From the imaging of individual molecular orbitals to the manipulation of the charge state. *Appl. Phys. A: Mater. Sci. Process.* **2006**, *85*, 399−406.
(13) Lauwaet, K.; Schouteden, K.; Janssens, E.; Van Haesendonck, C.; Lievens, P.; Trioni, M. I.; Giordano, L.; Pacchioni, G. Resolving all atoms of an alkali halide via nanomodulation of the thin NaCl film surface using the Au(111) reconstruction. *Phys. Rev. B* **2012**, *85*, 245440.
(14) Matthaei, F.; Heidorn, S.; Boom, K.; Bertram, C.; Safiei, A.; Henzl, J.; Morgenstern, K. Coulomb attraction during the carpet growth mode of NaCl. *J. Phys.: Condens. Matter* **2012**, *24*, 354006.
(15) Bera, A.; Morgenstern, K. In Situ Growth and Bias-Dependent Modification of NaBr Ionic Layers on Ag(111). *J. Phys. Chem. C* **2022**, *126*, 10610−10617.
(16) Repp, J.; Fölsch, S.; Meyer, G.; Rieder, K.-H. Ionic Films on Vicinal Metal Surfaces: Enhanced Binding due to Charge Modulation. *Phys. Rev. Lett.* **2001**, *86*, 252−255.
(17) Kiguchi, M.; Entani, S.; Saiki, K.; Inoue, H.; Koma, A. Two types of epitaxial orientations for the growth of alkali halide on fcc metal substrates. *Phys. Rev. B* **2002**, *66*, 155424.
(18) Glöckler, K.; Sokolowski, M.; Soukopp, A.; Umbach, E. Initial growth of insulating overlayers of NaCl on Ge(100) observed by scanning tunneling microscopy with atomic resolution. *Phys. Rev. B* **1996**, *54*, 7705−7708.
(19) *Handbook of Chemistry and Physics*, 55th ed.; Weast, R. C., Ed.; CRC Press: Cleveland, 1974.
(20) Smoluchowski, R. Anisotropy of the Electronic Work Function of Metals. *Phys. Rev.* **1941**, *60*, 661−674.
(21) Müller, M.; Ikonomov, J.; Sokolowski, M. Structure of Epitaxial Layers of KCl on Ag(100). *Surf. Sci.* **2011**, *605*, 1090−1094.
(22) Mühlpointner, M. E. L. Investigations on the Growth of KCl-Films on the Ag(100) Surface via SPA-LEED. Bachelor's thesis, Rheinische Friedrich-Wilhelms Universität, Bonn, 2021.
(23) Bretel, R.; Le Moal, S.; Oughaddou, H.; Le Moal, E. Hydrogen-bonded one-dimensional molecular chains on ultrathin insulating films: Quinacridone on KCl/Cu(111). *Phys. Rev. B* **2023**, *108*, 125423.
(24) Hambling, P. J. The lattice constants and expansion coefficients of some halides. *Acta Crystallogr.* **1953**, *6*, 98.
(25) Barrett, W. T.; Wallace, W. E. Studies of NaCl-KCl Solid Solutions. I. Heats of Formation, Lattice Spacings, Densities, Schottky Defects and Mutual Solubilities. *J. Am. Chem. Soc.* **1954**, *76*, 366−369.
(26) Kantola, M. *X-ray studies on the thermal expansion of solid solutions of KCl and KBr*; VTT Technical Research Centre of Finland, 1947, Vol. 3, p 12.
(27) Walker, D.; Verma, P. K.; Cranswick, L. M.; Jones, R. L.; Clark, S. M.; Buhre, S. Halite-sylvite thermoelasticity. *Am. Mineral.* **2004**, *89*, 204−210.
(28) Humberg, N.; Guo, Q.; Bredow, T.; Sokolowski, M. Growth of Hydrogen-Bonded Molecular Aggregates on a Thin Alkali Halide Layer: Quinacridone on KCl/Ag(100). *J. Phys. Chem. C* **2023**, *127*, 23814−23826.
(29) Li, Z.; Schouteden, K.; Iancu, V.; Janssens, E.; Lievens, P.; Van Haesendonck, C.; Cerda, J. I. Chemically modified STM tips for atomic-resolution imaging of ultrathin NaCl films. *Nano Res.* **2015**, *8*, 2223−2230.
(30) Smakula, A.; Kalnajs, J. Precision Determination of Lattice Constants with a Geiger-Counter X-Ray Diffractometer. *Phys. Rev.* **1955**, *99*, 1737−1743.
(31) Straumanis, M. E. Neubestimmung der Gitterparameter, Dichten und thermischen Ausdehnungskoeffizienten von Silber und Gold, und Vollkommenheit der Struktur. *Mh. Chem.* **1971**, *102*, 1377−1386.
(32) Majee, R.; Kumar, A.; Das, T.; Chakraborty, S.; Bhattacharyya, S. Tweaking Nickel with Minimal Silver in a Heterogeneous Alloy of Decahedral Geometry to Deliver Platinum-like Hydrogen Evolution Activity. *Angew. Chem., Int. Ed.* **2020**, *59*, 2881−2889.
(33) Wolf, J.; Vicenzi, B.; Ibach, H. Step roughness on vicinal Ag(111). *Surf. Sci.* **1991**, *249*, 233−236.
(34) Poensgen, M.; Wolf, J.; Frohn, J.; Giesen, M.; Ibach, H. Step dynamics on Ag(111) and Cu(100) surfaces. *Surf. Sci.* **1992**, *274*, 430−440.
(35) Heidorn, S.; Gerss, B.; Morgenstern, K. Step Edge Induced Reconstructions of NaCl(100) Bilayers on Ag(111): A Route To Alter the Properties of Nanoscale Insulators. *ACS Appl. Nano Mater.* **2018**, *1*, 6818−6823.

https://doi.org/10.1021/acs.jpclett.4c02809
J. Phys. Chem. Lett. 2025, 16, 696−702

An Atomistic Analysis of the Carpet Growth of KCl Across Step Edges on the Ag(111) Surface

–Supporting Information–

Anna J. Kny,[†] Adam Sweetman,[‡] and Moritz Sokolowski[*,†]

[†]*Clausius Institut für Physikalische und Theoretische Chemie, Universität Bonn, Bonn, 53115, Germany*

[‡]*School of Physics and Astronomy, University of Leeds, Leeds, LS2 9JT, United Kingdom*

E-mail: sokolowski@pc.uni-bonn.de

1. Corrugation of KCl layers

To determine the difference in the corrugation of STM profiles for 2 ML and 3 ML KCl layers, line profiles were extracted from STM images which show both layer thicknesses. For demonstration purposes, Figure S1 (a) shows a line profile measured along the KCl [010] direction of the 3 ML and 2 ML layer displayed in Figure 2 (c). For the 2 ML layer both ions are visible in the profile, while only Cl^- anions are imaged in the 3 ML layer. Figure S1 (b) shows a direct comparison of these line profiles for both layer thicknesses measured along the KCl [110] direction. Similar to the data shown in Figure S1 (a), it is clearly visible that the measured corrugation of ions in the 3 ML KCl layer (blue profile) is much higher (roughly by a factor of 3.5) than in the 2 ML layer (orange profile).

2. Determination of the KCl(100) surface lattice constants

For all measurements, thermal drift of the STM was reduced by controlling the temperature of the cryostat attached to the sample stage which was kept stable at a value few Kelvin above the room temperature. In addition the drift compensation, implemented in the Nanonis software, was applied. The STM scan piezos were calibrated beforehand at steps (z-direction) and the atomic lattice of a clean Ag(100) surface which was used for previous experiments. The respective error of the calibration factors is estimated to be of about 1%.

In order to keep the errors for the determination of lattice constants small, all quantitative measurements were performed exclusively along the fast scanning direction.

For the determination of the KCl lattice constants we used a special procedure that was introduced by Gärtner et al.[1,2] It reduces the impact of the remaining drift and other distortions on the determined parameters. Several images were measured under different rotation angles. The measurements were performed on the same domain and close to a step edge, which allows for a safe assignment of the two KCl surface lattice constants **a** and **b**. Their lengths (a, b) were determined independently to account for a possible uniaxial lattice distortion. Importantly, we chose a KCl domain which grows across a Ag step, such that we could assign the two KCl surface lattice constants **a** and **b** to the Ag $\langle\bar{1}\,\bar{1}\,2\rangle$ and $\langle\bar{1}\,1\,0\rangle$ directions, respectively.

The measured images had a size of 5×5 nm and were recorded with a scan speed of 38 nm/s.

Further images of the same domain with varying image sizes and scan speed completed the data set (up to 30 × 30 nm and about 90 nm/s). For all images, distances d_{n_a,n_b} along the fast scanning direction were measured and described by the lattice constants a and b using the parameters n_a and n_b which are integer numbers determined from the STM images. For clarity this is visualized in the plot in Fig. S2 (a). The measured values for d_{n_a,n_b} (69 values in total) were plotted as a function of the values n_a and n_b as shown in Figure S2 (b). The respective values for a, b, and γ and the respective statistical errors were derived from a fit of the data points by using the cosine theorem:

$$d_{n_a,n_b} = \sqrt{(n_a a)^2 + (n_b b)^2 - 2n_a a \cdot n_b b \cdot \cos(\gamma)}. \quad (1)$$

Hereby, γ is the angle between **a** and **b**. Applying this procedure we obtained 4.34 ± 0.02 Å for a, parallel to the Ag $\langle \bar{1}\,\bar{1}\,2 \rangle$ direction, and 4.29 ± 0.02 Å for b, parallel to the Ag $\langle \bar{1}\,1\,0 \rangle$ direction. For γ we obtained $89.52° \pm 0.01°$. We expect γ to be 90°. The obtained deviation of γ from 90° by 0.48° thus gives an upper estimate for the statistical errors of our fitting routine. It is about 0.5%.

Taking the above estimated systematic errors (scanner calibration, drift) of about 1% and the statistical errors of 0.5% together, we estimate the total errors in the determination of the lattice constants to be about 1.5%.

References

(1) Gärtner, S. Die Adsorption von PTCDA auf der sauberen und der oxidierten Cu(100)-Oberfläche. Master's thesis, Rheinische Friedrich-Wilhelms Universität Bonn, 2012.

(2) Gärtner, S.; Fiedler, B.; Bauer, O.; Marele, A.; Sokolowski, M. Lateral ordering of PTCDA on the clean and the oxygen pre-covered Cu(100) surface investigated by scanning tunneling microscopy and low energy electron diffraction. *Beilstein J. Org. Chem.* **2014**, *10*, 2055–2064.

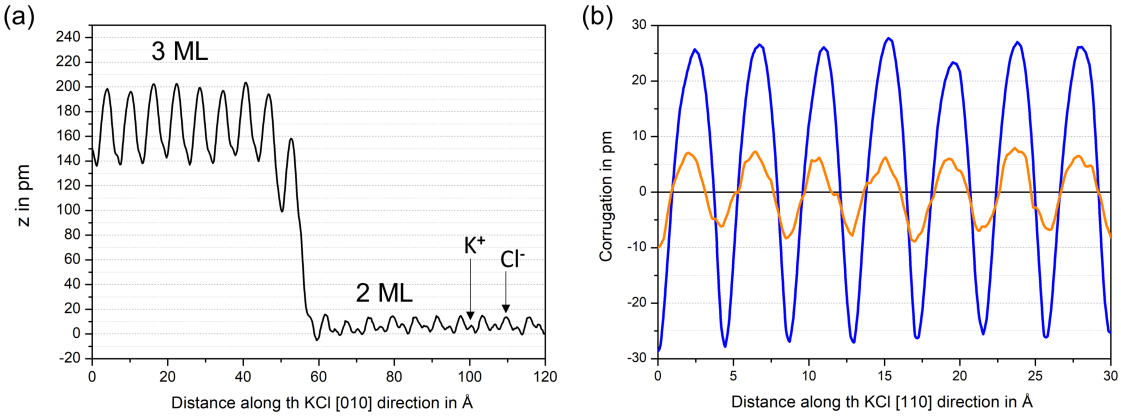

Figure S1: STM line profiles demonstrating the difference in the measured corrugation for 2 ML and 3 ML KCl layers. (a) Line profile measured along the KCl [010] direction showing both, a 2 ML KCl layer (both ions visible, right side), and a 3 ML KCl layer (left side). (b) Direct comparison of line profiles measured along the KCl [110] direction (in this direction only Cl^- anions are visible) for a 2 ML (orange profile) and 3 ML (blue profile) KCl layer. The respective STM image from which the profiles are extracted is displayed in Figure 2 (c). $U_{\mathrm{bias}} = -1.684$ V, I_t=3 nA.

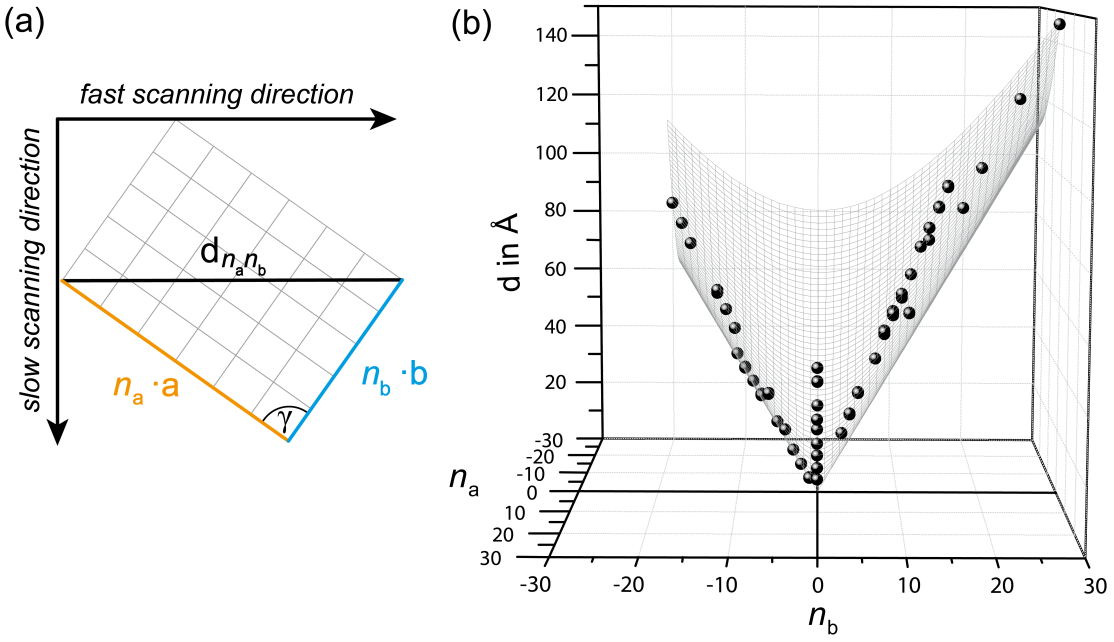

Figure S2: Determination of the surface lattice constants a, b, and γ of the strained KCl(100) lattice on the terraces. (a) Schematic drawing illustrating the measured parameters of the lattice. The plot in (b) shows the distances $d_{n_\mathrm{a},n_\mathrm{b}}$ measured along the fast scanning direction as a function of n_a and n_b (black data points) and a fit (thin mesh) to the data by adjusting a, b, and γ.

B. Crystallographic data of the investigated merocyanines

This Chapter summarizes the crystallographic information of the investigated merocyanines that were obtained in the context of the present thesis. The merocyanines were synthesized in the research groups of K. Meerholz in Cologne and F. Würthner in Würzburg. XRD measurements were performed in cooperation with G. Schnakenburg in Bonn.

As part of this thesis, the crystallographic structures of the merocyanines were investigated. Different from the crystallographic data of Chapter 2, the data presented here were obtained from merocyanine single crystals grown by temperature gradient sublimation in our lab at a reduced pressure of about 1.5×10^{-5} mbar. This was done to exclude the influence of impurities, i.e., solvents, on the crystal growth.

The crystallographic structures were measured by single-crystal XRD. Measurements were performed at room temperature and at 100 K. For all merocyanines, except the merocyanine HB238-D, an additional low-temperature phase was observed. The respective crystallographic data are summarized in Table B.2 for the room temperature structures and in Table B.3 for the structural data measured at 100 K. The molecular arrangement in the crystal structures is illustrated in Figures B.1 to B.5. The Figures present an illustration of the unit cell and the most planar molecular arrangement found in the respective crystal structures. The latter one is displayed in a top view and a side view. Hence, the crystallographic structures are directly comparable to the HB238-A polymorphs reported in literature that are summarized in Chapter 2.

Interestingly, the structures measured for HB238-A were found to be similar to two, in reference [29] reported polymorphs of HB238-A. The room temperature phase of HB238-A was found to be similar to the reported polymorph P1, and the phase observed at 100 K was found to be similar to the polymorph P2. However, the differences in the lattice constants (up to 0.02 Å) are larger than the respective error ranges.

Furthermore, the structure that was measured for HB238-B at 293 K was found to be similar to the structures of the solution-grown HB238-B crystals measured at 100 K (see Table 2.2) [45]. However, here, the deviations were found to be in a range of up to 0.4 Å. The same holds for the structure of HB238-C measured at 290 K. Again, this structure is found to be similar to the solution-grown HB238-C crystals measured at 100 K (see Table 2.2) [2]. Here, the deviations result in a maximum of 0.5 Å. Please note that not all lattice vectors deviate by the same amount, which indicates that the differences in the lattice vectors are not just due to thermal expansion but that the structures reported in literature [2, 45] are still affected by residual solvent molecules incorporated in the crystallographic merocyanine structures. All other crystal structures presented in this

chapter represent new polymorphs of the investigated merocyanines (HB238-C (100 K)), or even the first reported crystallographic data (HB238-D and HB238-E).

Although the molecular arrangement in the unit cell appears to be quite different for all of the investigated merocyanines, the binding motifs in the crystal structures are similar. For the structures of HB238-A and HB238-B displayed in Figures B.1 and B.2, the most planar arrangement of molecules exhibits a herringbone-like arrangement. In the structures of HB238-C, HB238-D, and HB238-E, the molecular packing transforms into a more chain-like arrangement with a head-to-tail orientation of the molecules. In all structures, hydrogen bonds are formed between the CN groups of one molecule and the thiophene ring or the methine bridge of the neighboring molecule. In all the Figures presented in this chapter, hydrogen bonds are indicated by orange dotted lines. The lengths of the hydrogen bonds and the intramolecular distance of the S atoms are documented in Table B.1.

Noticeable is that the buckling of the most planar crystallographic planes appears to increase with an increase in the alkyl side chain length. This effect seems to be even more pronounced for the low temperature phases of HB238-A and HB238-B. In addition to differing stackings of the displayed crystallographic planes, this difference in the layer buckling characterizes the observation of the different (polymorphic) structures despite the fact that the molecular arrangements in the individual layers are very similar to each other.

Table B.1.: Intermolecular hydrogen bond lengths and intramolecular S S distances. The values correspond to the crystallographic data of the investigated merocyanines measured at RT. For HB238-E two different bond lengths are present (see Figure B.5).

	Hydrogen bonds			Sulfur-Sulfur
	CN-R	CN-Thiophene	CN-Methin bridge	Distance
HB238-A	2.7167(1) Å	2.6968(1) Å	2.9688(1) Å	3.1420(1) Å
HB238-B	2.5298(1) Å	2.5611(1) Å	2.6731(1) Å	3.1190(1) Å
HB238-C	2.8831(2) Å	2.5782(2) Å	2.7352(2) Å	3.2203(3) Å
HB238-D	2.5360(1) Å	2.5631(1) Å	2.6826(1) Å	3.1264(1) Å
HB238-E	–	2.9359(2) Å/	2.5170(1) Å/	3.2159(2) Å/
	–	2.8592(2) Å	2.5264(1) Å	3.2043(2) Å

Table B.2.: Crystallographic data of the room temperature phases. Merocyanine crystals were obtained from temperature gradient sublimation and were analyzed by single crystal XRD.

Compound	HB238-A	HB238-B	HB238-C	HB238-D	HB238-E
T/K	293(2)	293(2)	290	293	298
Chem. formula	$C_{23}H_{30}N_4S_2$	$C_{21}H_{26}N_4S_2$	$C_{19}H_{22}N_4S_2$	$C_{17}H_{18}N_4S_2$	$C_{22}H_{28}N_4S_2$
M/g mol^{-1}	426.63	398.58	370.52	342.47	412.60
Crystal color	green	green	metallic blue	metallic blue	metallic blue
Crystal system	monoclinic	orthorhombic	monoclinic	monoclinic	triclinic
Space group	$P2_1c$	Pbca	$P2_1c$	$P2_1m$	P-1
a/Å	13.0896(5)	15.8447(7)	9.9603(8)	9.8761(3)	9.6941(4)
b/Å	19.3157(5)	14.3829(5)	7.1252(4)	6.89933(14)	15.5060(9)
c/Å	9.8424(4)	19.2231(8)	29.0358(22)	13.7303(4)	16.2467(8)
α/°	90	90	90	90	97.181(4)
β/°	101.645(3)	90	94.736(6)	102.4020(22)	100.191(4)
γ/°	90	90	90	90	3.871(4)
V/Å^3	2437.28(15)	4380.8(3)	2053.6(3)	913.72(4)	2374.7(2)
Z	4	8	4	2	4
ρ/g mol^{-3}	1.163	1.209	1.198	1.245	1.154

Table B.3.: Crystallographic data measured for the low temperature phases of the above single crystals. Note that no phase transition was observed for HB238-D at low temperatures. Accordingly, the values are reproduced here for comparison.

Compound	HB238-A	HB238-B	HB238-C	HB238-D	HB238-E
T/K	100	100	100	100	100
Chem. formula	$C_{23}H_{30}N_4S_2$	$C_{21}H_{26}N_4S_2$	$C_{19}H_{22}N_4S_2$	$C_{17}H_{18}N_4S_2$	$C_{22}H_{28}N_4S_2$
M/g mol^{-1}	426.63	398.58	370.52	342.47	412.60
Crystal color	green	green	metallic blue	metallic blue	metallic blue
Crystal system	monoclinic	orthorhombic	triclinic	monoclinic	triclinic
Space group	$P2_1c$	$P2_12_12_1$	P-1	$P2_1m$	P-1
a/Å	13.960(4)	14.3082(3)	7.3407(6)	9.8761(3)	9.5402(5)
b/Å	18.832(3)	15.4990(3)	9.8152(6)	6.89933(14)	16.1152(8)
c/Å	9.075(2)	19.1049(4)	14.1204(10)	13.7303(4)	30.0787(16)
α/°	90	90	102.014(5)	90	81.701(4)
β/°	105.59(2)	90	96.575(6)	102.4020(22)	87.968(4)
γ/°	90	90	101.747(6)	90	79.554(4)
V/Å^3	2298.0(9)	4236.76(15)	961.09(12)	913.72(4)	4499.9(4)
Z	4	8	2	2	8
ρ/g mol^{-3}	1.233	1.250	1.280	1.245	1.218

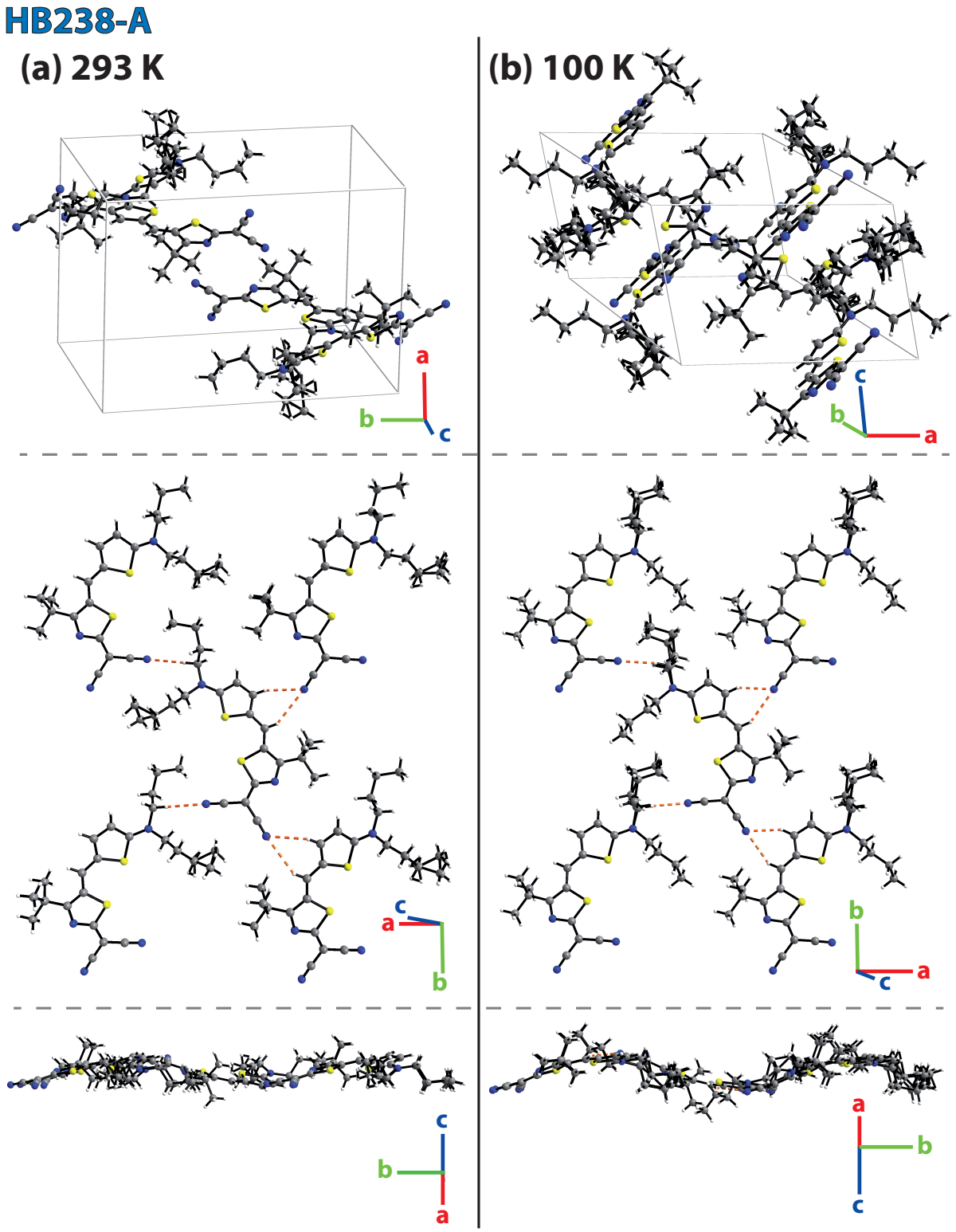

Figure B.1.: XRD data measured for the merocyanine HB238-A. The data displayed in panel (a) were measured at 293 K for the room temperature phase. The data of panel (b) displays the molecular arrangement of the low-temperature phase that was measured at 100 K. Color code as above.

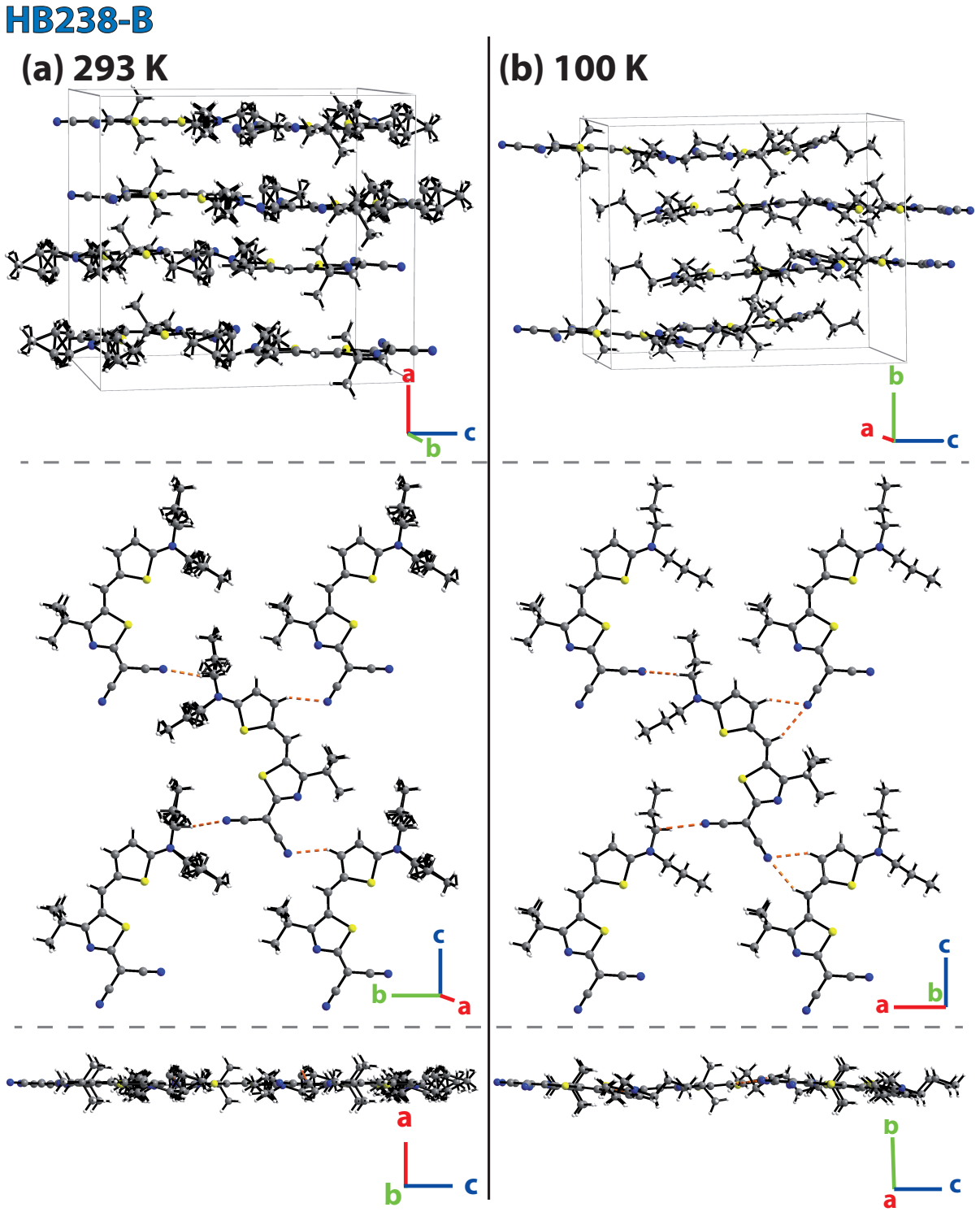

Figure B.2.: XRD data measured for the merocyanine HB238-B. The data displayed in panel (a) were measured at 293 K for the room temperature phase. The data of panel (b) displays the molecular arrangement of the low-temperature phase that was measured at 100 K. Color code as above.

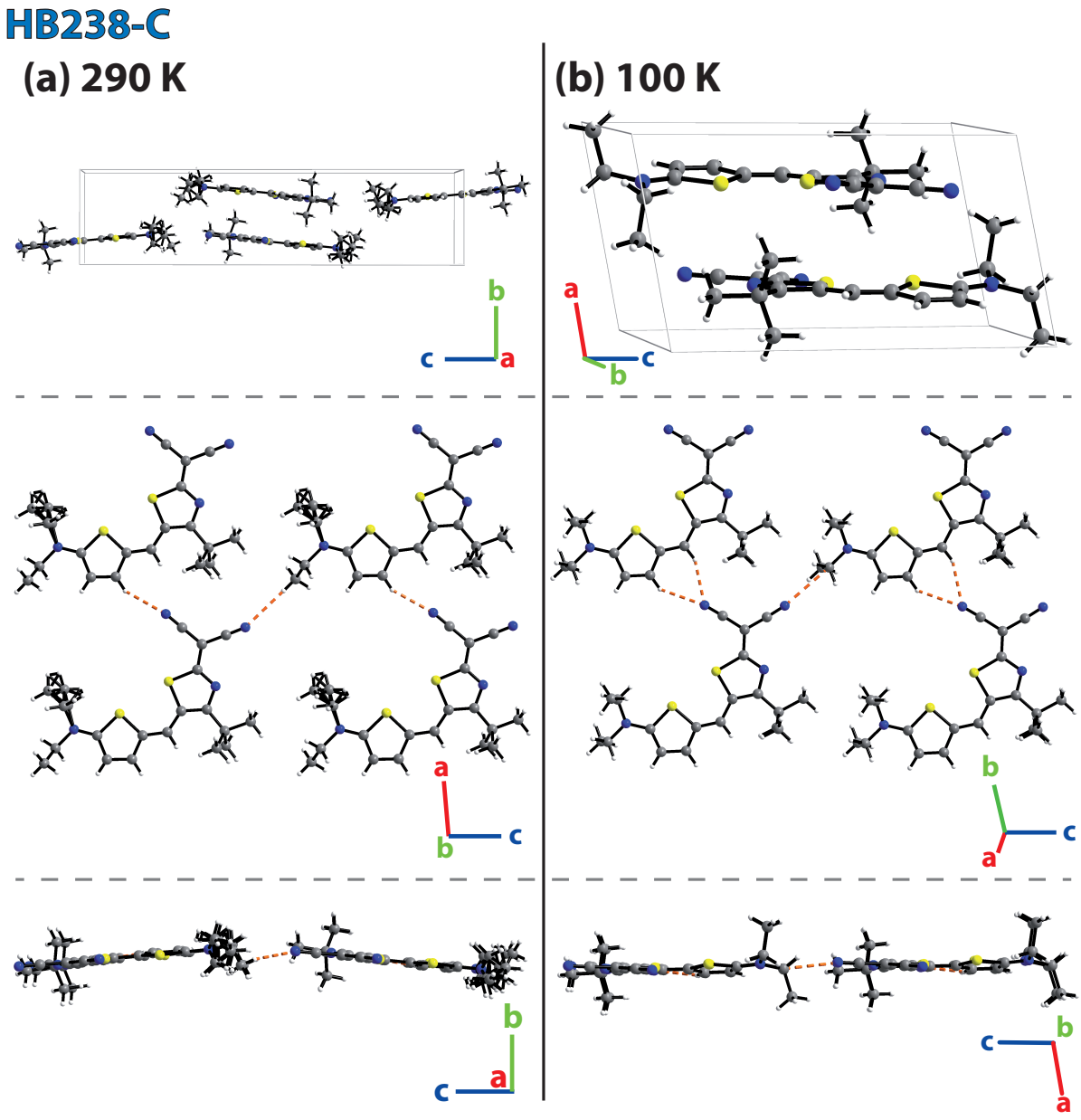

Figure B.3.: XRD data measured for the merocyanine HB238-C. The data displayed in panel (a) were measured at 290 K for the room temperature phase. The data of panel (b) displays the molecular arrangement of the low-temperature phase that was measured at 100 K. Color code as above.

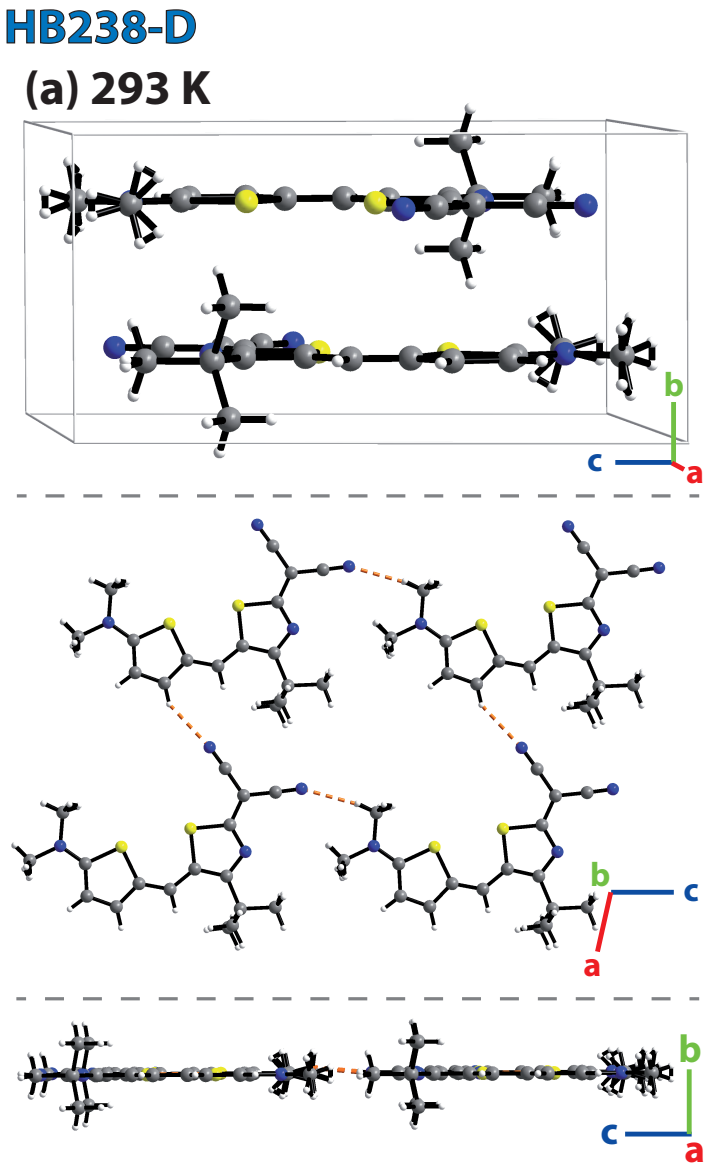

Figure B.4.: XRD data measured for the merocyanine HB238-D. The data displayed in panel (a) were measured at 293 K for the room temperature phase. The unit cell measured at 100 K was found to be equivalent to the room temperature phase. Color code as above.

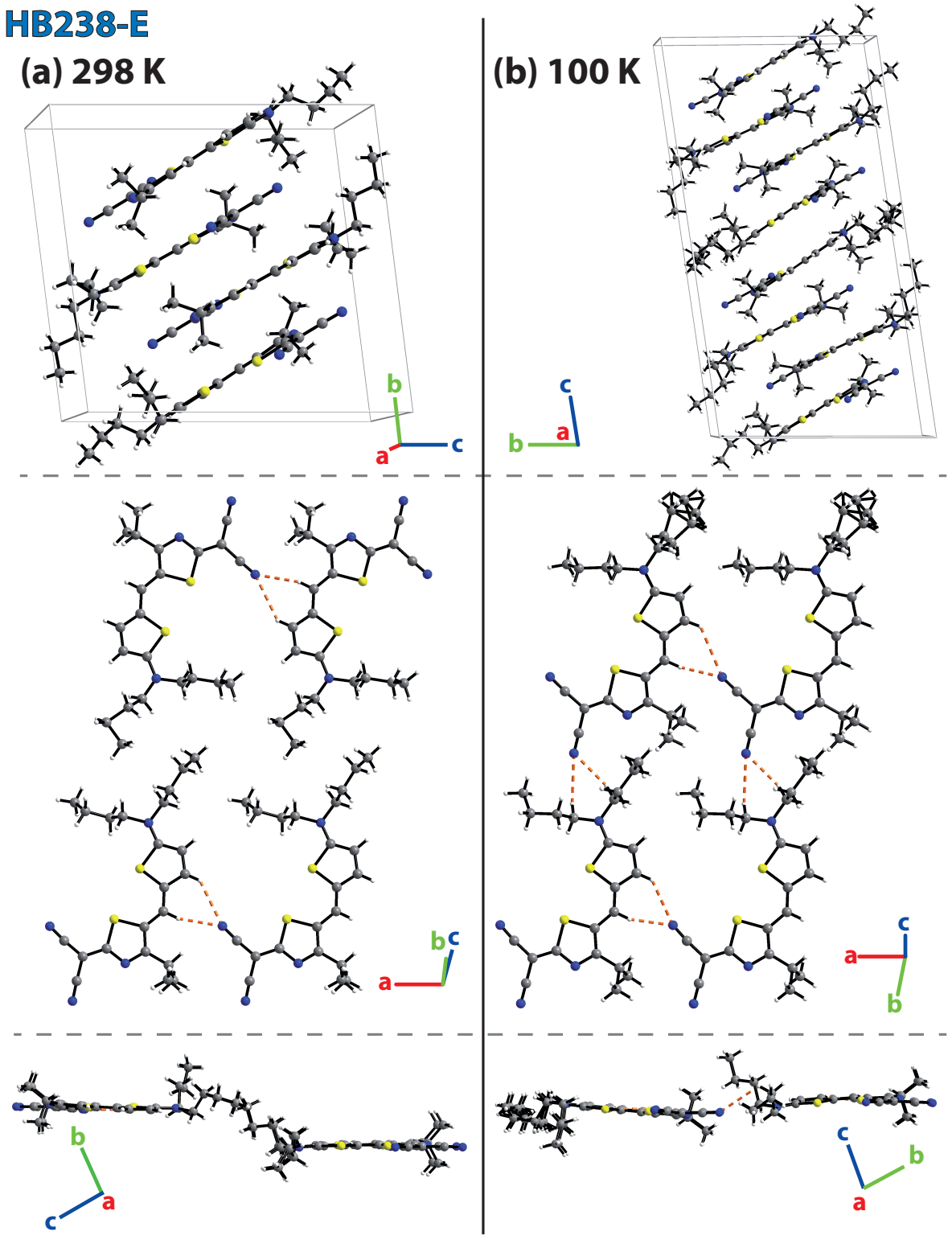

Figure B.5.: XRD data measured for the merocyanine HB238-E. The data displayed in panel (a) were measured at 298 K for the room temperature phase. The data of panel (b) displays the molecular arrangement of the low-temperature phase that was measured at 100 K. Color code as above.

C. Experimental evidence of the molecular arrangement in the α-phase

This chapter provides experimental evidence for the enantiopure tetramer formation of the merocyanines in the α-phase on the Ag(100) surface. Investigations were performed by STM and LEED for monolayers of the merocyanine HB238-E, which exhibits the same molecular structure as HB238-A but an iPr group instead of the tBu group.

The molecular arrangement of the α-phase was probed by investigations of an HB238-A derivative for which the *t*Bu group was replaced by an *i*Pr group. This HB238-A derivative is called HB238-E. The molecular structures of both merocyanines are illustrated in Figure C.1. Here, the *t*Bu group of HB238-A and the *i*Pr group of HB238-E are indicated in blue color.

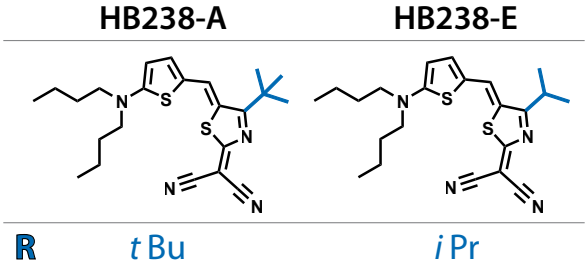

Figure C.1.: Molecular structures of the merocyanines HB238-A and HB238-E. R denotes the alkyl side groups in which the merocyanines differ. In the molecular structures, these groups are indicated in blue.

As explained in Chapter 6, HB238-A forms the commensurate α-phase on the Ag(100) surface. In the respective STM images, the *t*Bu groups are visible as bright lobes (see Figure 6.2 of Chapter 6). The high topographic contrast of the *t*Bu groups observed in the STM images is due to their tetrahedral geometry. Due to this geometry, one of the three Me groups of the *t*Bu group is always at a larger distance with respect to the Ag(100) surface than the π-system of the molecule. Thus, for constant current images, the *t*Bu group is measured as a bright lobe as the smaller distance to the STM tip leads to a higher measured LDOS than for alkyl side groups that are located close to the surface. However, this leads to the problem that the STM images of HB238-A provide only limited information about the orientation of the molecules in the α-phase, as the molecular π-systems are barely visible.

To obtain experimental information about the molecular orientations in the α-phase, the merocyanine HB238-E was investigated. As visible in Figure C.1, HB238-E exhibits the same π-system and the same functional groups as HB238-A. Only the *t*Bu group was replaced by an *i*Pr group. Thus, HB238-E exhibits the same lateral sterical demand in the monolayer as HB238-A and should form the same commensurate monolayer phase as observed for HB238-A. However, the decreased three-dimensional sterical demand of the *i*Pr group in comparison to the *t*Bu group should decrease the topographic contrast of the group in the respective STM images. Accordingly, the bright lobes in the STM images should vanish for HB238-E, and the molecular π-systems should become imageable by STM.

That HB238-E forms indeed the α-phase on the Ag(100) surface was demonstrated by SPA-LEED measurements. The resulting SPA-LEED pattern is displayed in Figure C.2. As expected, the SPA-LEED pattern is identical to the SPA-LEED pattern measured for HB238-A (see Figure 7.2 of Chapter 7). Accordingly, the existence of the α-phase was confirmed. The respective lattice parameters of the α-phase can be found in Table 7.1 of Chapter 7.

Interestingly, the LEED pattern of HB238-E shows an asymmetry, indicating the preferred growth of two out of four structurally equivalent domains, i.e., the preferred domain growth for molecules of one of the two HB238-E enantiomers. As HB238-E is like HB238-A a pro-chiral molecule, this asymmetry is surprising, but can be explained by the presence of chiral steps on the Ag(100) crystal surface, i.e., a miscut of the crystal, or the presence of chiral impurities that may act as nucleation seeds for the domain growth. However, according to the information that we have on the synthesis and purification of HB238-E, the latter can be excluded.

Figure C.3 shows an STM image of the HB238-E α-phase. As expected, the bright lobes that referred to the topographic contrast of the *t*Bu groups are not observed for the HB238-E monolayer. The left STM image of Figure C.3 depicts a magnification of the STM image on the right side, showing the structural details of one tetramer. The topographic features that correspond to the four molecules of the tetramer are indicated by blue frames. They reveal the enantiopure arrangement of molecules in the tetramers as all molecules in the structure exhibit the same shape and can be transferred into each other by rotations and translations. Small differences that can be observed in the topographic contrast of the molecules might be due to an asymmetric shape of the STM tip. The positions of the *i*Pr groups, and hence, the centers of the tetramer, are indicated by frames in yellow. For clarity, two of the molecules are superimposed by hardsphere models of HB238-E. The respective hydrogen bonds are indicated by orange dotted lines. Furthermore, the STM image on the right side shows that all molecules of the α-phase exhibit the same handedness. For the tetramer that is indicated by the framed molecules, the handedness is illustrated by the blue arrow.

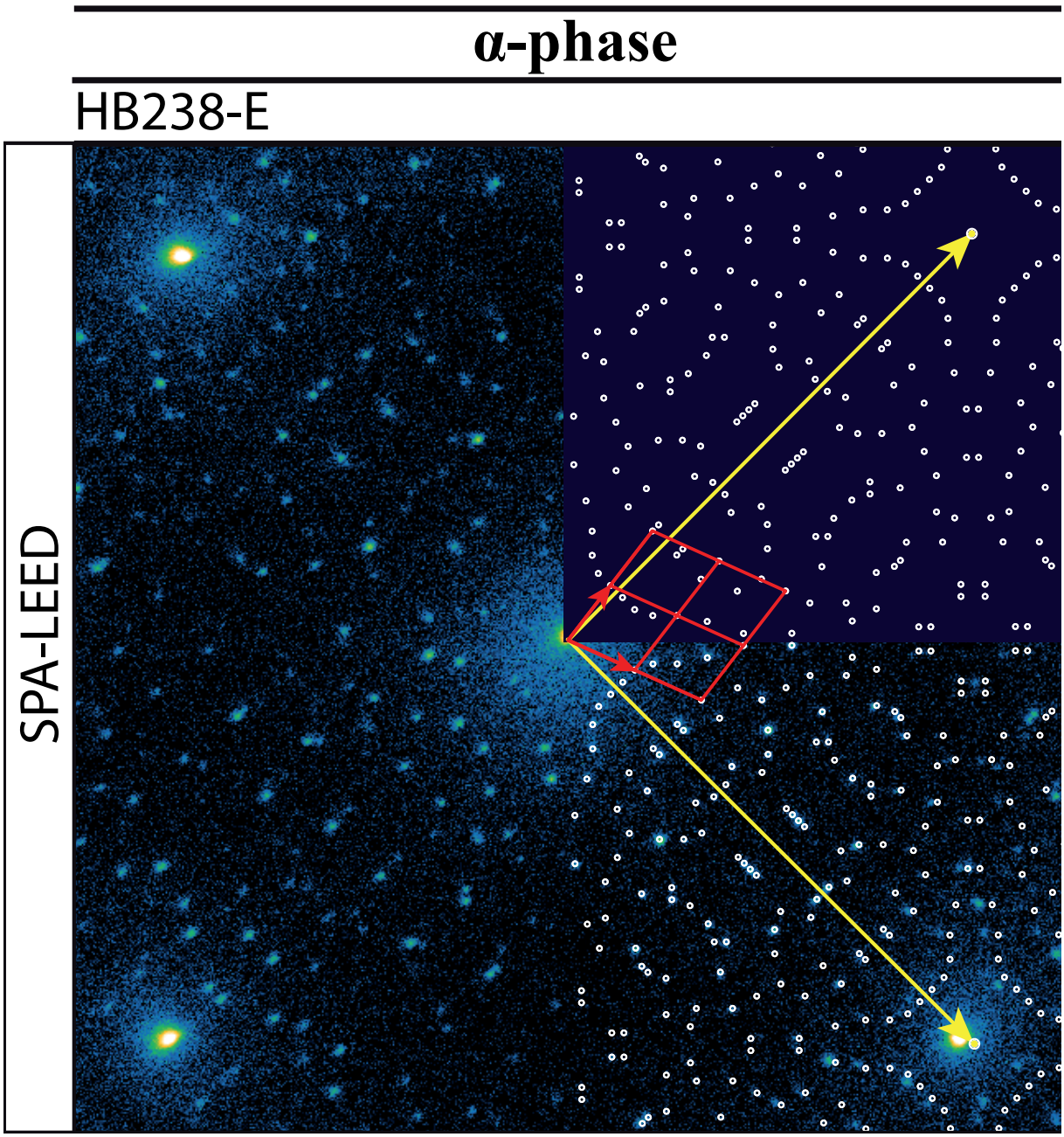

Figure C.2.: SPA-LEED pattern measured for a monolayer of the merocyanine HB238-E on the Ag(100) surface. Measurements were performed with an electron energy of 81 eV for a coverage of less than one monolayer and sample temperatures lower than 100 K. The right side of the SPA-LEED pattern is superimposed by a simulation of the diffraction spots (white dots). Here, the upper right quarter of the pattern shows only the simulation without the diffraction pattern in the background. This provides a better contrast and allows for a better comparison of the measured and simulated patterns. Reciprocal lattice vectors of the Ag(100) surface are indicated in yellow. They correspond to a length of 2.17 $Å^{-1}$. Four reciprocal unit cells of one merocyanine domain are indicated in red. The real space unit cell parameters are listed in Table 7.1.

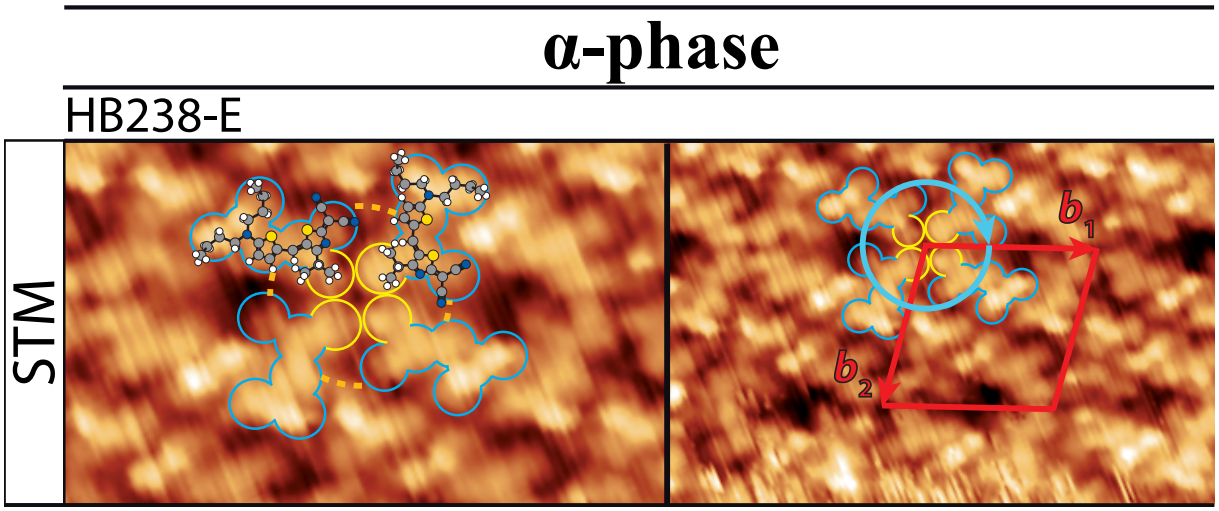

Figure C.3.: STM data of the α-phase of HB238-E on the Ag(100) surface. The left STM image depicts a zoom-in of the STM image on the right side and indicates the molecular orientations exemplarily for one tetramer. The molecules are schematically indicated by blue frames. For indicating the positions of the *i*Pr-groups in the center of the tetramer, these are displayed in yellow. For clarity, two of the frames are superimposed by hardsphere models of the HB238-E molecules. Hydrogen bonds are indicated by orange dotted lines. The STM image on the right side indicates the handedness of the tetramer and the unit cell vectors of the α-phase. The lattice constants equal $b_1 = 23.30$ Å, and $b_2 = 24.69$ Å. (300 K, $U_{\text{bias}} = -0.10$ V, $I_t = 50$ pA)

D. Thermal programmed desorption spectra of merocyanine layers

The following temperature programmed desorption spectroscopy (TPD) spectra were measured as part of the bachelor's thesis of Lucas Hirschfeld. The data presented in this Chapter provide only a brief overview of the desorption behavior of the merocyanines HB238-A, HB238-D, and HB238-E from the Ag(100) surface. In addition, it provides further information about the effects of polymorphism on the desorption behavior of HB238-D. For more details about the data evaluation and the results, the reader is referred to the respective bachelor's thesis in reference [137].

The following data were measured to investigate the desorption behavior of the merocyanines HB238-A, HB238-D, and HB238-E from the Ag(100) surface. The data shows the desorption of the multilayers. A desorption of the monolayer was not observed, which indicates a dissociation of the molecules in the first layer at elevated sample temperatures.

For TPD measurements, the desorption rate r_{des} of the molecules from the surface, i.e., the decrease of coverage θ per time t, is monitored in dependence on the sample temperature T. The desorption rate can be described by the Polanyi-Wigner equation [13, 53]

$$-\frac{d\theta}{dt} = r_{\mathrm{des}} = \nu_{\mathrm{m}} \cdot \theta^{\mathrm{m}} \cdot \exp\left(-\frac{E_{\mathrm{a}}}{\mathrm{k_B}T}\right). \tag{D.1}$$

Here, ν_{m} is the frequency factor, $\mathrm{k_B}$ is the Botzmann constant, and E_{a} is the activation energy of the desorption process [13].

m denotes the order of desorption and can have the integer values of 0, 1, and 2. A zeroth-order desorption describes the desorption of molecules from multilayers, i.e., a desorption without an impact of the substrate surface. A first-order desorption describes the desorption of molecules from the monolayer. Here, the interactions of the molecules with the surface impact the desorption behavior. A desorption of second-order describes a recombinative desorption and was not observed for the present data.

For a desorption of zeroth-order, Equation D.1 can be used to determine the frequency factor and the activation energy. This is done via an Arrhenius plot [13, 53] according to

$$\ln(r_{\mathrm{des}}) = \ln(\nu_{\mathrm{m}}) \cdot \left(-\frac{E_{\mathrm{a}}}{\mathrm{k_B}}\right) \cdot \frac{1}{T}. \tag{D.2}$$

Hence, by plotting $\ln(r_{\mathrm{des}})$ versus $\frac{1}{T}$, ν_{m} can be determined from the intercept and E_{a} from the slope of the linear curve.

For a desorption of first-order, E_a can be determined by the Redhead equation [13, 53]

$$E_a = RT_p \left(\ln \left(\frac{\nu_m T_p}{\beta} \right) - 3.46 \right). \tag{D.3}$$

For the evaluation below, a frequency factor of $\nu_m = 10^{13}\,s^{-1}$ was assumed [53]. In general, ν_m is assumed to be larger for strongly bonded molecules and smaller for molecules that are only weakly bonded [13]. T_p denotes the sample temperature for which the maximum of the desorption peak was observed. β is the heating rate and was 1 K/s for the here described measurements. R is the universal gas constant.

D.1. Polymorphism for multilayer coverages

As was already mentioned in the introduction of this thesis, the structural growth of multilayers can be influenced by the structure of the monolayer. In case of the merocyanine HB238-D, the TPD spectra indicate that this is indeed the case. As discussed in Chapter 7, HB238-D forms the Q-phase and the small α-phase on the Ag(100) surface. Which phase is formed depends on the deposition rate of the molecules (for details see Chapter 4).

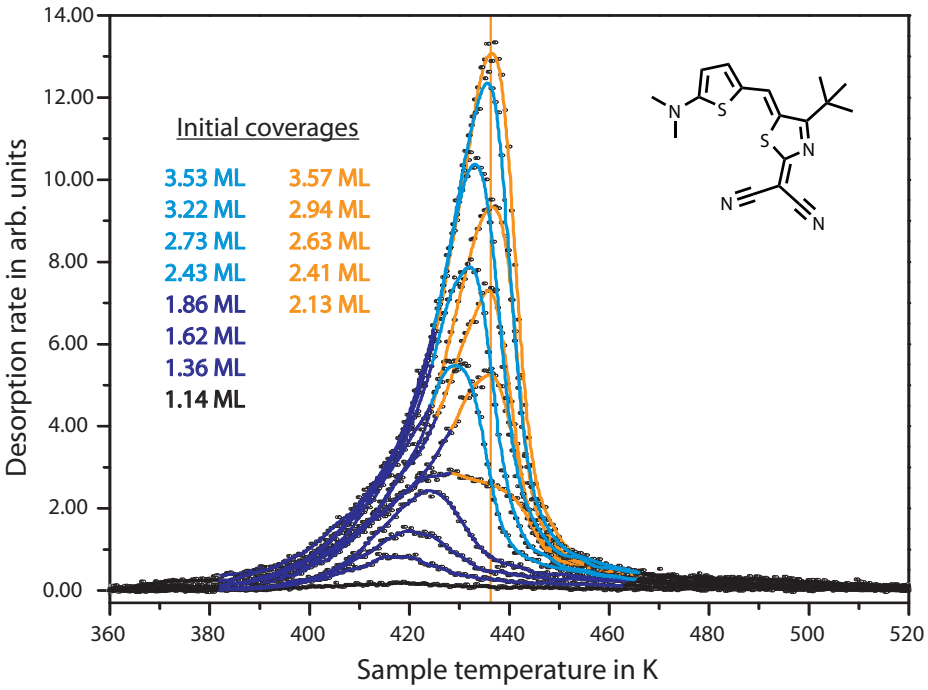

Figure D.1.: TPD spectra measured for HB238-D layers of different coverages as indicated in the spectrum. The heating rate was 1 K/s. The preparation of the layers was performed according to Chapter 4. Multilayer spectra in orange and light blue indicate the presence of two structural HB238-D polymorphs. For the set of orange spectra, T_p is marked by an orange vertical line. For further information, see text.

Figure D.1 displays two series of TPD spectra. The signals in dark blue correspond to spectra measured for an initial coverage between 1 and 2 monolayers. The spectra displayed in light blue and in orange were measured for higher initial coverages, as indicated

in the spectrum. All layers were prepared with deposition rates of about 0.1 ML/min. However, in the case of the light blue spectra, the deposition of HB238-D was started with lower deposition rates of about 0.03 ML/min. This suggests the formation of the Q-phase in the monolayer (compare to Chapters 4 and 7). On the contrary, the orange spectra were deposited with a constant deposition rate. Accordingly, the formation of the small α-phase is more likely for the monolayer. Please note that LEED measurements of the samples were restricted to coverages of about 1 ML. Higher coverages did not show a long-range order of the multilayer structures, as would be noticeable by the appearance of additional diffraction spots. Instead, higher coverage led to an increase in the background intensity of the diffraction pattern. Thus, the intensity of the monolayer diffraction spot decreased for increasing coverages, leading to the fact that LEED patterns of multilayer coverages were hard to measure.

As visible in Figure D.1, multilayers for which a formation on the Q-phase is assumed (light blue signals) show different desorption behaviors in comparison to the multilayers which presumably grow on the small α-phase. The signals in light blue show a desorption behavior similar to a zeroth-order desorption kinetics. The left flank of the desorption signal exhibits the same increase as the other light blue signals, but the desorption maximum shifts to higher temperatures for increasing initial coverages. In contrast, the orange signals exhibit a first-order desorption kinetics with a desorption maximum at constant temperature T_p of 436.1 ± 0.3 K.

While a zeroth-order kinetics is expected for the desorption of multilayers, in contrast to that, the first-order desorption of the orange signals is surprising. However, it might be explained by a gradual phase transition of the multilayer towards the structure of the light blue signals. This is supported by the orange spectrum measured for the highest initial coverage, which would also fit into the series of light blue spectra.

Thus, the desorption energy obtained from the orange signals should be considered with care. Applying Equation D.3, E_a results for $T_\mathrm{p} = 436.1 \pm 0.3$ K and $\nu_\mathrm{m} = 10^{13}\,\mathrm{s}^{-1}$ in 117.37 ± 0.06 kJ/mol. For comparison, the value of E_a determined for blue signals of zeroth-order desorption results according to Equation D.2 in 114.14 ± 7.65 kJ/mol [137]. The respective frequency factor was determined to be $\nu_\mathrm{m} = 7.55 \cdot 10^{11}\,\mathrm{s}^{-1}$, indicating a weak bonding of the molecules in the respective multilayer structure.

D.2. Desorption behavior of three merocyanines

Figure D.2 displays a series of TPD spectra that were measured for the merocyanines HB238-D, HB238-A, and HB238-E (top to bottom), respectively on the Ag(100) surface. Please note that the spectra displayed for HB238-D are the same as the spectra with the light blue signals of Figure D.1. For the layer preparation of the merocyanines HB238-A and HB238-E, the deposition of the merocyanines was performed with constant deposition rates of $0.1 - 0.2$ ML/min.

All of these spectra show a zeroth-order desorption kinetics for coverages larger than 2 monolayers. Again, these signals are indicated in light blue. Signals that correspond to a desorption of the second layer are indicated in dark blue. Interestingly, the spectra of

HB238-E (bottom part of Figure D.2) show an additional signal (purple color) that is observed with a peak maximum at 466 ± 1 K. This signal saturates with the completion of the second layer and might indicate the presence of a second phase in the second layer on the surface. Due to the higher desorption temperature, the desorbing molecules of this signal (purple color) must correspond to a phase in which the molecules are bonded more strongly to the molecules of the monolayer than in the phase that corresponds to the signal in dark blue. This might be explained by a phase of edge-on oriented molecules and a phase of face-on oriented molecules. Here, molecules in a phase with face-on adsorbed molecules are expected to bind more strongly to the molecules of the first layer than edge-on oriented molecules. Thus, desorption of those molecules should be observed at higher temperatures.

Table D.1.: Desorption energies E_a and frequency factors ν_m determined for the desorption of merocyanine (MC) multilayers from the Ag(100) surface. The data were determined from TPD spectra of the merocyanines HB238-D, HB238-A, and HB238-E, displayed in Figure D.2. Data evaluation was performed according to Equ. D.2. The data was taken from reference [137] to which the reader is referred for further information.

MC	E_a	ν_m
HB238-D	114.14 ± 7.65 kJ/mol	$7.55 \cdot 10^{11}\,s^{-1}$
HB238-A	170.51 ± 6.98 kJ/mol	$1.04 \cdot 10^{18}\,s^{-1}$
HB238-E	191.49 ± 3.99 kJ/mol	$2.46 \cdot 10^{21}\,s^{-1}$

The resulting E_a and ν_m values that were obtained by the evaluation of the zeroth-order signals are summarized in Table D.1. Accordingly, merocyanines with longer alkyl side chains (HB238-A and HB238-E, *n*Bu groups) are more strongly bonded in the respective multilayer phases compared to the merocyanine HB238-D, which exhibits much shorter alkyl side groups (Me groups). Furthermore, the decreased three-dimensional sterical demand of HB238-E (*i*Pr group) in comparison to HB238-A (*t*Bu group) seems to increase the temperature stability of the structures. The increase of E_a and to some extent also of ν_m is expected for the present series of merocyanines, as the differences in the molecular structures from HB238-D to HB238-E most probably favor the intermolecular interactions. This might be due to an increase of the van der Waals interactions in the case of longer alkyl side groups, or reduced distances between neighboring molecules as it can be expected for a decreased sterical demand of the alkyl side groups (*t*Bu to *i*Bu group).

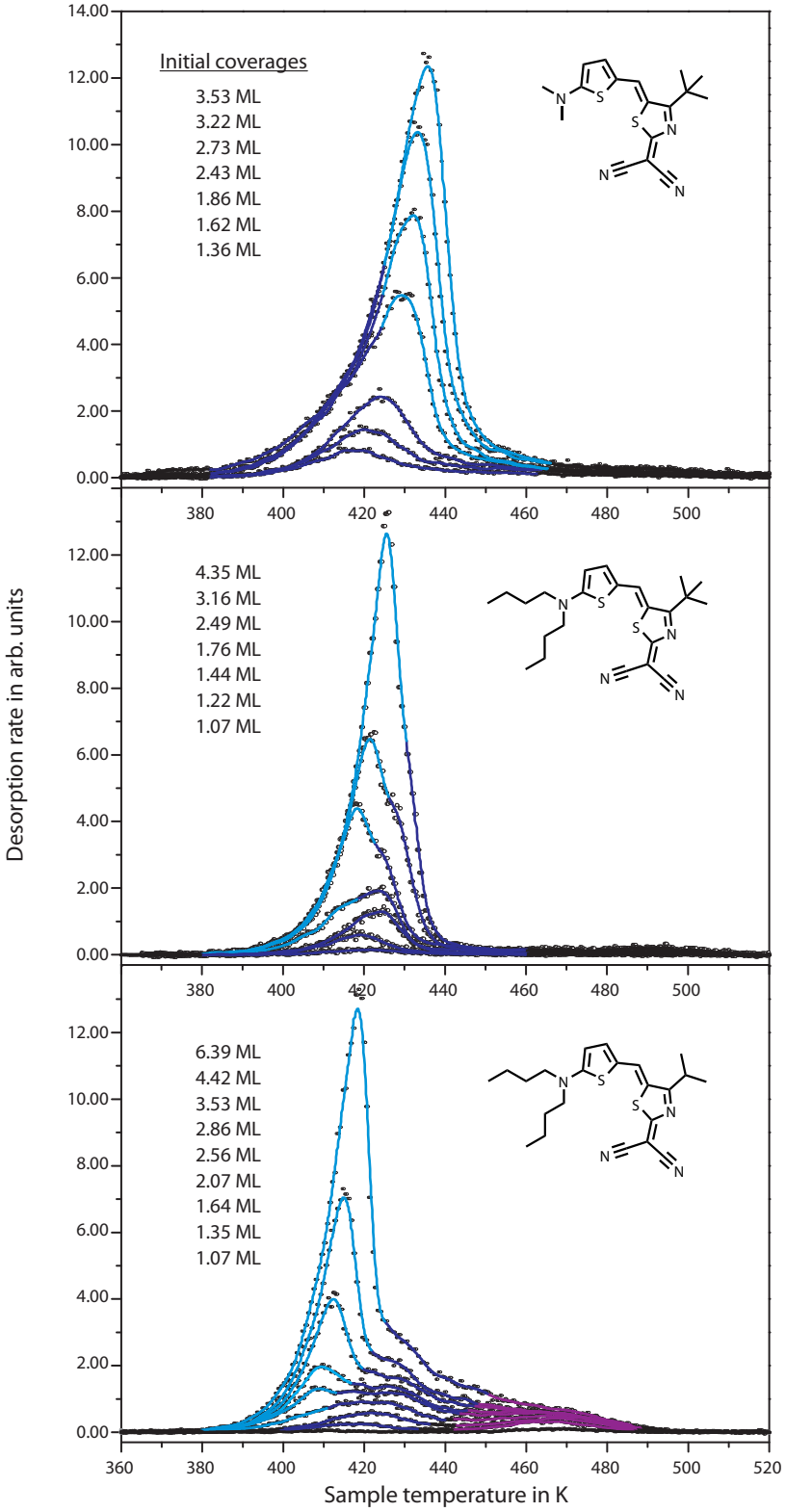

Figure D.2.: TPD spectra measured for merocyanine layers of different coverages as indicated in the spectra. The spectra at the top show the data of HB238-D, the spectra in the middle show the data of HB238-A, and the spectra at the bottom of the figure correspond to the merocyanine HB238-E. The heating rate of the sample was 1 K/s. The preparation of the layers was performed according to Chapter 4. For further information, see text or reference [137].

Abbreviations

AFM atomic force microscopy

DFT density functional theory

DLS Diamond Light Source

FWHM full width at half maximum

HOMO highest occupied molecular orbital

LDOS local density of states

LEED low energy electron diffraction

LUMO lowest unoccupied molecular orbital

MCP multi channel plate

ML monolayer

NIXSW normal incidence x-ray standing wave

PES photoelectron spectroscopy

QMS quadrupole mass spectrometer

RT room temperature

SPA-LEED spot profile analyzing low energy electron diffraction

STM scanning tunneling microscopy

TPD temperature programmed desorption spectroscopy

UHV ultra high vacuum

UPS ultraviolet photoemission spectroscopy

VT variable temperature

XPS x-ray photoemission spectroscopy

XRD x-ray diffraction

XSW x-ray standing wave

Bibliography

[1] Bürckstümmer, H., Tulyakova, E. V., Deppisch, M., Lenze, M. R., Kronenberg, N. M., Gsänger, M., Stolte, M., Meerholz, K. and Würthner, F., "Efficient Solution-Processed Bulk Heterojunction Solar Cells by Antiparallel Supramolecular Arrangement of Dipolar Donor–Acceptor Dyes", Angew. Chem. Int. Ed. **50**, 11628 (2011).

[2] Liess, A., Arjona-, A., Kudzus, A., Albert, J., Krause, A.-M. and Lv, A. and Stolte, M., Meerholz, K. and Würthner, F., "Ultranarrow Bandwidth Organic Photodiodes by Exchange Narrowing in Merocyanine H- and J-Aggregate Excitonic Systems", Adv. Funct. Mater. **29**, 1805058 (2019).

[3] M. Gsänger, D. Bialas, L. Huang, M. Stolte, and F. Würthner, "Organic Semiconductors based on Dyes and Color Pigments", Adva. Mater. **28**, 3615 (2016).

[4] M. Fahlman, S. Fabiano, V. Gueskine, D. Simon, M. Berggren, and X. Crispin, "Interfaces in organic electronics", Nat. Rev. Mater. **4**, 627 (2019).

[5] K. Liu, B. Ouyang, X. Guo, Y. Guo, and L. Y., "Advances in flexible organic field-effect transistors and their applications for flexible electronics", njp Flex. Electron. **6**, 627 (2022).

[6] A. Arjona-Esteban, J. Krumrain, A. Liess, M. Stolte, L. Huang, D. Schmidt, V. Stepanenko, M. Gsänger, D. Hertel, K. Meerholz, and F. Würthner, "Influence of Solid-State Packing of Dipolar Merocyanine Dyes on Transistor and Solar Cell Performances", J. Am. Chem. Soc. **137**, 13524 (2015).

[7] B.-G. Kim, K. Chung, and J. Kim, "Molecular Design Principle of All-organic Dyes for Dye-Sensitized Solar Cells", Chem. Eur. J **19**, 5220 (2013).

[8] H. Chung and Y. Diao, "Polymorphism as an emerging design strategy for high performance organic electronics", J. Mater. Chem. C **4**, 3915 (2016).

[9] J. Yang, D. Yan, and T. S. Jones, "Molecular Template Growth and Its Applications in Organic Electronics and Optoelectronics", Chem. Rev. **115**, 5570 (2015).

[10] N. N. Nguyen, H. Lee, H. C. Lee, and K. Cho, "van der Waals Epitaxy of Organic Semiconductor Thin Films on Atomically Thin Graphene Templates for Optoelectronic Applications", Acc. Chem. Res. **55**, 673 (2022).

[11] D. P. Woodruff, *Modern Techniques of Surface Science*, 3rd ed., 3 vols. (Cambridge University Press, Cambridge, 2016).

[12] G. Witte, K. Hänel, S. Söhnchen, and C. Wöll, "Growth and morphology of thin films of aromatic molecules on metals: the case of perylene", Appl. Phys. A **82**, 447 (2006).

[13] K. W. Kolasinski, *Surface science, Foundations of catalysis and nanoscience*, 2nd ed. (John Wiley & Sons, Ltd, Chichester, 2007).

[14] Clymer, D. A. and Mattin, M. A., "Characterization of thin-metal anode buffers in organic devices", Microw. Opt. Technol. Lett. **48**, 2070 (2006).

[15] Kulinich, A. V. and Ishchenko A., A., "Merocyanine dyes: synthesis, structure, properties and applications", Russ. Chem. Rev. **78**, 141 (2009).
[16] F. Würthner, R. Wortmann, and K. Meerholz, "Chromophore Design for Photorefractive Organic Materials", Chem. Phys. Chem. **3**, 17 (2002).
[17] F. Würthner, G. Archetti, R. Schmidt, and H.-G. Kuball, "Solvent Effect on Color, Band Shape, and Charge-Density Distribution for Merocyanine Dyes Close to the Cyanine Limit", Angew. Chem. **120**, 4605 (2008).
[18] A. V. Kulinich and A. A. Ishchenko, "Design and Photonics of Merocyanine Dyes", Chem. Rec. **24**, e202300262 (2024).
[19] J. Vanderspikken, W. Maes, and K. Vandewal, "Wavelength-Selective Organic Photodetectors", Adv. Funct. Mater. **31**, 2104060 (2021).
[20] D. Bialas, A. Zitzler-Kunkel, E. Kirchner, D. Schmidt, and F. Würthner, "Structural and quantum chemical analysis of exciton coupling in homo- and heteroaggregate stacks of merocyanines", Nat. Commun. **7**, 12949 (2016).
[21] A. Liess, L. Huang, A. Arjona-Esteban, A. Lv, M. Gsänger, V. Stepanenko, M. Stolte, and F. Würthner, "Organic Thin Film Transistors Based on Highly Dipolar Donor–Acceptor Polymethine Dyes", Adv. Funct. Mater. **25**, 44 (2015).
[22] O. Bauer, "Surface bonding of a functionalized aromatic molecule: Adsorption configurations of PTCDA on coinage metal surfaces.", PhD-thesis (Rheinische Friedrich-Wilhelms Universität Bonn, 2014).
[23] F. Rosei, M. Schunack, Y. Naitoh, P. Jiang, A. Gourdon, E. Laegsgaard, I. Stensgaard, C. Joachim, and F. Besenbacher, "Properties of large organic molecules on metal surfaces", Prog. Surf. Sci. **71**, 95 (2003).
[24] L. Wolthaus, A. Schaper, and D. Möbius, "Brickstone arrangement in J-aggregates on an amphiphilic merocyanine dye", Chem. Phys. Lett. **225**, 322 (1994).
[25] S. De Feyter, A. Miura, S. Yao, Z. Chen, F. Würthner, P. Jonkheijm, A. P. H. J. Schenning, E. W. Meijer, and F. C. De Schryver, "Two-Dimensional Self-Assembly into Multicomponent Hydrogen-Bonded Nanostructures", Nano Lett. **5**, 77 (2005).
[26] A. Lohr, S. Uemura, and F. Würthner, "Trimeric Cyclic Assemblies of Calix[4]arene-Tethered Bismerocyanines", Angew. Chem. **121**, 6281 (2009).
[27] H. Malik, T. Halbritter, A. Heckel, and T. G. Gopakumar, "Light-Induced Quantitative and Electrical-Field-Induced Barrierless Switching of Spiropyran Derivative on Graphite Surface", J. Phys. Chem. Lett. **12**, 5463 (2021).
[28] H. Bürckstümmer, "Merocyanine dyes for solution processed organic bulk heterojunction solar cells", PhD-thesis, Universität Würzburg (Universität Würzburg, 2011).
[29] N. Gildemeister, G. Ricci, L. Böhner, J. M. Neudörfl, D. Hertel, F. Würthner, F. Negri, K. Meerholz, and D. Fazzi, "Understanding the structural and charge transport property relationships for a variety of merocyanine single-crystals: a bottom up computational investigation", J. Mater. Chem. C **9**, 10851 (2021).
[30] A. V. Kulinich and A. A. Ishchenko, "Merocyanines: Electronic Structure and Spectroscopy in Solutions, Solid State, and Gas Phase", Chem. Rev. **124**, 12086 (2024).
[31] F. Würthner and K. Meerholz, "Systems Chemistry Approach in Organic Photovoltaics", Chem. Eur. J. **16**, 9366 (2010).

[32] S. R. Marder, C. B. Gorman, F. Meyers, J. W. Perry, G. Bourhill, J.-L. Brédas, and B. M. Pierce, "A Unified Description of Linear and Nonlinear Polarization in Organic Polymethine Dyes", Science **265**, 632 (1994).

[33] C. B. Gorman and S. R. Marder, "An investigation of the interrelationships between linear and nonlinear polarizabilities and bond-length alternation in conjugated organic molecules.", Proc. Natl. Acad. Sci. U.S.A. **90**, 11297 (1993).

[34] Y. Siqueira, M. L. Lyra, T. N. Ramos, B. Champagne, and V. Manzoni, "Unveiling the relationship between structural and polarization effects on the first hyperpolarizability of a merocyanine dye", J. Chem. Phys. **156**, 014305 (2022).

[35] T. Schembri, J. H. Kim, A. Liess, V. Stepanenko, M. Stolte, and F. Würthner, "Semitransparent Layers of Social Self-Sorting Merocyanine Dyes for Ultranarrow Bandwidth Organic Photodiodes", Adv. Opt. Mater. **9**, 2100213 (2021).

[36] R. Tomar, L. Bernasconi, D. Fazzi, and T. Bredow, "Theoretical study on the optoelectronic properties of merocyanine-dyes", J. Phys. Chem A **127**, 9661 (2023).

[37] G. J. Ashwell, G. A. N. Paxton, A. J. Whittam, W. D. Tyrrel, M. Berry, and D. Zhou, "Merocyanine dyes: self-assembled monolayers", J. Mater. Chem. **12**, 1631 (2002).

[38] F. Würthner, "Dipole–Dipole Interaction Driven Self-Assembly of Merocyanine Dyes: From Dimers to Nanoscale Objects and Supramolecular Materials", Acc. Chem. Res. **49**, 868 (2016).

[39] A. Riemann, L. Browning, and H. Goff, "Conformational behavior of naphthomerocyanine dimers on Au(111)", Surf. Sci. **709**, 121837 (2021).

[40] C. Bronner, G. Schulze, K. J. Franke, J. I. Pascual, and P. Tegeder, "Switching ability of nitro-spiropyran on Au(111): electronic structure changes as a sensitive probe during a ring-opening reaction", J. Phys. Condens. Matter. **23**, 484005 (2011).

[41] P. Tegeder, "Optically and thermally induced molecular switching processes at metal surfaces", J. Phys. Condens. Matter. **24**, 394001 (2012).

[42] B. Öcal, P. Weitkamp, K. Meerholz, and S. Olthof, "Chemical interaction and molecular growth of a highly dipolar merocyanine molecule on metal surfaces: A photoelectron spectroscopy study", Surf. Sci. **754**, 122690 (2025).

[43] R. Schäfer, L. Böhner, M. Schiek, D. Hertel, K. Meerholz, and K. Lindfors, "Strong Light–Matter Interaction of Molecular Aggregates with Two Excitonic Transitions", ACS Photonics **11**, 111 (2024).

[44] L. Böhner, P. Weitkamp, T. Limböck, N. Gildemeister, D. Fazzi, M. Schiek, R. Bruker, D. Hertel, R. Schäfer, K. Lindfors, and K. Meerholz, "Influencing optical and charge transport properties by controlling the molecular interactions of merocyanine thin films", Org. Chem. Front., 10.1039/D4QO02088J (2025).

[45] A. Liess, A. Lv, A. Arjona-Esteban, D. Bialas, A.-M. Krause, V. Stepanenko, M. Stolte, and F. Würthner, "Exciton coupling of merocyanine dyes from h- to j-type in the solid state by crystal engineering", Nano Lett. **17**, 1719 (2017).

[46] Private communication with K. Meerholz and D. Hertel, (2021).

[47] M. Piantek, G. Schulze, M. Koch, K. J. Franke, F. Leyssner, A. Krüger, C. Navío, J. Miguel, M. Bernien, M. Wolf, W. Kuch, P. Tegeder, and J. I. Pascual, "Reversing the Thermal Stability of a Molecular Switch on a Gold Surface: Ring-Opening Reaction of Nitrospiropyran", J. Am. Chem. Soc. **131**, 12729 (2009).

[48] A. J. Kny, M. Reimer, N. Al-Shamery, R. Tomar, T. Bredow, S. Olthof, D. Hertel, K. Meerholz, and M. Sokolowski, "Chiral self-organized single 2D-layers of tetramers from a functional donor–acceptor molecule by the surface template effect", Nanoscale **15**, 10319 (2023).

[49] M. P. Seah and W. A. Dench, "Quantitative electron spectroscopy of surfaces: A standard data base for electron inelastic mean free paths in solids", Surf. Interface Anal. **1**, 2 (1979).

[50] W. M. Moritz and M. A. Van Hove, *Surface Structure Determination by LEED and X-rays* (Cambridge University Press, Cambridge, 2022).

[51] U. Scheithauer, G. Meyer, and M. Henzler, "A new LEED instrument for quantitative spot profile analysis", Surf. Sci. **178**, 441 (1986).

[52] M. Horn-von Hoegen, "Growth of semiconductor layers studied by spot profile analysing low energy electron diffraction", Z. Kristallogr. **214**, 684 (1999).

[53] Attard, G. and Barnes, C., *Surfaces* (Oxford Science Publications, New York, 2011).

[54] E. Meyer, R. Bennewitz, and H. J. Hug, *Scanning Probe Microscopy: The Lab on a Tip*, 2nd ed. (Springer, Berlin Heidelberg, 2021).

[55] Hansma, P. K. and Tersoff, J., "Scanning tunneling microscopy", J. Appl. Phys. **61**, R1 (1987).

[56] H. J. Zandvliet and A. van Houselt, "Scanning Tunneling Spectroscopy", Annu. Rev. Anal. Chem. **2**, 37 (2009).

[57] J. Tersoff and D. R. Hamann, "Theory and application for the scanning tunneling microscope", Phys. Rev. Lett. **50**, 1998 (1983).

[58] J. Tersoff and D. R. Hamann, "Theory of the scanning tunneling microscope", Phys. Rev. B **31**, 805 (1985).

[59] Z. Li, K. Schouteden, V. Iancu, E. Janssens, P. Lievens, C. Van Haesendonck, and J. I. Cerdá, "Chemically modified STM tips for atomic-resolution imaging of ultrathin NaCl films", Nano Res. **8**, 2223 (2015).

[60] J. F. Moulder, W. F. Stickle, P. E. Sobol, and K. D. Bomben, *Handbook of X-ray Photoelectron Spectroscopy*, edited by J. Chastain (Perkin-Elmer Corporation, Physical Electronics Division, Minnesota, 1992).

[61] Henzler, M. and Göpel, W., *Oberflächenphysik des Festkörpers* (B. G. Teubner, Stuttgart, 1994).

[62] N. Fairley, V. Fernandez, M. Richard-Plouet, C. Guillot-Deudon, J. Walton, E. Smith, D. Flahaut, M. Greiner, M. Biesinger, S. Tougaard, D. Morgan, and J. Baltrusaitis, "Systematic and collaborative approach to problem solving using X-ray photoelectron spectroscopy", Appl. Surf. Sci. Adv. **5**, 100112 (2021).

[63] J. Zegenhagen and A. Kazimirov, eds., *The X-ray Standing Wave Technique, Principles and Applications* (World Scientific, Singapore, 2013).

[64] G. van Straaten, M. Franke, F. C. Bocquet, F. C. Tautz, and C. Kumpf, "Non-dipolar effects in photoelectron-based normal incidence X-ray standing wave experiments", J. Electron Spectrosc. Relat. Phenom. **222**, 106 (2018).

[65] P. D. Woodruff, "Normal Incidence X-Ray Standing Wave Determination of Adsorbate Structures", Prog. Surf. Sci. **57**, 1 (1998).

[66] A. Gerlach, F. Schreiber, S. Sellner, H. Dosch, I. A. Vartanyants, B. C. C. Cowie, T.-L. Lee, and J. Zegenhagen, "Adsorption-induced distortion of $F_{16}CuPc$ on Cu(111) and Ag(111): An x-ray standing wave study", Phys. Rev. B **71**, 205425 (2005).

[67] S. Weiß, I. Krieger, T. Heepenstrick, S. Soubatch, M. Sokolowski, and F. S. Tautz, "Determination of the adsorption geometry of PTCDA on the Cu(100) surface", Phys. Rev. B **96**, 075414 (2017).

[68] F. Bocquet, G. Mercurio, M. Franke, G. van Straaten, S. Weiß, S. Soubatch, C. Kumpf, and F. Tautz, "Torricelli: A software to determine atomic spatial distributions from normal incidence x-ray standing wave data", Comp. Phys. Commun. **235**, 502 (2019).

[69] A. Jablonski, F. Salvat, and C. Powell, "NIST electron elastic-scattering cross-section database", Version 3.2, National Institute of Standards and Technology, Gaithersburg, MD (2010).

[70] A. J. Kny, "Adsorption and Ordering of the Merocyanine HB238 on the Ag(100) Surface", MA thesis (Rheinische Friedrich-Wilhelms Universität Bonn, 2020).

[71] H. N. Humberg, "One-dimensional aggregates of the organic dye quinacridone on metallic and dielectric surfaces", PhD-thesis (Rheinische Friedrich-Wilhelms Universität Bonn, 2024).

[72] C. Brülke, "Structural and electronic decoupling of a large organic molecule from a metal surface by a single layer of hexagonal boron nitride", PhD-thesis (Rheinische Friedrich-Wilhelms Universität Bonn, 2021).

[73] J. Ozcomert, W. Pai, N. Bartelt, and I. Reutt-Robey, "Step configurations near pinning sites on Ag(110)", Surf. Sci. **293**, 183 (1993).

[74] R. C. Weast, ed., *Handbook of Chemistry and Physics*, 55th ed. (CRC Press, Cleveland, 1974).

[75] A. Smakula and J. Kalnajs, "Precision Determination of Lattice Constants with a Geiger-Counter X-Ray Diffractometer", Phys. Rev. **99**, 1737 (1955).

[76] M. E. Straumanis, "Neubestimmung der Gitterparameter, Dichten und thermischen Ausdehnungskoeffizienten von Silber und Gold, und Vollkommenheit der Struktur", Mh. Chem. **102**, 1377 (1971).

[77] R. Majee, A. Kumar, T. Das, S. Chakraborty, and S. Bhattacharyya, "Tweaking Nickel with Minimal Silver in a Heterogeneous Alloy of Decahedral Geometry to Deliver Platinum-like Hydrogen Evolution Activity", Angew. Chem. Int. Ed. **59**, 2881 (2020).

[78] Hesse, M., Meier, H. and Zeeh, B., *Spektroskopische Methoden in der organischen Chemie*, 6th ed. (Thieme Verlag, Stuttgart, 2002).

[79] A. J. Kny, A. Sweetman, and M. Sokolowski, "An Atomistic Analysis of the Carpet Growth of KCl Across Step Edges on the Ag(111) Surface", J. Phys. Chem. Lett. **16**, 696 (0).

[80] M. Müller, "Optische Spektroskopie von PTCDA auf Alkalihalogenidoberflächen: vereinzelte Moleküle und Monolagen", PhD-thesis (Rheinische Friedrich-Wilhelms Universität Bonn, 2011).

[81] P. Kury, "WinSPA, Version 3", Out-of-the-box Systems (2022).

[82] A. J. Kny, M. Sokolowski, and P. Kury, "Increasing the scan speed in high resolution, low energy electron diffraction measurements by presetting the gate time", Rev. Sci. Instr. **94**, 064707 (2023).

[83] Sojka, F. and Fritz, T., "LEEDCal, Version 5.1", Fritz & Sojka GbR, Apolda (2018).

[84] Sojka, F., Meissner, M., Zwick, Ch., Forker, R. and Fritz, T., "Determination and correction of distortions and systematic errors in low-energy electron diffraction.", Rev. Sci. Instr. **84**, 015111 (2013).
[85] Ikonomov, J., Bauer, O. and Sokolowski, M., "Highly ordered thin films of perylene-3,4,9,10-tetracarboxylic acid dianhydride (PTCDA) on Ag(100)", Surf. Sci. **602**, 2061 (2008).
[86] Sojka, F. and Fritz, T., "LEEDLab 2018 Version v1.2", Fritz & Sojka GbR, Apolda, Germany (2019).
[87] P. Bayersdorfer, "Spot-Plotter, Version 1.2.1.4", Universität Würzburg (2008).
[88] P. Feulner and D. Menzel, "Simple ways to improve "flash desorption" measurements from single crystal surfaces", J. Vac. Sci. Technol. **17**, 662 (1980).
[89] "LabVIEW 2014, Version 14.0.0", National Instruments, München (2014).
[90] N. Humberg, "Untersuchung der Desorption von Borazin von der Cu(111)-Oberfläche mittels TPD", Focusing labcourse (Rheinische Friedrich-Wilhelms Universität Bonn, 2017).
[91] B. Wolff, "Determination of the desorption energy of PTCDA on hBN/Cu(111) by thermal desorption spectroscopy", MA thesis (Rheinische Friedrich-Wilhelms Universität Bonn, 2019).
[92] RHK Technology, "XPMPro 2.0.1.5", Troy, MI, USA (2010).
[93] RHK Technology, "R10 7.0.2.0", Troy, MI, USA (2023).
[94] SPECS Surface Nano Analysis GmbH, "Nanonis", Berlin, Germany (2023).
[95] Necas, D. and Klapetek, P., "Gwyddion: an open-source software for SPM data analysis", Cent. Eur. J. Phys. **10**, 181 (2012).
[96] I. Horcas, R. Fernández, J. M. Gómez-Rodríguez, J. Colchero, J. Gómez-Herrero, and A. M. Baro, "WSXM: A software for scanning probe microscopy and a tool for nanotechnology", Rev. Sci. Instr. **78**, 013705 (2007).
[97] *Diamond light source: i09 endstation*, www.diamond.ac.uk/Instruments/Structures-and-Surfaces/I09.html; 01.12.2024.
[98] Humberg, N. and Kny, A. J. and Mühlpointner, M. and Haags, A. and Soubatch, S. and Duncan, D.A. and Lee, T.-L. and Sokolowski, M., "Phosphorene on the Au(111) Surface - an X-Ray Standing Wave Analysis", in preparation.
[99] S. Kowarik, A. Gerlach, S. Sellner, L. Cavalcanti, and F. Schreiber, "Dewetting of an Organic Semiconductor Thin Film Observed in Real-time", Adv. Eng. Mater. **11**, 291 (2009).
[100] B. Krause, A. C. Dürr, F. Schreiber, H. Dosch, and O. H. Seeck, "Thermal stability and partial dewetting of crystalline organic thin films: 3,4,9,10-perylenetetracarboxylic dianhydride on Ag(111)", J. Chem. Phys. **119**, 3429 (2003).
[101] N. Humberg, R. Bretel, A. Eslam, E. Le Moal, and M. Sokolowski, "Hydrogen-Bonded One-Dimensional Chains of Quinacridone on Ag(100) and Cu(111): The Role of Chirality and Surface Bonding", J. Phys. Chem C **124**, 24861 (2020).
[102] F. Tautz, "Structure and bonding of large aromatic molecules on noble metal surfaces: The example of PTCDA", Prog. Surf. Sci. **82**, 479 (2007).
[103] U. Müller, *Anorganische Strukturchemie*, 5th ed. (Teubner Verlag, Wiesbaden, 2006).
[104] O. Bauer, G. Mercurio, M. Willenbockel, W. Reckien, H. S. C., B. Fiedler, S. Soubatch, T. Bredow, F. S. Tautz, and M. Sokolowski, "Role of functional groups

in surface bonding of planar π-conjugated molecules", Phys. Rev. B **86**, 235431 (2012).

[105] Brülke, C., Heepenstrick, T., Krieger, I., Wolff, B., Yang, X., Shamsaddinlou, A., Weiß, S., Bocquet, F. C., Tautz, F. S., Soubatch, S. and Sokolowski, M., "Quantitative analysis of the electronic decoupling of an organic semiconductor molecule at a metal interface by a monolayer of hexagonal boron nitride", Phys. Rev. B **99**, 121404 (2019).

[106] Tomar, R. and Kny, A. J. and Sokolowski, M., and Bredow, T., "Modeling the Monolayer Formation of Merocyanine HB238 on the Ag(100) Surface", J. Phys. Chem. C **129**, 7427 (2025).

[107] J. Wan, Y. L. Fan, D. W. Gong, S. G. Shen, and X. Q. Fan, "Surface relaxation and stress of fcc metals: Cu, Ag, Au, Ni, Pd, Pt, Al and Pb", Model. Simul. Mater. Sci. Eng. **7**, 189 (1999).

[108] A. Bondi, "van der Waals Volumes and Radii", J. Phys. Chem **68**, 441 (1964).

[109] M. Mantina, A. C. Chamberlin, R. Valero, C. J. Cramer, and D. G. Truhlar, "Consistent van der Waals Radii for the Whole Main Group", J. Phys. Chem A **113**, 5806 (2009).

[110] M. A. Stoodley, L. A. Rochford, T.-L. Lee, B. P. Klein, D. A. Duncan, and R. J. Maurer, "Structure of Graphene Grown on Cu(111): X-Ray Standing Wave Measurement and Density Functional Theory Prediction", Phys. Rev. Lett. **132**, 196201 (2024).

[111] W. Liu, F. Maaß, M. Willenbockel, C. Bronner, M. Schulze, S. Soubatch, F. S. Tautz, P. Tegeder, and A. Tkatchenko, "Quantitative Prediction of Molecular Adsorption: Structure and Binding of Benzene on Coinage Metals", Phys. Rev. Lett. **115**, 036104 (2015).

[112] G. Mercurio, O. Bauer, M. Willenbockel, N. Fairley, W. Reckien, C. H. Schmitz, B. Fiedler, S. Soubatch, T. Bredow, M. Sokolowski, and F. S. Tautz, "Adsorption height determination of nonequivalent C and O species of PTCDA on Ag(110) using x-ray standing waves", Phys. Rev. B **87**, 045421 (2013).

[113] J. Stanzel, W. Weigand, L. Kilian, H. Meyerheim, C. Kumpf, and E. Umbach, "Chemisorption of NTCDA on Ag(111): a NIXSW study including non-dipolar and electron-stimulated effects", Surf. Sci. **571**, L311 (2004).

[114] P. Milligan, J. McNamarra, B. Murphy, B. Cowie, D. Lennon, and M. Kadodwala, "A NIXSW and NEXAFS investigation of thiophene on Cu(111)", Surf. Sci. **412**, 166 (1998).

[115] Kilian, L., Weigand, W., Umbach, E., Langner, A., Sokolowski, M., Meyerheim, H. L., Maltor, H., Cowie, B. C. C., Lee, T. and Bäuerle, P., "Adsorption site determination of a large π-conjugated molecule by NIXSW: end-capped-quaterthiophene on Ag(111)", Phys. Rev. B **66**, 075412 (2002).

[116] P. Knecht, P. T. P. Ryan, D. A. Duncan, L. Jiang, J. Reichert, P. S. Deimel, F. Haag, J. T. Küchle, F. Allegretti, T.-L. Lee, M. Schwarz, M. Garnica, W. Auwärter, A. P. Seitsonen, J. V. Barth, and A. C. Papageorgiou, "Tunable Interface of Ruthenium Porphyrins and Silver", J. Phys. Chem. C **125**, 3215 (2021).

[117] J. Repp, G. Meyer, S. M. Stojković, A. Gourdon, and C. Joachim, "Molecules on Insulating Films: Scanning-Tunneling Microscopy Imaging of Individual Molecular Orbitals", Phys. Rev. Lett. **94**, 026803 (2005).

[118] L. Gross, B. Schuler, N. Pavliček, S. Fatayer, Z. Majzik, N. Moll, D. Peña, and G. Meyer, "Atomic Force Microscopy for Molecular Structure Elucidation", Angew. Chem. Int. Ed. **57**, 3888 (2018).

[119] K. Kaiser, L.-A. Lieske, J. J. Repp, and L. Gross, "Charge-state lifetimes of single molecules on few monolayers of NaCl", Nat. Commun. **14**, 10.1038/s41467-023-40692-1 (2023).

[120] C. Bombis, F. Ample, L. Lafferentz, H. Yu, S. Hecht, C. Joachim, and L. Grill, "Single Molecular Wires Connecting Metallic and Insulating Surface Areas", Angew. Chem. Int. Ed. **48**, 9966 (2009).

[121] R. Bretel, S. Le Moal, H. Oughaddou, and E. Le Moal, "Hydrogen-bonded one-dimensional molecular chains on ultrathin insulating films: Quinacridone on KCl/ Cu(111)", Phys. Rev. B **108**, 125423 (2023).

[122] A. Riemann, S. Fölsch, and K. H. Rieder, "Epitaxial growth of alkali halides on stepped metal surfaces", Phys. Rev. B **72**, 125423 (2005).

[123] A. Bera and K. Morgenstern, "In Situ Growth and Bias-Dependent Modification of NaBr Ionic Layers on Ag(111)", J. Phys. Chem. C **126**, 10610 (2022).

[124] M. Müller, J. Ikonomov, and M. Sokolowski, "Structure of Epitaxial Layers of KCl on Ag(100)", Surf. Sci. **605**, 1090 (2011).

[125] C. Schwennicke, J. Schimmelpfennig, and H. Pfnür, "Morphology of thin NaCl films grown epitaxially on Ge(100)", Surf. Sci. **293**, 57 (1993).

[126] R. Bennewitz, V. Barwich, M. Bammerlin, C. Loppacher, M. Guggisberg, A. Baratoff, E. Meyer, and H.-J. Güntherodt, "Ultrathin films of NaCl on Cu(111): a LEED and dynamic force microscopy study", Surf. Sci. **438**, 289 (1999).

[127] J. Kramer, C. Tegenkamp, and H. Pfnür, "The growth of NaCl on flat and stepped silver surfaces", J. Phys. Condens. Matter. **15**, 6473 (2003).

[128] C. Loppacher, U. Zerweck, and L. M. Eng, "Kelvin probe force microscopy of alkali chloride thin films on Au(111)", Nanotechnol. **15**, S9 (2003).

[129] F. Matthaei, S. Heidorn, K. Boom, C. Bertram, A. Safiei, J. Henzl, and K. Morgenstern, "Coulomb attraction during the carpet growth mode of NaCl", J. Phys. Condens. Matter. **24**, 354006 (2012).

[130] R. Smoluchowski, "Anisotropy of the Electronic Work Function of Metals", Phys. Rev. **60**, 661 (1941).

[131] J. E. Huheey, "Electronegativity, acids, and bases. IV. Concerning the inductive effect of alkyl groups", J. Org. Chem. **36**, 204 (1971).

[132] D. Vaughan, ed., *X-ray data booklet*, 2nd ed. (Laurence Berkeley Laboratory, California, 1986).

[133] R. W. G. Wyckoff, *Crystal structures*, Vol. 1 (Wiley, New York, 1963).

[134] Russell, S. M., Shen, M., Liu, D.-J. and Thiel, P. A., "Adsorption of sulfur on Ag(100)", Surf. Sci. **605**, 520 (2011).

[135] M. Yu, D. P. Woodruff, C. J. Satterley, R. G. Jones, and V. R. Dhanak, "Structural investigation of the interaction of molecular sulfur with Ag(111)", J. Phys. Chem. C **111**, 3152 (2007).

[136] G. R. Desiraju, J. J. Vittal, and A. Ramanan, *Crystal engineering: a textbook*, Vol. 1 (World Scientific, Singapore, 2011).

[137] L. Hirschfeld, "Thermische Desorptionsspektroskopie von Merocyaninen auf Ag(100)", Bachelor's thesis (Rheinische Friedrich-Wilhelms Universität Bonn, 2023).

Danksagung

An dieser Stelle möchte ich mich bei all den Personen bedanken, die mich während der Zeit meiner Doktorarbeit unterstützt und ermutigt haben.

- An allererster Stelle möchte ich mich bei Prof. Dr. Moritz Sokolowski bedanken. Danke, dass ich das Thema dieser Arbeit so frei gestalten durfte und danke für all die aufbauenden und inspirierenden Worte während der ganzen Zeit.
- Ein großes Danke geht an dieser Stelle an Dr. Anja Haags und Dr. Sergey Subach (Forschungszentrum Jülich), sowie Niklas Humberg und Prof. Dr. Moritz Sokolowski für die großartige, tatkräftige Unterstützung bei all den Messzeiten an der Diamond Light Source, die wir gemeinsam gemeistert haben. Bedanken möchte ich mich auch bei Ralf Karrenbauer, der uns die Abwicklung der Zollformalitäten in Zeiten des Brexit sehr erleichtert hat.
- In diesem Zusammenhang möchte ich mich auch bei dem Team der I09 Beamline an der Diamond Light Source in Großbritannien bedanken. Insbesondere Dr. David Duncan, Dr. Tien-Lin Lee, Dr. Fulden Eratam und Dave McCue für ihre Unterstützung und all die konstruktiven Diskussionen während der Messzeiten.
- Ebenso gebührt mein Dank den Mitgliedern des TIDE Graduiertenkollegs. Insbesondere möchte ich an dieser Stelle die folgenden Personen hervorheben:
  - Prof. Dr. Klaus Meerholz, Dr. Dirk Hertel und Dr. Philipp Weitkamp (Universität Köln), die mir die in dieser Arbeit untersuchten Merocyanine zur Verfügung gestellt haben.
  - Prof. Dr. Selina Olthof (Universität Wuppertal), die uns die ersten HB238-A XPS- und UPS-Daten zur Verfügung stellte und damit die weiteren XPS Messungen an der Diamond Light Source motivierte. Ebenso danke ich ihr für ihre Unterstützung bei der Interpretation der an der Diamond Light Source gemessenen soft XPS Daten.
  - Und last but not least Prof. Dr. Thomas Bredow und Ritu Tomar (Universität Bonn), die unsere experimentell entwickelten Strukturmodelle mit detaillierten theoretischen Berechnungen bestätigen konnten.
- Ich möchte auch Dr. Adam Sweetman (University of Leeds, UK) danken, der mich für drei Monate in seine Arbeitsgruppe aufgenommen hat und es mir ermöglichte, dünne KCl-Filme und darauf adsorbierte Merocyanine mit STM und AFM zu untersuchen. In diesem Rahmen möchte auch Callum Hayward, Dr. Dylan Barker, Dr. Timothy Brown und Dr. Phil Blowey danken, die mich sofort ins Team ihrer Arbeitsgruppe integriert haben.

- Besonders bedanken möchte ich mich bei Morris Mühlpointner, Noah Al-Shamery, Florian Schneider, Mara Scheuermann, Henryk Gottschalk, Lukas Grönwoldt, Leyao Yang und Lucas Hirschfeld, die meine Forschung im Rahmen ihrer Bachelor- und Masterarbeiten unterstützt haben.
- Auch möchte ich mich bei Dr. Peter Kury (Out-of-the-box Systems GmbH) dafür bedanken, dass er die in Kapitel 5 beschriebene Speed-up Routine für SPA-LEED Messungen so schnell in die WinSPA Software implementiert und damit nutzbar gemacht hat. Danke auch für all die konstruktiven Diskussionen, die zur Entwicklung der Routine beigetragen haben.
- Mein herzlicher Dank gilt auch Martin Specht, Daniel Poetes und Rolf Paulig für ihre tatkräftige Unterstützung bei allen technischen Projekten. Dies gilt auch für Toni Hanfland, der mich immer mit flüssigem Helium für meine Tieftemperatur-Experimente versorgt hat. Außerdem möchte ich mich bei Knut Hinzen bedanken, der mir bei IT-Problemen immer zur Seite gestanden hat.
- Vor allem möchte ich mich bei allen aktiven und ehemaligen Mitgliedern der Arbeitsgruppe „Organische Filme“ bedanken, die mich während meiner Dissertation begleitet haben. Ohne die freundliche Arbeitsatmosphäre und all die wissenschaftlichen Diskussionen wäre die Zeit nur halb so schön gewesen.
- Ich danke der Deutschen Forschungsgemeinschaft (DFG) für die finanzielle Förderung meines Projekts im Rahmen des TIDE Graduiertenkollegs RTG 2591, sowie der Diamond Light Source für die Förderung von vier Messzeiten, insbesondere jedoch der Messzeit SI33276-1.
- Abschließend möchte ich mich bei meiner Familie und all meinen Freunden dafür bedanken, dass sie während der gesamten Zeit für mich da waren und mich immer unterstützt und ermutigt haben. Danke, dass es so wundervolle Menschen wie euch gibt.

Eidesstattliche Erklärung

Hiermit versichere ich an Eides statt, dass ich die Dissertation "Adsorption and Ordering of Merocyanines on the Ag(100) surface - About the interplay of intermolecular and interfacial interactions" persönlich, selbstständig und ohne Benutzung anderer als der angegebenen Hilfsmittel angefertigt habe, die benutzten Quellen kenntlich gemacht sind und die Arbeit nicht anderweitig als Dissertation eingereicht ist.

Als kumulative Dissertation ist die vorliegende Arbeit an den nachfolgenden Stellen veröffentlicht:

- Anna J. Kny, Max Reimer, Noah Al-Shamery, Ritu Tomar, Thomas Bredow, Selina Olthof, Dirk Hertel, Klaus Meerholz, and Moritz Sokolowski, "Chiral self-organized single 2D-layers of tetramers from a functional donor-acceptor molecule by the surface template effect" Nanoscale **15** 10319 (2023).
- Anna J. Kny, Moritz Sokolowski, and Peter Kury, "Increasing the scan speed in high resolution, low energy electron diffraction measurements by presetting the gate time" Review of Scientific Instruments **94** 064707 (2023).
- Anna J. Kny, Adam Sweetman, and Moritz Sokolowski, "An Atomistic Analysis of the Carpet Growth of KCl Across Step Edges on the Ag(111) Surface" The Journal of Physical Chemistry Letters **16** 696 (2025).

Statement zur Verwendung von künstlicher Intelligenz (KI): Für die Erstellung der vorliegenden Arbeit wurden KI basierte Programme zur Überprüfung der sprachlichen Richtigkeit verwendet. Dies betrifft die Anwendungen Grammarly und DeepL Translator.

Bonn, Mai 2025

(Anna Juliana Kny)